Bragg magnifier optics for dose-efficient X-ray phase contrast imaging

Zur Erlangung des akademischen Grades einer

Doktorin der Naturwissenschaften (Dr. rer. nat.)

von der KIT-Fakultät für Physik des
Karlsruher Instituts für Technologie (KIT)
genehmigte

DISSERTATION

von

M.Sc. Rebecca Spiecker

Referent:	Prof. Dr. Tilo Baumbach
Korreferent:	Prof. Dr. Michael Fiederle
Tag der mündlichen Prüfung:	19.04.2024

Abstract

Propagation-based X-ray phase contrast imaging (PB-PCI) enables the visualization of soft materials and tissues by exploiting the coherent self-interference of the diffracted wavefield behind the sample, which evolves into intensity contrast as the propagation distance between the sample and the detector increases. While phase contrast imaging allows significantly reducing the dose compared to conventional X-ray absorption imaging, the ionizing nature of X-rays still induces radiation damage. The dose therefore needs to be further reduced both for high, micrometer resolution *in vivo* and *in situ* imaging of biological or radiation-sensitive samples, as well as for imaging at moderate resolution of tens to hundreds of micrometers, e.g., in (bio)medical research and diagnostics. However, both resolution regimes face severe constraints. On the one hand, conventional high-resolution detectors suffer from decreasing efficiency with increasing resolution. On the other hand, PB-PCI at moderate resolution requires propagation distances of hundreds of meters to generate sufficient image contrast.

The main objective of this work is to push the limits of dose-efficient X-ray imaging by optimizing the entire imaging process of PB-PCI with respect to the deposited dose. In a first part, high-resolution imaging with highest dose efficiency is realized by combining PB-PCI, asymmetric Bragg crystal optics, and a single photon counting detector, thereby operating close to the theoretical limit of dose efficiency for PB-PCI. The superior imaging performance of the developed system compared to conventional detector systems is demonstrated theoretically and experimentally, and in particular, a substantial increase in dose efficiency is shown for high spatial frequencies, which comprise the relevant high-resolution components of the image. The technique's potential is exemplified by a pilot *in vivo* study of submillimeter-sized parasitoid wasps inside their hosts with unprecedentedly long observation times.

Second, for imaging large, centimeter-sized samples at moderate resolution, a new technique is introduced that allows achieving high propagation-based image contrast within a meter-scale setup, thereby eliminating the need for very long wavefield propagation distances. Simultaneously, the technique reduces image blur caused by the finite size of the X-ray source. The strong increase in image contrast is demonstrated in a proof-of-concept experiment, realized by asymmetric Bragg crystal optics with reversed optical path. This approach paves the way for low-dose studies of large radiation-sensitive specimens, with potential applications ranging from biomedical soft tissue and small animal *in vivo* imaging up to medical diagnostics, e.g., the early detection of breast cancer.

Contents

1. Introduction

With the discovery of X-rays by W. C. Röntgen in 1895, X-ray imaging has found widespread applications, ranging from medical diagnostics over security scanners and nondestructive testing in industry up to present-day research [1]. The high penetration power of X-rays allows studying internal structures in optically opaque samples, rendering X-ray imaging a unique analysis tool. However, soft materials and tissues have for a long time been omitted in X-ray imaging, since they exhibit only low X-ray absorption and thus provide hardly any image contrast. In addition, the ionizing nature of X-rays induces radiation damage in the sample, which limits the amount of radiation that can be used. Nonetheless, X-ray imaging of soft tissues and soft materials is highly desirable for biological, medical and materials science research. Especially in the context of *in situ* or *in vivo* imaging, there exists a high demand to improve image contrast of soft tissues and to reduce the necessary radiation dose, for example for medical diagnostics, to reveal morphodynamics and physiological processes in living organisms, or to provide information about the mechanical properties of a radiation-sensitive material by *in situ* studies.

In the last decades, significant efforts have been made to increase image contrast for objects consisting of light elements. The most successful approach to image light elements is phase contrast imaging, facilitated by the ongoing development of X-ray sources and especially the high coherence provided by modern synchrotrons [2]. Instead of relying solely on the absorption properties of matter, phase contrast methods reveal the phase shift imprinted on a wavefield when traveling through an object. For light elements, phase variation dominates absorption by several orders of magnitude, enabling a strong increase in image contrast [3]. The most common phase contrast approaches include propagation-based imaging [4, 5], interferometric methods based on crystals [6, 7] or gratings [8, 9], analyzer-based imaging [10, 11], and coded-aperture or speckle-based methods [12–14]. The latter are geometrical methods that detect the deflection of the X-ray beam induced by the sample: In coded-aperture and speckle-based imaging, the incident wavefront is modulated by a mask, and the influence of the sample on the intensity distribution is measured. In analyzer-based imaging, the deflection of X-rays is measured by reflecting the X-rays behind the sample with a crystal having a small angular acceptance and detecting the reflected intensity for several angular positions of the crystal. Grating interferometry measures the sample-induced changes in the self-image of a periodic pattern, generated by a grating placed in the beam path and detected by stepping a second grating laterally to the detector. A crystal interferometer splits the beam into two

branches and reunites them after one branch has passed through the sample. If an X-ray source with sufficient coherence is available, propagation-based phase contrast imaging (PB-PCI) has a rather simple realization compared to the previous techniques, since it utilizes solely a detector placed at a certain distance from the sample and does not require further optical elements. By coherent self-interference of the diffracted wavefield behind the sample, the phase shift increasingly evolves into measurable intensity contrast as the distance between the sample and the detector increases. PB-PCI is nowadays widely used, not only in biology and biomedicine [15, 16], but also in natural and cultural heritage [17], materials science [18], and industrial applications [19].

In principle, PB-PCI can be employed for imaging soft materials and tissues both at high, micrometer resolution and at moderate resolutions of several tens of micrometers. However, both resolution ranges come with severe constraints. Increasing the resolution for a given signal-to-noise ratio inherently requires to increase the necessary X-ray fluence, i.e., the amount of X-ray photons per unit area. Therefore, a high dose is needed, and although PB-PCI enables dose reduction compared to absorption imaging, so far, for example, *in vivo* studies at micrometer resolution could only be realized for very short time sequences of a few seconds to minutes before the onset of severe radiation damage in the biological specimens [20–23]. In these studies, conventional high-resolution scintillator-based indirect detector systems have been used. They are constrained by a trade-off between X-ray detection efficiency and achievable resolution. Conversely, PB-PCI of large, centimeter-sized samples at moderate resolution would require less dose per se, which is essential for, e.g., medical diagnostics. However, a propagation distance between the sample and the detector of several tens to hundreds of meters would be necessary to generate sufficient image contrast. Recently, a new synchrotron beamline was built at the European Synchrotron Radiation Facility (ESRF, Grenoble, France) to enable remarkably long propagation distances of up to 36 m. Such long experimental hutches are not only expensive, but often inherently not realizable due to space restrictions. Further, image blur by the finite X-ray source size limits the longest useful propagation distance.

The aim of this thesis is to develop suitable methods to push the limits of dose-efficient X-ray imaging. This goal encompasses two key aspects:

(i) to minimize the dose in PB-PCI of small samples at high resolution, and

(ii) to enable PB-PCI of large samples at moderate resolution within a meter-scale setup, which in turn also allows for a reduced dose.

In general, the imaging process can be divided into three main steps, as visualized in Fig. 1.1: First, the sample information is imprinted on the incident X-ray wavefield. Second, the information encoded in the wavefield is rendered accessible by the generation of detectable image contrast. Third, the provided information is extracted by detecting the X-ray image.

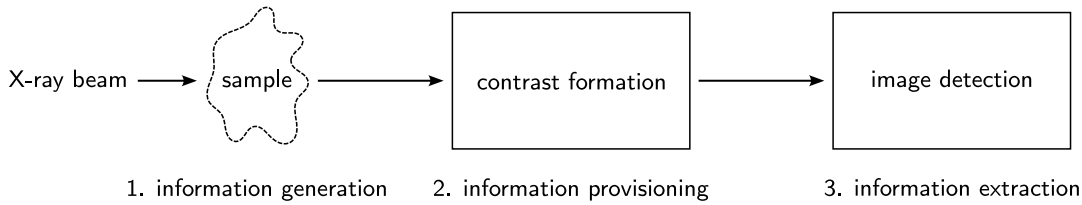

Figure 1.1.: Optimizing dose-efficient X-ray imaging. The process of X-ray imaging can be delineated into three stages, each of which needs to be optimized for achieving highest dose efficiency. First, the sample information is conveyed to the incident X-ray wavefield. Second, the information encoded in the wavefield is made available by generating detectable image contrast. Last, the provided information is extracted by image detection.

This thesis focuses on optimizing each of these steps with regard to the dose deposited in the sample in order to achieve highest dose efficiency.

The first step is addressed by considering the energy-dependent phase shift and dose deposition in the sample in order to determine the ideal operating energy of the X-ray illumination. For high resolution imaging, the second step is readily solved by realizing PB-PCI, while the third step requires overcoming current limitations of high-resolution indirect detector systems, especially their rather low detection efficiency and poor transmission of high spatial frequencies into the final image, which contain the high-resolution components of the object. As a potential solution to this challenge, direct magnification of the X-ray imaging would allow exploiting the high detection efficiency of large-area detectors while maintaining high resolution. For imaging at moderate resolution, the bottleneck is given by the second step, i.e., to generate contrast at low spatial frequencies without building unrealistically long beamlines. Approaching this challenge by modulating the spatial frequency distribution of the diffracted wavefield behind the sample promises to strongly increase image contrast.

These two approaches are addressed by employing Bragg crystal optics, specifically Bragg magnifiers and demagnifiers. A Bragg magnifier enlarges the cross section of an X-ray beam through asymmetric Bragg diffraction, and a Bragg demagnifier reduces it [24]. Here, dose-efficient X-ray imaging at micrometer resolution is tackled by combining PB-PCI, a Bragg magnifier and an efficient detector. By magnifying the diffracted wavefield behind the sample with a Bragg magnifier, the image can be recorded by a large-area detector. In this way, the low detection efficiency of conventional indirect detectors can be overcome by exploiting the high detection efficiency provided by, e.g., single photon counting detectors. Second, for imaging large, centimeter-sized samples at moderate resolution, a new technique is presented here that can achieve high propagation-based image contrast within a meter-scale setup, which eliminates the need for the very long distances that would conventionally be required. By magnifying the spatial frequencies of the diffracted X-ray wavefield behind the sample, the propagation distance is virtually increased to hundreds of meters, whereby the image contrast is considerably enhanced within a short physical distance. Magnification in reciprocal space

is tantamount to demagnification in real space, which is realized by a Bragg demagnifier. Simultaneously to the strong increase in effective propagation distance, the Bragg demagnifier reduces image blur caused by the finite X-ray source size. Both approaches are addressed by theoretical considerations and by an experimental validation.

Outline of the thesis

The thesis is structured as follows: Chapter 2 describes the underlying theoretical concepts. The focus lies on dynamical X-ray diffraction from asymmetrically cut crystals and propagation-based phase contrast imaging. The detection of X-rays by indirect and direct detectors is also briefly discussed.

Chapter 3 introduces the general functionality of Bragg magnifiers and presents an experimental characterization of the developed system. The chapter starts with a historical overview of Bragg magnifiers, followed by a description of the working principle and the operation modes. Next, the image formation is derived and the resulting equations are applied to enable image simulations. Finally, the experimental setup is described and characterized. This combined theoretical groundwork and practical demonstration forms the basis for the following chapters.

Chapter 4 deals with dose-efficient imaging by means of the Bragg magnifier introduced in the previous chapter. It starts with a discussion of the ideal experimental parameters for high dose efficiency and the advantages of using a Bragg magnifier system over a conventional scintillator-based indirect detector system. Next, the developed Bragg magnifier system is compared experimentally to an indirect detector system. Finally, the high dose efficiency of the Bragg magnifier system is demonstrated by a pilot *in vivo* study of parasitoid wasps within their host eggs.

Chapter 5 describes the approach of using a Bragg demagnifier for phase contrast imaging of large samples. The principle of increasing the effective propagation distance by image demagnification is discussed in the first part of this chapter. The second part presents a proof-of-concept experiment, demonstrating the validity of the proposed method.

The thesis concludes in Chapter 6 with a summary of the presented work and an outlook on possible avenues for future research activities in the field of dose-efficient X-ray imaging with Bragg crystal optics.

2. Fundamentals of X-ray diffraction and phase contrast imaging

Since this work combines aspects of crystal X-ray diffraction and phase contrast imaging via Fresnel diffraction, the basic principles of both fields are introduced in this chapter. Section 2.1 provides an overview of X-ray diffraction, which can be described by the kinematical theory, neglecting multiple scattering, or by the dynamical theory for large perfect crystals, taking multiple scattering into account. Emphasis is placed on the latter, with a focus on the parameters that are important for the imaging performance of a Bragg magnifier. The second part of this chapter, Section 2.2, introduces the aspects of X-ray phase contrast imaging that are relevant to the work presented here. Finally, direct and indirect X-ray detectors are briefly discussed in Section 2.3.

2.1. Basics of crystal X-ray diffraction

The discovery of X-ray diffraction dates back to the year 1912, when Paul Ewald was finalizing his thesis with the aim '*to find the optical properties of an anisotropic arrangement of isotropic resonators*' [25] and contacted Max von Laue to discuss his newly established theory. During the conversation, Laue asked Ewald about the distances between the resonators, to which Ewald replied that they were probably in the order of a thousandth of the wavelength of visible light, and that his thesis made no assumptions about the wavelength of the electromagnetic waves. Laue immediately realized that if the atoms in a crystal did indeed form a lattice, the crystal should give rise to interferences of X-rays. With the help of Walter Friedrich and Paul Knipping, Laue experimentally demonstrated the diffraction of X-rays on a copper sulfate crystal and elaborated his geometrical theory of X-ray diffraction, relating the scattering angle to the size and spacing of the crystal's unit cells [26]. He received the Nobel Prize in 1914. Inspired by Laue's work, William Laurence Bragg and his father William Henry Bragg repeated the diffraction experiments, interpreted the results as a reflection on families of lattice planes and derived Bragg's law [27], whereupon they were awarded the Nobel prize in 1915. The theory of dynamical X-ray diffraction, which takes into account multiple scattering effects, was shaped by both Charles Galton Darwin [28, 29], who coined the term Darwin's reflectivity curve, and Ewald, who provided a theoretical basis for the X-ray interferences by crystals [30–32]. Later, Laue reformulated the dynamical theory in a macroscopic way,

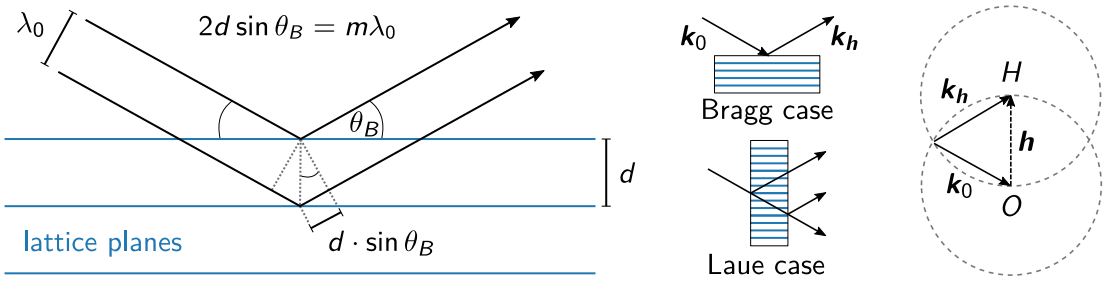

Figure 2.1.: Bragg's law. The diffraction condition is fulfilled when the optical path difference of the diffracted waves corresponds to a multiple of the wavelength. Depending on the exit direction of the reflected waves, a distinction is made between Bragg and Laue geometry. The Laue condition is sketched on the right and is equivalent to Bragg's diffraction condition.

describing a crystal by a continuous distribution of the dielectric susceptibility [33].

More details on the history of the discovery of X-ray diffraction can be found in Refs. [34, 35]. In the following, the approaches of kinematical and dynamical diffraction theory are briefly outlined. It is not intended to give a complete and detailed description, which can be found elsewhere, for example in Refs. [34, 36–38]. It should rather introduce concepts used in the course of this thesis.

2.1.1. Kinematical diffraction

Let us first introduce Bragg's law. As shown schematically in Fig. 2.1, the diffraction condition for an incident wave with angular wavevector $\boldsymbol{k}_0$ and wavelength $\lambda_0 = 2\pi/|\boldsymbol{k}_0|$ at a crystal is given by [27]

$$2d \sin\theta_B = m\lambda_0, \tag{2.1}$$

where $m \in \mathbb{N}$, θ_B is the Bragg angle and d the distance between the reflecting lattice planes. The condition can only be fulfilled for $\lambda_0 < 2d$, i.e., for very short wavelengths. The Laue condition $\boldsymbol{k}_0 - \boldsymbol{k}_{\boldsymbol{h}} = \boldsymbol{h}$ is equivalent to Bragg's formulation and states that constructive interference is obtained when the difference between the incident wavevector $\boldsymbol{k}_0$ and the diffracted wavevector $\boldsymbol{k}_{\boldsymbol{h}}$ corresponds to a reciprocal lattice vector $\boldsymbol{h}$, which points from the reciprocal lattice point O to the lattice point H, see right panel of Fig. 2.1. The Ewald construction shows geometrically whether the Laue condition is fulfilled [34]. As a side note, a distinction is made between Bragg and Laue geometry depending on whether the reflected beam stays on the same side of the crystal as the incident beam or exits on the opposite side, see also Fig. 2.1. In this thesis, the Bragg geometry is used.

In the kinematical or geometrical diffraction theory, the first Born approximation leads to a description of the diffracted intensities [38, 39]. In this theory, each scatterer is assumed to experience the incident field as the driving field, and each scattered wave exits the crystal

without being re-scattered. Since this assumption violates energy conservation, it is only a good approximation for small or imperfect crystals [38].

Being a 3D periodic array of atoms, a crystal can be described by the electron density $\rho_0(\boldsymbol{r})$ of one unit cell convolved by Dirac delta distributions $\delta(\boldsymbol{r} - \boldsymbol{r}_i)$ centered at the periodically spaced position vectors $\boldsymbol{r}_i$ of the origin of each unit cell. Here, $\boldsymbol{r} = (x, y, z)^{\mathrm{T}}$ denotes the spatial coordinate vector, where T stands for the transposition of the vector. To account for the finite size of the crystal, the shape function $y(\boldsymbol{r})$ is introduced, being 1 inside the crystal and 0 outside. The total electron density is then given by

$$\rho(\boldsymbol{r}) = \left[\rho_0(\boldsymbol{r}) * \sum_{i=-\infty}^{\infty} \delta(\boldsymbol{r} - \boldsymbol{r}_i)\right] \cdot y(\boldsymbol{r}), \tag{2.2}$$

where $*$ denotes the convolution operator. The total diffracted amplitude A is obtained by adding all diffracting centers while considering the optical path differences and taking the diffracted amplitude of each diffraction center to be unity. In reciprocal space, one thus obtains [38]

$$A(\boldsymbol{k}) = \int \rho(\boldsymbol{r}) e^{-\mathrm{i}\boldsymbol{k}\cdot\boldsymbol{r}} \mathrm{d}^3\boldsymbol{r} \tag{2.3}$$

with $\boldsymbol{k} = \boldsymbol{k_h} - \boldsymbol{k}_0$ being the diffraction vector between the incident and the diffracted wave. The diffracted amplitude is therefore given by the Fourier transform of the electron density. Introducing the structure factor

$$F_{\boldsymbol{h}} = \int_{-\infty}^{\infty} \rho_0(\boldsymbol{r}) e^{-\mathrm{i}\boldsymbol{h}\cdot\boldsymbol{r}} \mathrm{d}^3\boldsymbol{r} \tag{2.4}$$

of a reciprocal lattice point H with reciprocal lattice vector $\boldsymbol{h}$, and the Fourier transform

$$Y(\boldsymbol{k}) = \int_{-\infty}^{\infty} y(\boldsymbol{r}) e^{-\mathrm{i}\boldsymbol{k}\cdot\boldsymbol{r}} \mathrm{d}^3\boldsymbol{r} \tag{2.5}$$

of the shape function, Eq. 2.3 can now be rewritten as [38]

$$A(\boldsymbol{k}) = \frac{1}{V} \sum_{\boldsymbol{h}} F_{\boldsymbol{h}} Y(\boldsymbol{k} - \boldsymbol{h}). \tag{2.6}$$

Here, V is the volume element of the unit cell. As can be seen from Eq. 2.6, the diffracted amplitude is concentrated around each reciprocal lattice vector, and the distribution is given by the Fourier transform of the shape function weighted by the structure factor. For increasing crystal volumes, $Y(\boldsymbol{k})$ also increases, and the diffracted amplitude diverges to infinity. As mentioned before, the kinematical theory is therefore only valid for thin crystals.

2.1.2. Dynamical diffraction

In contrast to the kinematical theory, the dynamical theory provides a full description of the diffraction process including multiple diffraction by solving Maxwell's equations inside a crystal. The solutions inside the crystal are linked to the wavefields on the outside by the boundary conditions at the crystal surface. The resulting reflectivity curve describes the ratio of the incident and exit wavefields' intensities. This section discusses the derivation of Laue's formulation, following Ref. [34]. For better readability, uppercase $\boldsymbol{K}$ is used for waves inside the crystal, lowercase $\boldsymbol{k}$ outside the crystal, and the length of the vacuum wavevector, also called angular wavenumber, is denoted by $k_0 = 2\pi/\lambda_0$, where λ_0 is the wavelength in vacuum.

Maxwell's equations in a linear and isotropic medium

Maxwell's equations inside a medium in the absence of free charges are given by [40]

$$\nabla \cdot \boldsymbol{D} = 0, \tag{2.7}$$

$$\nabla \cdot \boldsymbol{B} = 0, \tag{2.8}$$

$$\nabla \times \boldsymbol{E} = \mathrm{i}\omega \boldsymbol{B}, \tag{2.9}$$

$$\nabla \times \boldsymbol{H} = -\mathrm{i}\omega \boldsymbol{D}, \tag{2.10}$$

where ω is the angular frequency of a time-periodic excitation. They describe the relationship between the electric and magnetic fields $\boldsymbol{E}$ and $\boldsymbol{B}$, the electric displacement field $\boldsymbol{D}$ and the magnetizing field $\boldsymbol{H}$. These quantities are connected by the polarization $\boldsymbol{P}$ and the magnetization $\boldsymbol{M}$ of the medium. The following considerations are restricted to a linear and isotropic medium, where

$$\boldsymbol{D} = \varepsilon_0 \boldsymbol{E} + \boldsymbol{P} = \varepsilon_0 \varepsilon_\mathrm{r} \boldsymbol{E}, \tag{2.11}$$

$$\boldsymbol{B} = \mu_0 (\boldsymbol{H} + \boldsymbol{M}) = \mu_0 \mu_\mathrm{r} \boldsymbol{H}, \tag{2.12}$$

with ε_0 and μ_0 being the permittivity and permeability of vacuum, and ε_r and μ_r the scalar relative permittivity and permeability of the medium. In the media treated in this thesis, μ_r can safely be set to 1. The relative permittivity $\varepsilon_\mathrm{r} = 1 + \chi$ is usually expressed via the electric susceptibility $\chi(\boldsymbol{r}, \omega)$, which is in general spatially- and frequency-dependent.

In a homogeneous medium or empty space, χ is spatially constant. Taking the curl of Eq. 2.9 and using the curl of the curl identity as well as $\nabla \cdot \boldsymbol{E} = 0$ leads to the wave equation [41]

$$\nabla^2 \boldsymbol{E} + \omega^2 \mu_0 \varepsilon_0 \varepsilon_\mathrm{r} \boldsymbol{E} = 0. \tag{2.13}$$

The electric field can be decomposed into monochromatic plane waves of the form $\boldsymbol{E}(\boldsymbol{r}) = \tilde{\boldsymbol{E}} e^{\mathrm{i}\varphi} \cdot e^{\mathrm{i}\boldsymbol{k}\boldsymbol{r} - \mathrm{i}\omega t}$, each solving Eq. 2.13. Here, $\tilde{\boldsymbol{E}}$ is the amplitude vector pointing in the direction of the polarization, $\boldsymbol{k} = (k_x, k_y, k_z)^\mathrm{T}$ defines the propagation direction, and φ is a phase shift

of the plane wave. The wavevector $\boldsymbol{k} = \boldsymbol{k}_\mathrm{r} + \mathrm{i}\boldsymbol{k}_\mathrm{i}$ is in general complex-valued, leading to a damping of the electric field. Insertion of the plane wave ansatz into Eq. 2.13 leads to the equation [42]

$$(-\boldsymbol{k}^2 + k_0^2 n^2) \cdot \tilde{\boldsymbol{E}} = 0, \tag{2.14}$$

where $k_0 = \omega/c$ is the angular wavenumber in vacuum, and $c = 1/\sqrt{\mu_0 \varepsilon_0}$ is the speed of light in vacuum. In addition, the complex refractive index of the medium

$$n = \sqrt{\varepsilon_\mathrm{r}} = \sqrt{1+\chi} = 1 - \delta + \mathrm{i}\beta \tag{2.15}$$

has been introduced.

In Eq. 2.14, it seems that the components of $\tilde{\boldsymbol{E}}$ can be chosen arbitrarily. However, it follows from Eq. 2.7 that $\boldsymbol{k} \perp \tilde{\boldsymbol{E}}$. Since X-ray imaging deals with the diffraction of X-rays to small angles, changes in the electric field polarization can be neglected, and it is sufficient to consider the scalar equation [43]

$$(\nabla^2 + k_0^2 n^2)\psi(\boldsymbol{r}) = 0 \tag{2.16}$$

for a monochromatic wavefield $\psi(\boldsymbol{r})$ describing the electric field along the polarization axis. This so-called Helmholtz equation is the cornerstone for X-ray imaging and will be used in Section 2.2.

In a non-homogeneous medium, $\chi(\boldsymbol{r})$ is spatially dependent. Thus, the wave equation is of the form

$$\nabla(\nabla \cdot \boldsymbol{E}) - \nabla^2 \boldsymbol{E} = k_0^2 (1+\chi)\boldsymbol{E}. \tag{2.17}$$

This is the basic equation of dynamical diffraction theory and will be the starting point for the following considerations [34].

Dynamical diffraction by perfect crystals

In a perfect crystal, the charge density $\rho(\boldsymbol{r})$ and hence the susceptibility $\chi(\boldsymbol{r})$ are periodic. To find solutions to the basic equation of dynamical diffraction (Eq. 2.17), $\chi(\boldsymbol{r})$ can be decomposed into a Fourier series

$$\chi(\boldsymbol{r}) = \sum_{\boldsymbol{h}} \chi_{\boldsymbol{h}} e^{\mathrm{i}\boldsymbol{h}\cdot\boldsymbol{r}}, \tag{2.18}$$

where the sum goes over all reciprocal lattice vectors $\boldsymbol{h}$ that point from O to any reciprocal lattice point H. Choosing as ansatz the Ewald wavefield [34]

$$\begin{aligned}\boldsymbol{E}(\boldsymbol{r}) &= e^{\mathrm{i}\boldsymbol{K_o}\boldsymbol{r}} \sum_{\boldsymbol{h}} \boldsymbol{E_h} e^{\mathrm{i}\boldsymbol{h}\cdot\boldsymbol{r}} \\ &= \sum_{\boldsymbol{h}} \boldsymbol{E_h} e^{\mathrm{i}\boldsymbol{K_h}\cdot\boldsymbol{r}},\ \boldsymbol{K_h} = \boldsymbol{K_o} + \boldsymbol{h},\end{aligned} \tag{2.19}$$

where $\boldsymbol{K_o}$ is the wavevector of the Ewald wave inside the crystal[1], it holds for the left side of Eq. 2.17

$$\nabla(\nabla\cdot\boldsymbol{E}(\boldsymbol{r})) - \nabla^2\boldsymbol{E}(\boldsymbol{r}) = -\sum_{\boldsymbol{h}} (\boldsymbol{K_h} \underbrace{(\boldsymbol{K_h}\cdot\boldsymbol{E_h})}_{\approx 0} - K_{\boldsymbol{h}}^2 \boldsymbol{E_h}) e^{\mathrm{i}\boldsymbol{K_h}\cdot\boldsymbol{r}}, \tag{2.20}$$

with $K_{\boldsymbol{h}}^2 := \boldsymbol{K}_{\boldsymbol{h}}^2$. The wave is assumed to be transverse, as the interaction term is small for X-rays. Together with Eq. 2.18, Eq. 2.17 becomes

$$\sum_{\boldsymbol{h}} K_{\boldsymbol{h}}^2 \boldsymbol{E_h} \cancel{e^{\mathrm{i}\boldsymbol{K_o}\boldsymbol{r}}} e^{\mathrm{i}\boldsymbol{h}\cdot\boldsymbol{r}} = k_0^2 \sum_{\boldsymbol{h}} \sum_{\boldsymbol{h'}} (1 + \chi_{\boldsymbol{h'}} e^{\mathrm{i}\boldsymbol{h'}\cdot\boldsymbol{r}}) \boldsymbol{E_h} \cancel{e^{\mathrm{i}\boldsymbol{K_o}\boldsymbol{r}}} e^{\mathrm{i}\boldsymbol{h}\cdot\boldsymbol{r}}. \tag{2.21}$$

Multiplying this equation by $e^{-\mathrm{i}\boldsymbol{h''}\cdot\boldsymbol{r}}$ and integrating over the entire space yields

$$\begin{aligned}&\sum_{\boldsymbol{h}} K_{\boldsymbol{h}}^2 \boldsymbol{E_h} \underbrace{\int e^{\mathrm{i}(\boldsymbol{h}-\boldsymbol{h''})\boldsymbol{r}} \mathrm{d}^3\boldsymbol{r}}_{(2\pi)^3\delta(\boldsymbol{h}-\boldsymbol{h''})} \\ &\quad = k_0^2 \sum_{\boldsymbol{h}} \sum_{\boldsymbol{h'}} \left(\underbrace{\int e^{\mathrm{i}(\boldsymbol{h}-\boldsymbol{h''})\cdot\boldsymbol{r}} \mathrm{d}^3\boldsymbol{r}}_{(2\pi)^3\delta(\boldsymbol{h}-\boldsymbol{h''})} + \chi_{\boldsymbol{h'}} \underbrace{\int e^{\mathrm{i}(\boldsymbol{h}+\boldsymbol{h'}-\boldsymbol{h''})\cdot\boldsymbol{r}} \mathrm{d}^3\boldsymbol{r}}_{(2\pi)^3\delta(\boldsymbol{h}+\boldsymbol{h'}-\boldsymbol{h''})} \right) \boldsymbol{E_h}.\end{aligned} \tag{2.22}$$

It follows that

$$k_0^2 \boldsymbol{E_h} - K_{\boldsymbol{h}}^2 \boldsymbol{E_h} = -k_0^2 \sum_{\boldsymbol{h'}} \chi_{\boldsymbol{h'}} \boldsymbol{E}_{\boldsymbol{h}-\boldsymbol{h'}}, \tag{2.23}$$

or equivalently

$$\boldsymbol{E_h} = \frac{k_0^2}{K_{\boldsymbol{h}}^2 - k_0^2(1+\chi_{\boldsymbol{o}})} \sum_{\boldsymbol{h'}\neq\boldsymbol{h}} \chi_{\boldsymbol{h'}} \boldsymbol{E}_{\boldsymbol{h}-\boldsymbol{h'}}. \tag{2.24}$$

This infinite set of equations is called the fundamental equations of dynamical theory [34]. They imply that the amplitude $\boldsymbol{E_h}$ of a diffracted wave depends on all other diffracted waves. The denominator indicates that only waves whose wavevector has a length close to $K := k_0 n = k_0\sqrt{1+\chi_{\boldsymbol{o}}}$ will have a non-negligible amplitude.

[1] The same concept was introduced 15 years later by F. Bloch for solid state physics [44].

Two-beam case

There exists no rigorous solution to the fundamental equations. However, in many cases the problem can be reduced to the case where only one reciprocal lattice vector contributes to the scattering process, and there are only two non-negligible plane waves $\boldsymbol{E_o}$ and $\boldsymbol{E_h}$ [34]. Eq. 2.23 then becomes

$$[K^2 - K_{\boldsymbol{o}}^2]\boldsymbol{E_o} + k_0^2 \chi_{\bar{\boldsymbol{h}}} \boldsymbol{E_h} = 0, \tag{2.25}$$

$$k_0^2 \chi_{\boldsymbol{h}} \boldsymbol{E_o} + [K^2 - K_{\boldsymbol{h}}^2]\boldsymbol{E_h} = 0, \tag{2.26}$$

where $\chi_{\bar{\boldsymbol{h}}} = \chi_{-\boldsymbol{h}}$. Projecting Eq. 2.25 to $\boldsymbol{E_o}$ and Eq. 2.26 to $\boldsymbol{E_h}$, respectively, and defining the polarization factor $C = 1$ for σ-polarization and $C = \cos 2\theta_{\mathrm{B}}$ for π-polarization, one obtains [34]

$$[K^2 - K_{\boldsymbol{o}}^2]E_{\boldsymbol{o}} + k_0^2 C \chi_{\bar{\boldsymbol{h}}} E_{\boldsymbol{h}} = 0, \tag{2.27}$$

$$k_0^2 C \chi_{\boldsymbol{h}} E_{\boldsymbol{o}} + [K^2 - K_{\boldsymbol{h}}^2]E_{\boldsymbol{h}} = 0. \tag{2.28}$$

To solve this set of equations, the determinant is set equal to zero, resulting in the dispersion equation for the two-beam case:

$$(K_{\boldsymbol{o}}^2 - K^2) \cdot (K_{\boldsymbol{h}}^2 - K^2) = k_0^4 C^2 \chi_{\boldsymbol{h}} \chi_{\bar{\boldsymbol{h}}}. \tag{2.29}$$

The dispersion surface consists of two spheres centered at the reciprocal lattice points O and H with radius K and connected to each other, where the strength of the connection is given by the right-hand side of Eq. 2.29. The intersection of the dispersion surface with the scattering plane is plotted in Fig. 2.2 (for details, see Appendix A.1). Note that the dispersion curves for the two polarization directions are slightly different (light and dark blue lines in Fig. 2.2a, b). The spheres with radius k_0 in vacuum can be understood as the dispersion surface in vacuum and are indicated by dashed lines. Their intersection is called the Laue point L_a and defines the Bragg angle θ_{B}. The intersection of the inner spheres with radius K is called the Lorentz point L_o.

As a next step, a semi-infinite planar crystal is considered. The considerations here are restricted to the case of Bragg geometry (see Fig. 2.1). The boundary condition states that the components of the wavevector parallel to the crystal surface are preserved [34]. This condition is visualized in Fig. 2.2 for the case of coplanar scattering geometry, where $\boldsymbol{k}_0$, $\boldsymbol{h}$ and the normal vector $\boldsymbol{e}_n$ to the crystal surface lie in one plane. The incident wave $\boldsymbol{k}_0$ defines the position of the normal on the dispersion surface. The boundary condition is satisfied for all waves pointing from the intersections of the normal with the dispersion surface, the so-called tiepoints, to O or H. As a result, there exist four pairs of solutions $\boldsymbol{K}_{\boldsymbol{o},\boldsymbol{h}}^{(j)}$ inside the crystal (Fig. 2.2b). The reflected and diffracted waves in vacuum $\boldsymbol{k}_r$ and $\boldsymbol{k_h}$ as well as the reflected diffracted wave $\boldsymbol{k}_{\boldsymbol{h}r}$ are shown in Fig. 2.2a. For symmetric reflection, $\boldsymbol{e}_n$ and $\boldsymbol{h}$ are

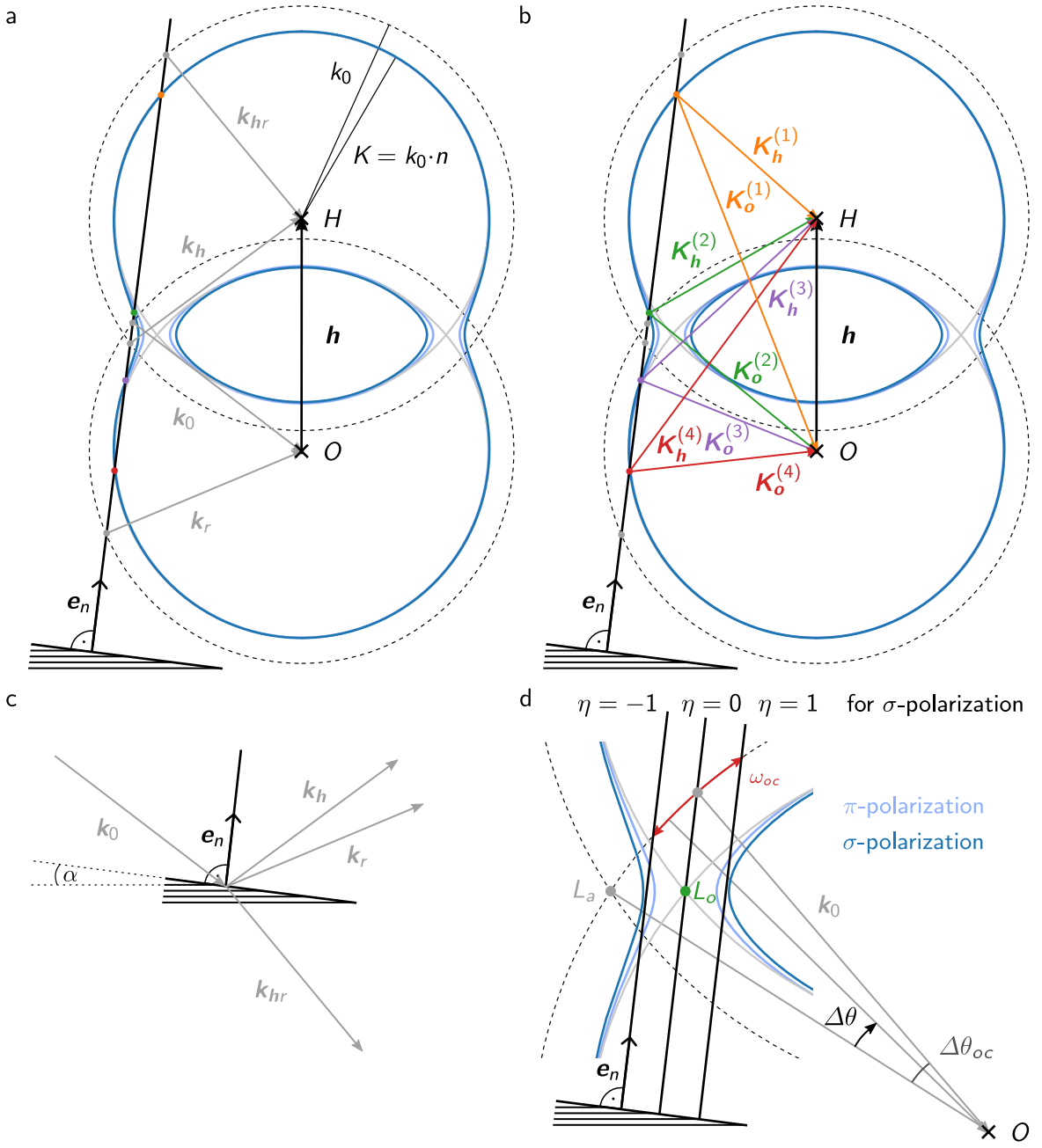

Figure 2.2.: Schematic of the dispersion surface. The dispersion surface shows the solutions of the dispersion equation for σ- (dark blue) and π-polarization (light blue), neglecting absorption in the crystal and showing all quantities as real-valued. The boundary conditions are satisfied at the intersections with the normal $\boldsymbol{e}_n$ to the crystal surface, which here has a positive asymmetry angle α to the lattice planes. **a** The wavevectors in vacuum are shown separately from **b** the wavevectors inside the crystal. The incident plane wave $\boldsymbol{k}_0$ defines the position of the surface normal and thus the reflected, the diffracted, and the reflected diffracted waves $\boldsymbol{k}_r$, $\boldsymbol{k}_{\boldsymbol{h}}$ and $\boldsymbol{k}_{\boldsymbol{h}r}$. Inside the crystal, there are four intersections, each with two waves $\boldsymbol{K}_{\boldsymbol{o}}^{(j)}$ and $\boldsymbol{K}_{\boldsymbol{h}}^{(j)}$. **c** Vacuum wavevectors in real space. **d** Zoom-in on the gap between the two branches of the dispersion surface. The center of the reflection curve is reached when $\boldsymbol{e}_n$ crosses the Lorentz point L_o, with the angular deviation $\Delta\theta_{oc}$ from the Laue point L_a. The deviation parameter η goes from -1 to 1 through the Bragg gap. The Darwin width ω_{oc} is shown in red. For further details see Appendix A.1.

parallel, and the angle of the incident wavevector to the crystal surface corresponds to the exit angle. In the case of asymmetric reflection, which is used in this work, the reflecting lattice planes are not parallel to the crystal surface. The angle between $\boldsymbol{e}_n$ and $\boldsymbol{h}$ is called the asymmetry angle α. In the case of a positive asymmetry angle, as shown in Fig. 2.2, the exit angle of $\boldsymbol{k_h}$ to the crystal surface is increased compared to the incident angle of $\boldsymbol{k}_0$.

The amplitude ratio of the waves is obtained from Eq. 2.27 [34]:

$$\frac{E_{\boldsymbol{h}}^{(j)}}{E_{\boldsymbol{o}}^{(j)}} = \frac{K_{\boldsymbol{o}}^{(j)2} - K^2}{k_0^2 C \chi_{\bar{\boldsymbol{h}}}} = \frac{k_0^2 C \chi_{\boldsymbol{h}}}{K_{\boldsymbol{h}}^{(j)2} - K^2}. \tag{2.30}$$

The task is to find non-propagating solutions inside the crystal, i.e., complex solutions for $\boldsymbol{K_o}, \boldsymbol{K_h}$. In Fig. 2.2d, the situation is considered where $\boldsymbol{k}_0$ is at such an angle that $\boldsymbol{e}_n$ lies inside the gap between the two branches, and the wavevectors become imaginary. The intensity of the diffracted wave is highest when these waves are excited inside the crystal. By changing the incident angle of $\boldsymbol{k}_0$, the normal crosses the gap between the two branches. The resulting reflectivity curves over the angles of incidence or exit are also known as the Darwin curves [37]. The Darwin width ω_{oc} or ω_{hc} of the incident or outgoing curve, respectively, is marked in Fig. 2.2d in red.

By geometrical considerations, several characteristics and analytical expressions can be derived, which are briefly described in the following. For a precise derivation, see Refs. [34, 37, 45]. An overview of the parameters relevant for this thesis is given in Fig. 2.3 for the case of a positive asymmetry angle. The angle $\Delta\theta$ is defined as the difference of the angle between the beam to the crystal lattice planes and the Bragg angle, i.e., $\Delta\theta = 0$ when the kinematical Bragg condition is satisfied (marked in green in Fig. 2.3, and see also Fig. 2.2d). In Fig. 2.3, the reflectivity curve for the silicon (Si) (220) reflection with $\alpha = 5.92°$ and at 29 keV is shown in blue for the incident beam and in purple for the exit beam. The curves for σ- and π-polarization are almost identical, since $C = \cos 2\theta_\mathrm{B} = 0.98$, which is why only the curves for σ-polarization are depicted. Due to refraction inside the crystal, the center of the reflectivity curves is not reached when $\boldsymbol{e}_n$ crosses the Laue point L_a, but when it crosses the Lorentz point L_o (see Fig. 2.2d). This deviation from the kinematical Bragg condition is denoted as $\Delta\theta_{oc}$ or $\Delta\theta_{hc}$ for the incident and exit direction, respectively (marked in orange in Fig. 2.3). The Darwin width ω_{oc} for the incident direction is strongly increased, while ω_{hc} is compressed for the exit direction (both shown in red). This effect will be exploited in the remaining chapters.

Analytical expressions for the mentioned parameters and the reflectivity curve can be obtained by approximating the dispersion equation as a second order equation, which is valid when the tiepoint is close to the Lorentz point [34]. For highly asymmetric reflection, however, the approximation is no longer valid, and a correction term must be included [34, 37, 45]. From the considerations detailed in Ref. [34], it follows that the deviation from the kinematical

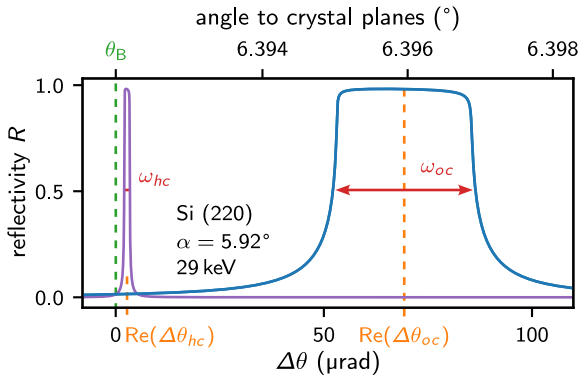

Figure 2.3.: Parameters resulting from dynamical diffraction theory. To illustrate the most important parameters resulting from dynamical diffraction theory, the incident (blue) and exit (purple) reflectivity curves of the Si (220) reflection with a positive asymmetry angle $\alpha = 5.92°$ is shown for 29 keV. The center of the incident and outgoing curves is shifted from the Bragg angle θ_B (green) by $\mathrm{Re}(\Delta\theta_{oc})$ or $\mathrm{Re}(\Delta\theta_{hc})$, respectively (orange). The width of the curves is given by the Darwin width ω_{oc} or ω_{hc}, respectively (red). The angle $\Delta\theta$ is defined such that $\Delta\theta = 0$ when the kinematical Bragg condition is fulfilled.

Bragg condition is given by the real part of

$$\Delta\theta_{oc} = \frac{-\gamma_o + \sqrt{\gamma_o^2 - (\gamma_o - \gamma_h)\sqrt{1-\gamma_o^2}\chi_{\boldsymbol{o}}/\sin 2\theta_B}}{\sqrt{1-\gamma_o^2}}. \tag{2.31}$$

The quantity $\Delta\theta_{oc}$ itself is complex because of absorption inside the crystal, i.e., $\chi_{\boldsymbol{o}}$ is complex. The parameters $\gamma_h = -\sin(\theta_B + \alpha)$ and $\gamma_o = \sin(\theta_B - \alpha)$ define the asymmetry ratio

$$\gamma = \frac{\gamma_h}{\gamma_o}. \tag{2.32}$$

An expression similar to Eq. 2.31 (replacing γ_o by $-\gamma_h$ and vice versa) defines the deviation $\Delta\theta_{hc}$ of the outgoing beam. The Darwin width for symmetric reflection is given by twice the real part of the parameter [34]

$$\delta_o = \frac{|C|\sqrt{\chi_{\boldsymbol{h}}\chi_{\bar{\boldsymbol{h}}}}}{\sin 2\theta_B}. \tag{2.33}$$

The stronger the susceptibility $\chi_{\boldsymbol{h}}$ and thus the interaction of the waves with matter, the larger the Darwin width. For asymmetric reflection, the Darwin width $\omega_{oc} = 2\mathrm{Re}[\delta_{oc}]$ of the incident beam is given by the parameter [34]

$$\delta_{oc} = \delta_o\sqrt{|\gamma|}\frac{\theta_B - \alpha}{\Delta\theta_{oc} + \theta_B - \alpha}. \tag{2.34}$$

The expression Re[...] denotes the real part. Again, an according expression can be found for δ_{hc} and the Darwin width ω_{hc} of the outgoing beam. To express the amplitude ratio given by

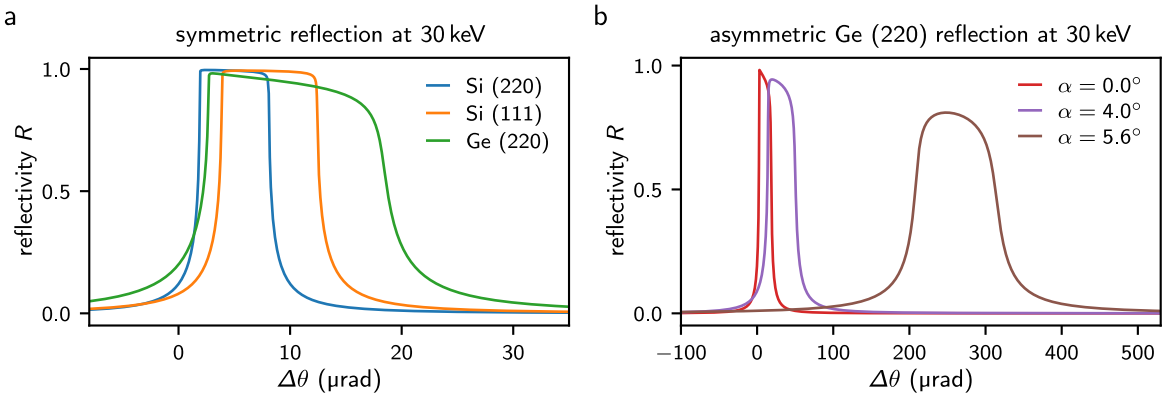

Figure 2.4.: Example of reflectivity curves. a Reflectivity curves for the Si (111), Si (220) and Ge (220) reflections at an X-ray photon energy of 30 keV. Ge (220) has the highest susceptibility and therefore the largest Darwin width. **b** Reflectivity curves for the Ge (220) reflection at different asymmetry angles α. The closer α is to the Bragg angle, the larger the Darwin width and the shift of the reflection curve from the kinematical Bragg condition. The peak reflectivity decreases with increasing asymmetry angle.

Eq. 2.30, the deviation parameter η is introduced:

$$\eta = \frac{\Delta\theta - \Delta\theta_{oc}}{\delta_{oc}}. \tag{2.35}$$

The complex field amplitude ratio can then be written as [34]

$$A = -\frac{\mathrm{sgn}(C)}{\sqrt{|\gamma|}} \frac{\sqrt{\chi_{\boldsymbol{h}}\chi_{\bar{\boldsymbol{h}}}}}{\chi_{\bar{\boldsymbol{h}}}} \left[\eta - \mathrm{sgn}(\mathrm{Re}[\eta])\sqrt{\eta^2 - 1}\right], \tag{2.36}$$

where $\mathrm{sgn}(\mathrm{Re}[\eta])$ is the sign of the real part of η. It is -1 for the outer branch and $+1$ for the inner branch (see Fig. 2.2d). Accordingly, the reflectivity curve is given by

$$R = |\gamma| \cdot |A|^2 = \left|\frac{\chi_{\boldsymbol{h}}}{\chi_{\bar{\boldsymbol{h}}}}\right| \cdot \left|\eta - \mathrm{sgn}(\mathrm{Re}[\eta])\sqrt{\eta^2 - 1}\right|^2. \tag{2.37}$$

Besides these analytical expressions, the amplitude and reflectivity of the refracted and reflected waves can also be calculated numerically for non-coplanar diffraction from the dispersion equation and the boundary conditions, see, e.g., the algorithm of X. Huang [46]. For the purpose of this work, all relevant parameters are obtained by the analytical expressions.

Fig. 2.4a shows reflectivity curves of the symmetric Si (220) and (111) reflections and the symmetric germanium (Ge) (220) reflection at an X-ray photon energy of 30 keV. Ge (220) has a large susceptibility, resulting in a comparatively broad reflectivity curve. In Fig. 2.4b, the reflectivity curves for different asymmetry angles are shown. The Darwin width increases with α, while the peak reflectivity decreases due to absorption and smaller incident angles close to specular reflection. Here, the curves are shown for the Ge (220) reflection as an

example, since the effect of decreasing reflectivity is best visible. Note that the described behavior holds only until α reaches the Bragg angle and the geometry changes to the Laue case [34].

The characteristics of asymmetric Bragg diffraction will be further elucidated in Chapter 3 in the context of Bragg magnifier imaging. In particular, the relation between the incident and outgoing wavefields is exploited to modify the spatial frequencies k_x, k_y of the object wavefield, which are related to the angle $\Delta\theta$ and carry information about the sample.

2.2. X-ray phase contrast imaging

In the 20th century, most applications of full-field X-ray imaging were based on absorption contrast, where the absorption of X-rays in a sample leads to a measurable image contrast [47]. By rotating the sample and acquiring projection images at different angles, the 3D distribution of the sample's X-ray mass attenuation coefficient can be reconstructed [48]. While absorption-based imaging is still the predominant imaging method at laboratory sources, phase contrast methods have emerged with the establishment of modern synchrotrons with highly coherent X-ray beams [2]. Meanwhile, phase contrast imaging has become the standard method for visualizing soft tissues and materials, e.g., in biological or medical specimens, revealing phase changes of the X-rays penetrating through the specimen. Especially in the case of light elements, phase variation dominates absorption by several orders of magnitude [3]. The most common full-field phase contrast imaging techniques can be divided into two areas, namely propagation-based phase contrast imaging (PB-PCI) [4, 49, 50] and differential phase contrast imaging (DPCI) [51–53]. DPCI techniques are typically used for spatial resolutions of several to hundreds of micrometers and require additional elements in the beam path to convert phase shifts into measurable intensity contrast. Here, the focus lies on parallel-beam PB-PCI, which is the method of choice for micrometer resolution and is characterized by a simple experimental implementation without the need for advanced optical elements.

The aim of the following sections is to introduce the contrast formation by free space propagation and to outline methods for reconstructing the object function from an intensity pattern. In Fig. 2.5, a schematic of the general working principle and an example of PB-PCI of a biological sample are given. The incident X-ray wavefield is transmitted through the sample, thereby experiencing a modulation in phase and amplitude. By free space propagation, the phase information encoded in the wavefield evolves into intensity contrast as the propagation distance between the sample and the detector increases. The phase information can finally be reconstructed from the recorded interference pattern. The following considerations start by describing the influence of an object on the illuminating wavefield using the complex index of refraction and introducing the projection approximation, which is valid for sufficiently thin objects. Next, the diffraction of plane waves in free space is derived, leading to the so-called free space propagator. By introducing the Fresnel approximation and the assumption of weak

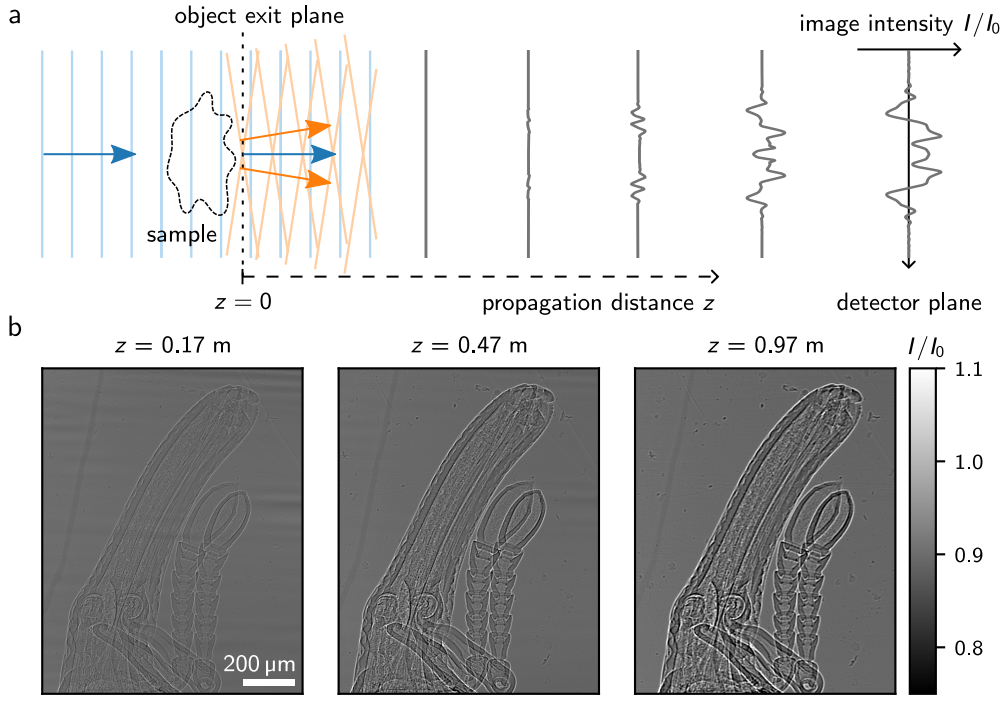

Figure 2.5.: Schematic of propagation-based phase contrast. a Working principle of PB-PCI. The incident wavefield is diffracted by the sample, thereby experiencing attenuation and a phase shift. By free space propagation of the transmitted wavefield, the phase shift increasingly evolves into intensity contrast with increasing propagation distance z between sample and detector. **b** Examples of increasing contrast in PB-PCI of a weevil at increasing propagation distances. The data were acquired at the P23 beamline at PETRA III in Hamburg, Germany, at 30.5 keV and with an indirect detector system having an effective pixel size of $\Delta x = 0.72\,\mu\text{m}$. For details on the indirect detector system, see Section 4.2.

or weakly varying phase objects, well-known phase retrieval methods based on the transport of intensity equation (TIE) [50] and the contrast transfer function (CTF) [49] are derived. In addition, a phase retrieval method is described that considers the mean absorption in the sample and, in the limiting cases of short distances or low absorption, corresponds to the well-known algorithms derived from TIE and CTF. A more detailed consideration of the contrast formation and phase retrieval algorithms can be found in Refs. [41, 43].

2.2.1. Complex index of refraction

The coherent interaction of X-rays with matter can be described by the complex index of refraction

$$n = 1 - \delta + \mathrm{i}\beta, \tag{2.38}$$

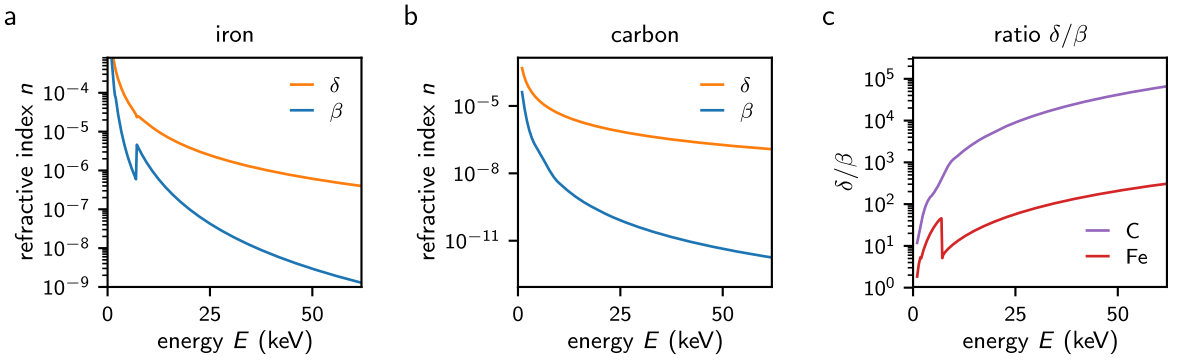

Figure 2.6.: Complex index of refraction. a, b Decrement δ of the real part and imaginary part β of the refractive index n over photon energy E for iron and carbon. **c** Ratio δ/β for the elements shown in panels a and b. Especially for light elements like carbon and for high energies, the phase factor δ is several orders of magnitude higher than the absorption factor β. The data was taken from the NIST database [56].

see also Eq. 2.15. Far from atomic resonances, it holds [54, 55]

$$\delta = \frac{r_e \lambda_0^2 n_e}{2\pi} \propto \frac{1}{E^2} \text{ and } \beta = \frac{\mu \lambda_0}{4\pi} \propto \frac{1}{E^4}, \tag{2.39}$$

where r_e is the classical electron radius, n_e the electron density and μ the mass absorption coefficient. For X-rays, the deviation of the index of refraction from unity is very small, i.e., $0 \leq \beta \ll 1$ and $0 \leq \delta \ll 1$. Therefore, it holds that

$$n(\boldsymbol{r})^2 = 1 + \chi(\boldsymbol{r}) = (1 - \delta(\boldsymbol{r}) + \mathrm{i}\beta(\boldsymbol{r}))^2 \approx 1 - 2\delta(\boldsymbol{r}) + 2\mathrm{i}\beta(\boldsymbol{r}). \tag{2.40}$$

Typically, the values for δ are several orders of magnitude higher than β, especially for light elements and high energies [3], see Fig. 2.6. For this reason, phase contrast methods offer great potential for imaging light elements.

2.2.2. Projection approximation

The first step is to find an expression for the influence of an object on a monochromatic X-ray wavefield passing through the sample at $z = 0$. Following the argumentation line of Ref. [43], the projection approximation can be derived for a sufficiently thin object. An X-ray wave $\psi(\boldsymbol{r})$ propagating a distance z inside matter along the optical axis can be separated into a slowly varying envelope function $A(\boldsymbol{r})$ and a rapidly oscillating term, whose changes are on a much shorter scale than the changes in the medium [43]:

$$\psi(\boldsymbol{r}) = A(\boldsymbol{r}) e^{\mathrm{i}k_0 z}. \tag{2.41}$$

Inserting this expression into the Helmholtz equation Eq. 2.16 for a homogeneous medium and taking the derivative with respect to z yields

$$\begin{aligned} &\nabla^2 \left(A(\boldsymbol{r}) e^{\mathrm{i}k_0 z} \right) + k_0^2 n^2(\boldsymbol{r}) A(\boldsymbol{r}) e^{\mathrm{i}k_0 z} = 0 \\ \Rightarrow &\left[\nabla_\perp^2 A(\boldsymbol{r}) + \partial_z^2 A(\boldsymbol{r}) + 2\mathrm{i}k_0 (\partial_z A(\boldsymbol{r})) - k_0^2 A(\boldsymbol{r}) + k_0^2 n^2(\boldsymbol{r}) A(\boldsymbol{r}) \right] e^{\mathrm{i}k_0 z} = 0 \end{aligned} \tag{2.42}$$

with the lateral derivative $\nabla_\perp^2 = \partial_x^2 + \partial_y^2$. Using $\partial_z^2 A \ll k_0^2 A$ for paraxial beams and eliminating $e^{\mathrm{i}k_0 z}$, Eq. 2.42 becomes the paraxial wave equation:

$$\left[\nabla_\perp^2 + 2\mathrm{i}k_0 \partial_z + k_0^2 (n^2(\boldsymbol{r}) - 1) \right] A(\boldsymbol{r}) = 0. \tag{2.43}$$

Furthermore, diffraction within the object is neglected by assuming $\nabla_\perp^2 \ll \partial_z A$ for the second derivative of A in x, y, which is, however, only valid for thin objects. Together with Eq. 2.40, it holds [43]

$$\partial_z A(\boldsymbol{r}) = -\mathrm{i}k_0 \left[\delta(\boldsymbol{r}) - \mathrm{i}\beta(\boldsymbol{r}) \right] A(\boldsymbol{r}). \tag{2.44}$$

This first order differential equation leads to the envelope function propagated to d:

$$A(x, y, d) = A(\boldsymbol{r}) e^{-\mathrm{i}k_0 \int_0^d (\delta(\boldsymbol{r}) - \mathrm{i}\beta(\boldsymbol{r})) \mathrm{d}z}. \tag{2.45}$$

As it passes through the sample, the envelope function thus experiences an absorption $a(x, y)$ given by the imaginary part β of the refractive index and a phase shift $\phi(x, y)$ defined by the decrement δ of the real part of n, integrated over the sample thickness d:

$$A(x, y, d) = A(\boldsymbol{r}) \underbrace{e^{\mathrm{i}\phi(x,y)} e^{-a(x,y)}}_{=f(x,y)}, \tag{2.46}$$

with

$$\phi(x, y) = -k_0 \int_0^d \delta(\boldsymbol{r}) \mathrm{d}z, \tag{2.47}$$

$$a(x, y) = k_0 \int_0^d \beta(\boldsymbol{r}) \mathrm{d}z. \tag{2.48}$$

This is known as the projection approximation [43]. For an incident monochromatic plane wave parallel to the optical axis, the phase origin is typically set to the exit plane of the object at $z = 0$. The normalized wavefield at the exit plane is then given by the complex object transmission function $f(x, y)$. For a specimen consisting of a single material, the ratio β/δ is constant, and the object function can be expressed by the projected thickness $T(x, y)$ via

$$\phi(x, y) = -k_0 \delta T(x, y), \tag{2.49}$$

$$a(x, y) = k_0 \beta T(x, y). \tag{2.50}$$

The object thickness for which the projection approximation is valid depends on the minimum feature size that should be detected, expressible by the pixel size Δx. The first order diffraction lies at an angle $\theta = \lambda_0/\Delta x$ and reaches the next pixel after the distance $T = \Delta x/\theta$, which yields the criterion [43]

$$\frac{T \cdot \lambda_0}{(\Delta x)^2} \leq 1 \tag{2.51}$$

for the projection approximation to be valid. At 30 keV, this condition is still fulfilled for a 1 cm thick object and 1 µm resolution.

2.2.3. Free space propagation

A monochromatic wavefield $\psi(\boldsymbol{r})$ can be decomposed into a linear combination of plane waves, where $\boldsymbol{k} = (k_x, k_y, k_z)^{\mathrm{T}}$ defines the propagation direction of each plane wave [42]:

$$\psi(\boldsymbol{r}) = \frac{1}{(2\pi)^3} \iiint \tilde{\psi}(\boldsymbol{k}) e^{\mathrm{i}\boldsymbol{k}\boldsymbol{r}} \mathrm{d}^3\boldsymbol{k}. \tag{2.52}$$

Here, $\tilde{\psi}(\boldsymbol{k})$ is the 3D Fourier transform of the wavefield $\psi(\boldsymbol{r})$. Inserting a single plane wave $\tilde{\psi}(\boldsymbol{k})e^{\mathrm{i}\boldsymbol{k}\boldsymbol{r}}$ into the Helmholtz equation Eq. 2.16 in free space ($n = 1$) leads to [42]

$$k_0^2 = k_x^2 + k_y^2 + k_z^2. \tag{2.53}$$

Setting the coordinate z along the optical axis and considering only forward propagation with $k_z > 0$, the previous expression can be rewritten as

$$k_z = \sqrt{k_0^2 - k_x^2 - k_y^2}. \tag{2.54}$$

A monochromatic wavefield $\psi(x, y, z = 0) = \psi_0(x, y)$ given at $z = 0$ and propagating to $z > 0$ can thus be expressed as

$$\psi_z(x, y) = \frac{1}{(2\pi)^2} \iint \tilde{\psi}_0(k_x, k_y) e^{i(k_x x + k_y y)} \underbrace{e^{iz\sqrt{k_0^2 - k_x^2 - k_y^2}}}_{=H_z(k_x, k_y)} \mathrm{d}k_x \mathrm{d}k_y. \tag{2.55}$$

Each plane wave $\tilde{\psi}_0(k_x, k_y)e^{i(k_x x + k_y y)}$ given at $z = 0$ thus accumulates an additional phase $e^{iz\sqrt{k_0^2 - k_x^2 - k_y^2}}$ by propagating to a plane at $z > 0$, as also illustrated in Fig. 2.7. The term H_z is called the free space propagator. In position-space, the operation is equivalent to a convolution of the wavefield at $z = 0$ with the inverse Fourier transform $h_z(x, y)$ of $H_z(k_x, k_y)$:

$$\psi_z(x, y) = \psi_0(x, y) * h_z(x, y). \tag{2.56}$$

Due to the convolution, a lateral shift of the object yields the same, but shifted, image. This property is denoted as shift-invariance [41].

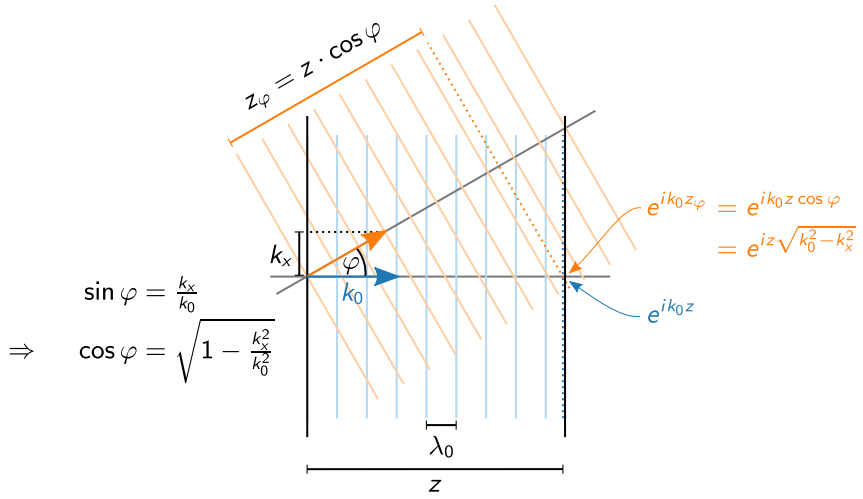

Figure 2.7.: Free space propagation. A plane wave propagating in free space at an angle φ to the optical axis from the plane $z = 0$ towards a parallel plane at $z > 0$ arrives with a phase of $e^{\mathrm{i}z\sqrt{k_0^2 - k_x^2}}$ at this plane. In contrast, a wave propagating parallel to the axis collects a phase of $e^{\mathrm{i}k_0 z}$.

Notation: In the following, the image formation is always considered within an x-y-plane at $z \geq 0$. For better readability, the vectors $\boldsymbol{r} = (x, y)^{\mathrm{T}}$ and $\boldsymbol{k} = (k_x, k_y)^{\mathrm{T}}$ are therefore used as 2D coordinates in the remainder of this work instead of the 3D notation. A 3D wavevector with length k_0 is denoted as $\boldsymbol{k}_0 = (k_x, k_y, k_z)^{\mathrm{T}}$. Also, the index z in the free space propagator $H_z(\boldsymbol{k})$ and in its Fourier transform $h_z(\boldsymbol{r})$ is omitted for better readability.

Paraxial Fresnel approximation

In X-ray imaging, it is usually sufficient to consider paraxial diffraction, i.e., forward propagation of all waves at only small angles to the optical axis. In this case, $k_z^2 \gg k_x^2, k_y^2$, and Eq. 2.54 can be approximated as [41]

$$k_z \approx k_0 - \frac{k_x^2 + k_y^2}{2k_0}. \tag{2.57}$$

Then, the free space propagator becomes

$$H(k_x, k_y) = e^{\mathrm{i}k_0 z} e^{-\mathrm{i}z\frac{k_x^2 + k_y^2}{2k_0}}. \tag{2.58}$$

The term $e^{\mathrm{i}k_0 z}$ is the global phase shown in Fig. 2.7, which can often be omitted in the case of imaging, where only intensities are considered, and the remainder is the so-called Fresnel propagator, quantifying the phase difference with respect to the unscattered wave in second

order. It is convenient to define the unitless Fresnel number [43]

$$N_{\mathrm{F}} = \frac{k_0 t^2}{2\pi z}, \tag{2.59}$$

where t is the feature size. Typically, the smallest sampled spatial wavelength $2\Delta x$ is inserted for t, which defines the Nyquist frequency $k_{\mathrm{Nyq}} = \frac{2\pi}{2\Delta x}$. It now becomes clear that for $N_{\mathrm{F}} = 1$, destructive interference with the unscattered plane wave occurs at the Nyquist frequency, since the exponent of the Fresnel propagator equals π.

2.2.4. Propagation-based phase contrast

So far, the influence of an object on an incident wavefield and the propagation of electromagnetic waves in vacuum have been elucidated. It is now of interest to see how the information contained in the wavefield behind the object can be transformed into a recordable image intensity. By detecting the wavefield directly behind the object, the absorption of the object becomes visible. For an incident plane wave with unity amplitude $I_0 = 1$, the intensity in the object exit plane is given by

$$I(\boldsymbol{r}) = |f(\boldsymbol{r})|^2 = |e^{\mathrm{i}\phi(\boldsymbol{r}) - a(\boldsymbol{r})}|^2 = e^{-2a(\boldsymbol{r})}. \tag{2.60}$$

In this so-called contact image at $z = 0$ the phase information of the object is lost. For weakly absorbing objects, such as biological tissues or soft materials, there will therefore be only little contrast in the image. As an aside, for a single material, Eq. 2.60 can also be expressed in terms of the linear mass absorption coefficient μ (Eq. 2.39) as [43]

$$I(\boldsymbol{r}) = I_0 e^{-\mu T(\boldsymbol{r})}, \tag{2.61}$$

which is known as the Lambert-Beer law.

On the contrary, converting the phase information contained in the wavefield into measurable image intensity can increase image contrast, since $\delta \gg \beta$ (Fig. 2.6). The phase contrast method with the simplest implementation is PB-PCI, provided that an X-ray source with sufficient coherence is available [57]. It exploits the self-interference of the transmitted wavefield behind the object, which increasingly evolves into intensity contrast with increasing propagation distance [43]. The full propagation of a wavefield behind an object can be simulated using the free space propagator in Eq. 2.55. As an example, Fig. 2.8a shows the propagated image intensity of an iron and a carbon sphere for different propagation distances z. Three different regimes can be defined according to the Fresnel number: the contact regime ($N_{\mathrm{F}} \to \infty$), the direct contrast regime ($N_{\mathrm{F}} \approx 1$), and the holographic regime ($N_{\mathrm{F}} \ll 1$). In the contact regime, the phase information is completely lost, and only absorption is visible. In Fig. 2.8a at $z = 0\,\mathrm{cm}$, the iron sphere (top row) shows absorption contrast, while the carbon sphere (bottom row) is not visible due to its low absorption. In the direct contrast regime, an in-

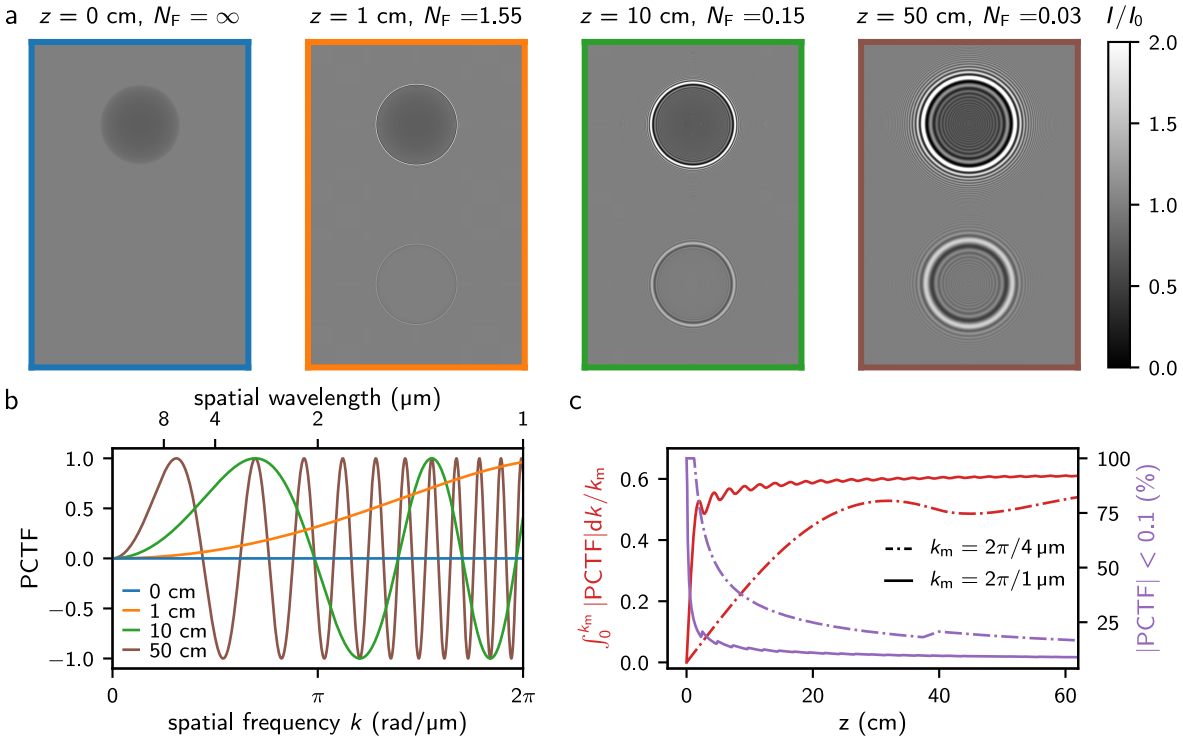

Figure 2.8.: Propagation-based phase contrast imaging. **a** Simulated image intensity after free space propagation of a wavefield behind two spheres of different materials at several propagation distances z. In the contact image at $z = 0\,\mathrm{cm}$ (Fresnel number $N_\mathrm{F} = \infty$) the iron sphere (upper row) shows absorption contrast, while the carbon sphere (lower row) is not visible at all due to its vanishing absorption. With increasing propagation distance, the phase information contained in the wavefield evolves into measurable intensity contrast due to self-interference. The colorbar shows the normalized image intensity. The simulation was performed for an X-ray photon energy of 30 keV and a sphere diameter of 50 µm. **b** PCTF for the parameters shown in panel a. The PCTF indicates how strongly a phase signal with spatial frequency component k is converted into measurable image intensity. **c** Integral of the |PCTF| over k from 0 to two exemplary maximum frequencies k_m as a function of z (red), and corresponding percentage of k-values where $|\mathrm{PCTF}| < 0.1$ (purple).

terference fringe appears at the edges of the sample. By further increasing the propagation distance, the holographic regime is reached. The Fresnel diffraction pattern exhibits multiple interference fringes and the images show high contrast, but no longer directly resemble the sample. Under certain assumptions, the phase and amplitude information of the object function can be reconstructed by suitable reconstruction algorithms, see Section 2.2.7.

2.2.5. Temporal and transverse coherence

PB-PCI requires a sufficiently high degree of coherence of the illuminating X-ray field. Coherence describes the ability of electromagnetic waves to interfere with each other. An ideal monochromatic point source emits perfectly coherent and monochromatic electromagnetic waves. Real X-ray sources, however, emit X-rays within a certain bandwidth, and the sources

are spatially extended. These two aspects result in finite temporal and transverse partial coherence [41].

Temporal coherence Light with a finite temporal coherence can only interfere with itself within a limited time interval. According to the Wiener-Khinchin theorem, such light can be assigned a power spectral density [58, 59], which is usually determined by the bandwidth of the X-ray source or the monochromator. The power spectral density corresponds to a distribution of wavelengths $\lambda_0 = \bar{\lambda}_0 \pm \Delta\lambda_0$ with $\Delta\lambda_0$ being a deviation around the mean wavelength $\bar{\lambda}_0$. The resulting intensity image is composed of the incoherent superposition of the single monochromatic images. Considering the free space propagator in Eq. 2.58, it becomes clear that a monochromatic wavefield with wavelength $\bar{\lambda}_0 + \Delta\lambda_0$ will effectively propagate further by a distance $z' = (1 + \Delta\lambda_0/\bar{\lambda}_0)z$ compared to a wavefield with wavelength $\bar{\lambda}_0$. For synchrotron beamlines with a double-crystal monochromator, the bandwidth is typically such that $|\Delta\lambda_0|/\bar{\lambda}_0 \lesssim 10^{-4}$ [60], which implies that this effectively varying propagation distance is often negligible compared to the influence of transverse coherence. To estimate the resolution limit of propagation-based phase contrast given by the temporal coherence, the image intensities can be evaluated for a weak phase object using the phase contrast transfer function (see Section 2.2.6). Assuming a Gaussian wavelength distribution with standard deviation σ, the monochromatic phase contrast transfer function $\sin\left(\frac{1}{4\pi}\lambda_0 z k^2\right)$ degrades to

$$\int_{-\infty}^{\infty} \frac{1}{\sqrt{2\pi\sigma^2}} e^{-\frac{(\lambda_0-\bar{\lambda}_0)^2}{2\sigma^2}} \sin\left(\frac{1}{4\pi}\lambda_0 z k^2\right) \mathrm{d}\lambda_0 = e^{-\frac{k^4}{32\pi^2}\sigma^2 z^2} \sin\left(\frac{1}{4\pi}\bar{\lambda}_0 z k^2\right). \tag{2.62}$$

A damping of the image contrast by partial temporal coherence below $e^{-2} \approx 0.14$ is reached for structure periods of

$$2\pi/k \leq \sqrt{\pi\sigma z/2}. \tag{2.63}$$

For a bandwidth $\sigma = 10^{-4}\bar{\lambda}_0$, an energy of 30 keV, and a propagation distance of $z = 1\,\mathrm{m}$, image degradation by temporal coherence only becomes relevant for resolutions smaller than $2\pi/k \approx 80\,\mathrm{nm}$.

Transverse coherence An extended X-ray source incoherently illuminates the sample under different angles. With increasing source size, the transverse coherence of the probing X-rays is thereby degraded compared to parallel plane wave illumination [61]. When an obliquely incident plane wave with angular spatial frequency $\hat{k}$ and unity intensity illuminates an object $f(x)$, the wavefield $\psi_0(x)$ at $z = 0$ behind the object experiences a multiplicative phase factor:

$$\psi_{0,\hat{k}}(x) = f(x) e^{i\hat{k}x}. \tag{2.64}$$

For simplicity, only the 1D case is treated here. The wavefield after propagation by a distance z is denoted as $\psi_{z,\hat{k}}(x)$. For an extended X-ray source, the final image intensity $I_z(x)$ at z is given as the incoherent superposition of the intensities $|\psi_{z,\hat{k}}(x)|^2$ weighted by the source function $S(\hat{k})$:

$$I_z(x) = \int S(\hat{k})|\psi_{z,\hat{k}}(x)|^2 \mathrm{d}\hat{k}. \tag{2.65}$$

In most cases, the source illumination as a function of spatial frequencies k can be approximately described by a Gaussian distribution

$$S(\hat{k}) = \frac{1}{\sqrt{2\pi\sigma^2}} e^{-\frac{\hat{k}^2}{2\sigma^2}}. \tag{2.66}$$

The standard deviation σ of the illumination function is related to the source size s via the source-to-sample distance l by $\sigma = k_0 \cdot s/l$. Note that s is given here as the standard deviation of the source size, while it is also common to state the full width at half maximum (FWHM). With Eq. 2.66, one obtains

$$I_z(x) = \frac{k_0}{\sqrt{2\pi}\sigma z} e^{-\frac{k_0^2 x^2}{2\sigma^2 z^2}} * I_z^{\mathrm{coh}}(x) \tag{2.67}$$

for a shift-invariant system. For a derivation, see Appendix A.2. The total image intensity is thus given by the image intensity $I_z^{\mathrm{coh}}(x) = |\psi_{z,0}(x)|^2$ for perfect coherence convolved with a Gaussian function with standard deviation $\sigma z/k_0$. In Fourier space, this is equivalent to a multiplication with a Gaussian function:

$$\tilde{I}_z(k) = e^{-\frac{\sigma^2 z^2 k^2}{2k_0^2}} \cdot \tilde{I}_z^{\mathrm{coh}}(k), \tag{2.68}$$

where the standard deviation of the Gaussian function is given by $k_0/(\sigma z) = l/(sz)$. High spatial frequencies are thus suppressed, resulting in a blurred image. For this reason, the effect of an extended X-ray source on the image is called source blur or penumbral blur [62]. The amount of blur increases with the source size s and the propagation distance z and decreases with the source distance l. As a rough orientation for the largest reasonable propagation distance z, one may introduce the criterion that the Gaussian envelope should not fall below $e^{-2} \approx 0.14$ at the Nyquist frequency $k_{\mathrm{Nyq}} = \pi/\Delta x$. Using $\sigma = k_0 \cdot s/l$, one obtains

$$z = \frac{2l}{\pi s}\Delta x \tag{2.69}$$

as an estimate of the maximum useful propagation distance before the source blur becomes too dominant. Since the source has different extensions in the vertical and horizontal directions, especially in third-generation synchrotrons, the source blur will be different in the respective directions, and the propagation distance is typically adapted to the direction with stronger source blur [63]. For a simulation example including source blur, see Section 3.4.5.

2.2.6. Weak phase approximation and contrast transfer function

For a better understanding of the contrast formation in propagation-based phase contrast imaging, it is convenient to consider the weak phase object approximation. For objects with a weak or weakly varying phase, an expression for the CTF is obtained that describes how strongly spatial frequencies k contained in the wavefield behind the object are translated into measurable image intensity. While initially derived in electron microscopy by D. Gabor and O. Scherzer [64, 65], the concept of the CTF is equally applicable to X-ray imaging [49]. A widely used approach for deriving the CTF-formula in X-ray imaging was presented by P. Guigay et al. [66], as detailed in Appendix A.3. Here, an alternative approach is used, as pursued in electron microscopy [67–70], which involves linearizing the object wave function and directly calculating the resulting image intensity from a convolution with the Fourier transform of the free space propagator.

For an incident monochromatic plane wave, and assuming that the phase shift ϕ and the attenuation a of the object are small ($\phi < 1, a < 1$), the normalized wavefield $\psi_0(\boldsymbol{r})$ can be written as

$$\psi_0(\boldsymbol{r}) = f(\boldsymbol{r}) = e^{\mathrm{i}\phi(\boldsymbol{r})-a(\boldsymbol{r})} \approx 1 + \mathrm{i}\phi(\boldsymbol{r}) - a(\boldsymbol{r}). \tag{2.70}$$

This weak phase object approximation is valid for high energies or sufficiently thin samples, which is fulfilled for many cases of high-resolution biological X-ray imaging. Using Eq. 2.56, the intensity $I_z(\boldsymbol{r})$ of the propagated wavefield at a distance z is given by

$$\begin{aligned}
I_z(\boldsymbol{r})/I_0 &= |\psi_z(\boldsymbol{r})|^2 = |\psi_0(\boldsymbol{r}) * h(\boldsymbol{r})|^2 \\
&= |1 * h(\boldsymbol{r}) + i\phi(\boldsymbol{r}) * h(\boldsymbol{r}) - a(\boldsymbol{r}) * h(\boldsymbol{r})|^2 + \mathcal{O}(\phi^2) \\
&= |H(\mathbf{0})|^2 + \phi(\boldsymbol{r}) * i[H^*(\mathbf{0})h(\boldsymbol{r}) - H(\mathbf{0})h^*(\boldsymbol{r})] \\
&\qquad - a(\boldsymbol{r}) * [H^*(\mathbf{0})h(\boldsymbol{r}) + H(\mathbf{0})h^*(\boldsymbol{r})] + \mathcal{O}(\phi^2) \\
&= |H(\mathbf{0})|^2 - \phi(\boldsymbol{r}) * 2 \cdot \mathrm{Im}[H^*(\mathbf{0}) \cdot h(\boldsymbol{r})] \\
&\qquad - a(\boldsymbol{r}) * 2 \cdot \mathrm{Re}[H^*(\mathbf{0}) \cdot h(\boldsymbol{r})] + \mathcal{O}(\phi^2),
\end{aligned} \tag{2.71}$$

where $I_0 \approx$ const. is the intensity of the incident wavefield. Here, the identity

$$1 * h(\boldsymbol{r}) = \mathcal{F}^{-1}\left[2\pi\delta(\boldsymbol{k}) \cdot H(\boldsymbol{k})\right] = H(\mathbf{0}) \tag{2.72}$$

was used, where $\mathcal{F}^{-1}$ denotes the inverse Fourier transform and $\delta(\boldsymbol{k})$ the Dirac delta distribution. Using the convolution theorem [71], Eq. 2.71 can be written in Fourier space as

$$\tilde{I}_z(\boldsymbol{k})/I_0 \approx 2\pi|H(\mathbf{0})|^2\delta(\boldsymbol{k}) - 2\mathrm{Im}[H^*(\mathbf{0})H(\boldsymbol{k})] \cdot \tilde{\phi}(\boldsymbol{k}) - 2\mathrm{Re}[H^*(\mathbf{0})H(\boldsymbol{k})] \cdot \tilde{a}(\boldsymbol{k}), \tag{2.73}$$

with $\tilde{I}_z$, $\tilde{\phi}$ and $\tilde{a}$ being the Fourier transforms of I_z, ϕ and a, respectively. For the free space propagator given in Eq. 2.58, it holds $H^*(\mathbf{0}) = e^{-\mathrm{i}k_0 z}$ and $H(\boldsymbol{k}) = e^{\mathrm{i}k_0 z}e^{-\mathrm{i}\chi(\boldsymbol{k})}$, where

$\chi(\boldsymbol{k}) = z(k_x^2 + k_y^2)/2k_0$ was introduced for the exponent of the Fresnel propagator. Here, it becomes clear that the global phase term $e^{\mathrm{i}k_0 z}$ cancels out, and the intensity reads

$$I_z(\boldsymbol{r})/I_0 \approx 1 + 2\mathcal{F}^{-1}[\sin\chi(\boldsymbol{k}) \cdot \tilde{\phi}(\boldsymbol{k})] - 2\mathcal{F}^{-1}\left[\cos\chi(\boldsymbol{k}) \cdot \tilde{a}(\boldsymbol{k})\right]. \tag{2.74}$$

Under the further assumption of a single material sample, i.e., $\tilde{\phi}(\boldsymbol{k})/\tilde{a}(\boldsymbol{k}) = -\delta/\beta$ (see Eqs. 2.49 and 2.50), one obtains

$$I_z(\boldsymbol{r})/I_0 \approx 1 + 2\mathcal{F}^{-1}[\tilde{\phi}(\boldsymbol{k}) \cdot \underbrace{(\sin\chi(\boldsymbol{k}) + \frac{\beta}{\delta}\cos\chi(\boldsymbol{k}))}_{=\mathrm{CTF}}]. \tag{2.75}$$

The sine and cosine terms are called phase and absorption CTF, respectively, and describe the conversion of phase or absorption information into image intensity in PB-PCI [70]. The absorption CTF usually only plays a minor role for $z > 0$ due to $\beta/\delta \ll 1$ (Fig. 2.6). In Fig. 2.8b, the 1D phase contrast transfer function (PCTF) is shown for different propagation distances z, given by

$$\mathrm{PCTF}(\boldsymbol{k}) = \sin\left(\frac{z}{2k_0}(k_x^2 + k_y^2)\right) \tag{2.76}$$

or, expressed in spatial frequencies $\boldsymbol{q} = (q_x, q_y)^{\mathrm{T}} = \boldsymbol{k}/(2\pi)$,

$$\mathrm{PCTF}(\boldsymbol{q}) = \sin\left(\pi\lambda_0 z(q_x^2 + q_y^2)\right). \tag{2.77}$$

In the current chapter, the notation with angular spatial frequency $\boldsymbol{k} = 2\pi\boldsymbol{q}$ is used, while in the experimental part, a notation with $\boldsymbol{q}$ is sometimes chosen to make the conversion to corresponding structure sizes more convenient. The amplitude of the PCTF over spatial frequency defines how strongly information about the sample is translated to measurable image contrast. Fig. 2.8b shows the PCTF for different propagation distances. In the contact regime ($z \approx 0\,\mathrm{cm}$, blue), the PCTF is zero, and no phase contrast is transferred to the image. With increasing z (direct contrast regime, orange), the values of the PCTF increase, and thus the image contrast becomes higher. For even larger z (holographic regime, green, brown), the PCTF starts to oscillate and exhibits zero-crossings. On the one hand, the contrast for sufficiently small k increases steadily with z, on the other hand the number of zero-crossings in the considered k-interval also increases with z, making phase reconstruction more challenging (see Section 2.2.7).

The integral $\int_0^{k_\mathrm{m}} |\mathrm{PCTF}(k)|\mathrm{d}k$ can serve as a measure for the general contrast transfer at a certain distance z, averaged over all $k \leq k_\mathrm{m}$, where k_m is any maximum spatial frequency of interest. As can be seen from Fig. 2.8c (red curves), the overall contrast increases with z. A distance of only a few centimeters strongly increases the contrast integrated up to $k_\mathrm{m} = 2\pi/1\,\mu\mathrm{m}$, where the latter corresponds to a structure wavelength of 1 µm in position space. For

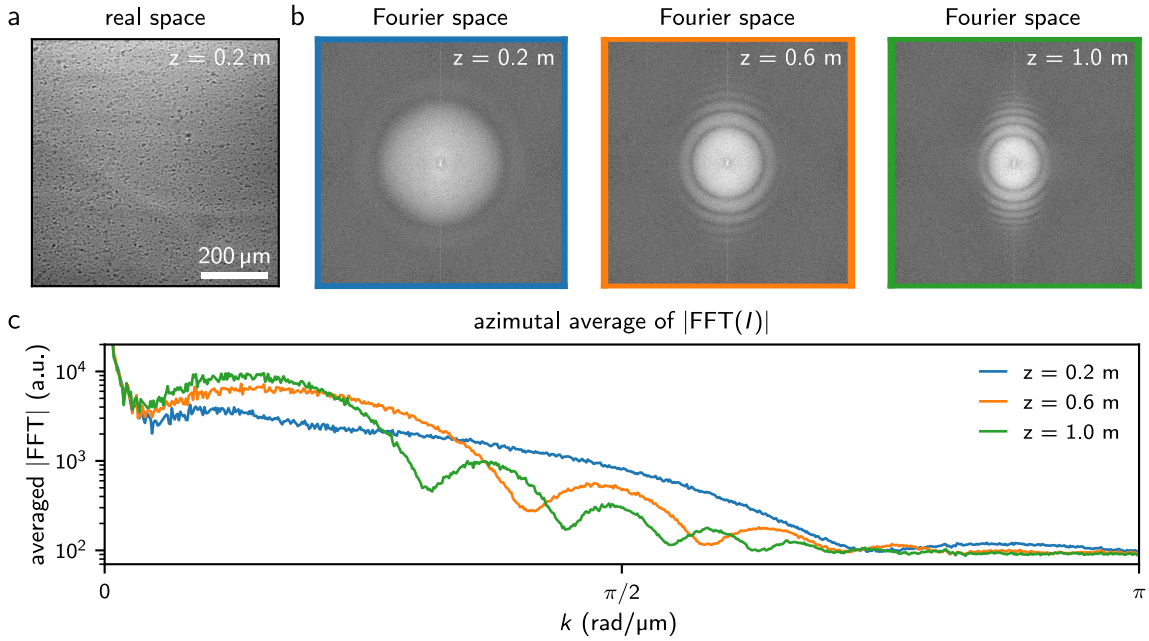

Figure 2.9.: Experimental visualization of the PCTF via Thon rings. **a** Experimental image of a thin piece of plastic representing a weak phase amorphous sample, acquired with an indirect detector system (see Chapter 4) at 30 keV at the P23 beamline at PETRA III, Hamburg, Germany. **b** Fourier transform of experimental images acquired at three different propagation distances z. So-called Thon rings appear at spatial frequencies k where the PCTF is close to zero. The decrease in signal towards higher k is attributed to partial coherence (see Section 2.2.5). Since the images were acquired at a third-generation synchrotron source, the coherence in the vertical direction is higher than in horizontal direction, which is especially well visible for $z = 1\,\mathrm{m}$. **c** Azimuthal average of the Fourier transforms shown in panel b. At low spatial frequencies, the signal increases with z, while at high k it decreases slightly due to source blur (Section 2.2.5).

lower spatial frequencies, here shown as an example for $k_\mathrm{m} = 2\pi/4\,\mu\mathrm{m}$, distances of at least several decimeters are favorable for high contrast. The integrals have been normalized to the integral for a hypothetical ideal contrast transfer ($\mathrm{PCTF}_\mathrm{ideal} = 1 \rightarrow \int_0^{k_\mathrm{m}} |\mathrm{PCTF}_\mathrm{ideal}| \mathrm{d}k = k_\mathrm{m}$). At frequencies where the PCTF is close to zero, the image signal may be below the noise floor, and the corresponding object information may be lost in the image. Fig. 2.8c (purple curve) shows the fraction of k-values where |PCTF| is less than a certain value, in this example 0.1. It decreases with increasing z, which means that less of the image signal lies below the noise floor.

The appearance of zero-crossings in the PCTF can be explored experimentally by acquiring images of an amorphous weak phase sample at several propagation distances. An example is shown in Fig. 2.9. Here, a thin piece of plastic was chosen that contains many different spatial frequencies and therefore behaves approximately like a white noise object. The Fourier transform of the sample images shows that the signal is lost at certain spatial frequencies where the PCTF is close to zero. In electron microscopy, these circular rings are called Thon

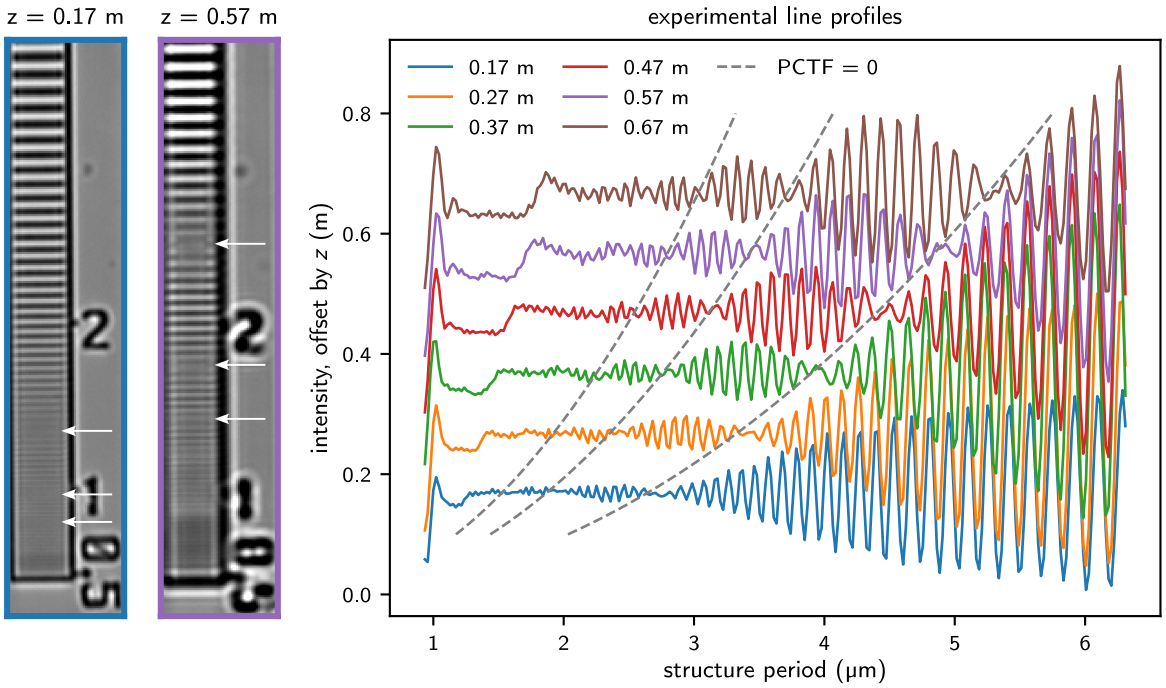

Figure 2.10.: Resolution line pattern imaged at different distances. The bar period in the line pattern changes continuously with height. Depending on the propagation distance z, some frequencies in the line pattern disappear due to zero-crossings in the PCTF, marked by white arrows in the flatfield-corrected holograms for two exemplary distances (left). In the right graph, vertical intensity line profiles are given for six distances, revealing that the missing frequencies shift towards larger structure periods with increasing z. For better visibility, the curves are offset by z. The gray dashed lines show which structure periods are expected to be suppressed due to the zero-crossings in the PCTF. The data were acquired with an indirect detector system (see Chapter 4) at 30.5 keV at the P23 beamline at PETRA III, Hamburg, Germany.

rings [72] and can be used, for example, to study astigmatism or the performance of optical devices [73, 74]. In PB-PCI, the position of Thon rings can be used to precisely determine the Fresnel number and thus the propagation distance.

The suppression of spatial frequencies can also be visualized by imaging a line pattern with a continuously changing bar period, see Fig. 2.10. Depending on the propagation distance, certain spatial frequencies are not transferred to the image, as marked by white arrows. In the intensity line profiles at different distances, the movement of these missing frequencies towards larger structure periods becomes apparent. The missing frequencies, which are to be expected due to the zero-crossings of the PCTF (Eq. 2.77), are marked by a dashed gray line and coincide with the experimental areas with no image contrast. The dark areas at the lower end of the line pattern can be attributed to suppression by source blur, which increases with z.

2.2.7. Phase reconstruction

The aim of phase retrieval algorithms is to reconstruct the projected object phase and attenuation in the object exit plane $z = 0$, which is encoded in the detected image intensity at $z > 0$. Several approaches have been proposed and successfully applied, which can be divided into non-iterative and iterative methods [75]. The focus of this section lies on non-iterative methods due to their relatively simple implementation and fast performance. Non-iterative methods describe the dependence between object phase and image intensity by a linear relationship in Fourier space, resulting in a Fourier filter [49, 50]. They are widely used because of their numerical simplicity and speed [75]. However, they make several assumptions on the imaging system and the object. Iterative methods are less stringent and allow for a priori constraints such as sample support, but are numerically more complex, resulting in rather long reconstruction times [76]. Here, only the case of a single material sample is considered, i.e., $a(\boldsymbol{r})/\phi(\boldsymbol{r}) = -\beta/\delta = \text{const.}$, which is a reasonable assumption for many biological samples and monochromatic illumination.

First, the TIE and CTF methods are summarized, which are the most popular approaches in the literature [49, 50, 75, 77]. Practical reconstruction examples are given in Chapters 3 and 4. For the limiting case of large Fresnel numbers, i.e., small propagation distances, the CTF formula is almost identical to the TIE formula, they only differ by a logarithm. In order to combine these two formulas and to explain the origin of their difference, another approach is presented below that takes into account the mean absorption of the sample and is therefore referred to as mean-field CTF here. In essence, the diffracted light interferes with the attenuated zero-order beam.

2.2.8. Transport of intensity equation (TIE) method

Starting with the paraxial wave equation (Eq. 2.43) in free space ($n = 1$) and expressing the envelope function $A(\boldsymbol{r}) = \sqrt{I(\boldsymbol{r})}e^{i\phi(\boldsymbol{r})}$ by its phase $\phi(\boldsymbol{r})$ and intensity $I(\boldsymbol{r}) = |A(\boldsymbol{r})|^2 = I_0 e^{-2a(\boldsymbol{r})}$ leads to the transport of intensity equation (TIE) [78]:

$$\nabla_\perp \left(I(\boldsymbol{r})\nabla_\perp \phi(\boldsymbol{r})\right) = -k_0 \partial_z I(\boldsymbol{r}). \tag{2.78}$$

The propagation distance z is assumed to be small so that the right-hand side of Eq. 2.78 can be expressed as a differential quotient between the intensity at the object exit plane and the intensity I_z measured at z. Then, for a single material sample with $a(\boldsymbol{r}) = -\beta/\delta \cdot \phi(\boldsymbol{r})$, the TIE leads to [50]

$$\begin{aligned}\nabla_\perp \left(I_0 e^{2\frac{\beta}{\delta}\phi(\boldsymbol{r})}\nabla_\perp \phi(\boldsymbol{r})\right) = \frac{I_0}{2\frac{\beta}{\delta}}\nabla_\perp^2 e^{2\frac{\beta}{\delta}\phi(\boldsymbol{r})} &\approx -k_0 \frac{I_z(\boldsymbol{r}) - I_0 e^{2\frac{\beta}{\delta}\phi(\boldsymbol{r})}}{z} \\ \rightarrow \left(-\frac{z\delta}{2k_0\beta}\nabla_\perp^2 + 1\right) e^{2\frac{\beta}{\delta}\phi(\boldsymbol{r})} &\approx \frac{I_z(\boldsymbol{r})}{I_0}.\end{aligned} \tag{2.79}$$

In Fourier space, one obtains

$$\mathcal{F}\left[e^{2\frac{\beta}{\delta}\phi(\boldsymbol{r})}\right] \approx \frac{\mathcal{F}\left[I_z(\boldsymbol{r})/I_0\right]}{\frac{\delta}{\beta}\cdot\chi(\boldsymbol{k})+1}, \tag{2.80}$$

where again $\chi(\boldsymbol{k}) = z(k_x^2+k_y^2)/2k_0$. The object phase can thus be reconstructed by

$$\phi(\boldsymbol{r}) = \frac{\delta}{2\beta}\ln\left(\mathcal{F}^{-1}\left[\frac{\mathcal{F}\left[I_z(\boldsymbol{r})/I_0\right]}{\frac{\delta}{\beta}\cdot\chi(\boldsymbol{k})+1}\right]\right). \tag{2.81}$$

The Fourier filter $1/(\delta/\beta\cdot\chi(\boldsymbol{k})+1)$ in Eq. 2.81 acts as a low-pass filter and suppresses high-frequency noise. The parameter β/δ can either be estimated by a priori knowledge on the sample material or adjusted during the reconstruction to yield a satisfying result. The method was derived by D. Paganin et al. [50] and is therefore often also referred to as the Paganin reconstruction. It is widely used in nearfield X-ray imaging of biological specimens and tissues due to its speed and robustness.

2.2.9. Contrast transfer function (CTF) method

The TIE method is only valid for small z. In the holographic regime and for homogeneous objects with a weak phase, the linearity of Eq. 2.75 can be exploited to retrieve the phase from the recorded intensity pattern, denoted as CTF phase retrieval [43, 49]:

$$\phi(\boldsymbol{r}) = \frac{1}{2}\mathcal{F}^{-1}\left(\frac{\mathcal{F}[I_z(\boldsymbol{r})/I_0-1]}{\sin\chi(\boldsymbol{k})+\frac{\beta}{\delta}\cos\chi(\boldsymbol{k})+\epsilon}\right). \tag{2.82}$$

Since the zero-crossings of the CTF discussed above hinder proper phase reconstruction, a regularization term ϵ is introduced to avoid amplification of noise at spatial frequencies where the denominator would become arbitrarily small. It is typically defined separately for low and high spatial frequencies [79]:

$$\epsilon = \begin{cases} \epsilon_0 & \text{for } |\chi| \leq \pi/2, \\ \epsilon_1 & \text{for } |\chi| > \pi/2. \end{cases}$$

In the case of an absorbing sample, ϵ_0 can be set to zero because β/δ itself acts as a regularization term for $z \approx 0$. Typical values for ϵ_1 are 10^{-1} [79]. Alternatively, small regions around the zero-crossings can be masked, which is known as quasi-particle approach and has the advantage of being also valid for non-weak phase objects, but introduces artifacts due to the missing frequencies [80].

Acquiring images at N multiple propagation distances reduces the amount of suppressed spatial frequencies in the set of images and leads to an overall higher information content and more accurate phase reconstruction. This method corresponds to a defocus series in electron

microscopy [81] and was transferred to X-ray imaging by P. Cloetens et al. [57]. Using a least-square minimization, the phase can be reconstructed by

$$\phi(\boldsymbol{r}) = \mathcal{F}^{-1}\left(\frac{\frac{1}{N}\sum_{n=1}^{N}\left(\sin\chi_n(\boldsymbol{k}) + \frac{\beta}{\delta}\cos\chi_n(\boldsymbol{k})\right)\cdot\mathcal{F}[I_z(\boldsymbol{r})/I_0 - 1]}{\frac{1}{N}\sum_{n=1}^{N} 2\left(\sin\chi_n(\boldsymbol{k}) + \frac{\beta}{\delta}\cos\chi_n(\boldsymbol{k})\right)^2 + \epsilon}\right), \tag{2.83}$$

referred to as multi-distance CTF method. Multi-distance phase reconstruction suppresses typical artifacts of single-distance reconstruction, but can only be applied to samples that do not move during acquisition at the different distances.

2.2.10. Relation between TIE and CTF: mean-field CTF

The TIE and CTF methods look very similar, the main difference being the logarithm and the first order approximation of the CTF in the TIE formula ($\sin\chi \approx \chi$, $\cos\chi \approx 1$). In this section, a formula is derived that takes into account the influence of a reduced mean intensity due to non-negligible absorption. It is referred to here as the mean-field CTF method and can be considered as a generalization of the TIE and CTF phase retrieval approaches, covering both methods simultaneously and converging to the TIE or CTF formula within the respective limits. The result is the same as in Ref. [82], and the approach is similar to Ref. [83], with the difference that here the derivation is performed by directly calculating the image intensity in real space. For a derivation analogous to Guigay's approach, see Appendix A.3.

In the CTF derivation presented in Section 2.2.6, the phase shift and attenuation are assumed to be small so that the exponential function in Eq. 2.70 can be linearized. Here, an object is considered where the deviation of phase and absorption to the mean phase ϕ_0 and mean absorption a_0 is small ($|\phi(\boldsymbol{r}) - \phi_0| < 1, |a(\boldsymbol{r}) - a_0| < 1$), but ϕ_0 and a_0 themselves may be large. The object function can then be written as

$$\begin{aligned}\psi_0(\boldsymbol{r}) = e^{i\phi(\boldsymbol{r}) - a(\boldsymbol{r})} &= e^{i\phi_0 - a_0} e^{i(\phi(\boldsymbol{r}) - \phi_0) - (a(\boldsymbol{r}) - a_0)} \\ &\approx e^{i\phi_0 - a_0}[1 + i(\phi(\boldsymbol{r}) - \phi_0) - (a(\boldsymbol{r}) - a_0)].\end{aligned} \tag{2.84}$$

In first order, the image intensity propagated in free space becomes

$$\begin{aligned}\frac{I_z(\boldsymbol{r})}{I_0} &\approx \left|e^{i\phi_0 - a_0}\left(1 + i(\phi(\boldsymbol{r}) - \phi_0) - (a(\boldsymbol{r}) - a_0)\right) * h(\boldsymbol{r})\right|^2 \\ &\approx e^{-2a_0}\left(|H(\boldsymbol{0})|^2 + (\phi(\boldsymbol{r}) - \phi_0) * 2\cdot\mathrm{Im}[H^*(\boldsymbol{0})\cdot h] - (a(\boldsymbol{r}) - a_0) * 2\cdot\mathrm{Re}[H^*(\boldsymbol{0})\cdot h(\boldsymbol{r})]\right) \\ &= e^{-2a_0}\left(1 + \mathcal{F}^{-1}\left[2(\tilde{\phi}(\boldsymbol{k}) - \phi_0 2\pi\delta(\boldsymbol{k}))\sin\chi(\boldsymbol{k}) - 2(\tilde{a}(\boldsymbol{k}) - a_0 2\pi\delta(\boldsymbol{k}))\cos\chi(\boldsymbol{k})\right]\right) \\ &= e^{-2a_0}\left(1 + 2a_0 + \mathcal{F}^{-1}\left[2\tilde{a}(\boldsymbol{k})\cdot\left(\frac{\delta}{\beta}\sin\chi(\boldsymbol{k}) + \cos\chi(\boldsymbol{k})\right)\right]\right).\end{aligned} \tag{2.85}$$

In the last step, a single-material object was assumed. Solving for $\tilde{a}(\boldsymbol{k})$ in Fourier space yields

$$2\tilde{a}(\boldsymbol{k}) = -\frac{\mathcal{F}[I_z(\boldsymbol{r})e^{2a_0}/I_0 - (1+2a_0)]}{\frac{\delta}{\beta}\sin\chi(\boldsymbol{k}) + \cos\chi(\boldsymbol{k})} \tag{2.86}$$

leading to

$$\begin{aligned} 2a(\boldsymbol{r}) &= -\mathcal{F}^{-1}\left[\frac{\mathcal{F}[I_z(\boldsymbol{r})e^{2a_0}/I_0 - (1+2a_0)]}{\frac{\delta}{\beta}\sin\chi(\boldsymbol{k}) + \cos\chi(\boldsymbol{k})}\right] \\ \Rightarrow a(\boldsymbol{r}) &= -\frac{1}{2}\mathcal{F}^{-1}\left[\frac{\mathcal{F}[I_z(\boldsymbol{r})e^{2a_0}/I_0 - 1]}{\frac{\delta}{\beta}\sin\chi(\boldsymbol{k}) + \cos\chi(\boldsymbol{k})}\right] + a_0, \end{aligned} \tag{2.87}$$

or expressed by ϕ:

$$\phi(\boldsymbol{r}) = \frac{1}{2}\mathcal{F}^{-1}\left[\frac{\mathcal{F}[I_z(\boldsymbol{r})e^{2a_0}/I_0 - 1]}{\sin\chi(\boldsymbol{k}) + \frac{\beta}{\delta}\cos\chi(\boldsymbol{k})}\right] + \phi_0. \tag{2.88}$$

By taking the mean attenuation a_0 into account, this formula is thus a generalization of the CTF-formula (Eq. 2.82). Intuitively, it becomes clear that the measured intensity I_z must be corrected for the mean intensity loss e^{-2a_0} to obtain a quantitatively more correct result. The global phase ϕ_0 does not affect the image intensity, but is kept here for consistency. In analogy to Ref. [57], the formula can also be extended to multi-distance data.

To understand the relation to the TIE-formula (Eq. 2.81), Eq. 2.87 can be rewritten as

$$1 - 2(a(\boldsymbol{r}) - a_0) = \mathcal{F}^{-1}\left[\frac{\mathcal{F}[I_z(\boldsymbol{r})/I_0]}{\frac{\delta}{\beta}\sin\chi(\boldsymbol{k}) + \cos\chi(\boldsymbol{k})}\right] \cdot e^{2a_0}. \tag{2.89}$$

The left-hand side came from the approximation $e^{-2(a(\boldsymbol{r})-a_0)} \approx 1-2(a(\boldsymbol{r})-a_0)$. In first order, one may therefore also write

$$\begin{aligned} e^{-2(a(\boldsymbol{r})-a_0)} &= \mathcal{F}^{-1}\left[\frac{\mathcal{F}[I_z(\boldsymbol{r})/I_0]}{\frac{\delta}{\beta}\sin\chi(\boldsymbol{k}) + \cos\chi(\boldsymbol{k})}\right] \cdot e^{2a_0} \\ \Rightarrow \qquad a(\boldsymbol{r}) &= -\frac{1}{2}\ln\left(\mathcal{F}^{-1}\left[\frac{\mathcal{F}[I_z(\boldsymbol{r})/I_0]}{\frac{\delta}{\beta}\sin\chi(\boldsymbol{k}) + \cos\chi(\boldsymbol{k})}\right]\right), \end{aligned} \tag{2.90}$$

or expressed by ϕ:

$$\phi(\boldsymbol{r}) = \frac{\delta}{2\beta}\ln\left(\mathcal{F}^{-1}\left[\frac{\mathcal{F}[I_z(\boldsymbol{r})/I_0]}{\frac{\delta}{\beta}\sin\chi(\boldsymbol{k}) + \cos\chi(\boldsymbol{k})}\right]\right). \tag{2.91}$$

In first order approximation, Eq. 2.87 and Eq. 2.90 have mathematically the same validity. However, with the logarithm and not having to determine the mean absorption a_0, the latter is more convenient. Furthermore, in the case of vanishing propagation ($\chi \approx 0$), it returns the

correct attenuation $a(\boldsymbol{r}) = -1/2 \cdot \ln(I_z(\boldsymbol{r})/I_0)$. In the approximation of short distances, i.e., $\chi \ll 1 \rightarrow \sin\chi \approx \chi, \cos\chi \approx 1$, Eq. 2.90 coincides with the TIE formula. In summary, the mean-field CTF formulas Eq. 2.87 and Eq. 2.90 have a broader validity, while being equally simple to implement as the TIE and CTF formulas.

Nonlinear Tikhonov method

Assumptions on the sample or the imaging system can be relaxed by iterative phase retrieval algorithms. However, iterative phase retrieval is typically numerically orders of magnitude more expensive than the direct methods presented above. Numerous approaches have been proposed and investigated [76, 84–87]. In this thesis, the nonlinear Tikhonov regularization (NLTikh) is employed, which can be considered as a nonlinear generalization of the CTF method [79]. It also assumes a homogeneous object (β/δ = const.), but is valid not only for objects with weakly varying phase, but also for moderately strong phase gradients. Furthermore, it offers the possibility to introduce a priori constraints on the sample support or on the phase range. The algorithm uses the CTF method as an initial guess and iteratively optimizes the result using the full nonlinear Fresnel propagator as forward model (Eq. 2.58). In contrast to other iterative methods, it shows reasonable numerical efficiency so that it can also be applied to large datasets [79].

2.3. X-ray area detectors

While in the past X-ray images were mainly detected using photographic films, these have been replaced by digital sensors over the last few centuries. Digital detector systems can be divided into two groups – direct and indirect detectors [88]. The main difference lies in the way in which X-ray photons are converted into a measurable electrical signal. In direct detectors, X-ray photons generate an electric charge directly, whereas in indirect detectors X-rays photons are converted into visible light photons, which are then recorded by an electronic image sensor, see Fig. 2.11. The functional principle of these two detector systems is briefly outlined below.

2.3.1. Indirect detector systems

An indirect detector consists of a scintillator, a lens system or fiber optics, and an image sensor. The scintillator converts X-ray photons into visible light photons. Important properties of a scintillator for its performance are the absorption coefficient, the light yield, the decay time, and the thickness [89]. For a high detection efficiency, as many X-ray photons as possible should be absorbed by the scintillator, which is facilitated by a high absorption coefficient, e.g., provided by high-Z materials. The light yield is defined as the number of luminescence photons generated by one absorbed X-ray photon per energy. A short decay time between

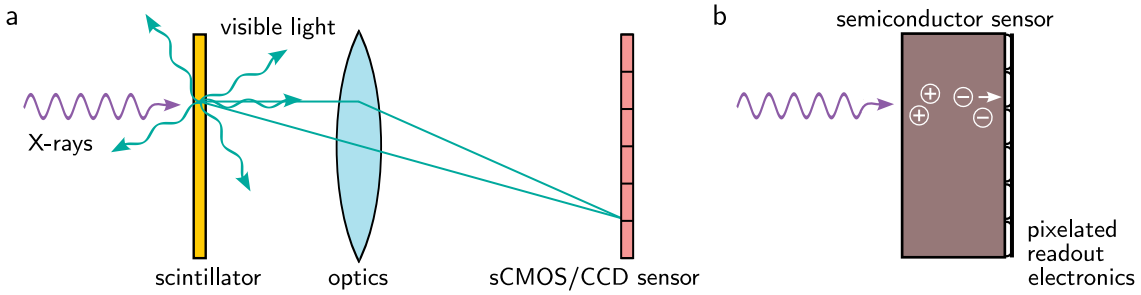

Figure 2.11.: Indirect and direct X-ray detectors. Working principle of **a** indirectly and **b** directly converting detectors. In indirect detectors, a scintillator converts the X-rays into visible light, which is either guided onto a camera sensor by fiber optics or, as sketched here, magnified by visible light optics. In direct detectors, an absorbed X-ray photon creates electron-hole pairs in the semiconductor sensor material, which are collected by pixelated readout electronics. Adapted from Ref. [88].

excitation and emission is especially important for fast time-resolved experiments. Typical scintillator materials employed for high-resolution X-ray imaging are YAG ($Y_3Al_5O_{12}$:Ce), LuAG ($Lu_3Al_5O_{12}$:Ce), and LSO (Lu_2SiO_5:Ce) [90], while Gadox (Gd_2O_2S:Tb) is often used in flat panel detectors with medium resolution [88]. The visible photons are imaged onto a camera sensor through a lens system or fiber optics. Flat panel detectors can achieve a large field of view of several centimeters with medium resolutions of several tens of micrometers. In contrast, to achieve high resolutions of 1 µm, a magnifying objective lens is placed between the scintillator and the sensor, allowing effective pixel sizes in the sub-micron resolution range. The numerical aperture (NA) of the objective is defined by half the opening angle θ as $\mathrm{NA} = n \sin\theta$, where n is the refractive index of the surrounding medium such as air or water. A high NA ensures a high collection efficiency η_c of the objective, i.e., the ratio of photons collected by the objective [91]:

$$\eta_c = \frac{1}{4\pi}\int_0^\theta 2\pi \sin\theta' \mathrm{d}\theta' = \frac{1}{2}\left(1 - \sqrt{1 - \frac{\mathrm{NA}^2}{n^2}}\right). \tag{2.92}$$

Furthermore, the NA affects the point spread function (PSF) of the optical system, which describes the response of the system to a point object. The Fourier transform of the PSF is the optical transfer function (OTF). The OTF specifies how strongly spatial frequencies are transmitted through the optics, i.e., the scintillator and the objective. The OTF of a perfect spherical lens is given by [92]

$$\mathrm{OTF}(\nu) = \frac{2}{\pi}\left(\arccos|\nu| - |\nu|\sqrt{1-\nu^2}\right). \tag{2.93}$$

Here, ν is the spatial frequency normalized to the highest transmitted spatial frequency $q_{\max} = k_{\max}/(2\pi) = 2\mathrm{NA}/\lambda_{\mathrm{optical}}$ with $\lambda_{\mathrm{optical}}$ being the wavelength of the scintillating light. For a diffraction-limited system and incoherent light, the finite aperture of the lens defines

the smallest resolvable spatial wavelength λ_{min}, which is given as Rayleigh's resolution criterion [93]:

$$\lambda_{\mathrm{min}} = 0.61 \frac{\lambda_{\mathrm{optical}}}{\mathrm{NA}}. \tag{2.94}$$

The objective has a certain depth of field [92], defined by the NA. The thickness of the scintillator should be within or at most slightly above the depth of field in order not to degrade the OTF and thus the spatial resolution. As a rule of thumb, a thickness of twice the depth of field has proven useful [90]. Finally, the image is detected by a camera sensor. The main types of image sensors are charge-coupled device (CCD) and complementary metal-oxide-semiconductor (CMOS) sensors. In the last decade, the development of so-called scientific CMOS (sCMOS) sensors has further improved the performance of cameras due to the sensors' low readout noise, high speed and good quantum efficiency, which describes the conversion efficiency of photons into electrical charges.

2.3.2. Single photon counting detectors

In a single photon counting detector (SPCD), X-rays directly create electron-hole pairs within a semiconductor sensor material. The probability that an X-ray will interact with the detector is determined by the absorption probability of the sensor and therefore by the sensor material and thickness. The sensor material and thickness can be optimized for the energy range of interest. Suitable sensor materials are Si, gallium arsenide (GaAs) and cadmium telluride (CdTe), and the typical thickness varies between 0.3 mm to 1 mm. Detailed information on the performance of the different sensor materials can be found in the literature [94–97]. In this work, a 500 µm thick GaAs sensor material is used, which exhibits nominally 97 % of absorption at 30 keV [98]. The sensor material is physically connected to a pixelated readout electronics by flip-chip bonding. This assembly is called hybrid detector [99]. The generated electron-hole pairs are accelerated towards the electrodes by an applied electric field and induce an electrical current. The signal of each X-ray photon is separately counted and amplified. It is further processed by a group of discriminators and counters. The amplitude of the pulse is proportional to the charge generated in the sensor. The discriminators compare the detected pulse amplitude with several energy thresholds and increment the counter of the energy bin in which the measured pulse lies. By this procedure, energy-resolved measurements are possible. Furthermore, electronic noise is rejected by setting the lowest energy threshold above the intrinsic system noise [100].

The electron-hole pairs induced by an X-ray photon in the sensor diffuse and generate a charge cloud with finite lateral extent. This leads to a sharing of the charge between neighboring pixels. This charge-sharing effect falsifies the detected energy or number of photons. Certain readout chips, such as the Medipix3RX [101] used in this work, can account for charge sharing

by event correlation. The corresponding readout mode is called charge-sharing mode (CSM), while in single-pixel mode (SPM) each pixel is read out independently [101].

The PSF of an SPCD is typically very sharp and only slightly degraded by charge sharing effects. In turn, the modulus of its Fourier transform, the modulation transfer function (MTF), shows only minor deviations from the ideal MTF of a detector with finite pixel size Δx, given by a sinc-function [97]:

$$\mathrm{MTF}_{\mathrm{ideal}}(q) = \frac{\sin(\pi \Delta x q)}{\pi \Delta x q}. \tag{2.95}$$

The MTF can be influenced by changing the energy threshold and operating mode [94], or by applying advanced single-event processing methods [102]. The linear regime of the detector is limited by pile-up, which occurs at high fluxes when two pulses arrive in close succession and the signals overlap due to their finite decay time. The Medipix3RX readout chip behaves linearly up to a flux of $\sim 2 \times 10^7\,\mathrm{counts/mm^2/s}$ for CSM and $\sim 1 \times 10^8\,\mathrm{counts/mm^2/s}$ for SPM [103].

3. X-ray imaging with Bragg crystal optics

The aim of this thesis is to improve dose efficiency in X-ray imaging of soft tissues and soft materials, which exhibit only weak absorption contrast. As approach to solving this task, the suitability of Bragg crystal optics in combination with phase contrast imaging is investigated. Bragg crystal optics can coherently magnify of demagnify an incident wavefield, making them a versatile tool for X-ray imaging. So far, however, Bragg crystal optics have not yet found widespread application in X-ray imaging due to their rather complex design and operation, coupled with the fact that they only accept a small energy bandwidth of $\Delta E/E \approx 10^{-4}$. For low-dose applications, however, the latter restriction becomes less significant, as low flux is required anyway. The following chapter lays the basis for Chapters 4 and 5, where the suitability of Bragg crystal optics for dose-efficient applications is investigated in detail.

This chapter introduces the concept of Bragg crystal optics and presents characterization measurements of the Bragg magnifier system developed and used in this work. First, a historical overview and an introduction to the working principle are given, followed by a theoretical description of the image formation, which allows image simulations. Furthermore, the alignment process of a Bragg magnifier is described, and the developed Bragg magnifier system is characterized experimentally in terms of resolution, magnification, and the achievable field of view (FOV). The system consists of two silicon (Si) crystals with an asymmetry angle of $\alpha = 5.92°$, and operates at X-ray energies of 29 keV to 31 keV. The choice of these parameters is explained in detail in Chapter 4. Parts of this chapter have been published in Ref. [104].

3.1. Historical overview

The idea of using asymmetric Bragg diffraction for beam magnification or demagnification dates back to the 20$^{\text{th}}$ century. W. Boettinger et al. developed the first 2D Bragg magnifier [24]. It consisted of two Si crystals and operated at 8 keV using the Si (111) diffraction. The authors experimentally demonstrated a magnification factor of 25 and recognized the potential to improve the spatial resolution of an imaging system while maintaining the efficiency of large-area detectors. A decade later, several works were performed that involved a Bragg magnifier [105–109]. For example, K. Sakamoto et al. used 1D magnification to improve the resolution in computed tomography [105]. M. Kuriyama et al. applied a 2D Bragg magnifier to topography and achieved micrometer resolution [106], while D. Korytar et al. built a Bragg

magnifier from a monolithic crystal [107] and U. Bonse et al. performed a material study using a Bragg magnifier [109].

The first combination of Bragg magnifiers with phase-contrast imaging was shown by Y. Kagoshima et al. [110]. They used the Bragg magnifier as a beam conditioner to expand the X-ray illumination (see next section) and placed a living insect and frog in the magnified beam. By positioning the detector several meters away from the sample to take advantage of propagation-based phase contrast imaging (PB-PCI), the image contrast was improved compared to absorption-based imaging. At the beginning of the 21st century, further progress was made, both in terms of the theoretical description [111, 112] and the experimental implementation [113–115]. Notably, the image quality improved with respect to distortions and aberrations caused by imperfections and strain in the crystals or by poor detector quality. M. Stampanoni et al. combined a Bragg magnifier and a single photon counting detector (SPCD) at 23 keV to exploit the increased efficiency of a PILATUS detector with a 300 µm thick Si sensor while maintaining high resolution [116, 117]. P. Vagovic et al. established an in-line configuration and the use of germanium (Ge) crystals, whose 220 reflection has a larger Darwin width and thus a higher intrinsic resolution than the 220 reflection of Si [118, 119]. A method to tune the magnification at constant energy has been introduced by K. Hirano et al. [120], with the drawback that the resulting image is distorted and must be corrected by post-processing.

While Bragg magnifiers enlarge the beam cross section, Bragg demagnifiers work in the opposite way and demagnify the beam. So far, they have been used to collimate and focus the incident X-ray beam [121, 122], to obtain a high angular sensitivity in analyzer-based imaging [10], or to resize a large X-ray image to fit on a smaller detector [123].

In the last decade, the development of Bragg crystal optics has tailed off, possibly due to the comparably low energy acceptance of $\sim 10^{-4}$, further improvements in high-resolution detector systems, and alternative beam expansion techniques based on, e.g., Fresnel zone plates [124], compound refractive lenses [125], or Kirkpatrick-Baetz mirrors [126], which allow even higher resolutions down to tens of nanometers [127, 128].

3.2. Working principle of Bragg crystal optics

Bragg crystal optics consist of one or more perfectly flat crystals with an asymmetry angle α between the crystal surface and the reflecting lattice planes. Most commonly, the 220 reflection of Si crystals is used [113], but other reflexes [114] or Ge crystals [119] can also be employed (see also Fig. 2.4). The crystals operate within a predefined energy range given by the asymmetry angle. Asymmetric Bragg reflection either enlarges or demagnifies the cross-section of a monochromatic incident beam. To enlarge the beam, a positive asymmetry angle $\alpha > 0$ is used, and one speaks of a Bragg magnifier (BM). Correspondingly, a Bragg

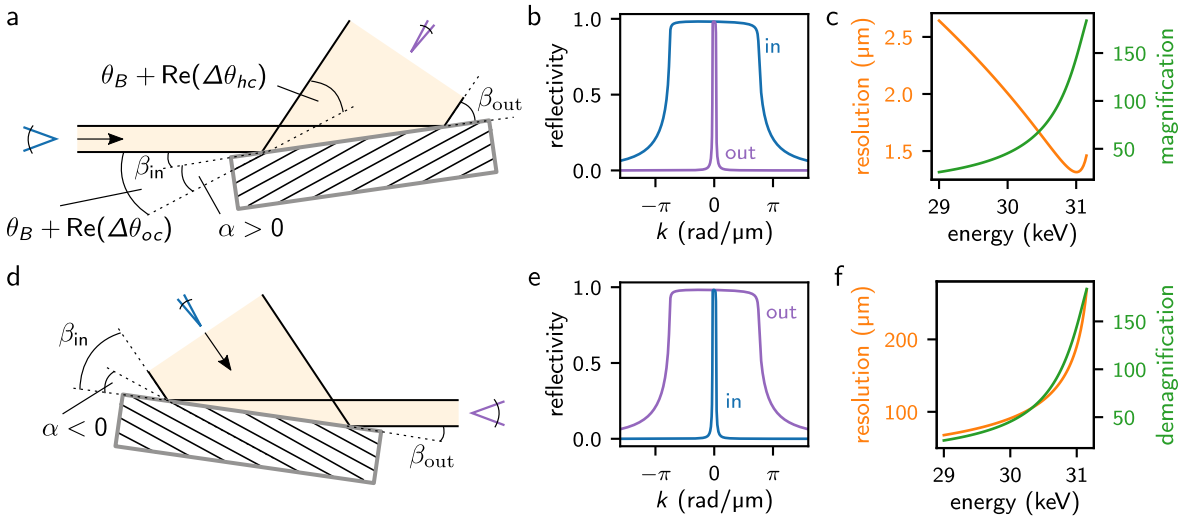

Figure 3.1.: Working principle of Bragg crystal optics. **a-c** Bragg magnifier and **d-f** Bragg demagnifier. **a** With a Bragg magnifier, the monochromatic millimeter-sized incident X-ray beam is magnified by asymmetric Bragg reflection. The diffracting crystal planes have an asymmetry angle $\alpha > 0$ to the crystal surface. The angle of incidence β_{in} between the crystal surface and the optical axis is adjusted to the center of the crystal's reflectivity curve, given by the Bragg angle θ_{B} and the correction term $\mathrm{Re}(\Delta\theta_{oc})$ from dynamical diffraction theory [34]. Correspondingly, $\mathrm{Re}(\Delta\theta_{hc})$ is the correction term for the outgoing beam, thereby defining the outgoing angle β_{out}. **b** Reflectivity curves on the incident and outgoing side of the Bragg magnifier crystal, shown for 29 keV and plotted over angular spatial frequencies k. The outgoing curves are compressed with respect to the incident curves, as also indicated in panel a. **c** Magnification and achievable resolution as a function of the X-ray photon energy, shown for the Si (220) reflection with $\alpha = 5.92°$. **d** A Bragg demagnifier works in the opposite direction of a Bragg magnifier. A large incident X-ray beam is demagnified using an asymmetry angle $\alpha < 0$. **e** The outgoing spatial frequency distribution is magnified compared to the incident curves. **f** Demagnification factor and intrinsic resolution limit for the case a Bragg demagnifier. Partly reproduced from Ref. [104].

demagnifier demagnifies the incident beam using a negative asymmetry angle $\alpha < 0$. A sketch of the working principles of a BM and a Bragg demagnifier are shown in Fig. 3.1a, d. The center of the crystal's reflectivity curve is aligned with the incident beam, which lies on the optical axis. Two crystals in a vertical arrangement magnify the beam in two dimensions.

3.2.1. Configurations

In principle, an arbitrary number of crystals can be arranged in a row and in different orientations. In the following, a brief overview of the configurations used in this work is presented.

Bragg magnifier microscope For microscopy, a millimeter-sized object is placed in front of the BM (Fig. 3.2a). In this way, the X-ray wavefield behind the sample is magnified, resulting in micrometer resolution even when using a large-area detector with a moderate pixel size of, e.g., 55 µm [98, 113]. By combining highly-efficient detectors with BMs, high dose efficiency at high resolution can be achieved, as will be exploited in Chapter 4.

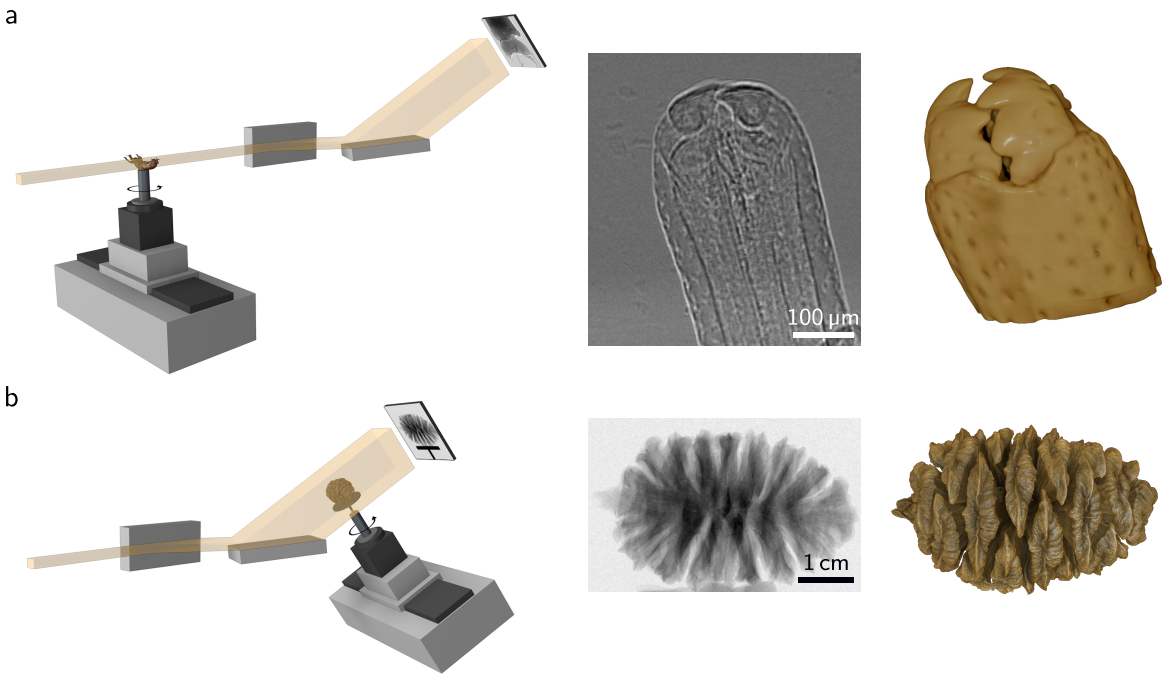

Figure 3.2.: Bragg magnifier as microscope and beam conditioner. a Sketch of the microscopy mode, flatfield-corrected radiograph and 3D volume rendering of the proboscis of a weevil. The specimen was preserved in ethanol. **b** Sketch of the conditioner mode and flatfield-corrected radiograph of a 5 cm large pine cone as well as 3D volume rendering of the reconstructed tomogram. The data in microscopy mode were acquired at 30.5 keV at the P23 beamline of PETRA III, DESY, Hamburg, Germany, and in conditioner mode at 29 keV at the IMAGE beamline of the KIT Light Source, Karlsruhe, Germany. As a side note, an additional pair of reflecting crystals was used here to bring the beam back in-line, see Ref. [129] and main text, and a Shad-o-box 1k HS detector was employed (*Teledyne DALSA, Waterloo, Canada*). Renderings were done in *Drishti* [130] and *Cinema 4D* by Thomas van de Kamp and Pauline Pfeiffer (IPS, KIT, Karlsruhe, Germany).

Bragg magnifier beam conditioner Typically, the beam diameter at a synchrotron is only a few millimeters large, which limits the applicability of full-field imaging to millimeter-sized samples. A BM allows single-shot imaging of large, centimeter-sized objects by placing the sample in the enlarged beam profile behind the BM (see Fig. 3.2b) [10, 131–133]. This operation mode is called a Bragg conditioner.

In-line configuration When imaging a sample stored in a liquid, it may be advantageous to mount the sample vertically in order to avoid sample movement during tomographic rotation. A second pair of reflecting crystals with little or no magnification can reflect the beam in front of or behind the magnifier crystals in such a way that the outgoing beam is parallel to the incident beam. This so-called in-line configuration allows vertical sample mounting in conditioner mode [118]. However, the Darwin width of the additional pair of reflecting crystals is in the range of a few microradians (see Fig. 2.4), which requires a high short- and long-term stability of the crystal mechanics and makes the experimental realization of

a stable in-line configuration challenging [129]. For the microscopy mode, there is no strong advantage of using the in-line configuration. For this reason, the present work focuses on the simpler two-crystal-configuration shown in Fig. 3.2.

Bragg demagnifier Demagnification of the wavefield behind the sample allows for PB-PCI of large, centimeter-sized samples at medium resolution, as discussed in detail in Chapter 5. To obtain a large illuminated area at the sample position, an additional Bragg conditioner is used in front of the sample. Since the Darwin width of the demagnifier crystals is very small ($\sim 1\,\mu$rad), the simplest 2D configuration of two conditioner and two demagnifier crystals is realized in this thesis for the proof-of-concept experiment.

3.3. Image formation with Bragg magnification

The remainder of this chapter is mainly dedicated to the Bragg magnifier in microscopy mode and lays the basis for Chapter 4. The following section starts by summarizing the most important properties of a BM, namely the magnification and achievable spatial resolution. Subsequently, a method for simulating the image formation process is elaborated. The image formation process is considered in reciprocal space in order to describe how the crystals affect the incident wavevectors. The presented approach results in a formalism similar to a method that was introduced by P. Modregger et al. [134] and extended to two dimensions by S. Hrivnak et al. [135]. The method presented here is exact in 1D, as it does not use the Fresnel propagator. The propagated wavefield is calculated by a non-uniform discrete Fourier transform (DFT). In the 2D case, the x and y components can in good approximation be treated independently, as discussed later, whereby rather efficient simulation times are achieved despite the non-uniform DFT.

3.3.1. Magnification

Since the Bragg angle θ_B changes with energy, the magnification can be adjusted continuously by slightly tuning the energy of the incident X-ray beam, see Fig. 3.1c (blue curve). The magnification M is given by [136]

$$M = \frac{\sin\beta_\mathrm{out}}{\sin\beta_\mathrm{in}} = \frac{\sin\left(\theta_\mathrm{B} + \mathrm{Re}(\Delta\theta_{hc}) + \alpha\right)}{\sin\left(\theta_\mathrm{B} + \mathrm{Re}(\Delta\theta_{oc}) - \alpha\right)}, \tag{3.1}$$

where $\beta_\mathrm{in} = \theta_\mathrm{B} + \mathrm{Re}(\Delta\theta_{oc}) - \alpha$ and $\beta_\mathrm{out} = \theta_\mathrm{B} + \mathrm{Re}(\Delta\theta_{hc}) + \alpha$ are the incoming and outgoing angles between the optical axis and the crystal surface, and $\mathrm{Re}(\Delta\theta_{oc,hc})$ are correction terms of the incoming and outgoing beam, obtained from dynamical diffraction theory (Eq. 2.31). The magnification in real space is tantamount to a demagnification in reciprocal space, as illustrated by the incident and outgoing reflectivity curves in Fig. 3.1b (see also Section 2.1.2).

3.3.2. Spatial resolution

The smallest spatial wavelength in an object that is transmitted through an imaging system defines the Abbe resolution limit, which is given by the system's numerical aperture as $\lambda_{\mathrm{min}} = \lambda_0/\mathrm{NA}$ [137]. For the BM in microscopy mode, the smallest resolvable spatial wavelength λ_{min} is therefore limited by the angular acceptance of the crystals, i.e., the Darwin width ω_{oc}, and given by [111]

$$\lambda_{\mathrm{min}} = \frac{\lambda_0}{\sin \omega_{oc}/2} \approx \frac{\lambda_0}{\mathrm{Re}(\delta_{oc})}, \tag{3.2}$$

as shown in Fig. 3.1b (orange curve). For examples of the Darwin curves, see Sections 4.1.2 and 4.1.3. The resolution can be further affected by source blur (Section 2.2.5) and by the resolution of the detector. The effective pixel size in the object is given by $\Delta x = \Delta x_{\mathrm{p}}/M$, where Δx_{p} is the physical pixel size of the detector, and should ideally be smaller than half the resolution limit. It is therefore advantageous to choose a crystal reflex and asymmetry angle that provide a large Darwin width and high magnification [129].

As a side note, the resolution can be increased by detuning the angular position of the crystals [138]. This approach is known as analyzer-based imaging, but requires acquisitions at multiple angles and is therefore not suitable for dose-efficient *in vivo* imaging.

In the case of a Bragg demagnifier, the optical path is reversed compared to the BM, i.e., $\alpha < 0$. In this case, the outgoing angle β_{out} is smaller than the incident angle β_{in}, and the beam cross section is demagnified (Fig. 3.1d), while the spatial frequency distribution is enlarged (Fig. 3.1e). This effect will be exploited for the realization of PB-PCI of large samples, see Chapter 5. Eqs. 3.1 and 3.2 for the magnification and resolution remain valid. For $\alpha < 0$, the incident angular acceptance is smaller than for $\alpha > 0$, which results in a lower achievable resolution compared to the BM (Fig. 3.1f).

3.3.3. Plane wave mapping

Let us consider the image formation process in a BM in reciprocal space. As described in Section 2.2.3, the wavefield $f(\boldsymbol{x}_{\mathrm{in}})$ in the object exit plane $z = 0$ can be decomposed into plane waves $\boldsymbol{k}_{0,\mathrm{in}}$ with amplitudes $\tilde{f}(\boldsymbol{k}_{\mathrm{in}})$ and angular spatial frequencies $\boldsymbol{k}_{\mathrm{in}}$ in the object exit plane. The aim is to find an expression that describes how each plane wave $\boldsymbol{k}_{0,\mathrm{in}}$ with angular spatial frequencies $\boldsymbol{k}_{\mathrm{in}}$ incident on the crystals is transformed into a corresponding outgoing plane wave $\boldsymbol{k}_{0,\mathrm{out}}$ with angular spatial frequencies $\boldsymbol{k}_{\mathrm{out}}$ in the detector plane. This procedure is called the plane wave mapping procedure here, because each incident plane wave is coherently mapped exactly to one outgoing plane wave by dynamical diffraction at the crystal. The resulting expression for $\boldsymbol{k}_{\mathrm{out}}$ is given as a function of $\boldsymbol{k}_{\mathrm{in}}$ and the angles β_{in} and β_{out}, which depend only on the working energy and the crystal parameters, and can be determined from dynamical diffraction theory (see Sections 2.1.2 and 3.3.1). In addition, the

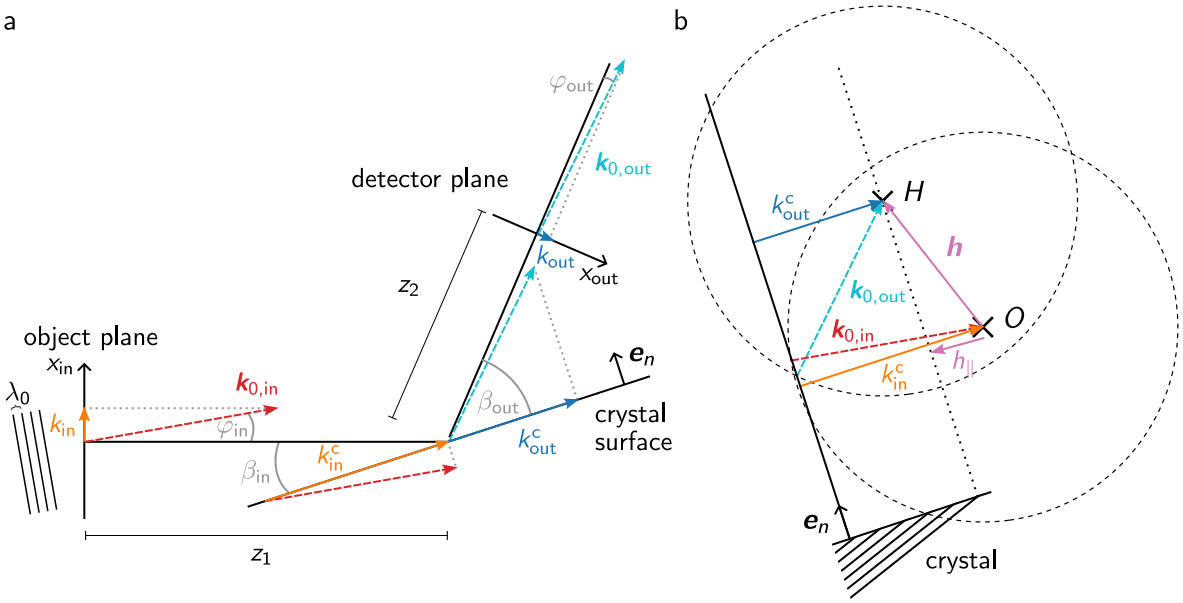

Figure 3.3.: Sketch for determining $\boldsymbol{k}_{\mathbf{out}}(\boldsymbol{k}_{\mathbf{in}})$. **a** A plane wave $\boldsymbol{k}_{0,\mathrm{in}}$ propagating at an angle φ_{in} to the optical axis has an angular spatial frequency k_{in} in the object plane and an angular spatial frequency $k_{\mathrm{in}}^{\mathrm{c}}$ on the crystal surface, which has the surface normal $\boldsymbol{e}_n$. It is diffracted by the crystal to a plane wave $\boldsymbol{k}_{0,\mathrm{out}}$ that propagates at an angle φ_{out} to the optical axis, resulting in an angular spatial frequency $k_{\mathrm{out}}^{\mathrm{c}}$ on the crystal surface and k_{out} in the detector plane. The optical axis runs along the zero-order beam ($k_{\mathrm{in}} = 0, \varphi_{\mathrm{in}} = 0$) and has an incident angle β_{in} to the crystal surface and an outgoing angle β_{out}, which can be computed from dynamical theory (see Section 2.1.2). **b** Situation in reciprocal space on the dispersion surface. During diffraction at the crystal, the incident plane wave experiences the crystal momentum $\boldsymbol{h}$. Due to the in-plane Bragg law, the angular spatial frequencies $k_{\mathrm{in}}^{\mathrm{c}}$ and $k_{\mathrm{out}}^{\mathrm{c}}$ are connected by $h_{\parallel} = k_0(\cos\beta_{\mathrm{out}} - \cos\beta_{\mathrm{in}})$, which is the component of $\boldsymbol{h}$ parallel to the crystal surface.

crystal imprints an attenuation and a phase shift on each plane wave $\boldsymbol{k}_{\mathrm{out}}$, which are given by the complex field amplitude ratio A and can likewise be computed from dynamical theory (Section 2.1.2). Knowing $\boldsymbol{k}_{\mathrm{out}}$ in the detector plane as well as the wavefield propagator allows the image to be determined by an inverse Fourier transformation.

> Notation reminder: A 3D plane wave with wavenumber $k_0 = 2\pi/\lambda_0$ is denoted as $\boldsymbol{k}_0 = (k_x, k_y, k_z)^{\mathrm{T}}$ with the index 0, while the angular spatial frequencies in the object plane, crystal plane or detector plane are written as $\boldsymbol{k} = (k_x, k_y)^{\mathrm{T}}$.

For simplicity and didactic reasons, the 1D case with coplanar diffraction is treated first, i.e., considering only the case where the spatial frequencies in y-direction are zero ($k_{y,\mathrm{in}} = 0$). After the following derivation, it will become apparent why the x- and y-directions can in good approximation be treated independently. The 1D situation is sketched in Fig. 3.3a in real space and Fig. 3.3b in reciprocal space. An object wavefield $f(x_{\mathrm{in}})$ propagates in free space and is diffracted by a crystal. The aim is to calculate the propagated wavefield in the detector plane behind the crystal. The optical axis is defined in such a way that a plane

wave $\boldsymbol{k}_{0,\mathrm{in}}$ with angular spatial frequency $k_{\mathrm{in}} = 0$ traveling perpendicular to the object plane propagates along this axis. The crystal is aligned so that the optical axis is in the center of the reflection curve. The incident angle of the optical axis to the crystal surface is given by β_{in} and the outgoing angle is β_{out} (Fig. 3.1). These angles can be computed from dynamical theory, see Section 2.1.2. An arbitrary plane wave $\boldsymbol{k}_{0,\mathrm{in}}$ with angular spatial frequency k_{in} in the object plane travels at an angle

$$\varphi_{\mathrm{in}} = \arcsin \frac{k_{\mathrm{in}}}{k_0} \tag{3.3}$$

to the optical axis, see Fig. 3.3a. On the tilted crystal surface, this plane wave has the angular spatial frequency

$$k_{\mathrm{in}}^{\mathrm{c}} = k_0 \cos(\beta_{\mathrm{in}} - \varphi_{\mathrm{in}}). \tag{3.4}$$

The crystal adds its reciprocal lattice vector $\boldsymbol{h}$ to the incident plane wave, causing a change in propagation direction [112].

However, as known from dynamical theory, the Bragg condition is only sharply fulfilled for the wavevectors inside the crystal (see Section 2.1.2). Since the components at the crystal surface are preserved as stated by the boundary condition, the outgoing angular spatial frequency $k_{\mathrm{out}}^{\mathrm{c}}$ in the crystal surface plane is related to the incident angular spatial frequency $k_{\mathrm{in}}^{\mathrm{c}}$ in the crystal plane by the in-plane Bragg law:

$$k_{\mathrm{out}}^{\mathrm{c}} = k_{\mathrm{in}}^{\mathrm{c}} + h_{\parallel}, \tag{3.5}$$

where

$$h_{\parallel} = k_0(\cos\beta_{\mathrm{out}} - \cos\beta_{\mathrm{in}}) \tag{3.6}$$

is the component of $\boldsymbol{h}$ parallel to the crystal surface, see Fig. 3.4. The outgoing angle φ_{out} and the angular spatial frequency k_{out} in the detector plane are then given by

$$\varphi_{\mathrm{out}} = \beta_{\mathrm{out}} - \arccos \frac{k_{\mathrm{out}}^{\mathrm{c}}}{k_0}, \tag{3.7}$$

$$k_{\mathrm{out}} = k_0 \sin\varphi_{\mathrm{out}}. \tag{3.8}$$

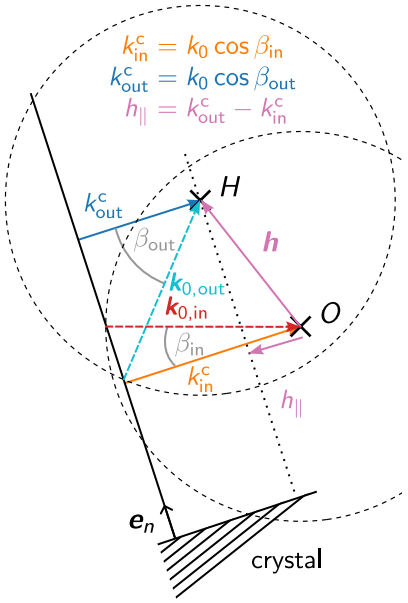

Figure 3.4.: Sketch for determining $\boldsymbol{h}_{\parallel}$. Situation from Fig. 3.3 for $k_{\mathrm{in}} = 0$, i.e., $\boldsymbol{k}_{0,\mathrm{in}}$ travels parallel to the optical axis and impinges on the crystal surface with the angle β_{in}. After diffraction, $\boldsymbol{k}_{0,\mathrm{out}}$ leaves the crystal at an angle β_{out}. The in-plane component of the crystal momentum $\boldsymbol{h}$ is $h_{\parallel} = k_0(\cos\beta_{\mathrm{out}} - \cos\beta_{\mathrm{in}})$.

Using Eqs. 3.3 - 3.6, the expression

$$k_{\mathrm{out}}(k_{\mathrm{in}}) = k_0 \sin\left(\beta_{\mathrm{out}} - \arccos\left[\cos\left(\beta_{\mathrm{in}} - \arcsin\frac{k_{\mathrm{in}}}{k_0}\right) + \cos\beta_{\mathrm{out}} - \cos\beta_{\mathrm{in}}\right]\right) \tag{3.9}$$

is obtained, which describes how each incident plane wave k_{in} is mapped to an outgoing plane wave k_{out}. As will be shown later, the nonlinear dependence of $k_{\mathrm{out}}(k_{\mathrm{in}})$ implies that the imaging system is shift-variant and therefore the propagated wavefield cannot be calculated by a simple fast Fourier transform (FFT).

3.3.4. Calculation of the propagated wavefield

After knowing how the incident wavevectors are transferred to the detector plane, the next step is to consider the propagator H that describes the phase and amplitude collected by each plane wave during propagation in free space and diffraction at the crystal. The free space propagator was introduced in Eq. 2.55. It describes the phase that each plane wave collects relative to a plane wave along the optical axis as it propagates along a distance z. Besides, the crystal imparts a frequency-dependent damping and phase shift to each plane wave, which is described by the complex field amplitude ratio A and can be calculated analytically using Eq. 2.36. Thus, the propagator for the 1D case is given by

$$H(k_{\mathrm{out}}) = A(k_{\mathrm{in}}) \cdot e^{iz_1\sqrt{k_0^2-k_{\mathrm{in}}^2}} \cdot e^{iz_2\sqrt{k_0^2-k_{\mathrm{out}}^2}}, \tag{3.10}$$

where z_1 and z_2 are the distances between the sample and the center of the crystal surface or the crystal surface and the detector, respectively.

Finally, the propagated wavefield in the detector plane is given by superimposing all propagated and reflected plane waves weighted by the object's Fourier transform $\tilde{f}(x_{\mathrm{in}})$ and multiplied by the phase of the plane waves at the coordinate x_{out}:

$$g(x_{\mathrm{out}}) = \frac{1}{2\pi}\int \tilde{f}(k_{\mathrm{in}}) \cdot A(k_{\mathrm{in}}) \cdot e^{iz_1\sqrt{k_0^2-k_{\mathrm{in}}^2}} \cdot e^{iz_2\sqrt{k_0^2-k_{\mathrm{out}}^2(k_{\mathrm{in}})}} \cdot e^{ik_{\mathrm{out}}(k_{\mathrm{in}})\cdot x_{\mathrm{out}}} \cdot \frac{\mathrm{d}k_{\mathrm{out}}(k_{\mathrm{in}})}{\mathrm{d}k_{\mathrm{in}}}\mathrm{d}k_{\mathrm{in}}. \tag{3.11}$$

The derivative

$$\begin{aligned}\frac{\mathrm{d}k_{\mathrm{out}}}{\mathrm{d}k_{\mathrm{in}}} &= \frac{\sin(\beta_{\mathrm{in}} - \arcsin\frac{k_{\mathrm{in}}}{k_0}) \cdot \cos(\beta_{\mathrm{out}} - \arccos[\cos\beta_{\mathrm{out}} - \cos\beta_{\mathrm{in}} + \cos(\beta_{\mathrm{in}} - \arcsin\frac{k_{\mathrm{in}}}{k_0})])}{\sqrt{1-\frac{k_{\mathrm{in}}^2}{k_0^2}} \cdot \sqrt{1-[\cos\beta_{\mathrm{out}} + \cos(\beta_{\mathrm{in}} - \arcsin\frac{k_{\mathrm{in}}}{k_0}) - \cos\beta_{\mathrm{in}}]^2}} \\ &= \frac{1}{M(k_{\mathrm{in}})}\end{aligned} \tag{3.12}$$

accounts for the substitution $k_{\mathrm{out}}(k_{\mathrm{in}})$ and corresponds to the inverse of the frequency-dependent magnification $M(k_{\mathrm{in}})$ with $M(0) = \sin\beta_{\mathrm{out}}/\sin\beta_{\mathrm{in}}$, cf. Eq. 3.1.

Numerically, $\tilde{f}(k_{\mathrm{in}})$ can be computed by an FFT, but the nonlinear dependence of $k_{\mathrm{out}}(k_{\mathrm{in}})$ prevents the use of an inverse FFT to compute $g(x_{\mathrm{out}})$. Instead, the propagated wavefield is computed by a non-uniform inverse DFT. In 1D, the non-uniform DFT can be computed rather quickly by storing the plane waves with non-equidistant frequencies in a matrix.

Two-dimensional formulation and multi-crystal arrangements

So far, the 1D case with $k_{y,\mathrm{in}} = 0$ has been considered. Since the reciprocal lattice vector $\boldsymbol{h}$ of the first crystal is, without loss of generality, aligned in the x-z-plane, it transfers its momentum only to the x- and z-components of the incident plane wave $\boldsymbol{k}_{0,\mathrm{in}}$, while $k_{y,\mathrm{in}}$ remains unchanged. As the length of $\boldsymbol{k}_{0,\mathrm{in}}$ is preserved, the z-component changes slightly for $k_{y,\mathrm{in}} \neq 0$ compared to the case $k_{y,\mathrm{in}} = 0$ considered above. However, since the diffraction of X-rays at the sample is small ($k_{x,y}/k_0 < 10^{-4}$), this change can in good approximation be neglected, and the angular spatial frequencies $k_{x,\mathrm{in}}$ and $k_{y,\mathrm{in}}$ can be treated independently. Eq. 3.9 thus remains valid for both components. For the sake of completeness, the image formation is presented in the following for two crystals with perpendicularly oriented surfaces. The first crystal magnifies the beam in the horizontal x-direction and the second crystal in the vertical y-direction. After propagating the distance $z_{1,x}$ to the first crystal and diffracting at this crystal, the wavefield propagates a distance $z_{1,y} - z_{1,x}$ to the second crystal, where $z_{1,y}$ is the distance along the optical path between the sample and the center of the second crystal. After diffraction at the second crystal, the wavefield further propagates a distance $z_{2,y}$ to the detector. The wavefield in the image plane is then given by

$$\begin{aligned} g(\boldsymbol{r}_{\mathrm{out}}) = \frac{1}{(2\pi)^2} \int \tilde{f}(\boldsymbol{k}_{\mathrm{in}}) \cdot A(\boldsymbol{k}_{\mathrm{in}}) \cdot e^{iz_{1,x}\sqrt{k_0^2 - k_{x,\mathrm{in}}^2 - k_{y,\mathrm{in}}^2}} \cdot e^{i(z_{1,y}-z_{1,x})\sqrt{k_0^2 - k_{x,\mathrm{out}}(k_{x,\mathrm{in}}) - k_{y,\mathrm{in}}^2}} \\ \cdot e^{iz_{2,y}\sqrt{k_0^2 - k_{x,\mathrm{out}}(k_{x,\mathrm{in}}) - k_{y,\mathrm{out}}(k_{y,\mathrm{in}})}} \cdot e^{i\boldsymbol{k}_{\mathrm{out}}(\boldsymbol{k}_{\mathrm{in}})\cdot\boldsymbol{r}_{\mathrm{out}}} \\ \cdot \frac{\mathrm{d}k_{x,\mathrm{out}}(k_{x,\mathrm{in}})}{\mathrm{d}k_{x,\mathrm{in}}} \frac{\mathrm{d}k_{y,\mathrm{out}}(k_{y,\mathrm{in}})}{\mathrm{d}k_{y,\mathrm{in}}} \mathrm{d}k_{x,\mathrm{in}} \mathrm{d}k_{y,\mathrm{in}}, \end{aligned} \tag{3.13}$$

where $A(\boldsymbol{k}_{\mathrm{in}})$ is the complex field amplitude ratio comprising both crystals. For propagation through multiple crystals, Eq. 3.9 is applied multiple times, resulting in a single formula for the final spatial frequencies as a function of the incident spatial frequencies, and the phase factors in the propagator are adapted accordingly. The method then allows the final wavefield to be calculated by a single non-uniform 2D DFT, which decomposes into two non-uniform 1D DFTs. To simulate various samples with identical setup parameters, the calculation of $\boldsymbol{k}_{\mathrm{out}}(\boldsymbol{k}_{\mathrm{in}})$ and the propagator $H(\boldsymbol{k}_{\mathrm{out}})$ needs to be performed only once, irrespective of the sample. This can be useful, e.g., for iterative phase retrieval, where the image intensity has to be simulated for various objects. As mentioned above, it would be even slightly more precise to consider the interdependence of the coordinates $k_{x,\mathrm{in}}$ and $k_{y,\mathrm{in}}$, and the vectorial character of light, i.e., the polarization. This small correction may be incorporated using the algorithm of X. Huang [46], which would, however, be computationally more demanding.

3.3.5. Shift-variance and linearization

The non-linearity of $k_{\mathrm{out}}(k_{\mathrm{in}})$ leads to a shift-variant behavior of the image formation, i.e., the propagated wavefield cannot be expressed by a convolution of the object function $f(x_{\mathrm{in}})$ with the propagator in real space. As a result, the propagated wavefield of a symmetric object will not be symmetric [112, 139]. A 1D simulation example using the formalism presented above is given in Fig. 3.5. The object consists of two Gaussians with a maximum thickness of 20 µm and a lateral spacing of 150 µm. The material is carbon, which gives a vanishing absorption $< 0.1\,\%$ and a maximum phase shift of 1.6 rad (Fig. 3.5a). The image in the detector plane reveals that the left object experiences less phase propagation than the right one (Fig. 3.5f). In position space, this can be understood from Fig. 3.5c. The lower part of the image has a shorter propagation distance z_{bottom} between object and crystal than the upper part z_{top}. The k_{out} values behind the crystal are much smaller than the k_{in} values, which causes the image propagation to be 'frozen' behind the crystal, see paragraph below and Fig. 3.5b. In good approximation, the phase contrast will therefore only evolve in front of the crystal, resulting in a shorter propagation distance z_{bottom} for the lower object. The effect of the shift-variance on the image depends on the sample itself and the imaging parameters, in particular the ratio between z_{bottom} and z_{top} [139].

In the case of negligible shift variance, a linear approximation of Eq. 3.9 can be performed:

$$k_{\mathrm{out}} = \frac{k_{\mathrm{in}}}{M}. \tag{3.14}$$

The linearization of k_{out} in Eq. 3.11 and the Fresnel approximation (Eq. 2.57) lead to a simple Fourier transform:

$$g(x_{\mathrm{out}}) \approx \frac{1}{2\pi} \int \tilde{f}(k_{\mathrm{in}}) \cdot A(k_{\mathrm{in}}) \cdot e^{ik_0(z_1+z_2)} \cdot e^{-iz_1 \frac{k_{\mathrm{in}}^2}{2k_0}} \cdot e^{-iz_2 \frac{k_{\mathrm{in}}^2}{2k_0 M^2}} \cdot e^{ik_{\mathrm{in}} \cdot \frac{x_{\mathrm{out}}}{M}} \frac{\mathrm{d}k_{\mathrm{in}}}{M}. \tag{3.15}$$

Here, it can be seen again that for large M the third exponential for propagation along z_2 behind the crystal is much smaller than the second exponential for propagation in front of the crystal. This means that the propagation along z_2 contributes very little to the overall propagation, and the propagation of the wavefield after magnification by the crystal can in good approximation be said to be 'frozen'. With $x_{\mathrm{out}} = M x_{\mathrm{in}}$, and omitting the constant phase term $e^{ik_0(z_1+z_2)}$ and the negligible propagation behind the crystal, Eq. 3.15 further simplifies to

$$g(x_{\mathrm{out}}) \approx \frac{1}{2\pi} \int \tilde{f}(k_{\mathrm{in}}) \cdot A(k_{\mathrm{in}}) \cdot e^{-iz_1 \frac{k_{\mathrm{in}}^2}{2k_0}} \cdot e^{ik_{\mathrm{in}} \cdot x_{\mathrm{in}}} \frac{\mathrm{d}k_{\mathrm{in}}}{M}, \tag{3.16}$$

which can be expressed by a convolution:

$$g(x_{\mathrm{out}}) \approx f(x_{\mathrm{in}}) * \mathcal{F}^{-1}\left[\frac{A(k_{\mathrm{in}})}{M} \cdot e^{-iz_1 \frac{k_{\mathrm{in}}^2}{2k_0}} \right]. \tag{3.17}$$

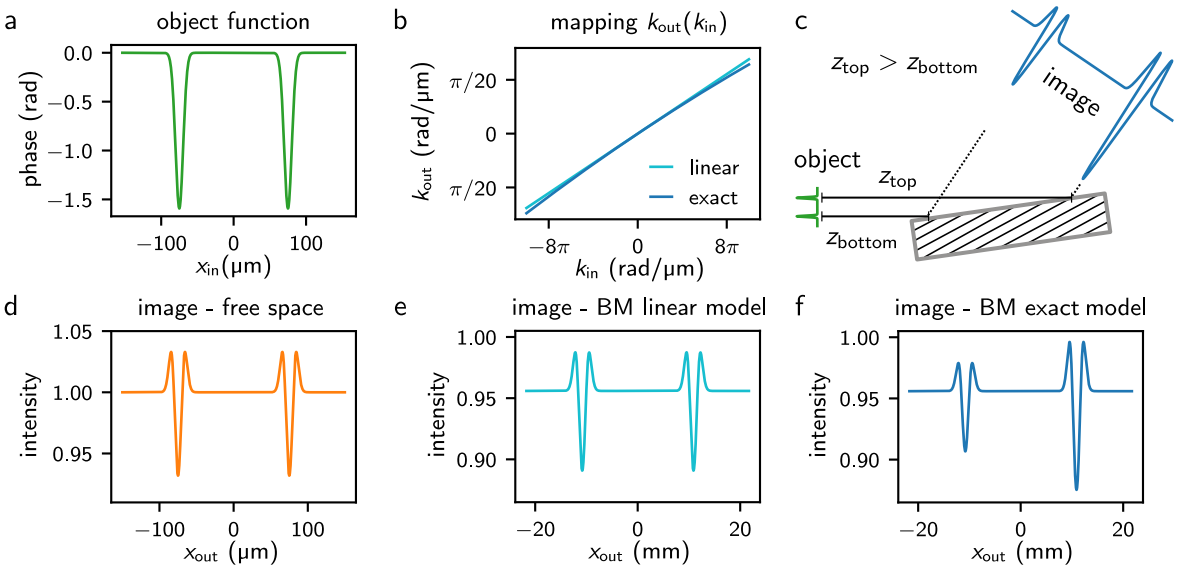

Figure 3.5.: Image simulation using the plane wave mapping procedure. The simulation was performed for a photon energy of 31 keV, a propagation distance of $z_1 = 0.2\,\mathrm{m}$ between the object and the center of the crystal surface, and using the Si 220 reflex with $\alpha = 5.92°$. **a** The object consists of two Gaussians with a spatial separation of 150 µm, a thickness of 20 µm and carbon as material. **b** Mapping the incident angular spatial frequencies k_{in} of the object function to the angular spatial frequencies k_{out} in the detector plane yields a non-linear dependence (exact model, dark blue curve, see also Eq. 3.9). The linearization $k_{\mathrm{out}} = k_{\mathrm{in}}/M$ of Eq. 3.9 is shown as well (light blue curve). Note that $k_{\mathrm{out}} \ll k_{\mathrm{in}}$, which leads to a magnification in position space and 'freezes' the propagation behind the crystal (see main text). **c** The shift-variance can be understood by looking at the situation in position space. The lower side of the object has a shorter distance z_{bottom} to the crystal than the upper side z_{top}, whereby the lower Gaussian experiences less propagation. **d** Image intensity at $z_1 = 0.2\,\mathrm{m}$ after free space propagation without crystal and **e** behind the crystal using the linear model, where the result is almost the same as for simple free space propagation, except that the mean intensity is slightly damped by the finite crystal reflectivity. Note also the magnification of x_{out}. **f** Image intensity behind the crystal with the full nonlinear model shows the shift-variant behavior.

Within the linear approximation in Eq. 3.14, the propagated wavefield can thus be computed by conventional free space propagation with the mean propagation distance z_1. For this case, Fig. 3.5e shows the simulated image intensity. Both objects have propagated the same distance and show the same intensity pattern as for conventional free space propagation (Fig. 3.5d), except for a damping of the mean intensity due to some minor absorption in the crystals. In the literature, Eq. 3.16 is referred to as the effective distance method [112, 135].

Source blur The image quality is degraded by the finite X-ray source. This effect can be incorporated in the simulations by incoherently superimposing the image intensities resulting from illumination at different angles, see also Eq. 2.65 and Appendix A.2. For the linear approximation (Eq. 3.14), i.e., a shift-invariant system, the operation reduces to a convolution of the coherent image intensity with the source function (Eq. 2.67).

Relation to reciprocal space coordinate transformation (RCT)

The reciprocal coordinates transformation (RCT) method was introduced by Modregger et al. [134] and further developed by Hrivnak et al. [135]. It is a numerically efficient simulation method for the image formation in a BM that takes into account the shift variance. The RCT method leads to a very similar result as the plane wave mapping procedure presented here, but is motivated mathematically by a coordinate transformation. In particular, the diffraction at the crystals is not described in the derivation of the RCT formula, while in the plane wave mapping procedure the diffraction at the crystal surface is taken as the basis for the derivation. Also, the mapping method does not require an interpolation of the object FFT. A more detailed comparison of the RCT method and the mapping procedure is given in Appendix A.4.

3.3.6. Phase reconstruction

In general, the phase reconstruction of holograms acquired with a BM is not straightforward due to the inherent shift-variance of the system, and iterative methods are required [139]. However, under certain conditions, such as small FOV, large propagation distances, or moderate magnifications, where shift-variance effects are negligible [139], the image formation can be described by a simple convolution, as shown in Eq. 3.17. In two dimensions and neglecting propagation behind the crystals, the propagator in Fresnel approximation reads

$$H(k_{x,\mathrm{in}}, k_{y,\mathrm{in}}) = \frac{A(k_{x,\mathrm{in}}, k_{y,\mathrm{in}})}{M^2} \cdot e^{-i\frac{z_{1,x}k_{x,\mathrm{in}}^2 + z_{1,y}k_{y,\mathrm{in}}^2}{2k_0}}. \tag{3.18}$$

Except for the field amplitude reflection curve and the separate horizontal and vertical propagation distances $z_{1,x}$ and $z_{1,y}$, the propagator is identical to the free space Fresnel propagator (Eq. 2.58). Hence, the reconstruction algorithms presented in Section 2.2.7 can be applied. In the simplest approach where the crystal function is also neglected, it is therefore sufficient to replace $z(k_x^2 + k_y^2)$ by $z_{1,x}k_{\mathrm{x,in}}^2 + z_{1,y}k_{\mathrm{y,in}}^2$ in existing implementations for phase retrieval of conventional propagation-based phase contrast [140]. The publicly available *HoloTomoToolbox* [77] and *Tofu* framework [141] provide such a functionality. In the reconstruction, A can also be taken into account, but its influence is generally not significant, especially in the presence of source blur, and is therefore omitted in the reconstructions performed here.

3.4. Realization of the Bragg magnifier system and experimental characterization

This section describes the general design of a BM and the specific implementation and characterization realized in this thesis. After a general description of the aspects that should be taken into account when designing a BM, this section presents the experimental setup

that was developed and applied in this work, describes the steps necessary to align a BM, and characterizes the BM system experimentally. Since the propagation after magnification can be neglected, the distances $z_{1,x}$ and $z_{1,y}$ are written as z_x, z_y in the following for better readability.

3.4.1. General requirements

For designing a BM experiment, several aspects have to be considered. In general, an X-ray source with sufficient coherence is required for being able to perform PB-PCI. Due to the small energy acceptance of the BM crystals, a monochromator is used in front of the sample. The amount of additional components in the beam path should be kept as low as possible in order not to degrade the coherence and to obtain a homogeneous illumination. Typically, beamline mirrors for suppression of higher harmonics are not required for reasons explained below.

For the crystals, it is essential to choose a high-quality material that is free of defects and can be polished well to obtain a strain-free and flat surface. The chosen reflex should have a high susceptibility, resulting in a large Darwin width ω_{oc}. In this way, the crystal reflex will have a large angular acceptance, allowing for a high spatial resolution. In addition, the chosen reflex requires a large Bragg angle to enable high magnification factors. According to the desired highest working energy, the asymmetry angle α should be specified such that ω_{oc} reaches its maximum at this energy (see also Fig. 4.4a). Due to the asymmetric reflection, the crystals typically have a considerably larger Darwin width than the preceding monochromator. The crystal dimensions define the FOV and should ideally be chosen to fit the incident beam size.

The crystal has to be precisely aligned with the beam in all six degrees of freedom. Therefore, the mechanics of the crystals require high angular precision and stability. Especially the motor for the pitch angle ϑ (see Fig. 3.6) should enable a step size and stability of at least about one tenth of the Darwin width. To simplify the alignment process, the rotation axes and the pivot point should lie as depicted in Fig. 3.6.

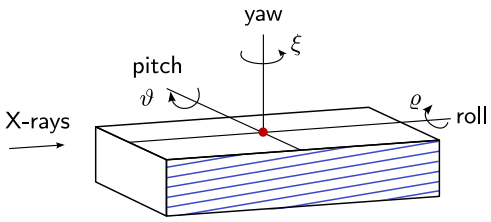

Figure 3.6.: Definition of the pitch, roll and yaw angles. The red dot indicates the pivot point in the center of the crystal surface.

The simplest realization of a 2D BM system comprises two identical crystals mounted vertically to each other and a highly-efficient large-area detector. In addition, a sample stage is required in front of the BM crystals. The propagation distances z_x and z_y in horizontal and vertical direction are given by the distances between the sample and the surface center of the horizontally or vertically diffracting crystal, respectively, and can be individually maximized according to the dimensions of the X-ray source (see also Eq. 2.69).

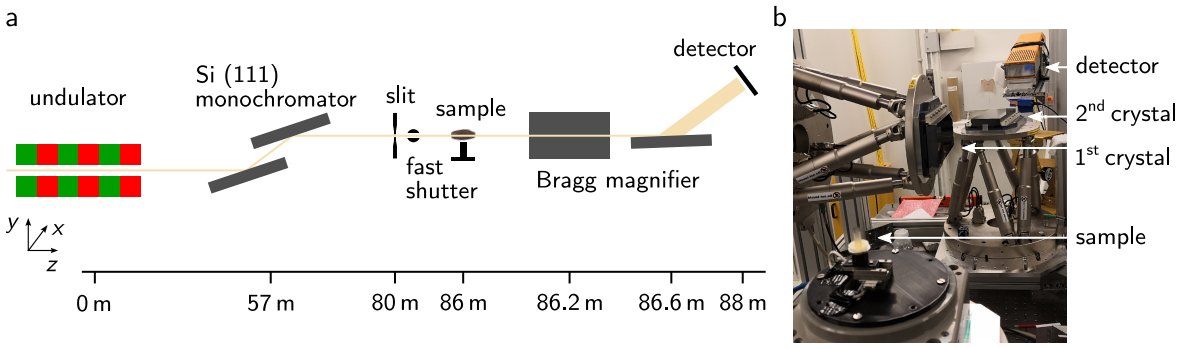

Figure 3.7.: Beamline layout and experimental setup. **a** Sketch of the P23 beamline and experimental layout in microscopy mode. An undulator serves as X-ray source, followed by a Si (111) double crystal monochromator, slits and a fast shutter. **b** Picture of the experimental setup at P23, PETRA III, DESY, Hamburg, Germany. Reproduced from Ref. [104].

3.4.2. Beamline layout and experimental setup

The specific BM system developed and realized in this work was designed for usage at the P23 beamline at PETRA III, DESY, in Hamburg. Unless otherwise stated, the data presented in this work were acquired at this beamline. For reasons detailed in Chapter 4, the working energy range was chosen to be 29 keV to 31 keV. A sketch of the P23 beamline layout and the experimental setup is given in Fig. 3.7. The main beamline components are the undulator source, a symmetrically diffracting double-crystal Si (111) monochromator, sample slits, and a fast shutter.

The BM consists of two Si crystals with dimensions of 21 cm x 8 cm x 2 cm and a nominal asymmetry angle of $\alpha = 5.92°$ between the crystal surface normal and the crystallographic [110] direction, resulting in a physical input FOV of 0.3 mm x 0.3 mm to 1.5 mm x 1.5 mm, depending on the magnification, and an output FOV of 45 mm x 45 mm. For more information on the crystal quality, see Ref. [129]. Both crystals are mounted on a hexapod each (HP-840.G1, *Physik Instrumente (PI) GmbH & Co. KG, 76228 Karlsruhe, Germany*). At third-generation synchrotrons such as PETRA III, the source is larger in the horizontal direction, which leads to more source blur in this direction. Therefore, the horizontal magnification is performed first (crystal surface is oriented vertically), resulting in a shorter horizontal propagation distance z_x.

After vertical magnification by the second crystal (with horizontal surface orientation), the X-ray image is detected by a large-area detector. Unless otherwise stated, the detector in use is a LAMBDA 750k detector (*X-Spectrum GmbH, 22547 Hamburg, Germany*) with a 500 µm thick gallium arsenide (GaAs) sensor [98]. It consists of a 6 x 2 Medipix3RX chip array, where a single chip has 256 x 256 pixels with a physical pixel size of 55 µm, resulting in a chip size of 1.4 cm x 1.4 cm and a total FOV of 8.4 cm x 2.8 cm. By design, there are 6 pixels wide dead zones between the individual chips, which are bridged by interpolation between the surrounding pixels. For automated data acquisition the control system *Concert* is used [142].

3.4.3. Alignment procedure

Before operating a BM in an experiment, the system has to be precisely aligned to the incident X-ray beam. In the following, a general procedure for aligning the crystals in a two-crystal BM is described. The procedure is illustrated in Fig. 3.8 using the specific implementation of the two-crystal BM realized in this work.

Prior to the crystal alignment, a detector is placed in the direct beam and the beamline is optimized to provide homogeneous illumination. Depending on the detector in use, filters should be added in front of the detector to avoid damage by the high flux of the direct beam. The beamline slits are centered around the beam.

Next, the actual alignment procedure for the crystals is performed. The pitch, roll and yaw angles ϑ, ϱ and ξ that are adjusted during alignment are designated in Fig. 3.6. Three alignment steps are conducted for each crystal: i) placing the crystal parallel to the beam and moving the crystal surface to the center of the beam, ii) finding the asymmetric Bragg reflex by aligning the pitch angle ϑ, and iii) adjusting the roll angle ϱ. Fig. 3.8a-c shows these three steps for the first crystal (the horizontally diffracting crystal in the present implementation), and Fig. 3.8d-f for the second crystal (vertically diffracting crystal, see also Fig. 3.7).

In the first step, the first crystal is moved into the beam so that its shadow becomes visible on the camera. The crystal is brought into parallel position by adjusting the pitch angle ϑ while minimizing the shadow, see Fig. 3.8a, and then centered to the center of the beam. In the experimental images in Fig. 3.8a, the crystal is positioned in the right part of the FOV. The total reflex appears when the crystal is tilted too much towards the source, see the middle image (red arrow). In the lower image (green frame), the shadow is minimized, meaning that the crystal is oriented parallel to the beam. Adjusting the crystal to this parallel position makes it easier to find the Bragg reflex in the next step. Finally, the crystal is moved laterally in such a way that it cuts the illuminated area in half.

In the second step, the pitch angle ϑ is rotated by $\theta_\mathrm{B}-\alpha$, revealing a diffracted and horizontally magnified beam (Fig. 3.8b). A subsequent rocking scan allows fine-tuning of the pitch angle to the center of the rocking curve. The graph shows the pitch angle relative to the peak position.

In the last alignment step for the first crystal, the roll angle ϱ is adjusted in such a way that the reflected beam lies in one line with the direct beam, as shown by the green line in Fig. 3.8c. As mentioned above, the direct beam on the right side of the image was attenuated by filters that were placed in front of the detector, and the contrast in the displayed image had to be adjusted to make the direct beam visible.

The alignment procedure for the second crystal is very similar. This time, the three steps are performed in the diffracted beam of the first crystal. First, the crystal is brought into

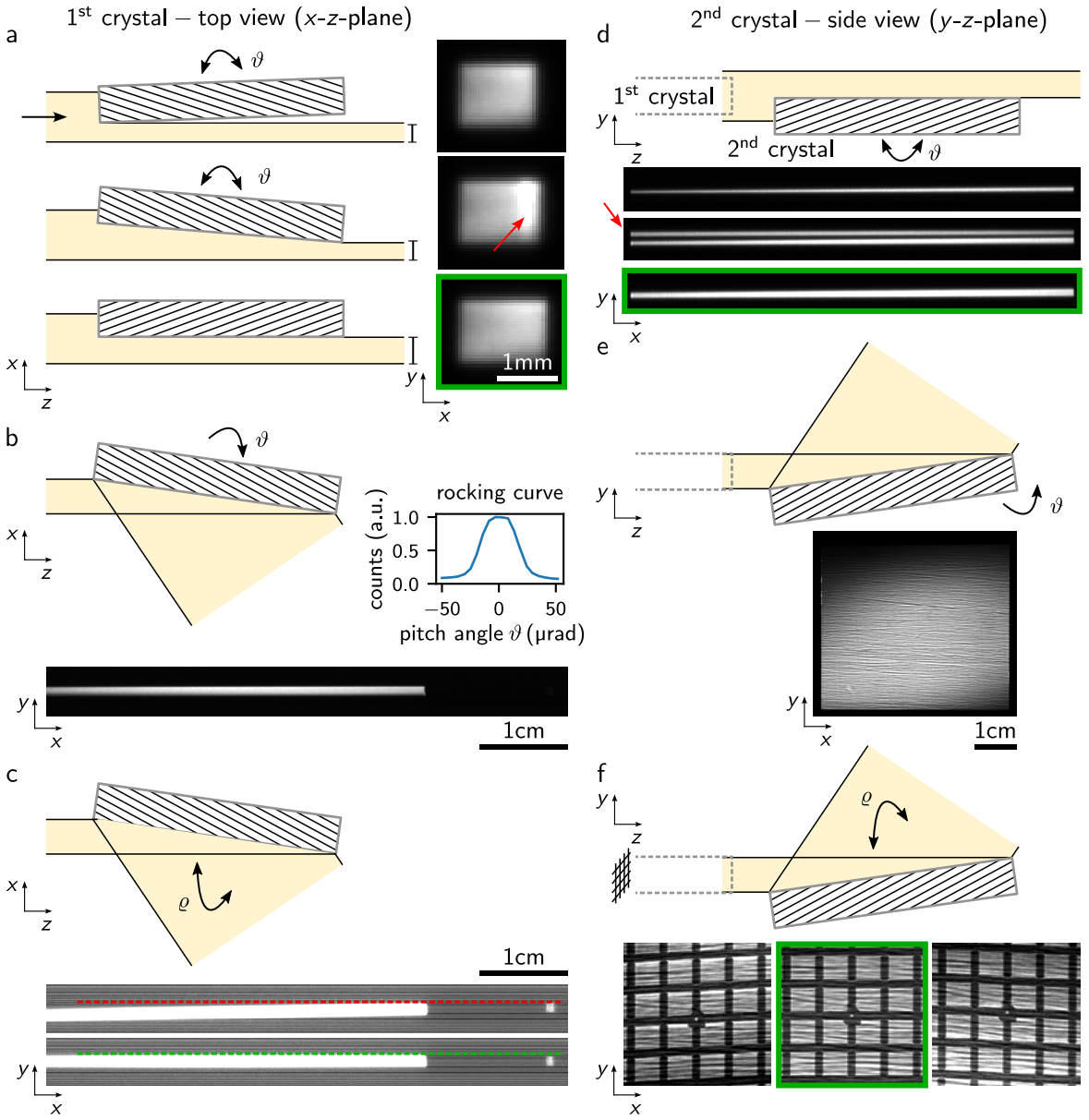

Figure 3.8.: Alignment procedure of the BM. Sketch of the alignment of **a-c** the first crystal and **d-f** the second crystal. **a** and **d** illustrate how to place the crystal into parallel position by minimizing its shadow on the camera. Afterwards, the crystal is moved laterally to cut half of the beam, so that the crystal center lies in the center of the beam. In panel **b** and **e**, the reflex is found by tilting the pitch angle ϑ to the expected Bragg angle and fine-tuning to the peak of the rocking curve. In **c** and **f**, the roll angle ϱ is aligned. In the rocking curve in panel b, the pitch angle ϑ is shown relative to the peak position.

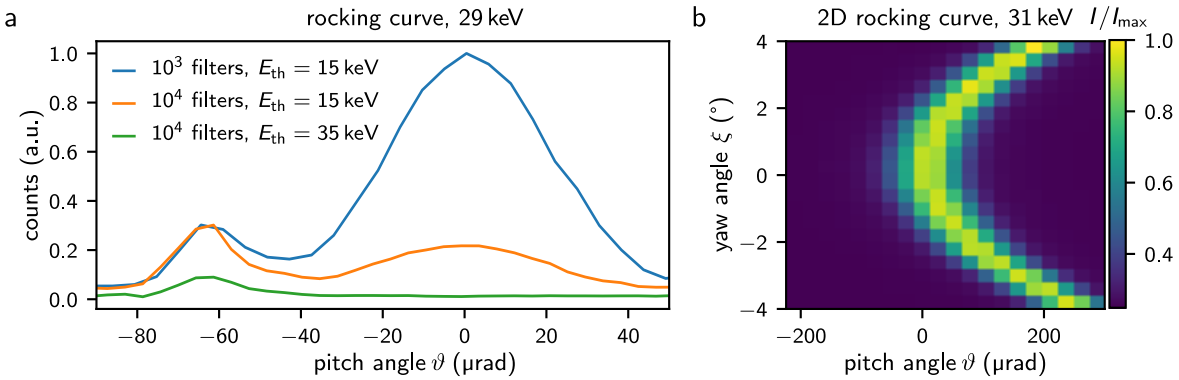

Figure 3.9.: Experimental rocking curves of the first crystal. a Rocking curve acquired with different filter strengths at P23, PETRA III. At 10^3 attenuation, the reflection peak of the main energy (29 keV) is well visible. The smaller peak on the left results from the reflection of higher harmonics. For a beam attenuation of 10^4, the intensity of the main peak decreases, while the peak from higher harmonics does not change, since higher energies are less affected by the filters. Setting the threshold energy E_{th} of the SPCD in use to 35 keV, the main peak disappears completely while the higher harmonics remain visible, which is consistent with the interpretation of the observed peaks. **b** 2D rocking curve over the pitch and yaw angles ϑ and ξ, acquired at 31 keV at the IMAGE beamline, KIT Light Source, Karlsruhe. The intensity is scaled to the maximum intensity I_{max}.

parallel position and centered to the beam (Fig. 3.8d). Again, the total reflex appears when the crystal is tilted too much towards the beam (middle image, red arrow). Second, after aligning the crystal to the parallel position, the reflex is found by moving the pitch angle ϑ to the Bragg condition and subsequent fine-tuning (Fig. 3.8e). Finally, the roll angle ϱ of the crystal is adjusted using a pattern with right angles, e.g., a grid (green frame in Fig. 3.8f). If ϱ is not well adjusted, the image will be sheared (left and right images).

For the alignment of the first crystal, it is worth noting that the higher harmonics are only weakly blocked by the filters added to protect the detector. The resulting rocking curve should therefore be interpreted with care: depending on the amount of filters, the diffracted higher harmonics might have a higher intensity than the primary energy, which can lead to a misinterpretation of the curve. An experimental example is shown in Fig. 3.9a. In the rocking curve acquired with a single photon counting detector and a filter attenuation factor of 10^3 (blue curve), two peaks are visible - the primary energy with highest intensity and a smaller peak from higher harmonics. The latter is shifted towards smaller angles due to asymmetric diffraction. As the amount of filters is increased, the main peak decreases and the higher harmonics become relatively more prominent (orange curve). The green curve shows the rocking scan when the threshold energy E_{th} of the SPCD is set above the primary energy. As expected, the main peak disappears completely. For correct alignment, the pitch angle has to be adjusted to the peak of the principal energy, thereby rejecting the higher harmonics. Due to this rejection, beamline mirrors are not required for suppressing higher harmonics, unless the intensity of the harmonics is so high compared to the primary energy that it would increase the dose deposited in the sample.

In principle, the yaw angle ξ can also be aligned for both crystals. A misalignment of the yaw angle results in a smaller effective asymmetry angle. For the alignment, a 2D scan is performed over the yaw and pitch angles, as shown in Fig. 3.9b. The yaw angle is aligned when the effective asymmetry angle is maximized. This is the case when the reflex appears at the smallest pitch angle. However, this alignment step can usually be skipped, since a minor misalignment in the yaw angle would cause only a negligible change in the effective asymmetry angle [143].

3.4.4. Characterization of the Bragg magnifier system

Magnification and field of view

The tunability of the magnification factor M is demonstrated by imaging a TEM gold grid with a mesh size of 127 µm at various X-ray photon energies. Flatfield-corrected radiographs are shown in Fig. 3.10b, and the extracted magnification factors are plotted in Fig. 3.10a. The asymmetry angles α_h and α_v of the horizontally and vertically diffracting Si crystals deviate from their nominal value of $\alpha = 5.920°$, resulting in a slightly stronger horizontal magnification. The values $\alpha_\mathrm{h} = 5.928°$ and $\alpha_\mathrm{v} = 5.916°$ have been determined experimentally in previous work [129], and the magnification factors calculated from these asymmetry angles

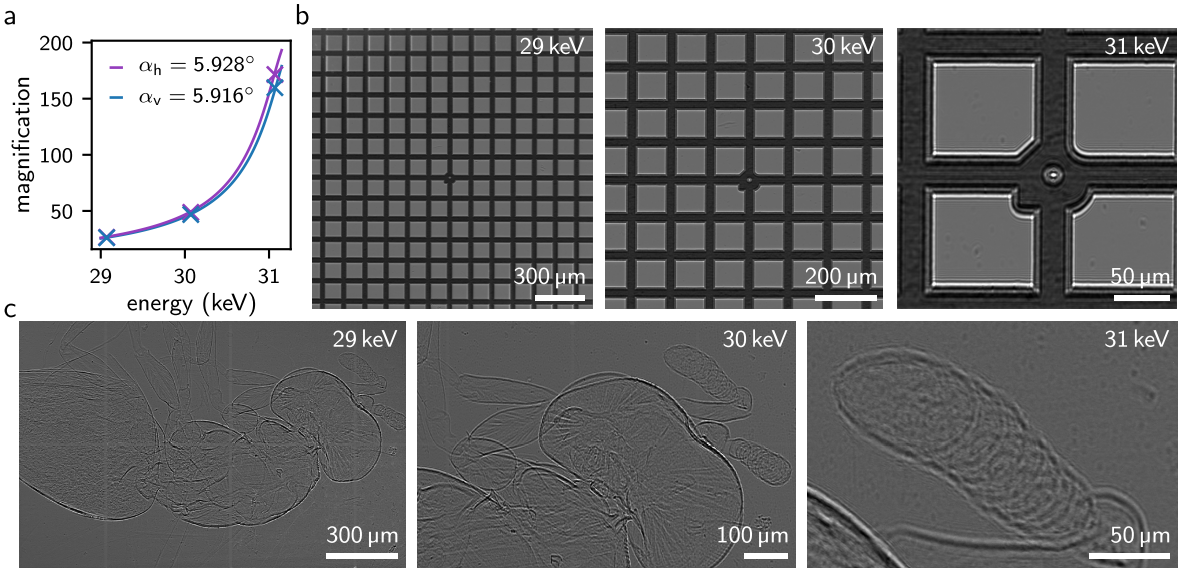

Figure 3.10.: Demonstration of variable magnification. **a** Horizontal and vertical magnification as expected from the experimentally measured asymmetry angles of the crystals given in Ref. [129] (solid lines) and extracted from the experimental images shown in panel b and marked by crosses. **b** Flatfield-corrected images of a TEM gold grid at various energies, acquired with the Shad-o-box. **c** Flatfield-corrected images of a chalcid wasp stored in ethanol, acquired at various energies. Note that the SPCD in use was close to saturation at 29 keV, leading to malfunctioning of the pixels in the bonding areas between the detector chips. At the higher energies, i.e., lower counts per pixel, this effect is no longer visible. Partly reproduced from Ref. [104].

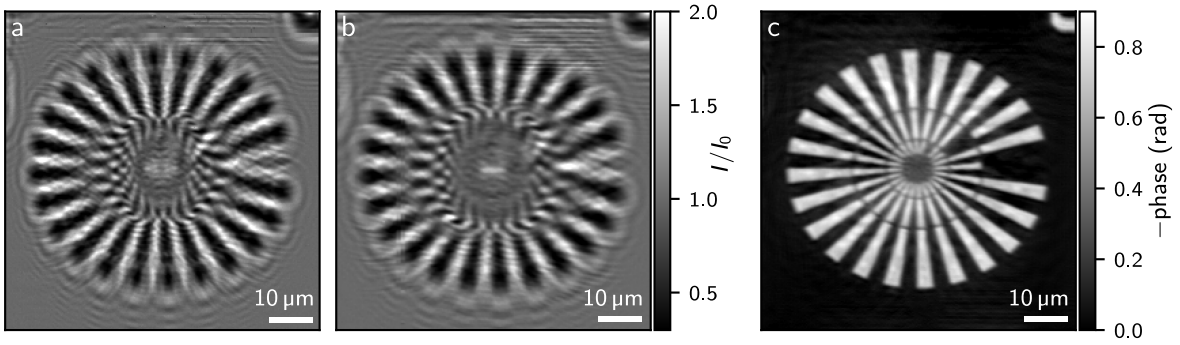

Figure 3.11.: Holograms and phase reconstruction of a Siemens star test pattern acquired with the BM system at 31 keV. Flatfield-corrected holograms at horizontal and vertical propagation distances of **a** $z_x = 0.15\,\mathrm{m}$, $z_y = 0.53\,\mathrm{m}$ and **b** $z_x = 0.41\,\mathrm{m}$, $z_y = 0.79\,\mathrm{m}$. **c** Multi-distance phase reconstruction using ten propagation distances. Smallest structure periods of 1 µm are discernible in the inner ring of the star. The reconstruction was performed with the NLTikh algorithm implemented in the *HoloTomoToolbox* [77].

agree well with the values obtained from the TEM images, see the blue and purple lines in Fig. 3.10a, computed from Eq. 3.1. The attainable input FOV was 1.6 mm x 1.6 mm at 29 keV and 0.3 mm x 0.3 mm at 31 keV, as expected from the length of the crystals, and the output FOV was 44.8 mm x 44.8 mm. To demonstrate the tunable magnification on a biological sample, Fig. 3.10c shows a chalcid wasp stored in ethanol and imaged at different magnification factors. Hot pixels in the detector were removed by interpolation.

Spatial resolution

For the crystals in use, the theoretical resolution limit as defined by Eq. 3.2 is 1.3 µm at 31 keV, cf. Fig. 3.1c. The resolution was investigated experimentally by imaging a test pattern (*model X500-200-16, Carl Zeiss Microscopy GmbH, 07745 Jena, Germany*). The test pattern contains gold structures with a nominal height of (1.6 ± 0.2) µm and structure periods down to 1 µm, i.e., 0.5 µm gold bridge followed by 0.5 µm empty space. Acquiring holograms at multiple propagation distances allows for a multi-distance phase reconstruction as described in Section 2.2.7. The *HoloTomoToolbox* [77] with the nonlinear Tikhonov algorithm [79] was employed for the reconstruction and ten distances were used ($z_x = 0.15\,\mathrm{m}$ to $0.41\,\mathrm{m}$ and $z_y = 0.53\,\mathrm{m}$ to $0.79\,\mathrm{m}$), taking into account the different horizontal and vertical propagation distances in the reconstruction (Chapter 3.3.6). Fig. 3.11 depicts flatfield-corrected holograms of a Siemens star structure at two exemplary distances as well as the phase reconstruction, where the smallest structures of 1 µm period in the inner ring are discernible in the vertical direction. In the horizontal direction, the resolution is partially degraded by source blur. In the reconstructed line patterns shown in Fig. 3.12, structure periods are resolved down to the theoretical limit as well, marked by a green line in the line profiles. In the latter, the background gradient has been subtracted for better visibility, which can be attributed to source blur and intrinsic partial suppression of high spatial frequencies by the detector MTF

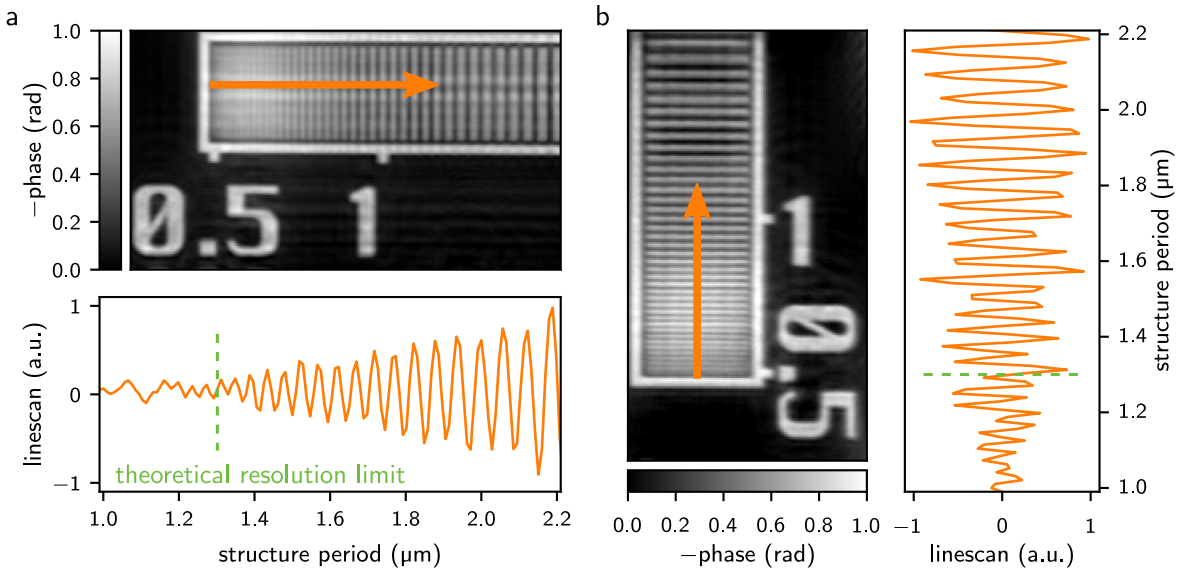

Figure 3.12.: Resolution line patterns. Multi-distance phase reconstruction of **a** horizontal and **b** vertical line patterns. Line profiles along the indicated direction are also shown. The background gradient has been subtracted for better visibility. The intrinsic resolution limit of 1.3 µm at 31 keV is indicated by a green line. Partly reproduced from Ref. [104].

(see Eq. 2.95). Also here, despite the larger vertical propagation distance, the resolution in vertical direction is slightly higher due to the asymmetric source properties at P23 [144]. The reconstruction parameters were $\beta/\delta = 10^{-1.33}$ (gold), and the regularization parameters were $\alpha_{\text{low-freq}} = 0$ and $\alpha_{\text{high-freq}} = 10^{-1}$ for low and high spatial frequencies, respectively.

Tomography

The suitability of BM imaging for tomography is demonstrated by acquiring a single-distance tomogram of a mouse nerve. The specimen is an EPON-embedded sciatic nerve stained with osmium tetroxide, borrowed from the Institut für Röntgenphysik, Georg-August-Universität Göttingen, Germany. Detailed information on the sample can be found in Ref. [145]. A 180° scan with 1000 projections and propagation distances of $z_x = 0.22\,\text{m}$ and $z_y = 0.60\,\text{m}$ was performed at 30.5 keV. Fig. 3.13a-c shows a projection image and its retrieved phase using the contrast transfer function (CTF) and transport of intensity equation (TIE) algorithms. In Fig. 3.13d-h, virtual slices through the reconstructed 3D volume are shown for different orientations as indicated by the colored lines. The good image quality and the small voxel size of 0.7 µm allows the distinction of axons and their myelin sheaths inside the nerve as well as fat and blood vessels on the outside of the nerve. To compare the three most common phase retrieval methods (CTF, nonlinear Tikhonov regularization (NLTikh) and TIE, see Section 2.2.7), the respective reconstructions are shown for the green orientation. In the zoom-in (Fig. 3.13i-k), CTF and NLTikh look identical, while TIE suppresses high spatial frequencies and thus induces a slight blurring due to the large propagation distance. Phase

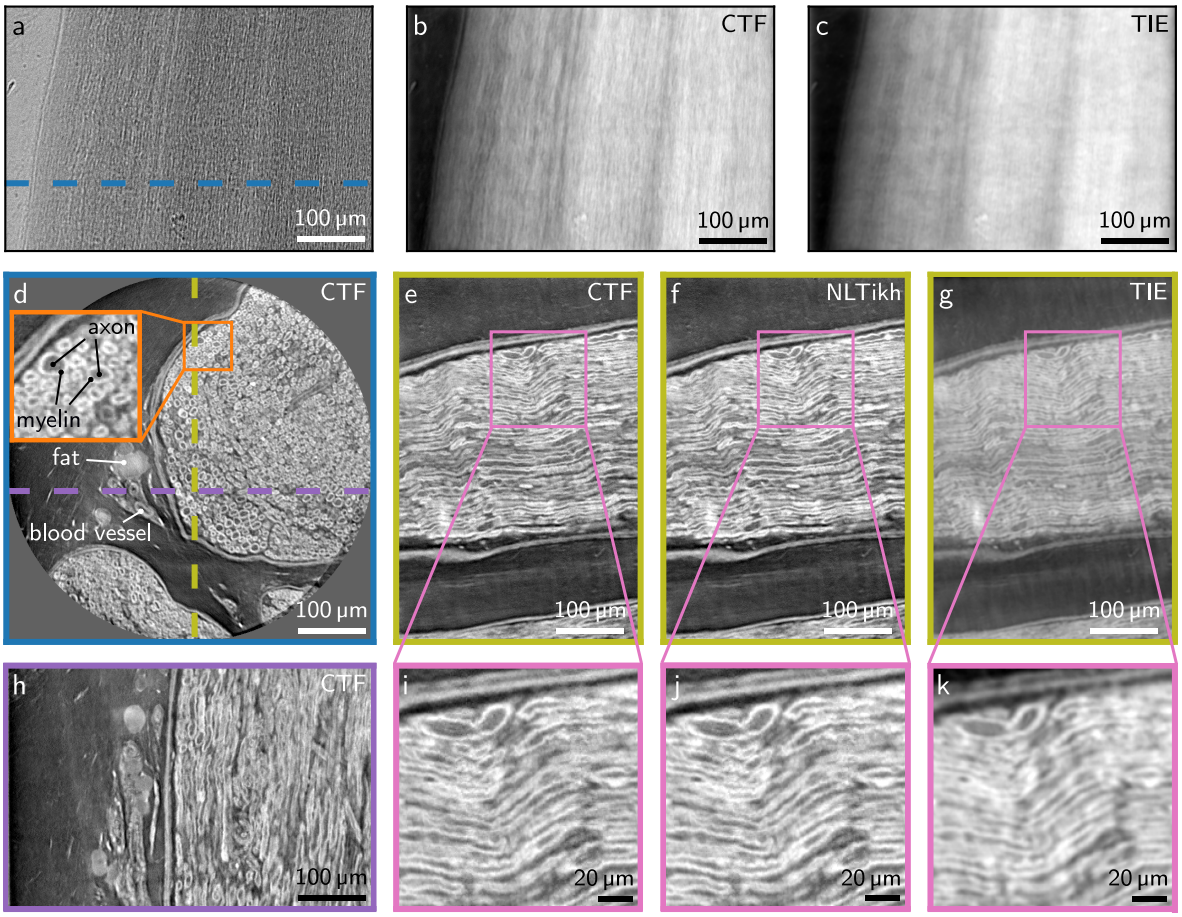

Figure 3.13.: Exemplary tomogram of a sciatic mouse nerve. a Flatfield-corrected projection image acquired with the BM at 30.5 keV. **b, c** Retrieved phase map obtained using the CTF algorithm and the TIE method. **d-h** Virtual slices through the reconstructed volume along the colored lines. For comparison, panels e-f show the same slice reconstructed using CTF, NLTikh, and TIE. **i-k** Zoom-in on the areas marked in panels e-g. Details about the specimen can be found in Ref. [145].

retrieval was performed with the *HoloTomoToolbox* [77] ($\beta/\delta = 10^{-1.34}$) and tomographic reconstruction with filtered back-projection with the *tofu* framework [141].

3.4.5. Comparison between experiment and simulation

Fig. 3.14 shows a comparison between experimental data and a simulation of the test pattern. The experimentally acquired hologram is shown in Fig. 3.14a. Vertical and horizontal line profiles of the experimental data and the simulations are depicted in Fig. 3.14b, c. The simulation was performed for perfect coherence (green curves) and including source blur (red curves) with the Gaussian distributions shown in Fig. 3.14d. The source blur was included via the general expressions Eq. 2.65 and Eq. 2.67, since the system is in general shift-variant. The image was recorded at 30.57 keV and propagation distances of $z_x = 0.21\,\mathrm{m}$ and $z_y = 0.59\,\mathrm{m}$. In the Fourier transform shown in the inset of Fig. 3.14a, the Thon rings exhibit an elliptical

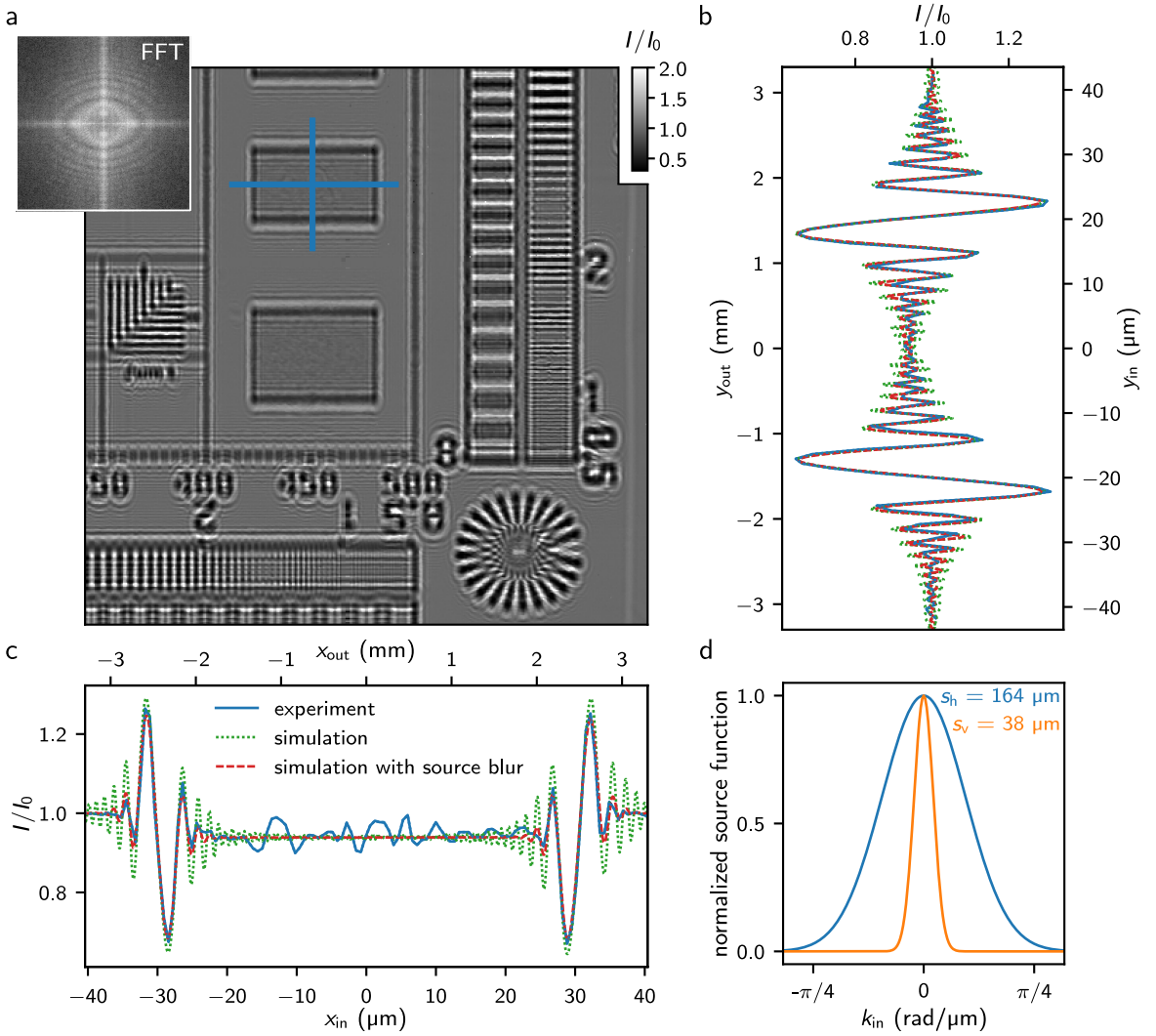

Figure 3.14.: Comparison between measurement and simulation. a Flatfield-corrected image of the gold test pattern acquired at 30.57 keV and inset showing the modulus of its Fourier transform. **b, c** Experimental (blue) and simulated (green, red) vertical and horizontal intensity profiles along the lines marked in panel a. **d** Gaussian source function used for the simulations with source blur (red curves in panels b and c). The fluctuations in the experimental line in panel c are surface irregularities of the test pattern.

shape due to the different horizontal and vertical propagation distances. The larger vertical propagation distance results in stronger phase contrast and broader Fresnel fringes in the vertical direction. The position of the fringes is in good agreement to the simulation. The strength of the experimental fringes, i.e., the image contrast, is partly reduced compared to the simulation with ideal coherence. This damping is well described by the simulation with source blur, assuming Gaussian functions with $s_\mathrm{h} = 164\,\mu\mathrm{m}$ and $s_\mathrm{v} = 38\,\mu\mathrm{m}$ for the horizontal and vertical source size, respectively. These determined values agree well with the values of $s_\mathrm{h} = 140\,\mu\mathrm{m}$ and $s_\mathrm{v} = 32\,\mu\mathrm{m}$ measured by the beamline scientists of P23. Note that the source size values are given by the standard deviation of the Gaussian source function here, while it

is often also common to state the full width at half maximum (FWHM) ($2.355s = \text{FWHM}$). For the simulation, a gold thickness of 1.2 µm had to be used to obtain congruence with the experimental data, indicating that the actual thickness of the test pattern deviates from the specified thickness. The manufacturer confirmed that the gold is diluted to 90 %, which explains the reduction in effective thickness. The good agreement between simulation and experiment illustrates the validity of the presented simulation method and at the same time confirms that the imaging performance of the BM system meets the expectations. Also, the results demonstrate that the Bragg magnifier can be used to estimate the X-ray source size.

3.5. Summary

In the first part of this section, the general working principle of a Bragg magnifier was introduced, and a formalism for describing the image formation in a Bragg magnifier including effects of shift-variance was given. The result is in agreement with previously published methods [134, 135], but here the image formation was derived similar to Ref. [112] by mapping each plane wave incident on the crystal surface onto its outgoing plane wave, taking into account the attenuation and phase shift induced by the crystal. This physical motivation allows to develop an intuitive understanding of the image formation process. In addition, an arbitrary number of crystals can be described by a single mapping function, which can be useful for image simulations or iterative phase reconstruction [135]. Furthermore, the formalism can also be applied to a reversed orientation of the crystals, i.e., in demagnifier mode.

Subsequently, the BM system developed in this work was introduced, the alignment procedure was described, and the system was experimentally characterized in terms of magnification and attainable resolution. The predicted magnification factors of 20- to 150-fold were shown, and the tunable magnification was further demonstrated on a biological sample. To prove the achievable resolution, multidistance phase contrast images of a test pattern were acquired at the highest magnification of 150-fold. In the reconstructed images, structures of 1.3 µm period could be discerned, which agreed to the expected resolution. Despite the longer vertical propagation distance, the observed resolution was better in this direction due to the smaller vertical source size. To demonstrate the applicability of Bragg magnifier imaging to tomography, a mouse nerve was imaged in 3D. The image quality was sufficient to distinguish axons and their surrounding myelin sheaths in all three perpendicular orientations. Finally, as an example, a test pattern was imaged experimentally and the image intensity was compared with simulations obtained with the mapping procedure. By including the effects of an extended X-ray source size in the simulations, the simulated data agreed well with the measurements, and the horizontal and vertical source sizes of the P23 source could be determined. The resulting source size values were in good agreement with those previously measured by the beamline scientists. The presented considerations form the basis for the next two chapters, in which the Bragg magnifier technology will be applied to achieve dose-efficient imaging.

4. Bragg magnifier for dose-efficient phase contrast imaging at micrometer resolution

High-resolution X-ray imaging enables visualizing the morphology of small organisms, addressing biological and biomedical questions in a wide range of fields [15, 146–151], e.g., developmental biology [147, 150] or functional morphology [146, 149]. In this context, also time-resolved *in vivo* X-ray imaging has gained increasing interest [20–23, 152–155]. However, the fact that biological samples tolerate only a limited radiation dose due to radiation damage is a major issue, especially for *in vivo* studies. With increasing resolution, the X-ray flux density has to be increased, which further exacerbates the dose issue.

The aim of this chapter is to increase the dose efficiency in X-ray imaging of millimeter-sized biological samples and other soft tissues at micrometer resolution. First, three main aspects are simultaneously optimized for this purpose: the generation of contrast, the overall X-ray detection efficiency, and the transfer of information from the virtual X-ray image to the detected digital image (Section 4.1). On the basis of these considerations, a highly dose-efficient imaging setup is realized by combining propagation-based phase contrast imaging (PB-PCI), a Bragg magnifier (BM) and a single photon counting detector (SPCD). In Section 4.2, an experimental investigation is given to compare the developed BM system with a conventional indirect detector system and to determine the gain in dose efficiency of the BM system. Finally, the high dose efficiency is exploited for a pilot *in vivo* study of parasitoid wasps emerging from their host eggs (Section 4.3). The main results of this chapter have been published in Ref. [104], while further essential details are given here.

4.1. Design considerations for dose efficiency

First, three aspects are considered that are decisive to achieve highest dose efficiency: (i) optimizing the generation of contrast, especially in view of the optimal X-ray photon energy that allows for highest information content on the sample per dose, (ii) achieving high X-ray detection efficiency for those energies, and (iii) ensuring a high optical transfer function of the detector system up to the resolution limit.

4.1.1. Relation between energy, dose and phase contrast - determining the optimal X-ray photon energy

By revealing phase changes of the X-rays penetrating through the specimen, propagation-based phase contrast imaging has turned out to be a highly effective method for generating high image contrast of soft tissues [5, 10] and is therefore the method of choice here. Both the contrast in PB-PCI and the dose deposited in the sample depend on the X-ray photon energy. As a first step, the X-ray photon energy E thus needs to be optimized such that the wavefield behind the sample achieves highest information content per dose. On the one hand, the deposited dose per incident X-ray photon decreases with increasing energy. On the other hand, the phase shift imposed on X-rays by a medium also decreases with increasing energy, leading to a reduction in image contrast in PB-PCI. In the following, these two points are considered in order to determine the ideal photon energy for dose-efficient imaging.

The dose D absorbed by a sample scales with the number of incident X-ray photons and their average deposited energy. It is defined as the total energy $E_{\mathrm{abs}}^{\mathrm{tot}}$ deposited per sample mass $m = \rho dA$, with ρ being the sample density, d the sample thickness, and A the area of the sample that is exposed to radiation, and reads

$$D = \frac{E_{\mathrm{abs}}^{\mathrm{tot}}}{m}. \tag{4.1}$$

Applying the Lambert-Beer law with the linear mass attenuation coefficient μ, the number of X-ray photons absorbed or scattered by the sample per unit area is given by [156]

$$n_{\mathrm{abs}} = n_0 - n_{\mathrm{tr}} = n_0 \cdot (1 - e^{-\mu d}). \tag{4.2}$$

Here, n_0 denotes the number of incident X-ray photons per unit area, known as photon fluence, and n_{tr} is the number of photons transmitted through the sample. In the energy range of interest (5 keV to 100 keV), the linear attenuation coefficient comprises photoelectric absorption as well as coherent Thomson and incoherent Compton scattering. For soft tissue, these contributions are shown in Fig. 4.1a together with the total linear mass attenuation coefficient (red curve). On average, only a fraction of the primary X-ray photon energy E is delivered to the sample, which is quantified by the energy absorption coefficient μ_{en} (green curve in Fig. 4.1a). The average absorbed energy per interacting photon is

$$E_{\mathrm{abs}} = \frac{\mu_{\mathrm{en}}}{\mu} \cdot E. \tag{4.3}$$

The dose deposited in the sample is therefore given by [156]

$$D = \frac{\mu_{\mathrm{en}}}{\mu}\frac{E}{\rho dA} \cdot n_{\mathrm{abs}} \cdot A = \frac{\mu_{\mathrm{en}}}{\mu}\frac{E}{\rho d} n_0 \cdot (1 - e^{-\mu d}). \tag{4.4}$$

For thin samples, it can be assumed that the probability of undergoing an interaction process

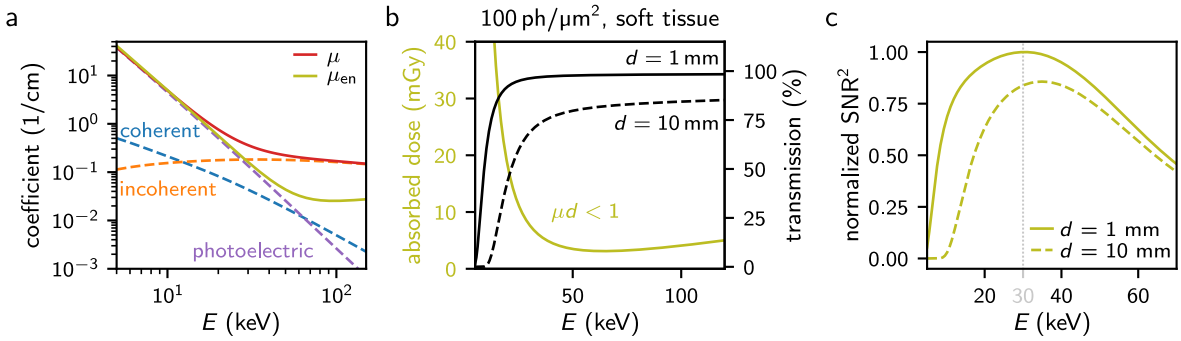

Figure 4.1.: Considerations for dose-efficient imaging. **a** Total linear attenuation coefficient μ of soft tissue as a function of energy E with its contributions (photoelectric absorption, coherent and incoherent scattering), and energy absorption coefficient μ_{en}. **b** Dose deposited in soft tissue as a function of E for the linear regime ($\mu d < 1$) and a fixed incident X-ray photon fluence of 100 ph/µm^2. **c** Achievable SNR^2 for a fixed dose in soft tissue and different sample thicknesses. These curves represent the theoretical limit of dose efficiency in PB-PCI and have been normalized to the maximum. Attenuation coefficients were taken from the NIST database [56]. Reproduced from Ref. [104].

is low, so that multiple scattering is negligible and the present considerations can be performed without the need for elaborate simulations. This assumption has been verified for $d = 1\,\mathrm{mm}$ by Monte Carlo simulations with the software tookit *Geant4* [157], where multiple scattering is taken into account (simulation performed by Marcus Zuber, IPS, KIT, Karlsruhe, Germany). For $\mu d < 1$, i.e., high energies or thin samples, Eq. 4.4 can be linearized, and the dose becomes independent of the sample thickness and the linear attenuation coefficient:

$$D = \frac{\mu_{\mathrm{en}}}{\rho} \cdot E \cdot n_0. \tag{4.5}$$

At low energies ($E < 20\,\mathrm{keV}$), photoelectric absorption is the dominant interaction process, while contributions from incoherent Compton scattering can be neglected (cf. Fig. 4.1a). Here, one finds $\mu_{\mathrm{en}} \approx \mu \propto E^{-x}$ with $x \approx 3$, and consequently, the dose decreases rapidly with $D \propto E^{-2}$ at low energies. At higher energies, Compton scattering becomes the dominant interaction process, and the curve for μ_{en} flattens out. This leads to a minimum in the deposited dose per incident photon fluence at 64 keV [156], see green curve in Fig. 4.1b. At this energy, one can in principle obtain the highest photon statistics for a given dose. However, as E increases, the phase shift imposed on X-rays as they pass through a medium decreases as well, and with it the image contrast in PB-PCI. The phase shift ϕ is proportional to $\delta \cdot E$ and therefore decreases with E^{-1}. Here, Eq. 2.39 is rewritten as

$$\delta = \frac{r_e \lambda_0^2 n_e}{2\pi} = \frac{r_e h^2 c^2 n_e^w}{2\pi} \underbrace{\frac{n_e}{n_e^w \rho}}_{\eta_s} \cdot \frac{\rho}{E^2} \propto \frac{\eta_s \rho}{E^2}, \tag{4.6}$$

where the electron density n_e^w of water is introduced as reference value and n_e is expressed via ρ and a material-dependent quantity η_s, which is approximately constant [158]. A measure

of image quality and dose efficiency is the signal-to-noise ratio (SNR), defined as the ratio of the phase-induced signal S and the noise N of the unscattered background field (zero-order beam). For PB-PCI and weak phase objects, the signal is proportional to the phase, as derived in Section 2.2.6, and hence $S \propto \phi \propto \eta_s \rho E^{-1}$. In total, one obtains the dependency

$$\mathrm{SNR} \propto \frac{n_{\mathrm{tr}} A_{\mathrm{px}} \cdot \phi}{\sqrt{n_{\mathrm{tr}} A_{\mathrm{px}}}} \propto \sqrt{n_{\mathrm{tr}} A_{\mathrm{px}}} \cdot \eta_s \rho E^{-1} = \eta_s \rho^{3/2} \sqrt{\frac{\mu}{\mu_{\mathrm{en}}} \frac{D d A_{\mathrm{px}}}{E^3} \frac{1}{e^{\mu d} - 1}} \tag{4.7}$$

with A_{px} being the pixel size of the detector. For a constant dose and different sample thicknesses, the energy-dependence of the attainable SNR^2 behind a soft tissue sample is shown in Fig. 4.1c. The SNR^2 is proportional to the dose because it scales with the number of X-ray photons. Since the signal in the SNR is sample-dependent, the curves have been normalized to the theoretical maximum. For $d \leq 1\,\mathrm{mm}$, the highest theoretically achievable SNR per dose is obtained at 30 keV, which is per se the optimal working energy. For thicker samples (dashed curve), the X-ray transmission decreases, especially at low energies (see also the black curves in Fig. 4.1b), thereby shifting the optimal working energy to slightly higher values.

As a side note, to get a better intuition for the energy regime where photoelectric absorption is dominant ($\mu_{\mathrm{en}} \approx \mu \propto E^{-3}$), Eq. 4.7 can be rewritten as

$$\mathrm{SNR} \propto \eta_s \rho^{3/2} \sqrt{\frac{D A_{\mathrm{px}}}{1 + \frac{\mu d}{2} + \frac{(\mu d)^2}{6} + \ldots}}. \tag{4.8}$$

Here, one sees the relevant dependencies. With increasing energy, i.e., decreasing μ, the SNR for a given dose increases at first and eventually becomes constant when the X-ray energy is high enough ($\mu d < 1$) so that most of the incident photons pass through the sample. For even higher energies where Compton scattering comes into play, the SNR decreases, leading to a maximum in the SNR curve at about 30 keV.

4.1.2. X-ray detection efficiency

Secondly, after selecting the optimal working energy, achieving high dose efficiency also requires the detection of ideally every X-ray photon that passes through the sample. However, this is technically challenging. For micrometer resolution X-ray imaging, the image has to be magnified before being recorded by a pixel-array camera. In commonly-used scintillator-based indirect detector systems, the X-ray wavefield is transformed into a visible light image by a scintillator, which is then magnified by light optics and detected by a sCMOS or CCD sensor (Fig. 4.2a). As described in Section 2.3.1, the applicable scintillator thickness is limited by the objective's depth of field, which is constrained by the desired spatial resolution [92]. The absorption of the scintillator is an upper bound on the indirect system's X-ray detection efficiency, i.e., the probability of detecting an X-ray photon. The limited thickness of the scin-

tillator results in a reduced X-ray detection efficiency, which exacerbates as the photon energy and resolution increase. An example of the expected absorption of LSO:Tb scintillators with three different thicknesses is shown in Fig. 4.3a. LSO is one of the most suited thin-film scintillators for high-resolution X-ray imaging [92, 159, 160]. At the targeted working energy of 30 keV, the X-ray detection efficiency is, e.g., only 12.5 % for 12 µm LSO. Multiplication with the theoretically achievable SNR^2 (Fig. 4.1c) yields the SNR^2 that can be maximally achieved by an indirect detector system with the respective scintillators, omitting any further possible losses due to electronic conversion and readout. The result is shown in Fig. 4.3c. For dose-relevant imaging, the indirect detector system would therefore be operated at a lower energy, for example at 11 keV for a millimeter-thick sample and the 12 µm LSO scintillator. With increasing sample thickness, e.g., in local tomography, the transmission of the sample decreases and one is thus forced to increase the operating energy, which in turn reduces the detection efficiency (dashed lines in Fig. 4.3c).

While indirect detector systems convert the X-ray image into a visible light image and magnify the latter by light optics, direct magnification of the X-ray image offers the advantage of exploiting the high detection efficiency of large-pixel array detectors (Fig. 4.2b). For the targeted X-ray energy of 30 keV, an X-ray detection efficiency of nearly 100 % can be achieved by direct-converting SPCDs with a reasonably thick high-Z sensor, e.g., GaAs or CdTe, see Section 2.3.2. Currently available readout chips have typical pixel sizes of 50 µm to 100 µm [101, 161]. To achieve micrometer resolution, the X-ray image can be magnified with a BM [24, 111–113, 119, 136, 162] as described in the previous chapter. In this way, the X-ray detection efficiency is inherently limited only by the reflectivity of the crystals. For energies > 20 keV the (220) reflection of a silicon (Si) crystal has a reflectivity of over 90 %. Taking into account that a 2D BM consists of at least two reflections, the reflectivity of two crystals is plotted in Fig. 4.3b (blue curve). Here, the asymmetry angle was chosen for each energy to yield a resolution of 1.6 µm, see Eq. 3.2 and Fig. 4.3b (black curve). Fig. 4.3c depicts the resulting SNR^2-curves (blue), which run just below the theory curve (green). At the targeted energy of 30 keV, the BM has a total reflectivity of 94 %, and the combination of BM and SPCD

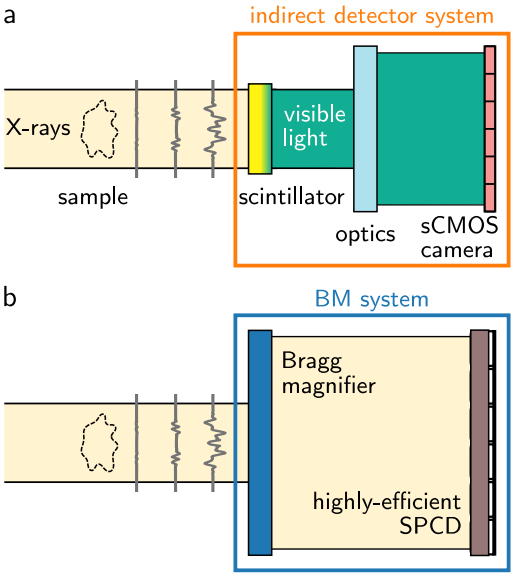

Figure 4.2.: Schematic of indirect detector system and BM system. a In an indirect system, the X-rays are transformed into a visible light image, which is then magnified and detected by a camera. **b** In the BM system, the X-ray wavefield is directly magnified by a BM and detected by a highly-efficient SPCD.

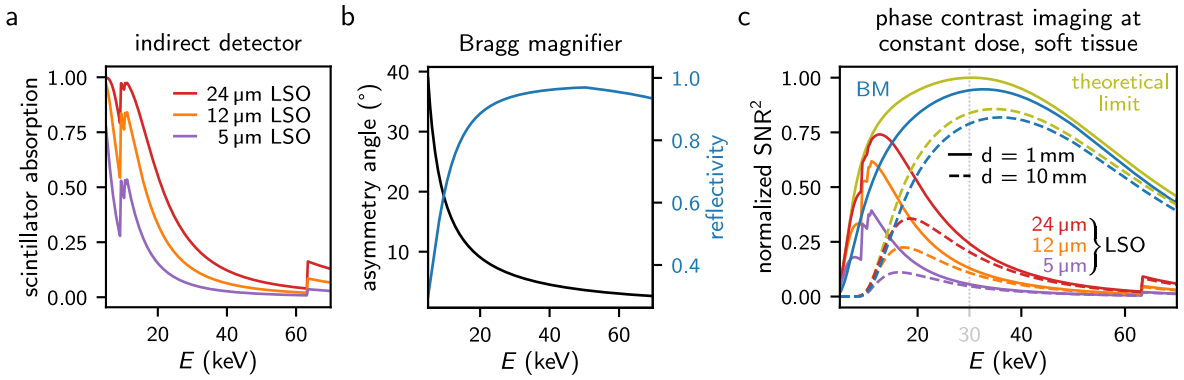

Figure 4.3.: X-ray detection efficiency of the indirect and the BM system. **a** Energy-dependent absorption of an LSO:Tb scintillator with different thicknesses. **b** Asymmetry angle required to obtain a resolution of 1.6 µm with the Si (220) reflection at the given energy, and resulting reflectivity of a BM composed of two Si crystals. **c** Normalized SNR^2 for a fixed dose in soft tissue and different sample thicknesses d. The green curves indicate the theoretical limit given by Poisson statistics, see Fig. 4.1c. The red, orange and purple curves show the SNR^2 achievable by an indirect detector with different LSO scintillator thicknesses, and the blue curves show the SNR^2 for a Si (220) BM system, omitting further possible losses in the specific pixel-array detectors used [94, 97, 163]. The asymmetry angle of the BM crystals was chosen for each energy according to panel b to yield 1.6 µm resolution. Attenuation coefficients were taken from the NIST database [56]. Partly reproduced from Ref. [104].

thus enables a factor of 7.5 higher X-ray detection efficiency than the indirect detector system with a 12 µm thick LSO scintillator. In addition, the BM system operates close to the highest achievable SNR per dose.

For the presented experiments, the BM asymmetry angle was chosen to be $\alpha = 5.92°$, optimized for a working energy of 29 keV to 31 keV and yielding a maximum Darwin width at 31 keV, see Fig. 4.4a, which corresponds to a nominal resolution limit of 1.3 µm. The Darwin curves of the Si (220) reflection are depicted in Fig. 4.4b for different energies. For comparison, the symmetric curve is also shown to highlight the increase in Darwin width due to asymmetric diffraction. Alternatively, the BM system developed in this work can be operated with Ge crystals with $\alpha = 5.66°$, which have twice the Darwin width and thus a factor of two higher resolution, i.e., 0.6 µm, at the expense of a slightly lower reflectivity, see Fig. 4.4c. At 30.5 keV, which was used in the experiments here, the Si crystals provide a resolution of 1.6 µm. To attain a similar nominal resolution with the indirect system, a numerical aperture (NA) of 0.28 and a 12 µm thick LSO scintillator were chosen.

4.1.3. Optical transfer function and detective quantum efficiency

Lastly, for the imaging performance of an optical system it is even more crucial how the spatial frequencies of the object are transferred into the digital image. After maximizing the information content carried by the X-ray wavefield as well as the X-ray detection efficiency, the phase shift imprinted by the sample must be converted into a measurable contrast. The image

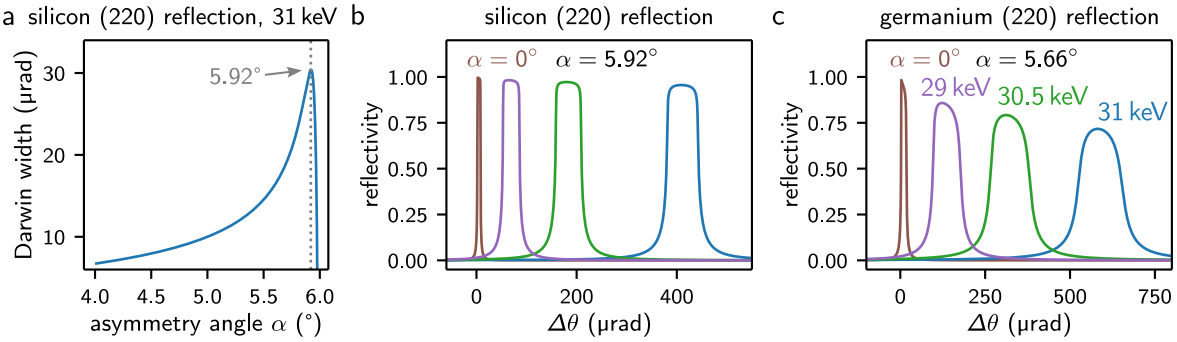

Figure 4.4.: Properties of the BM system. **a** Darwin width of the Si (220) reflection at 31 keV in dependency of the asymmetry angle α, taking into account dynamical diffraction with a strongly asymmetric diffraction geometry [34]. Here, an asymmetry angle of $\alpha = 5.92°$ was chosen in order to reach highest possible resolution at 31 keV. **b** Simulated reflectivity curves [34] of the Si (220) reflection for the symmetric case (brown) and for an asymmetry angle of 5.92° at several energies (for colors, see panel c). The Darwin width and thus the resolution limit vary with energy, as does the reflectivity of the crystal. **c** Simulated reflectivity curves of the Ge (220) reflection. Compared to Si, the Darwin width is larger, but the crystal reflectivity is reduced. Partly reproduced from Ref. [104].

formation is best described in Fourier space by a cascade of transfer functions that indicate how strongly the spatial frequency components q in the wavefield are transferred through the imaging system. For weak phase objects, the total transfer function is comprised of the contrast transfer function (CTF) for PB-PCI (see Section 2.2.6), the optical transfer function (OTF) of the magnifying optics (see Section 2.3.1), and the transfer functions of the pixel-array detector. The latter are strongly dependent on the particular device and are discussed in the literature [94, 97, 163]. The CTF and thus the contrast in the measurable holograms is maximized by choosing the largest reasonable propagation distance z of the X-ray wavefield behind the sample, which is typically limited by source blur due to the extended X-ray source size (see Eq. 2.69). Besides the propagation contrast formation, which both systems have in common, each detector system has its own additional OTF(q), which quantifies how strongly the signal is diminished by the respective magnifying optics and the detectors [71]. The coherent OTF of the BM system, relevant for PB-PCI of weak phase objects, is given by the square root of the reflectivity curves of the crystals [34, 164]. The OTF of the indirect system is determined by the transfer function of the scintillator and the OTF of the microscope. The former accounts for the spread of energy deposition generated by secondary particles [160], the latter is defined by the numerical aperture and is analytically accessible, see Eq. 2.93.

In Fig. 4.5, the normalized OTF of the BM and the microscope used in this work is shown for 30.5 keV. The ideal OTF of the microscope is only an upper bound. Additional losses in the indirect system due to the scintillator transfer function are not considered here, but can be accessed via Monte Carlo simulations [160] (see also Appendix A.5). The OTF of the indirect system suppresses image information, especially at high q, which contain the high-resolution components of the image. In contrast, the normalized modulus of the BM's OTF is close to unity up to the resolution limit, ensuring almost ideal transfer of information. Combined

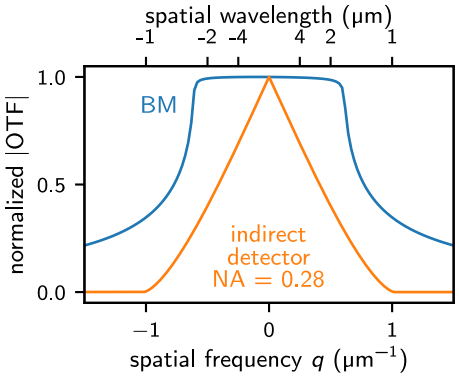

Figure 4.5.: Optical transfer function. Normalized coherent |OTF| of the magnifying optics of the Si (220) BM system and normalized incoherent OTF of the indirect system. The OTF of the BM system is shown for 30.5 keV, corresponding to a resolution of 1.6 µm. The OTF of the indirect system is depicted for an NA of 0.28. Partly reproduced from Ref. [104].

with its high X-ray detection efficiency, the BM system thus allows operation close to the highest achievable dose efficiency for PB-PCI.

To compare the image quality of the two imaging systems experimentally, it is useful to consider the q-dependent $\mathrm{SNR}^2(q, D)$, which is also referred to as noise-equivalent quanta [165]. Since it is proportional to the dose D, the dose efficiency can be defined as $\mathrm{SNR}^2(q, D)/D$. For a sample-independent comparison of the two imaging systems, the detective quantum efficiency (DQE)

$$\mathrm{DQE}(q) = \mathrm{SNR}^2(q)/\mathrm{SNR}_0^2(q) \tag{4.9}$$

is used here as a figure of merit for the dose efficiency [165]. Ensuring the same input $\mathrm{SNR}_0^2(q)$, the gain in DQE is given by

$$G(q) = \frac{\mathrm{DQE}_{\mathrm{BM}}(q)}{\mathrm{DQE}_{\mathrm{ind}}(q)} = \frac{\mathrm{SNR}_{\mathrm{BM}}^2(q)}{\mathrm{SNR}_{\mathrm{ind}}^2(q)}. \tag{4.10}$$

At $q = 0$, it is expected to be at least the X-ray detection efficiency ratio, as discussed in Section 4.1.2, while it increases even further with q due to the higher OTF of the BM system. In summary, the BM system is expected to significantly improve the q-dependent dose efficiency and thus the image quality compared to an indirect system.

It should be noted that the BM also acts as an energy discriminator and filters out inelastic scattering from the object, further improving its image quality compared to an indirect system, where inelastic scattering contributes to the background noise [24]. Furthermore, since the SPCD's modulation transfer function (MTF) is close to the ideal MTF (Eq. 2.95) [94, 97], one can generally expect aliasing at high spatial frequencies. Fortunately, the OTF of the BM suppresses this effect.

4.2. Experimental comparison of dose efficiency between the BM and a conventional indirect detector system

To prove the benefit of the BM system in terms of dose efficiency, an experimental comparison with the indirect system is performed. In the evaluation, particular attention is paid to the transfer of high spatial frequencies, which are decisive for high resolution. First, the high reflectivity of the BM crystals is confirmed experimentally. Combined with the nominal absorption of the scintillator, this allows for stating the expected gain in X-ray detection efficiency. In a second step, the imaging performance of the BM system is compared experimentally with that of the indirect system. The data are evaluated visually and quantitatively, the latter by extracting the SNR over spatial frequency q and thus determining the q-dependent gain in dose efficiency.

4.2.1. Reflectivity measurement of the BM crystals

The X-ray reflectivity of the BM is determined by using the photon-counting capability of the SPCD. Since the direct beam is too intense for the SPCD, filters are used to attenuate the beam by a factor of ~ 2000. However, higher harmonics generated by the X-ray source are hardly blocked by the filters, making it impractical to operate the SPCD in the direct beam. Instead of measuring the reflectivity of both crystals simultaneously, the reflectivity of only the second crystal is determined. Assuming that both crystals behave in the same way, the measured value can be squared to obtain the reflectivity of two successive crystals. First, the slits are closed so that the illuminated area behind the second crystal is $< 1\,\text{cm}$ x $1\,\text{cm}$ to ensure that all the diffracted photons can be collected by a single chip of the SPCD. In this way, the areas between two adjacent chips can be avoided, reducing the probability of including dead pixels. Next, the X-ray flux between the first and the second crystal is measured by acquiring 100 images with the SPCD. The amount of filters is chosen so that the flux remains below 20 000 counts/s/pixel, ensuring that the detector operates in the linear region [103]. Finally, the SPCD is placed in the reflex of the second crystal, and a comparison of the measured total counts yields the crystal reflectivity. The measurement is repeated for five different lateral positions of the SPCD in order to reduce the potential error from dead pixels. The SPCD is operated in charge-sharing mode (CSM) with lower and upper energy thresholds of 6 keV and 20 keV, respectively. The reflectivity of a single crystal is measured to be $(96.5 \pm 0.6)\,\%$ at 30.5 keV, which is in good agreement with the theoretical value of 97.4 %. The absorption of the 500 µm thick GaAs sensor of the SPCD is expected to be 97.6 % [56, 98]. The BM system consisting of two Si crystals and the SPCD therefore has an overall X-ray detection efficiency of 91 %.

4.2.2. The indirect detector system

The indirect detector system consists of a 12 µm thick LSO:Tb scintillator [166], a diffraction-limited optical microscope (*Optique Peter, 69210 Lentilly, France*, 10x objective lens with NA = 0.28, *model 378-803-3, Mitutoyo Deutschland GmbH, 41469 Neuss, Germany*, and 180 mm tubus lens giving 9x total magnification [90]), and a pco.edge 5.5 CMOS camera (*PCO AG, 93309 Kelheim, Germany*) with a physical pixel size of 6.5 µm x 6.5 µm, yielding an effective pixel size of 0.72 µm. The objective has a collection efficiency of the scintillation light of $0.5 \cdot (1 - \sqrt{1 - \mathrm{NA}^2/n^2}) = 0.6\,\%$ (Eq. 2.92), where $n = 1.82$ is the refractive index of the scintillator. With the light yield of the scintillator being 40 photons/keV [166], an average of 7.3 visible photons are expected to be collected by the objective per 30.5 keV X-ray photon absorbed by the scintillator. Taking into account the quantum efficiency of the camera ($> 60\,\%$), the Poisson distribution of the optical photons will therefore lead to only a small increase of the noise floor. Thus, the X-ray detection efficiency depends primarily on the X-ray absorption of the scintillator (12.3 % at 30.5 keV). In contrast to the SPCD, which is essentially free of readout noise, the CMOS camera adds a minor readout noise of 3 counts (root-mean-square) per pixel. This corresponds to $\sim$4 X-ray photons incident on the indirect system, meaning that for more than $\sim$16 incident X-ray photons per pixel, the photon shot noise is the dominant noise source.

Overall, given the measured reflectivity, the X-ray detection efficiency of the BM system is expected to be more than a factor of 7.4 higher than that of the indirect system at 30.5 keV.

4.2.3. Qualitative comparison of imaging performance

In order to assess the improvement in imaging performance, the BM system and the indirect system are installed one behind the other in the experimental hutch to allow for quick switching between the two setups. In this way, the two systems can be directly compared by imaging a test pattern with both systems at the same experimental parameters, i.e., the same incident X-ray beam with a photon energy of 30.5 keV, an exposure time of 67 ms, and horizontal propagation distances of $z = z_x = 0.15$–0.41 m. For the BM system, the vertical propagation distance is $z_y = 0.53$–0.79 m. Images were acquired at ten distances. Additionally, an acquisition was conducted at $z = 0.59$ m for the indirect system. The energy was set to 30.5 keV so that the effective pixel sizes of the BM system (0.72 µm horizontally and 0.66 µm vertically) are similar to the pixel size of the indirect system. Information on the test pattern can be found in Section 3.4.4.

Fist, images were taken at the same X-ray fluence of $\sim 6000\,\mathrm{ph/µm^2}$ per frame with both systems. The X-ray fluence was determined with the SPCD. Second, the fluence was increased by a factor $\sim$7 for the indirect system by removing absorption filters to compensate for the low X-ray absorption of the scintillator and to achieve the same nominal X-ray detection efficiency as in the BM system.

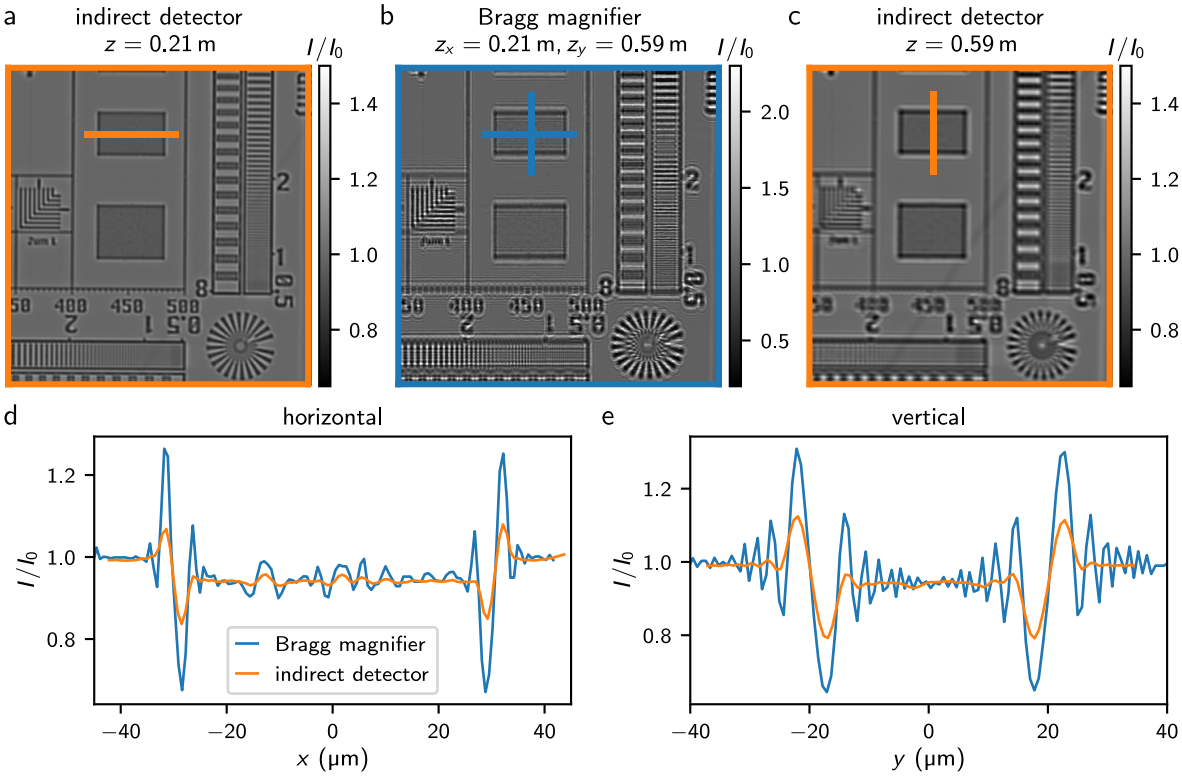

Figure 4.6.: Image contrast in the BM system and the indirect system. Flatfield-corrected holograms acquired with **a, c** the indirect system at an X-ray fluence of $\sim 44\,000$ ph/µm^2 and **b** the BM system at an X-ray fluence of ~ 6000 ph/µm^2 while keeping the other imaging parameters constant, i.e., 30.5 keV energy and 15 Hz image repetition rate. The propagation distances of the indirect system were adapted to **a** the horizontal distance $z_x = 21$ cm and **c** the vertical distance $z_y = 59$ cm of the BM system. Note the smaller color range in panels a and c compared to panel b. **d, e** Horizontal and vertical intensity profiles along the lines marked in panels a-c.

Fig. 4.6 depicts holograms of the test pattern acquired at the same nominal X-ray detection efficiency, averaged over 50 sample and flatfield images to obtain a low noise level. For the indirect system, the propagation distances were chosen to correspond to the horizontal (Fig. 4.6a) and vertical (Fig. 4.6c) distances in the BM image (Fig. 4.6b). In this way, horizontal and vertical intensity profiles can be directly compared (Fig. 4.6d, e). In both directions, the BM system provides significantly higher image contrast, which can be seen from the strength of the interference fringes.

Fig. 4.7 shows simulated and experimental images as well as multi-distance phase reconstructions of a Siemens star in the test pattern. The reconstructions and the simulated images will be discussed below. The second column of Fig. 4.7 shows experimental holograms of the Siemens star for the same X-ray fluence or the same nominal X-ray detection efficiency, respectively. Here as well, the contrast and visibility of fine interference patterns in the hologram of the BM image is by far superior, even at increased flux in the indirect system. The increased image contrast in the BM images can be attributed to the BM's higher OTF, especially at high spatial frequencies.

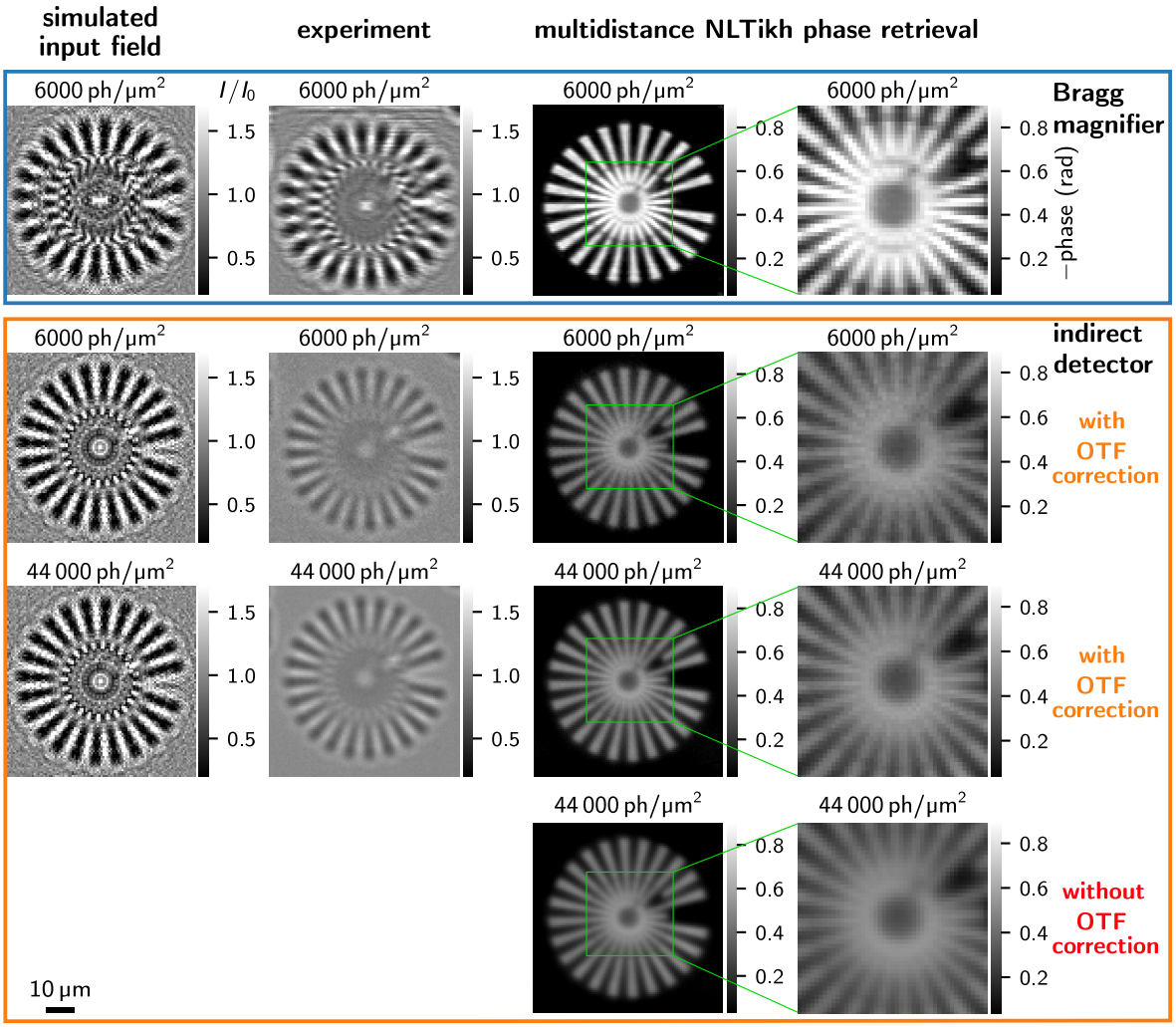

Figure 4.7.: Visual comparison of the BM system and the indirect system. Simulations, flatfield-corrected experimental holograms, and multi-distance NLTikh phase reconstructions of a Siemens star test pattern are shown for the BM and the indirect system. The X-ray fluence is given in the headings. Reproduced from Ref. [104].

The higher information content also translates to the multi-distance phase reconstructed images, see third and fourth columns of Fig. 4.7. Prior to phase reconstruction, the indirect system images were corrected by the incoherent OTF of the microscope [49] given by Eq. 2.93. The OTF of the scintillator can be estimated by Monte Carlo simulations [160] (see also Fig. A.4), but has not been included here, which explains the deviation of the reconstructed values for the indirect system from the expected phase shift of −0.8 rad. These findings emphasize the importance of correcting the indirect system data for the total transfer function of the optical system if a quantitative reconstruction is to be achieved. On the downside, noise is amplified by this correction as well. For comparison, the last row in Fig. 4.7 shows the reconstruction without OTF correction. As a side note, the test pattern unfortunately moved slightly out of the field of view (FOV) of the BM at four propagation distances. Therefore,

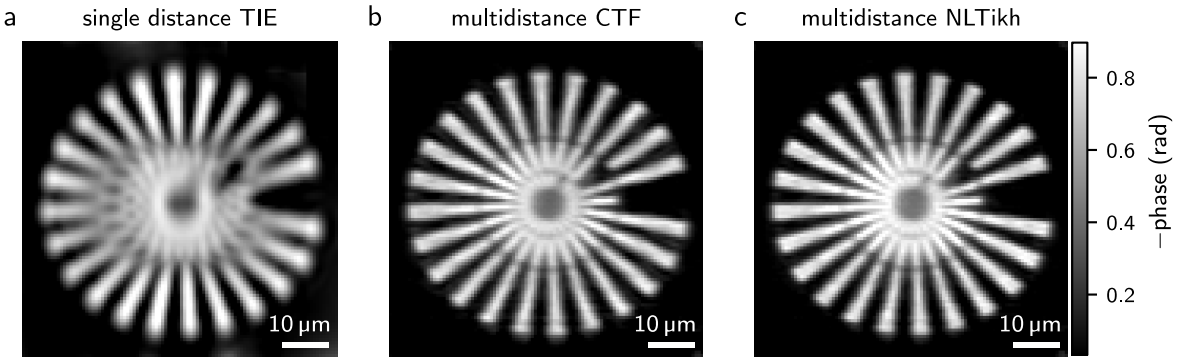

Figure 4.8.: Comparison of phase reconstruction algorithms for the BM data. a With the TIE algorithm, resolution is lost due to suppression of high spatial frequencies. The quality of **b** the CTF and **c** the NLTikh reconstruction is comparable, with NLTikh being slightly sharper and more homogeneous.

the missing pixel rows were completed by duplicating the corresponding pixel rows from the opposite side of the image (4 % of the total dataset). For the phase reconstruction, raw images acquired with the BM system were flatfield-corrected, and raw images from the indirect system were flat- and darkfield-corrected. In all images, hot pixels were removed by interpolation. Multi-distance phase reconstruction was performed with the *HoloTomoToolbox* [77] using the nonlinear Tikhonov regularization (NLTikh) algorithm [79] and taking into account the different horizontal and vertical propagation distances [135]. A comparison with the CTF and single-distance transport of intensity equation (TIE) phase reconstructions is given in Fig. 4.8. While TIE induces strong blurring due to suppression of high spatial frequencies, CTF and NLTikh yield almost identical results, with NLTikh being slightly sharper and more homogeneous.

4.2.4. Gain in detective quantum efficiency

For a further quantitative analysis, the q-dependent SNR of the Siemens star holograms is compared for the same incident X-ray intensity. In the following, the evaluation procedure is described and the results are presented and discussed.

Procedure for evaluating the SNR

The aim is to evaluate the gain $G(q)$ in DQE of the BM compared to the indirect system over spatial frequency q. According to Eq. 4.10, $G(q)$ is determined by evaluating $\mathrm{SNR}^2(q)$ of both systems at the same dose and energy. The procedure is illustrated in Fig. 4.9. At each of the ten propagation distances mentioned in the previous section, 50 sample images of a Siemens star test pattern as well as 50 flatfield images are recorded in quick succession.

For a precise determination of the noise (first row in Fig. 4.9), two subsequent flatfield images

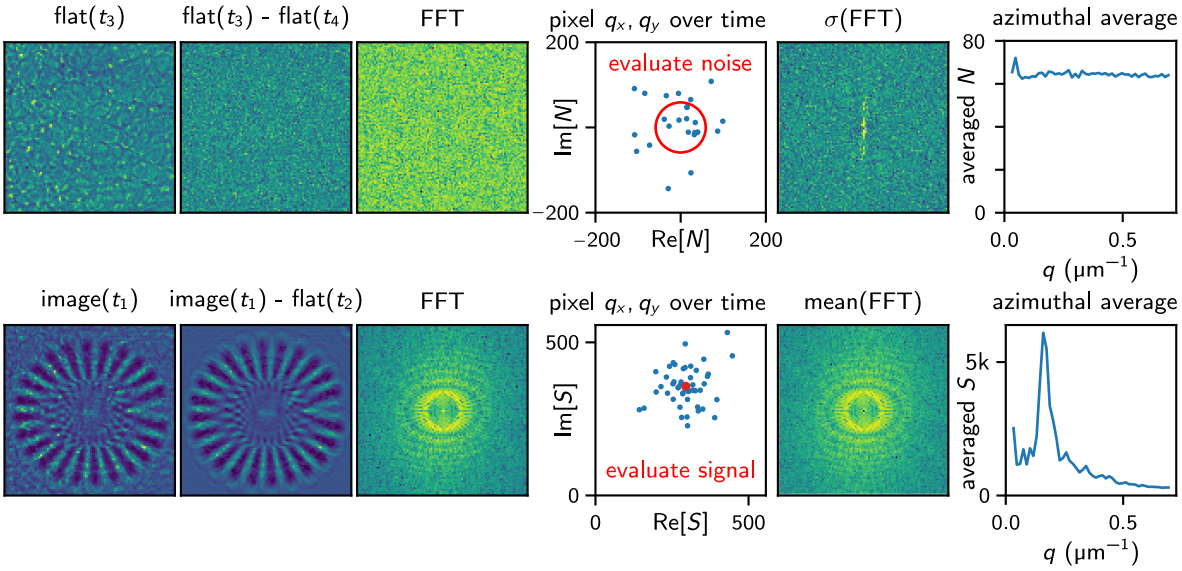

Figure 4.9.: Procedure for evaluating the signal and noise in Fourier space. 50 sample images and 50 flatfield images are used to extract the signal and noise. The top row shows the procedure for determining the noise and the bottom row for evaluating the signal. In both cases, flatfield images are subtracted in order to eliminate inhomogeneities in the illuminating wavefront and in the detector response. The resulting images are Fourier transformed, and for each q_x, q_y, the noise and signal are determined by computing the standard deviation σ and the mean value, respectively, over time. In a final step, the noise and signal are azimuthally averaged. A BM dataset is shown here as an example. The procedure is equivalent for the indirect system, but additionally the camera readout noise is extracted from 50 darkfield images.

are subtracted to eliminate inhomogeneities in the flatfields (second column in Fig. 4.9). The resulting additional factor of $\sqrt{2}$ in the noise (Gaussian error propagation) is taken into account in the further evaluation. From the resulting 25 images, the Fourier transform is computed (third column) and the noise $N(q_x, q_y)$ is obtained by determining the standard deviation of the 25 images for each q_x, q_y (fourth and fifth columns). Due to vertical shaking of the monochromator, the noise is increased along the central pixel column $q_y = 0$ for both systems. This column is omitted in the evaluation so that the shaking does not falsify the results. For the indirect system, N is corrected for the readout noise of the camera, extracted from 50 darkfield images (without X-ray illumination).

To determine the signal (second row in Fig. 4.9), the flatfields are first subtracted from the sample images at each propagation distance in order to remove inhomogeneities. In phase contrast imaging, strictly speaking, neither division [167] nor subtraction provides a perfect correction. Since it is found that subtraction works equally well as division for the removal of inhomogeneities here, subtraction is used due to the simpler error propagation. The complex measured signal $S_\mathrm{m}(q_x, q_y)$ is determined in Fourier space by averaging over all 50 sample images. Because of the averaging, S_m can be determined below the noise floor of a single image. To be precise, the variance of the average measured signal is $N^2/25$. The spectral

density S^2 of the signal $S(q_x, q_y)$ can then be determined by $S^2 = S_{\mathrm{m}}^2 - N^2/25$. Next, the azimuthal average of the energy density $S^2(q)$ and the squared noise $N^2(q)$ emitted at spatial frequencies with radius q is computed (last column in Fig. 4.9). Finally,

$$\mathrm{SNR}^2(q) = S^2(q)/N^2(q) \tag{4.11}$$

is obtained for each propagation distance. The procedure has been verified on artificial data.

As mentioned in Section 3.3, the BM system has a larger propagation distance in the vertical than in the horizontal direction. Here, the aim is to compare the indirect and the BM system independently of the free space contrast transfer function [43]. For the calculation of the DQE ratio, a small correction is therefore made by simulating holograms of the Siemens star test pattern for both systems and for each propagation distance. Using the measured incident photon fluence, 50 sample and 50 flatfield images are generated. Following the procedure described above for the measured data, the ideal input $\mathrm{SNR}_{0,\mathrm{BM}}^2$ and $\mathrm{SNR}_{0,\mathrm{ind}}^2$ are obtained. The simulation was performed for the ideal case of no source blur and an ideal $\mathrm{OTF}(q) = 1$. The sample is generated numerically and the propagated image intensity is simulated using the full free space propagator for the indirect system (Eq. 2.55) and the mapping procedure for the BM system (Section 3.3), though shift-variance does not have a visible effect here. The simulation includes oversampling, padding, and then binning and cropping to avoid aliasing. Furthermore, the simulation takes into account the different horizontal and vertical propagation distances z_x and z_y of the BM system and the slightly different magnifications M_x and M_y as well as the slight discrepancy in the pixel areas of both systems. Examples of the simulated image intensity are given in the first column of Fig. 4.7.

In summary, the gain in DQE is given by

$$G(q) = \frac{\mathrm{SNR}_{\mathrm{BM}}^2(q)}{\mathrm{SNR}_{\mathrm{ind}}^2(q)} \cdot \frac{\mathrm{SNR}_{0,\mathrm{ind}}^2(q)}{\mathrm{SNR}_{0,\mathrm{BM}}^2(q)}, \tag{4.12}$$

where $\mathrm{SNR}_{\mathrm{BM}}^2$ and $\mathrm{SNR}_{\mathrm{ind}}^2$ are extracted from the experimental data of the BM and indirect system, respectively.

Experimental results

As an example, the simulated and experimentally measured signal and noise are shown in Fig. 4.10a, b for one propagation distance. For the BM system, the experimental data run only slightly below the simulation of the input field $\mathrm{SNR}_{0,\mathrm{BM}}$, indicating that the system works close to the optimum. The minor deviation at high spatial frequencies can be explained by source blur and the MTF of the SPCD [94, 98], which behaves close to the sinc-shaped MTF of an ideal detector. The SPCD was operated in SPM with an energy threshold of 16 keV. Operation in CSM may increase the performance even further [94]. In contrast, the

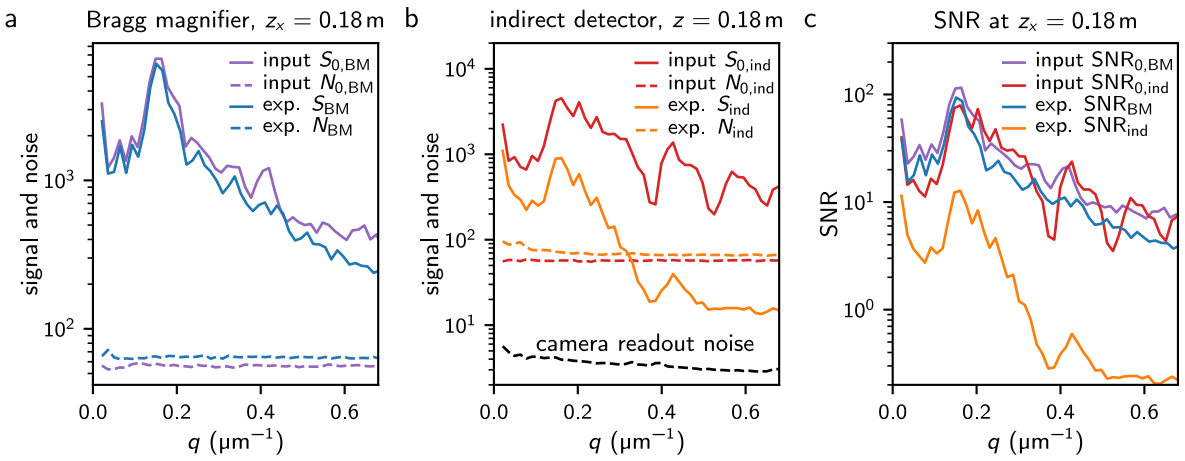

Figure 4.10.: Signal, noise, and SNR over spatial frequency q of the Siemens star holograms imaged with the BM and the indirect system at 30.5 keV. a Experimental signal S_{BM} and noise N_{BM} measured with the BM system (blue) and simulated signal $S_{0,\mathrm{BM}}$ and noise $N_{0,\mathrm{BM}}$ of the input wavefield (purple). As an example, the data are shown for a propagation distance of $z_x = 0.18\,\mathrm{m}$ and $z_y = 0.56\,\mathrm{m}$. **b** Experimental signal S_{ind}, noise N_{ind} and camera readout noise measured with the indirect system (orange) and simulated signal $S_{0,\mathrm{ind}}$ and noise $N_{0,\mathrm{ind}}$ of the input wavefield (red). The propagation distance is $z = 0.18\,\mathrm{m}$. **c** Resulting SNR(q) of the BM system (blue) and the indirect system (orange), as well as SNR(q) of the input fields for both systems. The data were acquired at an incident X-ray fluence of 6000 ph/µm^2 and a photon energy of 30.5 keV.

measured signal of the indirect system deviates considerably from the input field SNR$_{0,\mathrm{ind}}$, as expected from its lower X-ray detection efficiency and its OTF. As mentioned above, the camera readout noise is of no significance here, but has yet been subtracted to obtain the SNR of a camera without readout noise. Note that the Thon rings become visible in the azimutal scan of the signal for the indirect system, while they are not visible for the BM system due to the difference in horizontal and vertical propagation distances (see Section 2.2.6).

Fig. 4.10c shows the resulting SNR curves for the propagation distance used in Fig. 4.10a, b, and Fig. 4.11a displays the SNR averaged over all ten propagation distances. Compared to the indirect system, it is significantly higher for the BM system. Note that the expected contrast enhancement of the BM due to the larger vertical propagation distance becomes apparent when comparing the simulated SNR$_{0,\mathrm{BM}}$ with the simulated SNR$_{0,\mathrm{ind}}$, especially at low q (Fig. 4.11a, red and purple curve).

The resulting gain in DQE at this energy, obtained from Eq. 4.10, is shown in Fig. 4.11b, c without and with correction, respectively. The correction term $\mathrm{SNR}^2_{0,\mathrm{ind}}(q)/\mathrm{SNR}^2_{0,\mathrm{BM}}(q)$ reduces the spread in $G(q)$. For $q \approx 0$, the expected increase in DQE of $\gtrsim 7$ given by the scintillator's absorption is observed. For increasing q, $G(q)$ increases even further and reaches more than two orders of magnitude for $q > 0.3\,\mu\mathrm{m}^{-1}$ due to the distinct OTFs of the systems.

The measurements show that the indirect system behaves even less efficiently than expected from the scintillator absorption and the OTF of the microscope. This can be explained by the

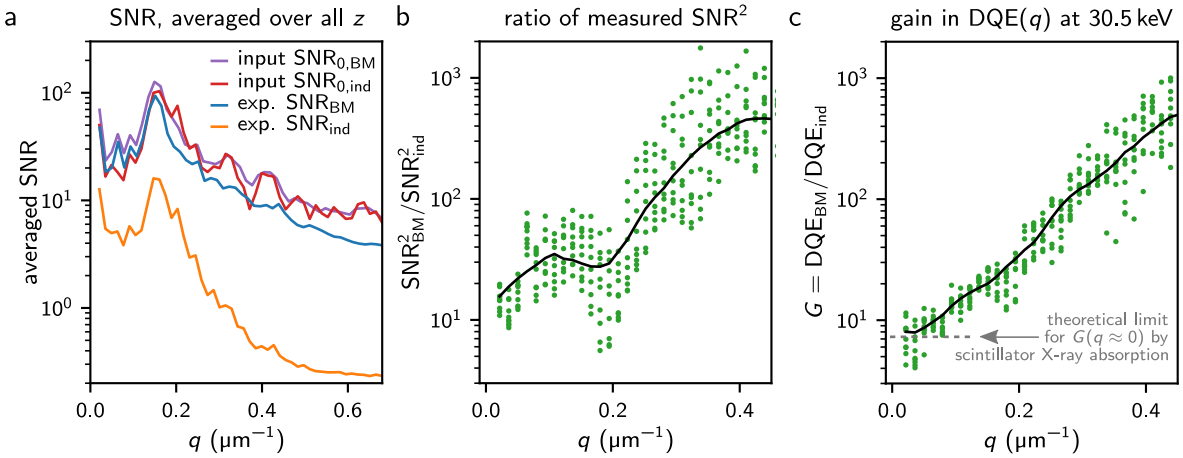

Figure 4.11.: Average SNR and resulting DQE at 30.5 keV. **a** SNR extracted from the Siemens star holograms over spatial frequency q, averaged over ten propagation distances. The SNR measured with the BM and the indirect system are shown, as well as the simulated input SNR_0 for perfect coherence. **b** Ratio of measured SNR^2 over q. The solid line is a moving average and serves as a guide for the eye. **c** Experimental gain $G(q)$ in DQE, given as the ratio of measured SNR^2 including the correction term (Eq. 4.12) that accounts for the different input signals. Partly reproduced from Ref. [104].

above-mentioned spread of energy deposition in the scintillator, which increases with X-ray energy [160, 168] (see also Fig. A.4). Thus, to operate the indirect system at the optimal energy $\sim 30\,\mathrm{keV}$ for the highest possible dose efficiency, the scintillator should not only have a high absorption but also a low spread of energy deposition.

As discussed in Fig. 4.3c, for the specific application with samples of size $d \lesssim 1\,\mathrm{mm}$ the indirect system would be best operated at a lower energy of $\sim 11\,\mathrm{keV}$. In this case, it can be estimated that the overall gain in dose efficiency of the BM system is about a factor of two at low spatial frequencies and one order of magnitude at the desired resolution (see also Appendix A.5). For thicker samples or samples in a medium, higher energies are required for the indirect system, and the gain in dose efficiency of the BM system increases accordingly.

4.2.5. Comparison on biological sample

The impact of the BM system's higher detection efficiency on biological imaging is illustrated by imaging a chalcid wasp (*Lariophagus distinguendus*) with both systems at 30.5 keV and identical and relatively low photon fluences of $200\,\mathrm{ph/\mu m^2}$ and $30\,\mathrm{ph/\mu m^2}$ per frame (Fig. 4.12). At $200\,\mathrm{ph/\mu m^2}$, attained by attenuating the beam by a factor of about 400, the specimen is barely discernible in the hologram of the indirect system (Fig. 4.12a), whereas the BM system exhibits good contrast (Fig. 4.12b). The superior imaging performance of the BM system becomes also evident in the tomographic reconstruction, where insets provide a closer look at the compound eye of the wasp, resolving finer details. At $30\,\mathrm{ph/\mu m^2}$, the data of the indirect

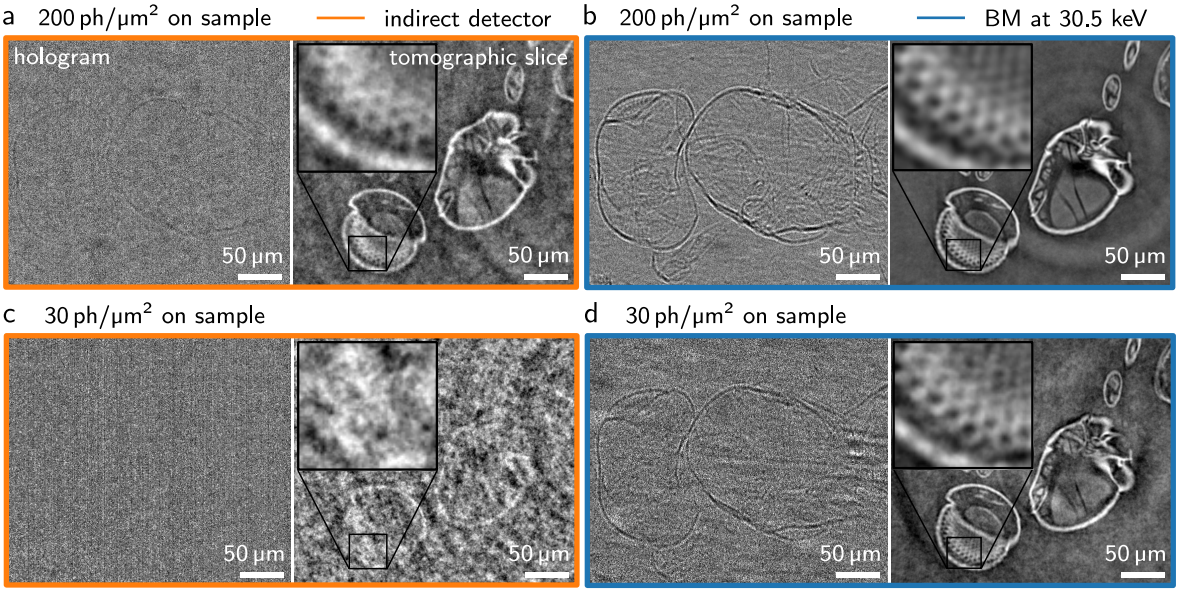

Figure 4.12.: Chalcid wasp imaged with the BM and the indirect system at 30.5 keV. Flatfield-corrected holograms and single-distance tomographic reconstruction of a critical point dried *Lariophagus distinguendus* for a comparatively low incident X-ray fluence of **a, b** 200 ph/µm² and **c, d** 30 ph/µm² per frame.

system are strongly dominated by noise (Fig. 4.12c), while the BM still reveals sample structures (Fig. 4.12d). The exposure time was 67 ms, propagation distances were $z = 0.22$ cm for the indirect detector and $z_x = 0.22$ m and $z_y = 0.60$ m for the BM system, and the tomograms were acquired with 1000 projections each. TIE phase retrieval [50] and tomographic reconstruction with filtered back-projection was performed with the *tofu* framework [141]. The value for β/δ was visually adjusted to $10^{-1.7}$.

4.3. *In vivo* study of *Trichogramma* wasps emerging from their host eggs

Increasing the dose efficiency in X-ray imaging is highly desirable for a wide range of fields and applications, ranging from dose-sensitive soft materials studies over biological tissue imaging up to *in situ* and *in vivo* imaging. The high dose efficiency of the developed Bragg magnifier system now enables the prolongation of observation times before the onset of radiation damage.

As *in vivo* pilot application, the high dose efficiency of the BM system is exploited to study the concealed behavior of parasitoid *Trichogramma* wasps related to the emergence from their host eggs over tens of minutes up to hours (see Fig. 4.13). *Trichogramma* wasps belong to the tiniest known insects. By parasitizing the eggs of numerous crop-infesting butterfly and moth species, they have become the most widely used biological control agent [169] and

therefore possess enormous economic value [170–172]. However, despite being extensively studied [173], their concealed behavior within their hosts is still largely unknown. The high dose efficiency of the BM system now allows the recording of long *in vivo* cine-radiographic data, revealing morphodynamics before and during emergence from the eggs. For the study, eggs of the Angoumois grain moth (*Sitotroga cerealella* (Lepidoptera: Gelechiidae)) were parasitized by *Trichogramma cacoeciae* (Hymenoptera: Chalcidoidea: Trichogrammatidae), incubated at 25 °C, 70 % relative humidity, under long-day conditions (16 h light, 8 h dark) until just before emergence and then brought to room temperature. The specimens were provided by Annette Herz (Julius Kühn-Institute, Dossenheim, Germany).

For a first specimen shortly before emergence, an *in vivo* tomogram was acquired with 1000 projections, an image repetition rate of 15 Hz, propagation distances of $z_x = 22$ cm and $z_y = 60$ cm, and a photon energy of 30.4 keV. At this energy, the nominal spatial resolution is 1.7 µm, the magnification is 64, and the whole insect fits into the FOV of 0.6 mm x 0.4 mm. The X-ray fluence was 100 ph/µm^2 per frame and the corresponding dose was ∼7 mGy, resulting in an estimated total dose of ∼7 Gy. TIE phase retrieval ($\beta/\delta = 10^{-2.5}$) and tomographic reconstruction were performed with the *tofu* framework [141]. The number of projections may be further reduced, e.g., by using algebraic methods or neural networks for tomographic reconstruction [174–176]. Fig. 4.13a shows a volume rendering of the egg shell and Fig. 4.13b depicts the sample with the egg shell virtually sliced, revealing the *Trichogramma* wasp that has developed inside the moth egg.

Radiographic *in vivo* data were acquired for 68 individuals with the same imaging parameters as listed above, of which six emerged during the observation under radiation and three datasets of the complete emergence process were acquired. The specimens were selected with a light optical microscope and individually scanned in Eppendorf tubes. Since it is not possible to predict the time of emergence from the outside, a dark discoloration of the egg shell was used as an indication of whether the wasp was about to emerge. The images were acquired in several sequences, intermitted by radiation-free pauses to reduce the total dose and to capture the emergence phase. The total exposure time to X-rays of the emerging wasps varied between 15–72 min with a total observation time of up to 2 h.

Fig. 4.13c-f displays phase reconstructed radiographs of a wasp during emergence at different times. The full cine-radiographic dataset spans a total duration of 1.25 h and a total X-ray exposure of 30 min and is given as a video in Ref. [104]. The wasp performs coordinated movements of the body, head, and mandibles in order to perforate the egg. At the beginning of the series (Fig. 4.13c), it bites continuously into the egg shell. After 43 minutes, the antennae protrude the egg shell (Fig. 4.13d). The wasp now tries to break through the shell by stretching its entire body several times, pushing its legs and still biting permanently into the shell. When a contiguous hole is large enough, the wasp manages to emerge (Fig. 4.13e). Finally, it grooms itself in vicinity of the egg (Fig. 4.13f) and eventually departs. No abnormalities in the wasp's behavior were observed after emergence. The estimated total dose is ∼200 Gy,

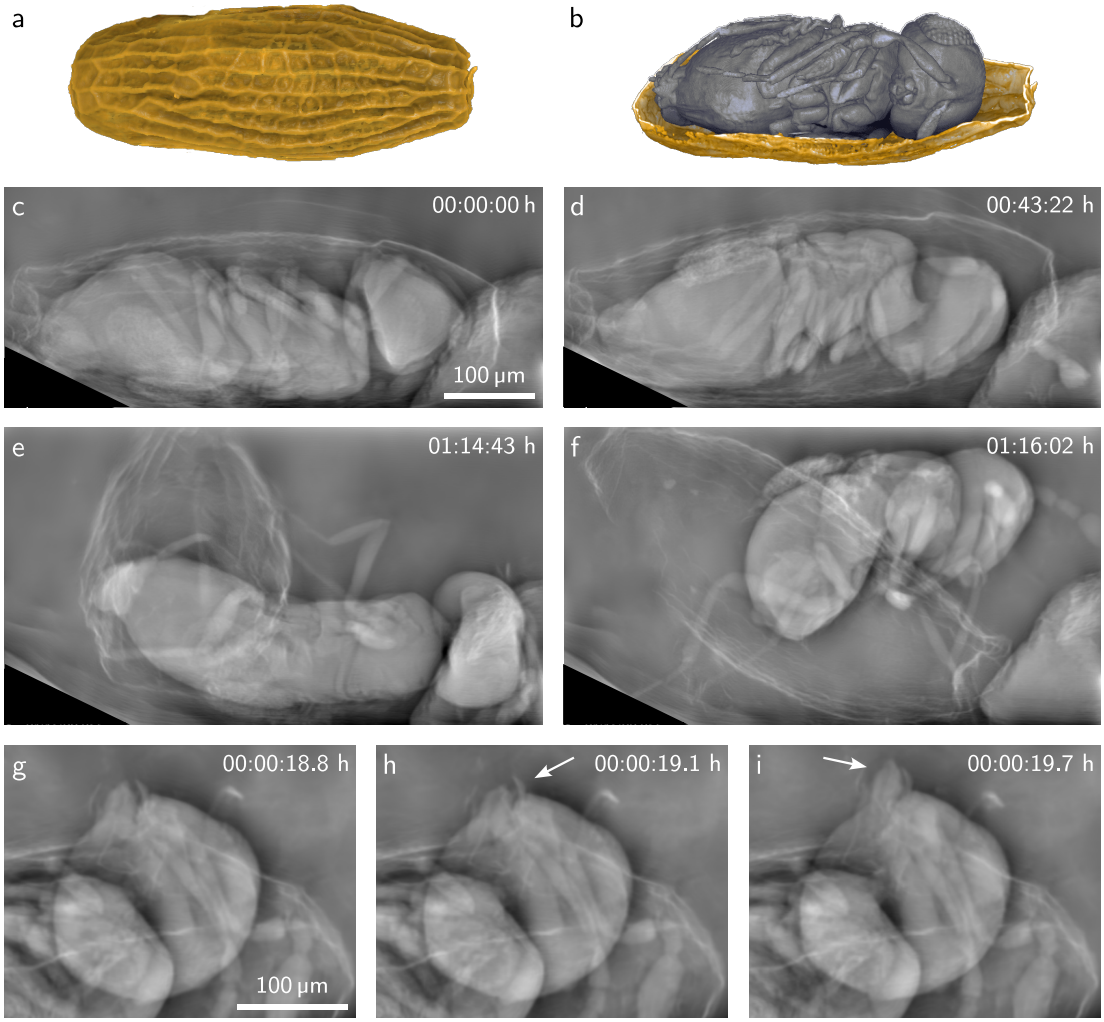

Figure 4.13.: ***Trichogramma cacoeciae*** **wasps imaged** ***in vivo*** **with the BM system.** Volume rendering of a tomographic dataset of a first individual inside its parasitized moth egg showing **a** the egg shell and **b** the wasp by virtual slicing of the egg shell. The renderings were created in *Drishti* [130] by Pauline Pfeiffer (IPS, KIT, Karlsruhe, Germany). **c-f** Phase reconstructed radiographs of a second individual emerging from its host egg. **g-i** Flexible movement of mandibles, observed in a third individual. The arrows highlight that the wasp moves its mandibles independently from each other. Reproduced from Ref. [104].

which agrees to dose levels reported in the literature to have no observable physiological effects on small animals [20]. Prior to phase retrieval, the images were denoised by a neural network trained with the Noise2Noise method [177]. The denoising was performed by Yaroslav Zharov (IPS, KIT, Karlsruhe, Germany). Details of the method application can be found in Ref. [178]. In order to fully exploit the information contained in the recorded image up to the resolution limit, phase retrieval for all *in vivo* radiographic measurements was performed using the NLTikh algorithm [79] implemented in the *HoloTomoToolbox* [77] ($\alpha_{\text{low-freq}} = 10^{-4.5}$, $\alpha_{\text{high-freq}} = 10^{-1}$).

In the dataset of another individual, the mandible movement during the biting process became particularly well visible (Fig. 4.13g-i). Here, a higher flux and Ge crystals were used at 30.5 keV, with a dose of ~ 70 mGy per frame and a total dose of ~ 90 Gy. Unlike the larger *Lariophagus distinguendus*, which employs its mandibles in a chisel-like manner to bite through a stiff wheat grain [179], *Trichogramma cacoeciae* is observed here to use its mandibles separately from one another to penetrate the more pliable egg shell. This versatility showcases how flexible mandibular movement allowed chalcid wasps to exploit a variety of hosts, which is likely a key factor for their evolutionary success and remarkable diversification [179].

4.4. Conclusion

A considerable increase in dose efficiency in micrometer-resolution X-ray imaging of soft tissues was achieved by combining highly coherent synchrotron radiation, a Bragg magnifier, and a high-Z single photon counting detector. Magnifying the propagated X-ray wavefield behind the sample by a Bragg magnifier and detection by a high-Z SPCD allows exploiting the high detection efficiency of the SPCD while maintaining micrometer resolution. The system was designed for X-ray energies ~ 30 keV, which allow a minimum dose for a desired SNR. The experiment showed that the BM system works close to the highest possible dose efficiency for PB-PCI, owing not only to its high X-ray detection efficiency of over 90 % but also its constantly high OTF over all spatial frequencies up to the micrometer resolution limit. In contrast, the OTF of the objective in conventional scintillator-based indirect detector systems decreases significantly with increasing spatial frequencies. Comparing the imaging performance of the BM system to an indirect detector system at the same energy of 30.5 keV revealed an increase in DQE of more than two orders of magnitude for high spatial frequencies, which are crucial for high spatial resolution. For applications where the efficiency of indirect systems can be improved by working at a lower energy, the estimated gain in dose efficiency of the BM system is still higher by one order of magnitude at the high spatial frequencies that contain the relevant high-resolution components of the image. Although indirect detectors benefit from continuously ongoing developments of scintillators [180], optics [181], and cameras [182], the BM system inherently outperforms any lens-based optically magnifying system by its constantly high OTF for all spatial frequencies up to its resolution limit.

The high dose efficiency of the BM system enables a substantial increase of observation times in *in vivo* studies at micrometer resolution, which was exploited for an *in vivo* pilot study of tiny parasitoid wasps inside their host eggs. The concealed behavior of *Trichogramma* wasps could be filmed for more than 30 minutes, providing the possibility for a detailed analysis of their movement patterns and behavioral acts before and during emergence. Due to its high dose efficiency, Bragg magnifier based X-ray imaging holds a wide range of potential applications, not only for high-resolution *in vivo* imaging in life sciences but also for *in situ* studies of dose-sensitive materials and processes.

5. Bragg demagnifier for propagation-based phase contrast imaging of large samples

In the last decade, there has been increasing interest in applying phase contrast imaging not only to small specimens but also to large, centimeter-sized samples [183–186]. In the pursuit of low-dose imaging, a compromise has to be taken between dose and spatial resolution, since for a given signal-to-noise ratio, the dose scales with the square of the desired resolution. For large samples, it is therefore essential to generate high contrast at low spatial frequencies. The same holds true for fast applications, where high contrast at low spatial frequencies allows a reduction in resolution and thus exposure times. The most prominent approaches for phase contrast imaging of large samples at moderate resolutions down to $\sim 10\,\mu m$ are differential phase contrast such as grating- [8, 187, 188], speckle- [13, 14], or analyzer-based [10, 11], and propagation-based phase contrast. In propagation-based phase contrast imaging (PB-PCI), the image contrast increases with increasing propagation distances. To visualize low spatial frequencies of $\sim 2\pi/10\,\mu m$ to $\sim 2\pi/1\,mm$, however, long propagation distances of tens to hundreds of meters are necessary [17, 183–185, 189–192]. Recently, a new beamline was built at the ESRF with a remarkably long experimental hutch of 45 m, facilitating PB-PCI at propagation distances of up to 36 m, tailored to the X-ray source size [17, 193, 194].

To overcome the need to build extremely long beamlines and experimental hutches, this chapter introduces a new imaging technique for PB-PCI at moderate resolution with a physical distance between sample and detector in the meter-range, yet allowing long effective propagation distances of hundreds to thousands of meters. The underlying concept is to broaden the spatial frequency distribution, whereby the image contrast is strongly amplified within a short physical distance. Simultaneously, the technique significantly reduces the image blur caused by the finite size of the X-ray source. Section 5.1 introduces the general working principle, which is realized by a Bragg demagnifier. Section 5.2 gives a description of the linear and the full image formation with the Bragg demagnifier, Section 5.3 discusses dispersion effects and source blur, and Section 5.4 shows simulation examples. In Section 5.5, the concept is experimentally proven and compared to conventional free space propagation at the same physical propagation distance. Parts of this chapter have been published in Ref. [195].

5.1. Working principle of a Bragg demagnifier

The aim of the presented method is to enable PB-PCI at moderate resolution with a physical distance between sample and detector in the meter range, yet allowing long effective propagation distances of hundreds to thousands of meters. For this purpose, the spatial frequency distribution of the diffracted X-ray wavefield behind the sample is magnified, resulting in a strongly increased effective propagation distance and thus an enhanced image contrast. This section introduces the basic working principle, followed by a description of its realization by Bragg crystal optics implemented as a Bragg demagnifier.

5.1.1. Boosting the propagation distance - basic idea

Let us revisit Eq. 2.55 for free space propagation with the Fresnel propagator (Eq. 2.58). The sample exit wavefield $f(\boldsymbol{r})$ can be expressed by its Fourier transform $\tilde{f}(\boldsymbol{k})$, where $\boldsymbol{r} = (x, y)^T$ and $\boldsymbol{k} = (k_x, k_y)^T$ are the spatial coordinate and angular frequency, respectively, in the object or image plane. After free space propagation along a propagation distance z, the propagated wavefield $g(\boldsymbol{r})$ in the image plane is given by

$$g(\boldsymbol{r}) = \frac{1}{(2\pi)^2} \iint \tilde{f}(\boldsymbol{k}) e^{i\boldsymbol{k}\boldsymbol{r}} e^{-\mathrm{i}\frac{\boldsymbol{k}^2}{2k_0}z} \mathrm{d}\boldsymbol{k}. \tag{5.1}$$

The argument $\frac{\boldsymbol{k}^2}{2k_0}z$ in the Fresnel propagator shows that low spatial frequencies in the wavefield must propagate a long distance z in order to accumulate a certain phase shift that can be transformed into measurable image contrast. For large samples, it would be advantageous to magnify the spatial frequencies before free space propagation. After magnification by a factor M, the wavefield $\tilde{f}'(\boldsymbol{k})$ is given by $\tilde{f}'(\boldsymbol{k}) = \tilde{f}(\boldsymbol{k}/M)$, where the $'$ (prime) sign denotes the wavefield after magnification of the spatial frequencies. Rewriting $\boldsymbol{k}/M \to \boldsymbol{k}$, the propagated wavefield reads

$$g'(\boldsymbol{r}) = \frac{M^2}{(2\pi)^2} \int \tilde{f}(\boldsymbol{k}) e^{-i\frac{\boldsymbol{k}^2}{2k_0}M^2 z} e^{i\boldsymbol{k}M\boldsymbol{r}} \mathrm{d}\boldsymbol{k}. \tag{5.2}$$

The magnification of the spatial frequencies thus results in a drastically increased effective propagation distance

$$z_{\mathrm{eff}} = M^2 z \tag{5.3}$$

that is quadratic in M. In other words, the image will have the same contrast as the unaltered wavefield propagated to a physical distance of $M^2 z$. The term $M\boldsymbol{r}$ in Eq. 5.2 shows that the magnification of the spatial frequencies by a factor M comes along with a demagnification by a factor M in real space.

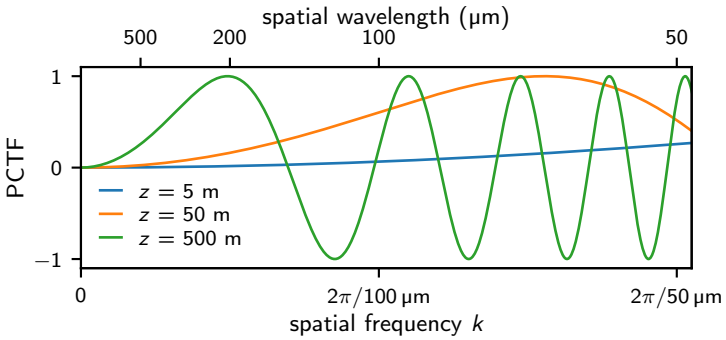

Figure 5.1.: PCTF for large objects. The PCTF is shown for different propagation distances z at low spatial frequencies k, which are decisive for imaging large objects at moderate resolution. Large distances of tens to hundreds of meters are required to attain phase contrast at low frequencies.

As discussed in Section 2.2.6, for weak phase objects the image formation reduces to a linear process, and the situation can be illustrated by the phase contrast transfer function (PCTF) (Eq. 2.77), which describes how strongly the phase signal at each spatial frequency is translated into measurable image contrast:

$$\mathrm{PCTF}(\boldsymbol{k}) = \sin\left(\frac{\boldsymbol{k}^2}{2k_0} z\right). \tag{5.4}$$

As an example, Fig. 5.1 displays the PCTF for different z and low spatial frequencies up to $2\pi/50\,\mu\mathrm{m}$. At a propagation distance of 5 m (blue), the PCTF reaches only low values. At 50 m (orange), the contrast transfer is high for frequencies between $2\pi/100\,\mu\mathrm{m}$ and $2\pi/50\,\mu\mathrm{m}$, while it is still rather low for structures of 200 µm and larger. At $z = 500\,\mathrm{m}$ (green), these structure sizes attain high contrast. However, the experimental realization of such long distances is exceedingly challenging. In contrast, after magnification of the spatial frequencies $\boldsymbol{k} \to M\boldsymbol{k}$, the PCTF becomes

$$\mathrm{PCTF}(\boldsymbol{k}) = \sin\left(\frac{\boldsymbol{k}^2}{2k_0} M^2 z\right). \tag{5.5}$$

The propagation distance $z_{\mathrm{eff}} = M^2 z$ is thus effectively enhanced by a factor M^2, thereby attaining strong phase contrast at a substantially shorter physical distance between the sample and detector.

5.1.2. Contrast amplification by demagnification with asymmetric Bragg diffraction

Demagnifying the X-ray wavefield behind the sample in two dimensions with minimal distortion can be achieved by using a Bragg magnifier with inverse diffraction geometry, i.e., using a negative asymmetry angle. So far, Bragg diffraction with a negative asymmetry angle has

been used to focus and collimate the incident X-ray illumination [121, 122], to achieve high angular sensitivity in analyzer-based imaging [10] or to fit a large X-ray image onto a smaller detector [123]. Here, demagnification of the X-ray wavefield is used to enhance the image contrast. The effect of a Bragg demagnifier on PB-PCI is illustrated in Fig. 5.2 in 1D. In conventional PB-PCI, the wavefield behind a large, centimeter-sized sample does not create measurable phase contrast within a rather short distance z_a of, say, 1 m. To obtain image contrast with conventional PB-PCI, the wavefield would have to propagate by a long distance z_b of, say, 625 m. By demagnifying the wavefield with a Bragg demagnifier, strong image contrast is achieved after the short physical distance $z_a = z_1 + z_2$, where z_1 is the distance between the sample and the demagnifier and z_2 is the distance between the demagnifier and the detector. The demagnification in real space and the magnification in reciprocal space results in a boost of the effective propagation distance by a factor of M^2. For example, a demagnification of $M = 25$ and subsequent propagation by a physical distance of $z_2 = 1\,\mathrm{m}$ would yield the same image contrast as the unaltered wavefield propagated by $z_b = 625\,\mathrm{m}$.

5.2. Image formation

For simplicity and to give a general idea of the image formation process for the Bragg demagnifier, this section first discusses the image formation under the assumption of shift-invariance. Subsequently, a full description including shift-variance is given. A method to counteract the shift-variance while simultaneously further increasing the dose efficiency is also presented.

5.2.1. Linear approximation

As discussed in Section 3.3, the dependence between the spatial frequencies $\boldsymbol{k}_{\mathrm{in}}$ and $\boldsymbol{k}_{\mathrm{out}}$ is in general a slightly nonlinear function, causing the image formation to be shift-variant. Approximating the dependency as $\boldsymbol{k}_{\mathrm{out}}(\boldsymbol{k}_{\mathrm{in}}) \approx M\boldsymbol{k}_{\mathrm{in}}$, the shift-invariance is fulfilled. Similar to the Bragg magnifier, the wavefield is demagnified in the horizontal and the vertical directions by one crystal each. Since the two crystals have a certain distance to each other, the demagnification takes place at different distances $z_{1,x}$ and $z_{1,y}$ along the optical axis between the sample and the crystal centers. Likewise, the distances $z_{2,x}$ and $z_{2,y}$ between the crystal centers and the detector differ as well. The demagnified wavefield in the detector plane is given by

$$g'(\boldsymbol{r}) = \frac{M_x M_y}{(2\pi)^2} \iint \tilde{f}(\boldsymbol{k}) H(\boldsymbol{k})\, e^{ik_x M_x x} e^{ik_y M_y y} \mathrm{d}\boldsymbol{k}, \tag{5.6}$$

with the propagator

$$H(\boldsymbol{k}) = A(\boldsymbol{k}) e^{-i\frac{k_x^2}{2k_0}(z_{1,x}+M_x^2 z_{2,x})} e^{-i\frac{k_y^2}{2k_0}(z_{1,y}+M_y^2 z_{2,y})}. \tag{5.7}$$

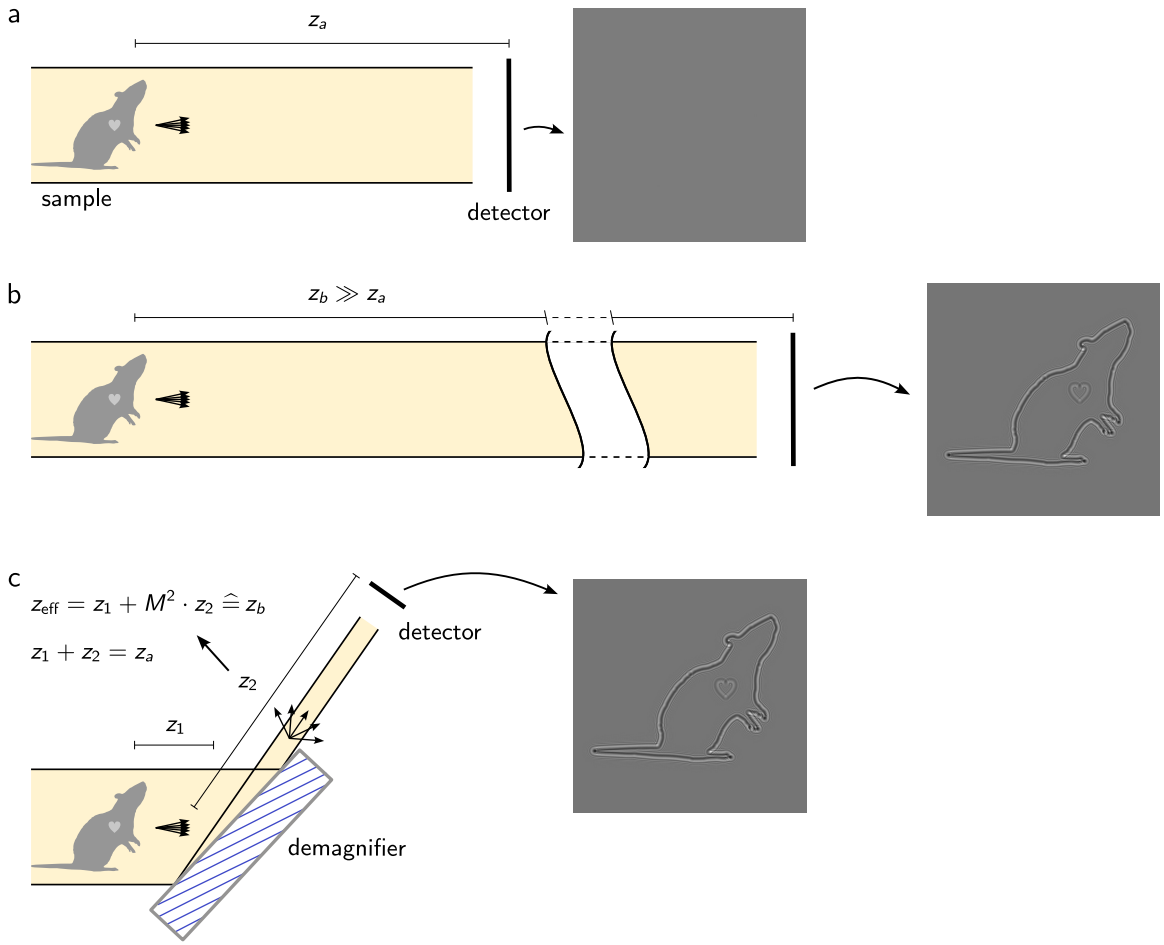

Figure 5.2.: Working principle of a Bragg demagnifier in 1D. a PB-PCI of a large object at moderate resolution yields hardly any phase contrast at rather short propagation distances of, e.g., $z_a \sim 1\,\text{m}$, as typically provided by experimental hutches at a synchrotron. **b** Obtaining measurable image contrast with conventional PB-PCI at moderate resolution requires very long propagation distances z_b of tens or hundreds of meters and more. **c** Demagnification of the X-ray wavefield by asymmetric Bragg diffraction by a factor M leads to a strongly increased effective propagation distance $z_{\text{eff}} = z_1 + M^2 z_2$, where z_1 and z_2 are the physical distances between the sample and the demagnifier or the demagnifier and the detector, respectively.

A is the complex field amplitude ratio comprised of both crystals (see also Eq. 2.36), M_x and M_y are the demagnification factors in horizontal and vertical direction, and $\boldsymbol{k}_{\text{in}}$ is written as $\boldsymbol{k}$ here for better readability. The different distances and possibly different magnifications lead to different effective propagation distances

$$z_{\text{eff},i} = z_{1,i} + M_i^2 z_{2,i}. \tag{5.8}$$

For large M, the propagation along $z_{1,i}$ in front of the demagnifier can be neglected.

Analogous to the Bragg magnifier, the demagnification factor is given by

$$M = \frac{\sin(\theta_\mathrm{B} + \mathrm{Re}(\Delta\theta_{oc}) - \alpha)}{\sin(\theta_\mathrm{B} + \mathrm{Re}(\Delta\theta_{hc}) + \alpha)}, \tag{5.9}$$

where $\alpha < 0$. The crystal function $A(\boldsymbol{k})$ acts as a low-pass filter. It cancels the contributions of high spatial frequencies to the background noise and defines the intrinsic spatial resolution of the Bragg demagnifier, given by the incident Darwin width ω_{oc}, see Eq. 3.2.

The PCTF for the demagnifier is obtained by inserting the propagator $H(\boldsymbol{k})$ into Eq. 2.73:

$$\mathrm{PCTF}(\boldsymbol{k}) = |A^*(0)A(\boldsymbol{k})| \sin\left(\frac{\boldsymbol{k}^2}{2k_0}\boldsymbol{z}_\mathrm{eff} + \phi_A\right), \tag{5.10}$$

where $\boldsymbol{k}^2\boldsymbol{z}_\mathrm{eff} = k_x^2 z_{\mathrm{eff},x} + k_y^2 z_{\mathrm{eff},y}$. The crystal reflection curve enters through an envelope function given by $|A^*(0)A(\boldsymbol{k})|$ and a slowly varying phase factor ϕ_A. Similarly, the amplitude contrast transfer function is obtained by replacing the sine with a cosine.

5.2.2. Shift-variant image formation

For a more precise description of the image formation, the nonlinear dependence of $k_\mathrm{out}(k_\mathrm{in})$ is considered. The mapping procedure described in Section 3.3 for the Bragg magnifier, which describes the transformation of a plane wave incident on a crystal into a plane wave diffracted by the crystal, is equally valid for the Bragg demagnifier. For clarity, only the 1D case is discussed here, but the considerations can easily be transferred to the 2D case by treating the x- and y-directions as independent. The nonlinear dependence of the outgoing spatial frequencies on the incident frequencies is given by Eq. 3.9, which is repeated here:

$$k_\mathrm{out}(k_\mathrm{in}) = k_0 \sin\left(\beta_\mathrm{out} - \arccos\left[\cos\left(\beta_\mathrm{in} - \arcsin\frac{k_\mathrm{in}}{k_0}\right) + \cos\beta_\mathrm{out} - \cos\beta_\mathrm{in}\right]\right). \tag{5.11}$$

A sketch for the demagnifier is given in Fig. 5.3a. The magnification of the spatial frequency distribution is further illustrated in Fig. 5.3b. The wavefield propagated by the distance z_2 behind the demagnifier is given by

$$g'(x) = \frac{1}{2\pi}\int \tilde{f}(k_\mathrm{in}) \cdot A(k_\mathrm{in}) \cdot e^{-i\frac{k_\mathrm{in}^2}{2k_0}z_1} \cdot e^{-i\frac{k_\mathrm{out}^2(k_\mathrm{in})}{2k_0}z_2} \cdot e^{ik_\mathrm{out}(k_\mathrm{in})x} \cdot \frac{\mathrm{d}k_\mathrm{out}(k_\mathrm{in})}{\mathrm{d}k_\mathrm{in}}\mathrm{d}k_\mathrm{in}. \tag{5.12}$$

5.2.3. Aberration-free demagnifier and high dose efficiency

The nonlinear dependence $k_\mathrm{out}(k_\mathrm{in})$ leads to a shift-variant behavior in the image formation (Section 3.3). Shift-invariance can be restored by re-magnifying the propagated wavefield behind the demagnifier with a Bragg magnifier of the same crystal type and the same (but

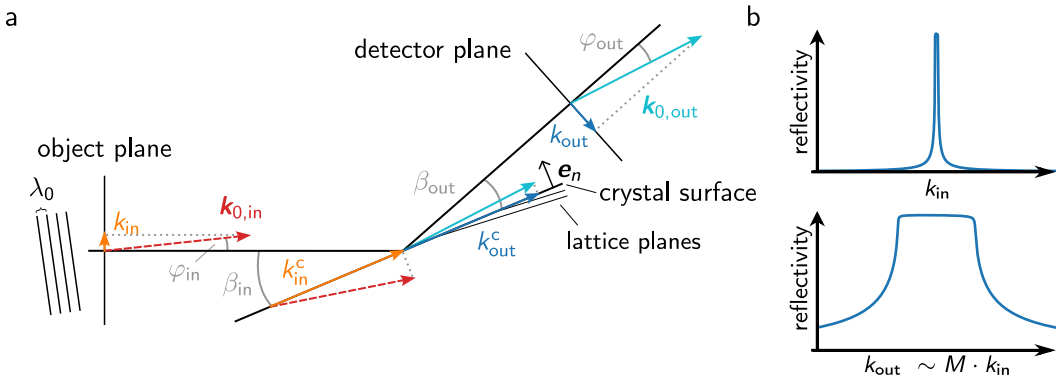

Figure 5.3.: Sketch for the calculation of $k_{out}(k_{in})$ for the Bragg demagnifier. **a** Mapping between incident and outgoing spatial frequencies k_{in} and k_{out}, which can be obtained in analogy to the Bragg magnifier. **b** Illustration of the magnification of the spatial frequencies, which corresponds to a demagnification in real space. In linear approximation, the incident waves k_{in} are magnified by a factor of M.

positive) asymmetry angle (see Fig. 5.4b). This follows from the fact that a plane wave with spatial frequency k_{in} incident on the demagnifier results in a plane wave with the same spatial frequency $k_{out} = k_{in}$, as can easily be derived from Eq. 5.11. Only the phase and amplitude are altered by the crystals and the free space propagation. The wavefield at a distance z_3 behind the Bragg magnifier is given by

$$g'_{BM}(x) = \frac{1}{2\pi} \int \tilde{f}(k_{in}) H(k_{in}) e^{ik_{in}x} \mathrm{d}k_{in} \tag{5.13}$$

$$= f(x) * h(x) \tag{5.14}$$

with the propagator

$$H(k_{in}) = A(k_{in}) e^{-i\frac{k_{in}^2}{2k_0}(z_1+z_3)} e^{-i\frac{k_{out}^2(k_{in})}{2k_0}z_2}. \tag{5.15}$$

Here, $A(k_{in})$ is the product of the complex amplitude ratios of all four crystals. The final image can thus be described by a convolution of the object wavefield $f(x)$ with the PSF $h(x) = \mathcal{F}^{-1}[H(k_{in})]$, which simplifies phase reconstruction and allows the use of conventional reconstruction techniques.

Even more importantly, the combination with a Bragg magnifier allows the detection of the propagated image with a highly-efficient large-area detector, see Chapter 4. This further increases the dose efficiency of the proposed technique, rendering it a potential candidate for low-dose medical diagnostics such as the early detection of breast cancer or other diseases, especially in conjunction with currently emerging compact X-ray sources [196–198].

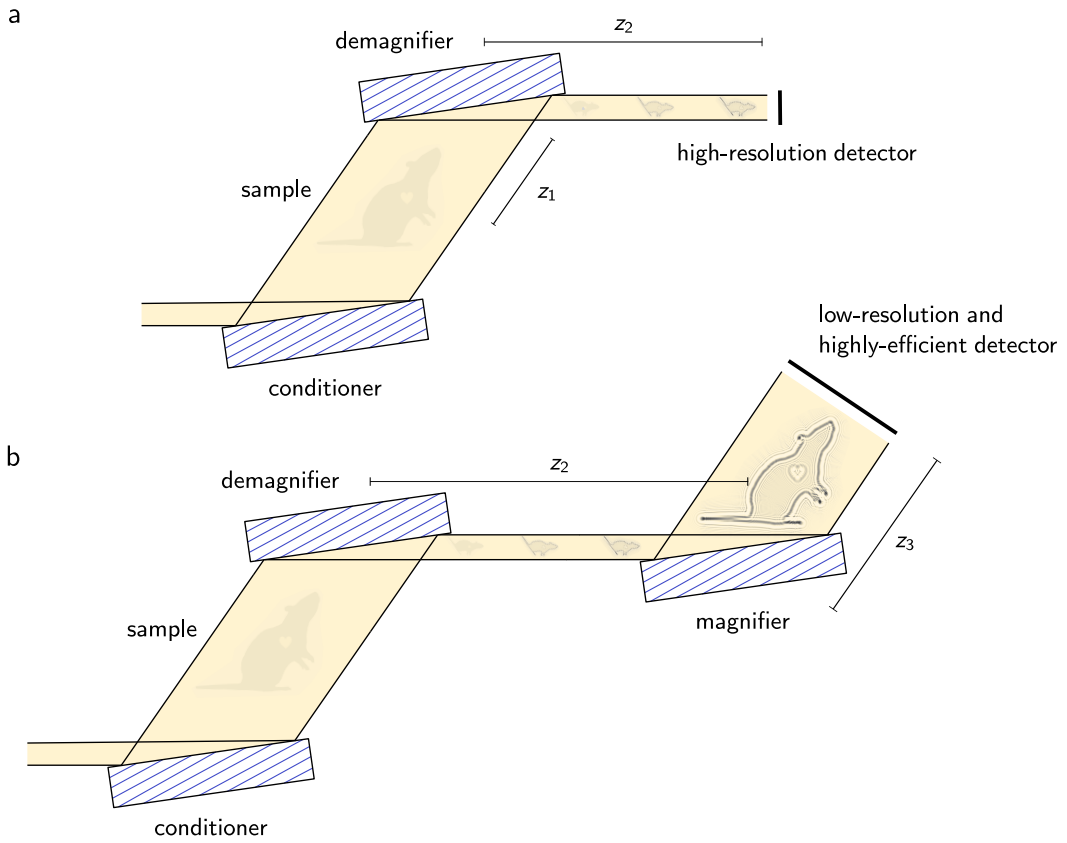

Figure 5.4.: Schematic of the combination of a Bragg conditioner and a Bragg demagnifier in 1D. First, the beam is magnified to obtain a sufficiently large field of view (FOV). After demagnification of the diffracted wavefield behind the sample by the demagnifier, free space propagation leads to strong interference of low spatial frequencies within a short distance. The generated intensity pattern can either **a** be recorded by a high-resolution indirect detector or **b** be re-magnified by a subsequent Bragg magnifier. The Bragg magnifier allows the use of an efficient large-area detector. In addition, the Bragg magnifier compensates for the shift-variance of the demagnifier if the same type of crystals is used. Partly reproduced from Ref. [195].

5.2.4. Bragg conditioner

Imaging of low spatial frequencies by PB-PCI with a Bragg demagnifier requires a monochromatic X-ray beam with sufficient transversal coherence and a large beam cross section to illuminate the centimeter-sized sample. To achieve a large FOV, a Bragg conditioner is placed in front of the sample, see also Fig. 3.2a. In addition, the Bragg conditioner can counteract dispersion effects induced by the demagnifier, as will be discussed in Section 5.3. Fig. 5.4a displays a 1D sketch of the setup with a Bragg conditioner, a demagnifier and high-resolution detector that records the demagnified image after propagation. In Fig. 5.4b, a Bragg magnifier has been added behind the demagnifier so that the shift-invariance is restored and the image can be acquired with a highly efficient large-area detector. A schematic for the 2D case is depicted in Fig. 5.5.

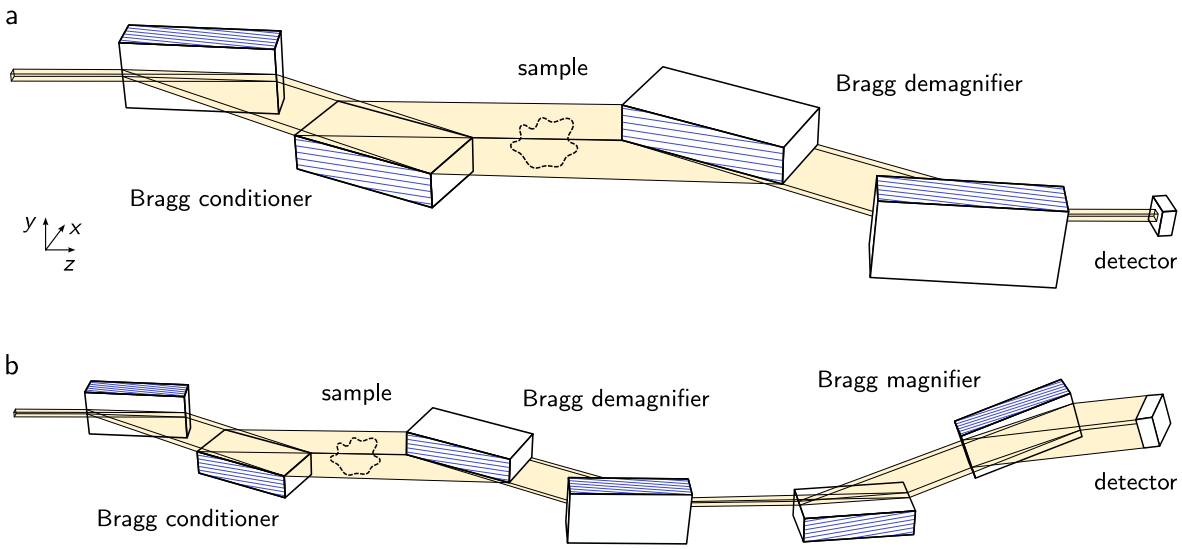

Figure 5.5.: Sketch of a 2D Bragg demagnifier. The incident beam is magnified by a Bragg conditioner in 2D to obtain an illuminated area of several centimeters despite the millimeter-sized beam cross section typically provided by synchrotrons. The wavefield behind the sample is then demagnified and **a** detected by a high-resolution detector or **b** re-magnified by a Bragg magnifier and detected by an efficient large-area detector. The order of the horizontal and vertical crystals in each component (conditioner, demagnifier, magnifier) may also be changed. Partly reproduced from Ref. [195].

5.3. Influence of Bragg demagnifier on transverse coherence

In the following, the influence of the Bragg demagnifier on the transverse coherence and thus on the source blur is discussed. The source blur depends on the angular distribution of the plane waves illuminating the sample and the propagation distance z between the sample and the detector (see Section 2.2.5). The former is defined by the ratio of the physical source size s and the source-to-sample distance l. Since a change in the angular distribution alters the source blur, the term *angular source size* is used here synonymously to the angular distribution seen by the sample.

From the perspective of a monochromatic wavefield, the Bragg conditioner in front of the sample reduces the angular distribution of the incident X-rays. However, for polychromatic X-rays, the total polychromatic angular distribution is increased by asymmetric diffraction [199, 200]. Since the radiation behind the monochromator has a small but finite bandwidth of $\sim 10^{-4}$, the total polychromatic angular distribution must be considered here. The following section shows that the demagnifier allows taking advantage of the monochromatic reduction in the angular source size provided by the conditioner and that the demagnifier reduces the source blur, which is a crucial advantage for enabling long propagation distances.

5.3.1. Dispersion effects

First, the influence of the Bragg conditioner and demagnifier on the angular source size is considered. An example of the propagation of the angular and energy-dispersive intensity distributions behind the source, monochromator, Bragg conditioner and demagnifier crystals is shown in Fig. 5.6 for the center of the crystal surface. For the simulation, the amplitude and spatial frequency k of each plane wave coming from the source with energy E and angle $\theta = \arcsin(k/k_0)$ is tracked on its way through the crystal arrangement. The nonlinear mapping between the incident waves and the diffracted waves is taken into account (Eq. 5.11). As described in Section 2.2.5, the amplitudes of the waves emanated from the source can be modeled by a normal distribution with a standard deviation $\sigma = k_0 \cdot s/l$. The source distribution is assumed to be identical for all energies. In Fig. 5.6a, the source distribution is shown for the horizontal source size $s_\mathrm{h} = 164\,\mu\mathrm{m}$ and a source-to-sample distance of $l = 86\,\mathrm{m}$ of the P23 beamline. Fig. 5.6b-d illustrates the E-k-intensity distribution of the X-rays behind each optical element, which are a double-crystal Si (111) monochromator followed by a conditioner and a demagnifier crystal with asymmetry angles $\alpha = 5.92°$ and $-5.92°$, respectively, and using the Si (220) reflection. All crystals are in a non-dispersive arrangement, i.e., the normal vectors $\boldsymbol{e}_\mathrm{n}$ to the crystal surfaces point alternately in opposite directions. The crystals are all aligned to an energy of 29 keV. The plots are shown as a function of spatial frequency k rather than angle θ, although the latter is more commonly used, because using k allows the values to be directly related to the object frequencies.

For the sufficiently small source sizes provided by 3$^\mathrm{rd}$ generation synchrotrons, the monochromator acts as an energy filter and transmits only a small energy bandpass of the order of 10^{-4} (Fig. 5.6b). The subsequent conditioner crystal transmits the entire incident beam due to its large angular acceptance. The angular acceptance of the conditioner crystal is indicated by the white area in Fig. 5.6b. From a monochromatic point of view, the k-values are compressed by the conditioner by a factor of M, as can be seen in Fig. 5.6c. However, waves of different energies are diffracted to different angles, whereby only the monochromatic angular distribution is reduced, not the polychromatic angular distribution. In fact, the total angular source size behind the conditioner is even slightly increased. This is shown in Fig. 5.7, where the intensity was integrated over the energy and is depicted as a function of k. The colors indicate the energy composition and show the dispersion over the angular range. The distribution behind the conditioner (middle row) is expanded by a factor of ~ 3 for the example shown at a central energy of 29 keV. Next, the demagnifier magnifies the monochromatic k-values to their original angular distribution, while inverting the energy-dependent shift. As a result, the E-k-distribution behind the demagnifier is the same as behind the monochromator (except for a slight attenuation). Thus, the Bragg demagnifier makes it possible to take advantage of the reduction in the monochromatic angular distribution caused by the Bragg conditioner. In other words, if the source size is small enough to provide reasonable phase

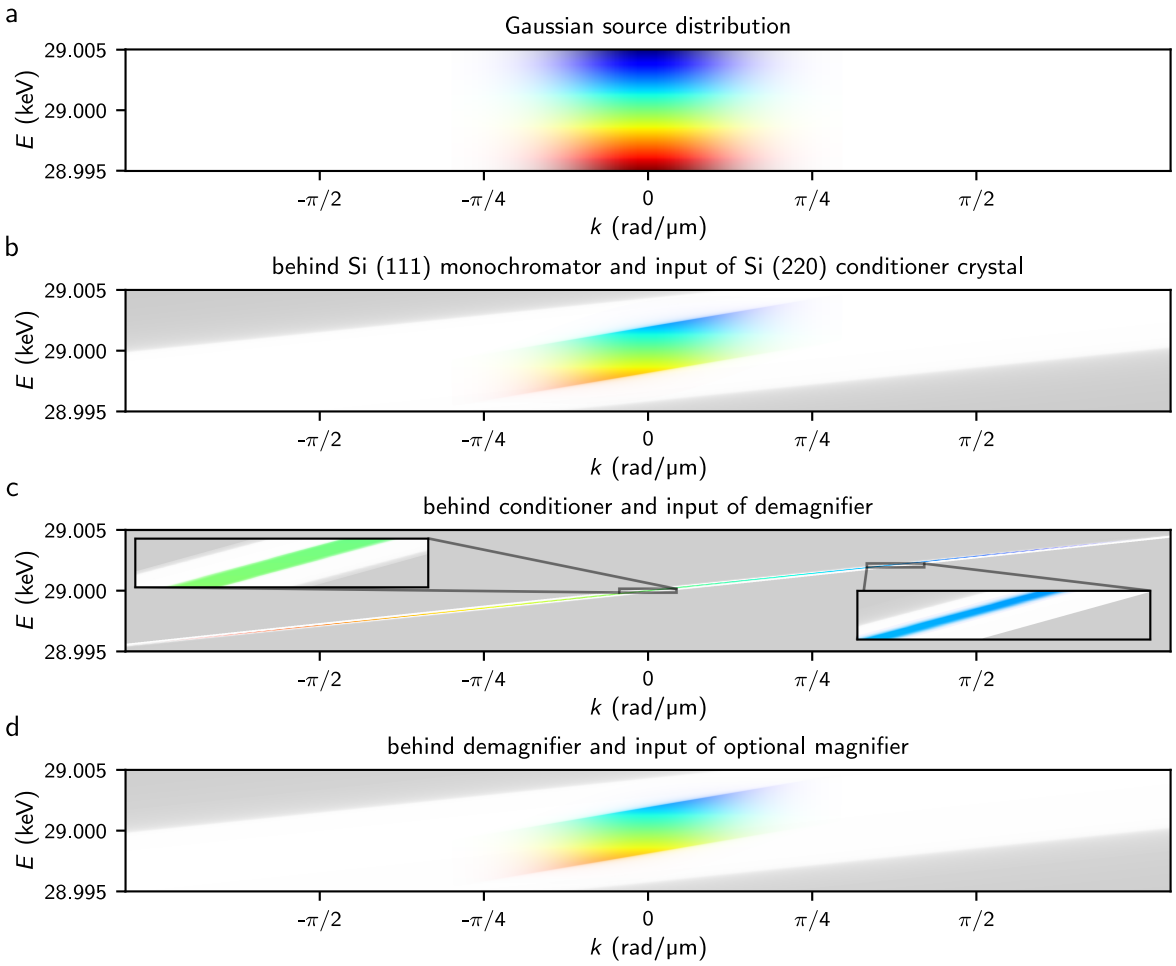

Figure 5.6.: Dispersion. Intensity distribution over E and k behind **a** the source, **b** the monochromator, **c** the conditioner and **d** the demagnifier. The color shows the energy. The intensity distribution is shown for the horizontal source size of P23 of $s_\mathrm{h} = 164\,\mu\mathrm{m}$ and the settings used in the proof-of-concept experiment, i.e., a source-to-sample distance of $l = 86\,\mathrm{m}$, a double-crystal Si (111) monochromator aligned to 29 keV, and a conditioner and a demagnifier Si (220) crystal with $\alpha = \pm 5.92°$. In panels b-d, the acceptance angles of the conditioner and demagnifier crystals are indicated by the white area.

contrast in free space propagation a for small sample, the same holds true for a large sample demagnified with the demagnifier and imaged at the same effective resolution.

5.3.2. Reduction of source blur

Knowing that the total angular distribution of the plane wave illumination is not affected by the combination of conditioner and demagnifier, the question remains how the magnification of the spatial frequencies affects the final image quality compared to conventional PB-PCI at the same effective propagation distance. In general, the finite source size leads to source

blur in the image (Section 2.2.5). The source blur increases with the propagation distance between the sample and the detector and with the spatial frequency k. Since the demagnified wavefield experiences the original source size, the source blur in the demagnified image is a factor of M larger compared to the original image at the same physical propagation distance. Simultaneously, demagnification increases the effective propagation distance by M^2. In total, the source blur for the demagnifier is thus improved by a factor of M compared to conventional PB-PCI at the same long effective propagation distance. This also becomes clear from Eq. 2.68. Recall that the image degradation is given by

$$\tilde{I}_z(k) = e^{-\frac{\sigma^2 z^2 k^2}{2k_0^2}} \cdot \tilde{I}_z^{\mathrm{coh}}(k).$$

The standard deviation of the Gaussian envelope is given by $k_0/(\sigma z) = l/(sz)$ for a conventional propagation-based phase contrast image at the physical propagation distance z. With the demagnifier, the same image contrast of the coherent wavefield is attained after the short physical distance z/M^2, while the small spatial frequencies k of the object are magnified by M. In total, the source blur for the demagnifier therefore becomes $Ml/(sz)$. This corresponds to an *effective* source size of

$$s_{\mathrm{eff}} = s/M. \tag{5.16}$$

The demagnifier thus reduces the source blur by a factor of M, allowing for longer effective propagation distances before the onset of source blur.

The maximum useful propagation distance before the onset of source blur can be calculated using Eq. 2.69. As an example, the maximum distances for the horizontal and vertical source sizes of the P23 beamline are $z_x = 17\,\mathrm{m}$ and $z_y = 72\,\mathrm{m}$ for conventional PB-PCI with a pixel size of $50\,\mu\mathrm{m}$, while employing a demagnifier with $M = 25$, the maximum distances would considerably increase to $z_x = 420\,\mathrm{m}$ and $z_y = 1800\,\mathrm{m}$.

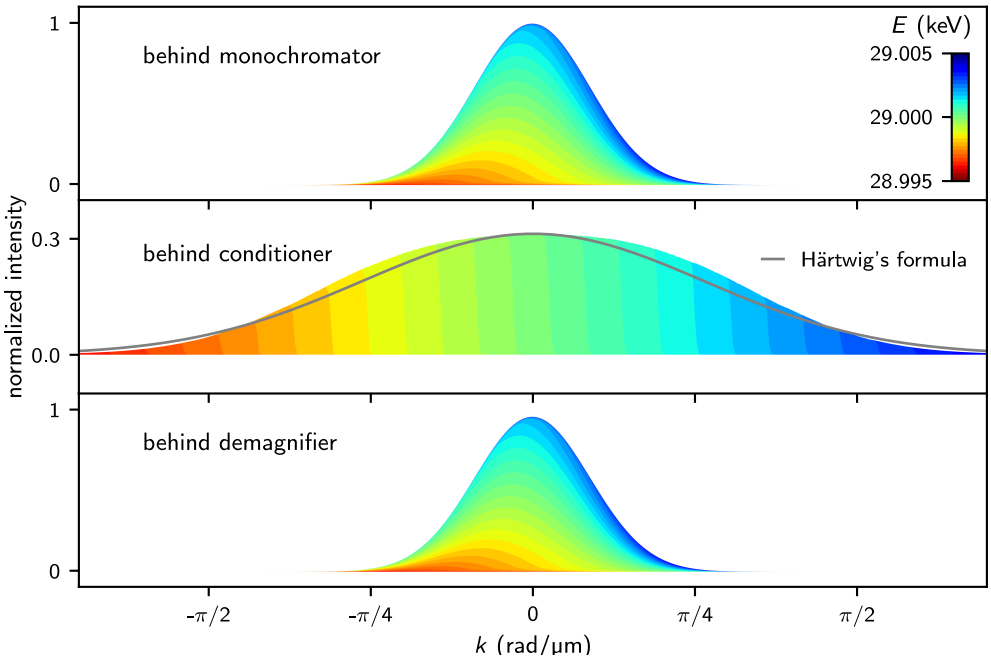

Figure 5.7.: Projected angular source size and dispersion. Angular intensity distribution behind the monochromator, conditioner and demagnifier, extracted from Fig. 5.6 and plotted as a function of k. The colors indicate the energy composition at each angle. The graph shows that although the monochromatic angular distribution is reduced by M behind the conditioner, the overall angular source size is increased. This is also predicted by the divergence formula given by J. Härtwig [199], which is shown in gray (for details, see Appendix A.7). Behind the demagnifier, the distribution is the same as behind the monochromator, showing that the demagnifier counteracts the angular spread of the conditioner. The curves are shifted vertically for better visibility.

5.4. Simulation of image formation

To visualize numerically the validity and benefits of the proposed approach, the image intensity is simulated for conventional PB-PCI and using a Bragg demagnifier. First, a 1D example is given, computed for ideal coherence, to show the increase in image contrast and the effects of shift variance. Second, a 2D object is simulated including source blur to illustrate not only the increase in contrast for the demagnifier but also the reduction of source blur. The simulation is performed with the framework derived in Chapter 3, which is implemented in such a way that an arbitrary number of crystals with both positive or negative asymmetry geometry can be added one after the other.

Fig. 5.8 shows 1D simulations for three Gaussian-shaped pure phase objects with a maximum phase shift of π, placed 15 mm apart from each other (Fig. 5.8a). The simulation is performed for perfect coherence, an energy of 29 keV and the crystals used previously in this work ($\alpha = \pm 5.92°$), resulting in a demagnification factor of $M = 25.7$. With conventional PB-PCI, the contrast at 1 m propagation distance is very low (Fig. 5.8b, note the intensity values), while 1 m propagation behind the demagnifier results in strong contrast (Fig. 5.8c). With

conventional free space propagation, a distance of $25.7^2 \cdot 1\,\mathrm{m} = 660\,\mathrm{m}$ would be required to achieve comparable image contrast (Fig. 5.8d). In the demagnifier image, the shift-variance is noticeable in the different intensities of the interference patterns, which increase from right to left, according to the orientation of the crystal. Adding a Bragg magnifier at a distance of 1 m behind the demagnifier restores the shift-variance (Fig. 5.8e). The PCTF for Fig. 5.8b and e is shown in Fig. 5.8f. Conventional PB-PCI at 1 m generates almost no contrast (orange), in agreement with the simulation. In contrast, the PCTF of the demagnifier after 1 m reaches high values and corresponds to the PCTF for conventional PB-PCI at 660 m, overlaid by the crystal amplitude reflection curve (blue, black envelope). A further example for the same 1D object measured at even higher demagnification ($M = 71.3$) is given in Fig. A.5 (Appendix).

As a 2D example, the image intensity is simulated for the pure phase object depicted in Fig. 5.9a for conventional PB-PCI at physical propagation distances of $z = 36\,\mathrm{m}$ and $z = 660\,\mathrm{m}$ (Fig. 5.9b, d) and an energy of 30 keV, and using a Bragg demagnifier with a demagnification factor of $M = 25.7$ ($E = 29\,\mathrm{keV}$) and $M = 71.3$ ($E = 30.5\,\mathrm{keV}$) and physical propagation distances of $z_x = 0.8\,\mathrm{m}$, $z_y = 1\,\mathrm{m}$, corresponding to effective propagation distances of $z_{\mathrm{eff},x} = 530\,\mathrm{m}$, $z_{\mathrm{eff},y} = 660\,\mathrm{m}$ or $z_{\mathrm{eff},x} = 4\,\mathrm{km}$, $z_{\mathrm{eff},y} = 5\,\mathrm{km}$, respectively (Fig. 5.9c, e). The simulations account for source blur, with a source-to-sample distance of 86 m and a source size of 38 µm, as derived in Section 3.4.5 for the vertical source size of P23. This value was used here for both the horizontal and the vertical source size, thereby simulating an achievable contrast at P23 towards the perspective PETRA IV synchrotron radiation facility [201]. A simulation example for the current values at PETRA III is given in Fig. A.6, revealing the benefits of the reduced horizontal source size expected for PETRA IV. While conventional PB-PCI at 36 m yields only vanishingly low contrast (Fig. 5.8b), the demagnifier with an effective propagation distance of $z_{\mathrm{eff}} = 660\,\mathrm{m}$ significantly increases the contrast (Fig. 5.8c). For a hypothetical physical propagation distance of 660 m in conventional PB-PCI, the source blur strongly impairs the image quality and resolution (Fig. 5.8d), which is not the case for the demagnifier, since the source size is effectively reduced by a factor M. Further increasing the demagnification factor leads to even stronger image contrast (Fig. 5.8e). Conventional PB-PCI at 5 km would not yield any contrast at all due to source blur, and is therefore not shown here. The contrast enhancement obtained by the demagnifier is also evident in the line profiles shown in Fig. 5.8f. An appropriate measure for the increase in dose efficiency is the mean squared deviation of the image (see also Section 4.2.4). In comparison to the longest currently available physical propagation distance of 36 m at BM18 [17, 193, 194] at the above-mentioned parameters of P23 and for this example object, a loss in dose efficiency of 0.2 is extracted for conventional PB-PCI at 660 m (due to source blur), but a gain in dose efficiency of 94 and 358 for the Bragg demagnifier with $M = 25.7$ and 71.3, respectively. Compared to a physical propagation distance of 10 m (not shown in Fig. 5.9), as used, e.g., at ID17 at the ESRF [189, 202] and at the Imaging and Medical Beamline (IMBL) of the Australian Synchrotron [191], the extracted gain in dose efficiency is a factor of 2, 488, and 1909 for conventional PB-PCI at 660 m and the demagnifier with $M = 25.7$ and 71.3, respectively.

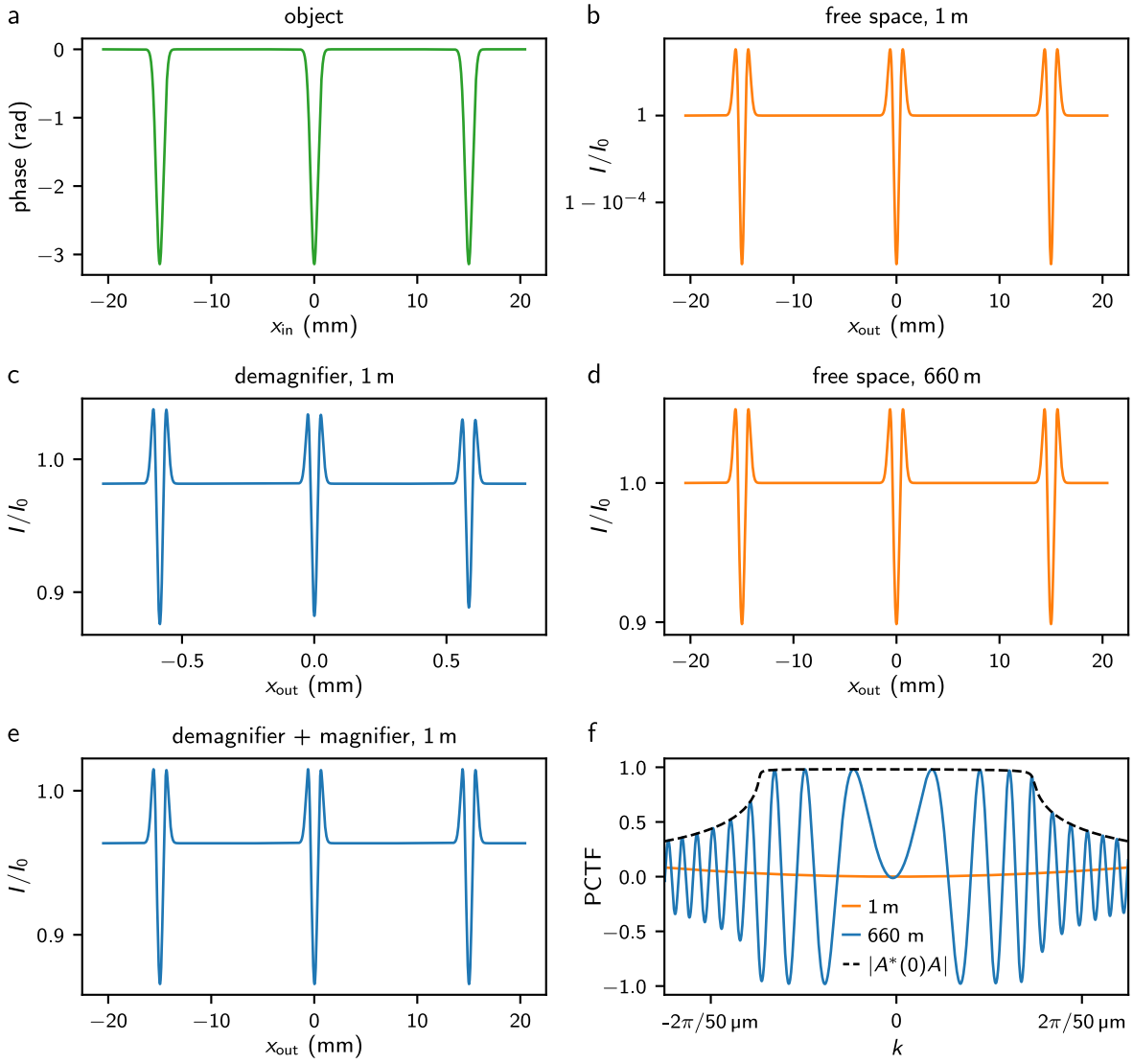

Figure 5.8.: Simulated image intensities for conventional PB-PCI and the Bragg demagnifier at 29 keV and $M = 25.7$. **a** Pure phase object consisting of three Gaussian-shaped peaks with a separation of 15 mm. **b** Image intensity after 1 m conventional free space propagation. **c** Image intensity at 1 m behind the demagnifier with $\alpha = -5.92°$. The image contrast is strongly increased (note the intensity scale). The average intensity is slightly reduced due to the finite reflectivity of the crystal. **d** To achieve a similar contrast in conventional PB-PCI, a propagation distance of 660 m would be required. **e** Re-magnifying the propagated wavefield behind the demagnifier with a Bragg magnifier with the same but positive asymmetry angle counteracts the shift-variance. In addition, the Bragg magnifier allows the resulting shift-invariant image to be acquired with a highly-efficient large-area detector. **f** PCTF at a physical distance of 1 m for conventional PB-PCI (orange) and for the demagnifier (blue, black envelope). Except for minor influences of the complex crystal reflection curve, the PCTF of the demagnifier corresponds to the free space PCTF at 660 m, multiplied by the envelope function. All simulations have been performed for perfect coherence.

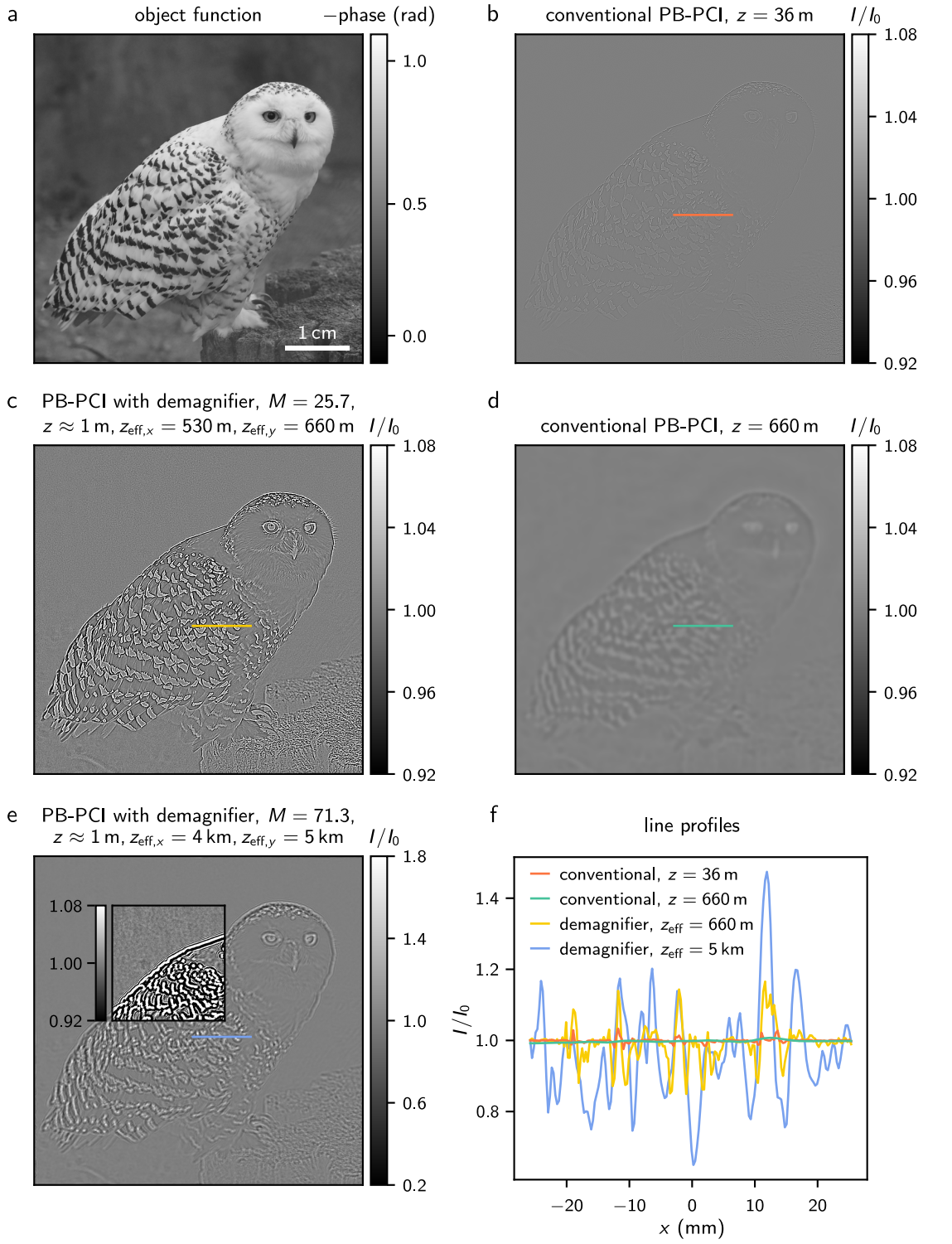

Figure 5.9.: Simulated 2D image intensities for conventional PB-PCI and the Bragg demagnifier. PB-PCI of the pure phase object shown in **a** for **b, d** conventional PB-PCI at 36 m and 660 m propagation distance, respectively, and **c, e** a Bragg demagnifier at 29 keV and 30.5 keV with physical propagation distances of $z_x = 0.8\,\mathrm{m}$, $z_y = 1\,\mathrm{m}$, corresponding to effective propagation distances of $z_{\mathrm{eff},x} = 530\,\mathrm{m}$, $z_{\mathrm{eff},y} = 660\,\mathrm{m}$ and $z_{\mathrm{eff},x} = 4\,\mathrm{km}$, $z_{\mathrm{eff},y} = 5\,\mathrm{km}$. The simulations take into account source blur (for details, see text). **f** Line profiles along the lines marked in **b-e**.

5.5. Proof-of-concept experiment - 0.6 km propagation distance

A 2D Bragg demagnifier was realized as a proof-of-concept experiment at the P23 beamline at PETRA III, DESY, Hamburg, Germany. The following sections describe the imaging properties of the demagnifier crystals, the setup, and the experimental results obtained at an operating energy of 29 keV.

5.5.1. Imaging properties

The imaging properties of the demagnifier are defined by the crystal material, the chosen reflex, the asymmetry angle, the size of the crystals, and the operating energy. Here, the same type of crystals was used as for the Bragg magnifier experiments presented in Chapter 3 and Chapter 4, i.e., an asymmetry angle of $\alpha = -5.92°$ and dimensions of 21 cm x 8 cm x 2 cm. Fig. 5.10 gives an overview of the crystals' imaging properties, and Tab. 5.1 lists the parameters for several energies. The demagnification factor M defines the gain factor M^2 in effective propagation distance (Fig. 5.10a). Theoretically, effective propagation distances of several kilometers can be reached. In practice, the setup requires a very high angular stability due to the extremely small angular acceptance of the demagnifier crystals ($\leq 2\,\mu$rad). The angular acceptance ω_{oc} decreases with increasing energy, which reduces the resolution (Fig. 5.10b). The input and output FOVs are set by the incident and outgoing angles β_{in} and β_{out} and the size of the crystals (Fig. 5.10c). The proof-of-concept experiment was performed at 29 keV. At this energy, the demagnification factor is $M = 25.7$, resulting in an increase of the propagation distance by $M^2 = 660$ and an effective pixel size of 37 µm in the indirect detector. The resolution limit at this energy is $\lambda_{\text{min}} = 68\,\mu$m.

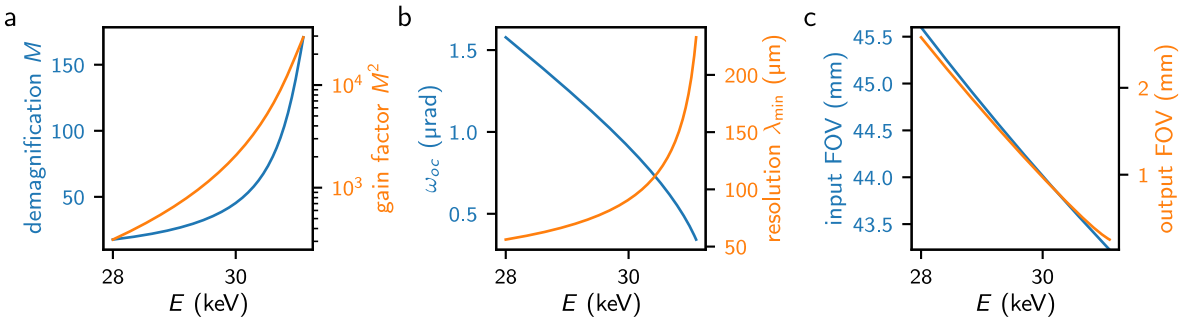

Figure 5.10.: Imaging properties of the Si (220) demagnifier used in the experiment. Energy-dependence of **a** the demagnification factor M and the resulting gain M^2 in effective propagation distance, **b** the angular acceptance given by the Darwin width ω_{oc} and the resulting resolution limit λ_{min}, and **c** the input and output FOV in front of and behind the demagnifier crystal, respectively.

E (keV)	input FOV (mm)	ω_{oc} (µrad)	$\lambda_{\min}$ (µm)	M	Gain factor M^2
27.0	46.5	1.9	48.7	13.4	178
28.0	45.6	1.6	56.1	17.7	312
29.0	44.8	1.3	67.8	25.7	659
30.0	44.0	0.9	91.0	45.4	2057
30.5	43.7	0.7	116.4	71.3	5090
31.0	43.3	0.4	190.4	144.7	20947

Table 5.1.: Imaging parameters for the Si (220) demagnifier used in the experiment (21 cm crystal length, $\alpha = -5.92°$). The input FOV, Darwin width ω_{oc}, intrinsic resolution limit $\lambda_{\min}$, demagnification factor M and gain factor M^2 are given for several energies E.

5.5.2. Experimental setup

The setup consists of two conditioner crystals that enlarge the beam in 2D in front of the sample, a sample stage, two demagnifier crystals and a high-resolution indirect detector system to detect the demagnified image after a certain physical propagation distance. A sketch of the crystal arrangement is depicted in Fig. 5.5a and a photograph of the experimental demonstrator setup at the P23 beamline is shown in Fig. 5.11. The same type of crystals was used for the conditioner as for the demagnifier. Each crystal was mounted on a high-precision hexapod, using the same type of hexapods as in Chapters 3 and 4. Due to the very small angular acceptance of the demagnifier crystals, the precision and stability of these hexapods would be too poor for routine use. Still, it was sufficient for being able to prove the working principle of the demagnifier. The hexapods were mounted on an item frame that was designed for the experiment (for a 3D CAD illustration, see Appendix A.8). Vertical demagnification was performed first because the smaller vertical source size allows for a longer propagation

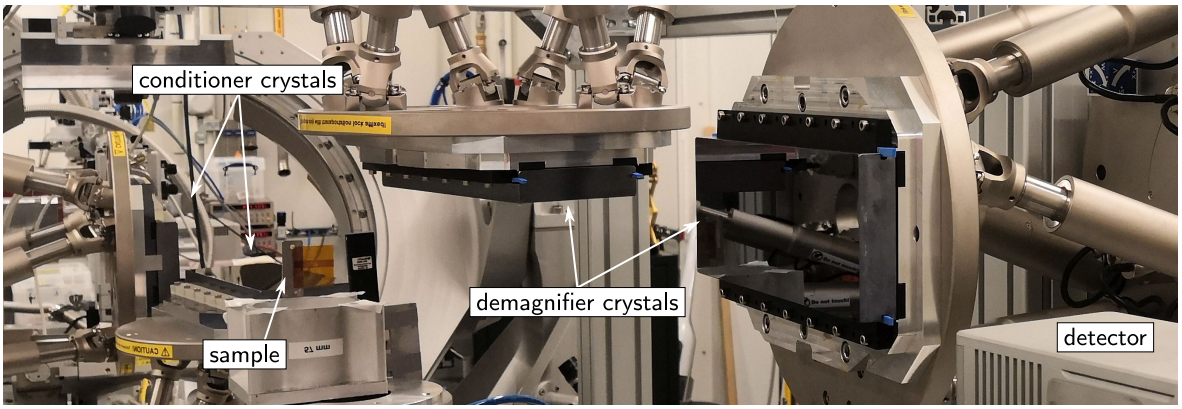

Figure 5.11.: Experimental setup for the proof-of-principle experiment. The synchrotron beam is magnified by two conditioner crystals, illuminates the centimeter-sized sample, and the wavefield behind the sample is demagnified by a second pair of crystals. The demagnified image is detected by a high-resolution indirect detector, placed at a certain distance from the demagnifier, here at 0.9 m from the first demagnifier crystal. The detector shown in the picture is a LAMBDA 250k detector (*X-Spectrum GmbH, 22547 Hamburg, Germany*), which was used for alignment.

distance before the onset of source blur. A single photon counting detector was used to align the crystals. The high-resolution detector (same model as employed in Chapter 4) was operated with a 5x objective (NA = 0.14, *model 378-802-6, Mitutoyo Deutschland GmbH, 41469 Neuss, Germany*), yielding a pixel size of 1.44 µm in the image plane and of 37 µm in the object plane, a 24 µm thick LSO scintillator and an exposure time of 67 ms. It was placed at a distance of $z_{2,y} = 0.9\,\mathrm{m}$ from the first demagnifier crystal and $z_{2,x} = 0.57\,\mathrm{m}$ from the second crystal. These distances result in effective propagation distances of $z_{\mathrm{eff},x} \approx 380\,\mathrm{m}$ and $z_{\mathrm{eff},y} \approx 600\,\mathrm{m}$. For a comparison with conventional free space propagation at the same physical distance, images were additionally acquired without the demagnifier and using a large-area detector of similar pixel size (49.5 µm, Shad-o-Box 1k HS, *Teledyne DALSA, Waterloo, Canada*), placed at 1 m from the sample. To prevent saturation of the camera at 67 ms exposure time, the beam was attenuated by a factor of 500 and the images were averaged over 20 acquisitions. The tiger salamander (*Ambystoma tigrinum*) used in the experiment is a museum specimen that was loaned for the experiment. The mouse liver was obtained from The Jackson Laboratory, USA. Both specimens were fixed in paraformaldehyde solution and subsequently stored in 70 % ethanol.

5.5.3. Experimental results and discussion

Increase in image contrast

Example images of several objects were acquired and are displayed in Fig. 5.12 (after flat- and darkfield correction), namely a blackberry leaf, a mouse liver lobe in a plastic bag filled with ethanol, and a salamander in a tube with ethanol. The left column shows images obtained with conventional PB-PCI, the right column presents the demagnifier images. With conventional PB-PCI, the blackberry leaf exhibits only very weak contrast caused by absorption in the sample, as shown in the inset (note the large difference in the intensity scale), while the leaf veins become well visible with the demagnifier (Fig. 5.12a). The mouse liver is not discernible at all in the conventional image. In contrast, the demagnifier brings to light a net of blood vessels (Fig. 5.12b). Also, a piece of tape becomes visible on the left of the liver, whereas in the conventional PB-PCI image, there is no contrast. A similar increase in contrast is observed for the salamander: in the conventional PB-PCI image, only the bones are weakly visible, while the demagnifier reveals internal structures (Fig. 5.12c). The experiment thus confirms that the demagnifier allows for significantly improved image contrast.

The stripes that appear mainly in the liver and salamander images can be attributed to crystal polishing artifacts in combination with drifts in the flatfield, which are related to the limited mechanical stability of the demonstrator setup compared to the very small angular acceptance of the demagnifier crystals ($\lesssim 1\,\mu\mathrm{rad}$). A dedicated setup for routine applications, such as recording tomograms, would require an appropriate mechanical stability.

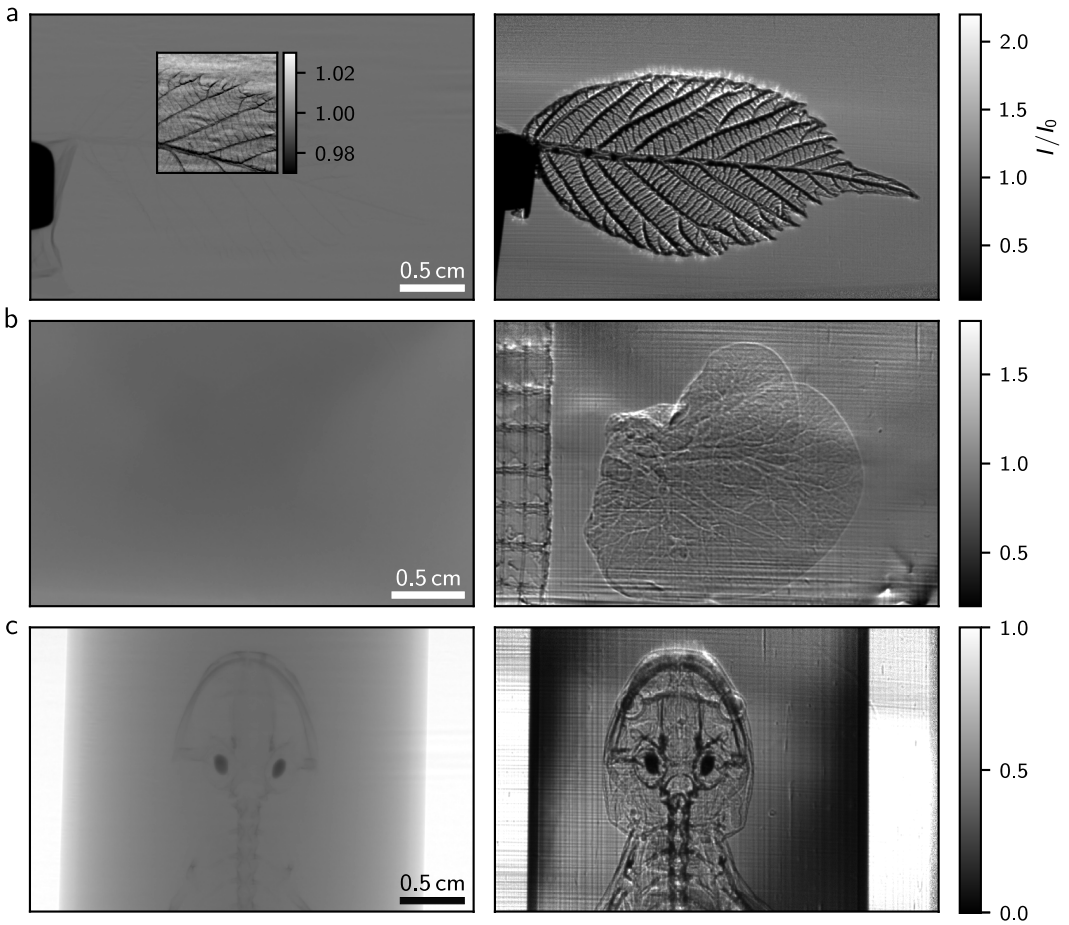

Figure 5.12.: Comparison of phase contrast imaging using conventional free space propagation (left) and the Bragg demagnifier (right). In both setups, the incident X-ray beam was expanded in front of the sample using a Bragg conditioner [10] to obtain a sufficiently large illuminated area, and the physical propagation distance was $\sim 1\,\mathrm{m}$. **a** Blackberry leaf in air. With conventional PB-PCI, only weak absorption contrast of $\sim 2\,\%$ can be seen at these energies, as shown in the inset with adjusted gray scale. The demagnifier provides strong propagation-based phase contrast. **b** Mouse liver lobe in ethanol. Conventional PB-PCI shows no contrast, while the demagnifier reveals a net of blood vessels. The tape left to the sample also becomes visible. **c** Salamander in ethanol. The demagnifier provides strong image contrast and allows visualization of soft tissues, while conventional PB-PCI yields only little absorption and no phase contrast. The colorbar indicates the intensity values of the flat- and darkfield-corrected images. Reproduced from Ref. [195].

Contrast contributions

The images taken with the Bragg demagnifier certainly show patterns that are brighter than the background intensity, indicating constructive interference generated by PB-PCI. However, at the edges of the crystals, where the background intensity is reduced, other bright patterns are also observed after flatfield correction, e.g., at the upper edge of the leaf and at the mouth of the salamander. These artifacts arise most likely due to the curvature of the incident wavefield, which, at the crystal edges, deviates from the center of the crystal reflectivity curve, generating diffraction-enhanced contrast [11]. In addition, the presented images partially contain extinction contrast, as known from analyzer-based imaging [203], which occurs when X-rays are scattered to angles higher than the crystal's angular acceptance and are therefore not transmitted into the image. For example, the dark spots in the salamander, presumably in the otic region, can be attributed not only to absorption but also to extinction contrast, since their intensity is reduced by the demagnifier. Extinction contrast can also be observed in the bones. Note that although the angular acceptance of the demagnifier crystals is small and therefore sensitive to extinction contrast, there is no average intensity decrease in the soft tissue regions of the specimens. This implies that valuable information is encoded in low spatial frequencies within the angular acceptance, which is now made visible by the Bragg demagnifier through the enhanced PB-PCI.

Thon rings as confirmation for the presence of interference

To prove the presence of interference resulting from the increased effective propagation distance, a plastic spoon with a rough surface was imaged, which acts as a weak phase noise object. The image formation can thus be described by the PCTF given by Eq. 5.10. The PCTF for the experimental settings is plotted in Fig. 5.13a, b for the horizontal and vertical directions, respectively. It is close to zero for conventional PB-PCI (orange), while it exhibits high values for the Bragg demagnifier (blue). The latter corresponds to conventional free space propagation with a very long distance of $z_{\mathrm{eff},x} = 380\,\mathrm{m}$ and $z_{\mathrm{eff},y} = 600\,\mathrm{m}$, superimposed by the field amplitude reflection of the crystals (black). In the Fourier spectrum of the plastic spoon, Thon rings become visible, see Fig. 5.13c, d. They correspond to spatial frequencies at which the PCTF is close to zero and are additional evidence for the presence of interference effects (see also Section 2.2.6). From the position of the Thon rings, the defocus and astigmatism can be extracted [204], as commonly done in electron microscopy [74, 205]. Here, propagation distances of $z_{\mathrm{eff},x} \approx 380\,\mathrm{m}$ and $z_{\mathrm{eff},y} \approx 600\,\mathrm{m}$ were extracted, in accordance with the experimental settings.

Source blur

Next, the effect of source blur on the image degradation is considered. As discussed in Section 5.3, the source blur in the demagnified image propagated to the physical distance z (and the effective distance $z_{\mathrm{eff}} = M^2 z$) is expected to be a factor of M better than the source

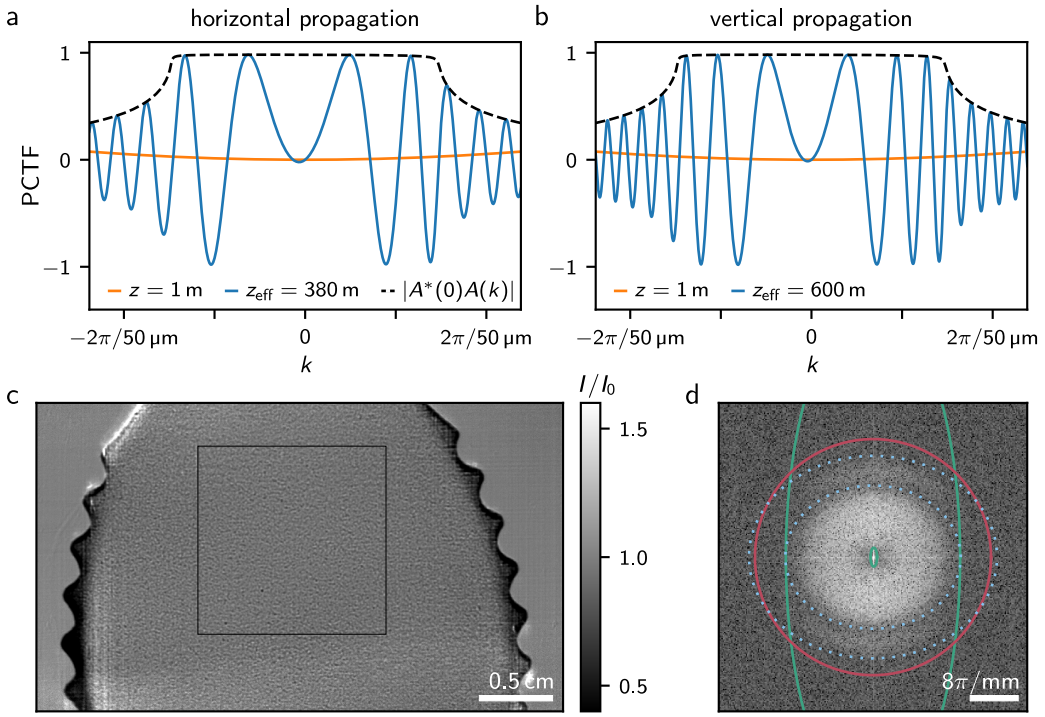

Figure 5.13.: PCTF with Bragg demagnifier. **a, b** PCTF of weak phase objects at moderate resolution for conventional PB-PCI (orange) and using the Bragg demagnifier (blue, black envelope) for the settings used in the experiment, i.e., $z_{2,x} = 0.57\,\mathrm{m}$, $z_{2,y} = 0.90\,\mathrm{m}$, $E = 29\,\mathrm{keV}$ and $M = 25.7$, resulting in effective propagation distances of $z_{\mathrm{eff},x} \approx 380\,\mathrm{m}$ and $z_{\mathrm{eff},y} \approx 600\,\mathrm{m}$ in horizontal and vertical direction, respectively. **c** Plastic spoon imaged with the Bragg demagnifier and **d** Fourier spectrum of the area marked in b, plotted as $\log(|\tilde{I}(\boldsymbol{k})|)$. The rough surface of the spoon acts as a weak phase noise object. The elliptic Thon rings originate from the roots of the PCTF with $z_{\mathrm{eff},x} \approx 380\,\mathrm{m}$ and $z_{\mathrm{eff},y} \approx 600\,\mathrm{m}$. The first two zero-crossings are indicated in blue. The contrast degradation to $1/e$ at $z_x = 0.57\,\mathrm{m}$ and $z_y = 0.90\,\mathrm{m}$ due to the finite source size is shown by the outer green line. The expected contrast degradation at a hypothetical physical propagation distance of $z_i = z_{\mathrm{eff},i}$ is indicated by the inner green line. The red circle shows the $1/e$ contrast degradation by the optical microscope. Reproduced from Ref. [195].

blur of the large image at a hypothetical physical propagation distance of $M^2 z$. This effect is demonstrated in Fig. 5.13d: In Section 3.4.5, source sizes of $s_{\mathrm{h}} = 164\,\mu\mathrm{m}$ and $s_{\mathrm{v}} = 38\,\mu\mathrm{m}$ have been extracted for the P23 beamline. The resulting contrast degradation to $1/e$ at the physical propagation distance of $z_x = 0.57\,\mathrm{m}$ and $z_y = 0.90\,\mathrm{m}$ is depicted by the outer green line (Eq. 2.68). A hypothetical physical propagation distance of $z_{\mathrm{eff},i}$ without demagnifier would suppress most of the image information, as shown by the inner green line. As predicted, signal is present in the Fourier spectrum up to the outer green line in horizontal direction. In vertical direction, the source blur is also strongly increased compared to the inner green line. However, the signal does not reach out to the outer green line. This degradation results from the limited optical transfer function (OTF) of the indirect system. The $1/e$ degradation by the OTF is indicated by a red line (Eq. 2.93). Adding a Bragg magnifier and a large-area detector behind the demagnifier would improve the OTF and the detection efficiency and presumably reveal even more Thon rings.

5.6. Prospects of Bragg demagnifiers

As demonstrated above, the proposed technique enables a strong increase of propagation-based phase contrast for low spatial frequencies by drastically increasing the effective propagation distance. Achieving high phase contrast at low spatial frequencies is crucial for imaging large specimens at moderate or low resolutions of tens to hundreds of micrometers. In addition, the source blur is reduced compared to a hypothetical image at the same physical propagation distance. The achieved image contrast would otherwise only be accessible by unrealistically long synchrotron beamlines and propagation distances of hundreds of meters up to kilometers. In combination with an additional Bragg magnifier, the method therefore promises highest dose efficiency for large soft tissue samples. Another advantage of a demagnifier is the vanishing absorption of X-rays in air along the short physical distance. The transmission of X-rays through 600 m or 5 km of air at 30 keV would be $I/I_0 = 0.2\,\%$ or $0.02\,\%$, respectively. A transmission of $95\,\%$ would require a vacuum of 2 mbar or 0.2 mbar along the flight tube.

A future dedicated setup should address several technical aspects, which were encountered in the course of the experiment with the presented demonstrator setup. Due to the very small Darwin width of the crystals ($< 2\,\mu$rad), a high angular mechanical stability and precision is required. With an accordingly high mechanical stability in the 0.1 µrad range, in principle even higher demagnifications of up to about $M = 150$ would be achievable, which would allow for even longer effective propagation distances of up to $z_{\text{eff}} \approx 20\,\text{km}$ (see also Tab. 5.1). In addition, the horizontal and vertical stripes observed in the images of the proof-of-concept experiment, which are presumably caused by the surface of the crystals, have to be counteracted, e.g., by better polishing or more sophisticated flatfield correction. Moreover, although the size of the current crystals would allow for a FOV of 4.5 cm x 4.5 cm, the actual FOV is currently limited to $\sim 2\,$cm vertically and $\sim 4\,$cm horizontally, presumably due to dispersion and a curvature of the wavefield at the edges of the crystals. These effects may be minimized by using the same crystal material and reflex for the monochromator, and by collimating the X-ray beam in front of the Bragg conditioner, e.g., with compound refractive lenses [206] or Kirkpatrick-Baez mirrors [207]. Then, the crystals can be replaced with larger ones to further increase the FOV. Furthermore, the Bragg demagnifier may be designed for even higher energies in order to reduce extinction contrast and to increase the possible sample thickness. In this way, the method may render useful for single-shot *in vivo* imaging of large biological samples or low-dose medical diagnostics, e.g., for the early detection of breast cancer or other diseases, especially in combination with currently emerging compact X-ray sources [196–198].

6. Conclusion and outlook

The aim of the present work was to push the limits of dose-efficient X-ray imaging of soft materials and tissues both at high, micrometer resolution and at moderate resolutions of tens to hundreds of micrometers. The imaging process can be divided into three main steps: First, the sample information is conveyed to the incident X-ray wavefield. Second, the information encoded in the wavefield is made accessible by generating detectable image contrast. Third, the provided information is extracted during image detection. This thesis addressed the optimization of each of these steps with respect to the dose deposited in the sample in order to achieve highest dose efficiency.

As a general approach for the generation of information (step 1), the phase shifting properties of the sample can be exploited, since they are typically several orders of magnitude stronger than attenuation and therefore have a high potential for reducing the dose. For the provisioning of the sample information (step 2), phase contrast methods convert the phase information encoded in the wavefield into measurable intensity contrast. With the advent of high-brilliance third-generation synchrotron radiation sources, propagation-based phase contrast imaging (PB-PCI) has become a widely used and effective technique, and was the method of choice here due to its simplicity, robustness, and the fact that it allows acquisition of single-shot images. In PB-PCI, the contrast is generated by self-interference of the propagating wavefield behind the sample, which increasingly evolves into intensity contrast as the propagation distance increases. To extract the provided information (step 3), a detector system that offers the desired spatial resolution is employed.

In this work, these three main aspects were optimized in view of the dose deposition in the sample. Since the contrast formation in PB-PCI and its detection depend strongly on the spatial frequency, the task was divided into two resolution regimes, namely high, micrometer resolution, and moderate resolutions of tens to hundreds of micrometers. These two regimes come along with distinct challenges. On the one hand, while for high resolution, i.e., large spatial frequencies, propagation-based phase contrast is readily generatable (step 2), conventional high-resolution indirect detector systems have a limited detection efficiency (step 3). On the other hand, for PB-PCI of large, centimeter-sized samples at moderate resolution, i.e., low spatial frequencies, propagation distances between the sample and the detector of ideally several hundreds to thousands of meters would be required to achieve sufficient image contrast (step 2).

The first step was tackled by simultaneously considering the energy dependence of the deposited dose and of the phase shift generated by the sample. To overcome the above-mentioned challenges (steps 2 and 3), the suitability of Bragg crystal optics was considered for both resolution regimes. They were found to be well suited to address the different challenges of both resolution regimes. For high resolution, the propagated wavefield behind the sample was magnified by a Bragg magnifier and detected by a highly-efficient single photon counting detector (SPCD), thereby maintaining micrometer resolution and achieving high detection efficiency. For moderate resolution, a new method has been introduced to allow long effective propagation distances up to kilometers, thereby generating high image contrast within a meter-scale setup. This method is based on magnifying the spatial frequency distribution of the diffracted wavefield behind the sample by image demagnification using a Bragg magnifier with reversed optical path, i.e., a Bragg demagnifier.

Experimental investigations and demonstrations of the increased dose efficiency were performed for both resolution regimes. For the experiments, the high coherence of the P23 beamline at PETRA III in Hamburg was exploited, and preparatory beamtime was carried out at the IMAGE beamline of the KIT Light Source in Karlsruhe. The experiments could demonstrate the increased dose efficiency, which opens new opportunities for studies of dose-sensitive materials and biological samples up to *in vivo* imaging and medical diagnostics.

6.1. Dose-efficient high-resolution imaging using a Bragg magnifier

In the pursuit of dose-efficient imaging of small, millimeter-sized samples at high, micrometer resolution, X-ray imaging close to the highest possible dose efficiency for PB-PCI was realized by optimizing the operating energy, the detection efficiency, and the optical transfer function (OTF) of the detector system. The energy that allows for the highest signal-to-noise ratio (SNR) per dose was determined to be 30 keV for a millimeter-sized soft tissue sample. For thicker samples, the ideal energy increases slightly. The low detection efficiency of high-resolution scintillator-based indirect systems at these energies can be overcome by direct magnification of the propagated wavefield behind the sample. This allows the detection of the magnified image by an SPCD with a detection efficiency of nearly 100 % while maintaining high, micrometer resolution despite the rather large pixel sizes of SPCDs. Coherent magnification of the X-ray wavefield was realized by a Bragg magnifier. In addition to the high detection efficiency, the combination of a Bragg magnifier and an SPCD provides a constantly high OTF over all spatial frequencies up to the micrometer resolution limit. In contrast, the OTF of the objective in indirect systems decreases significantly with increasing spatial frequencies. In sum, since the crystals' reflectivity is nominally above 90 %, the Bragg magnifier (BM) system allows operation close to the highest possible dose efficiency for PB-PCI.

After a theoretical description of the image formation process in a Bragg magnifier, a BM system was designed according to the considerations of dose efficiency optimization. The sys-

tem consisted of two asymmetrically cut crystals with an operating energy around 30 keV and a highly-efficient GaAs SPCD. An experimental characterization of the developed BM system showed micrometer resolution, the expected magnification factors, and a good agreement between image simulations and experiment.

An experimental comparison of the developed BM system with a conventional high-resolution indirect detector system at the same energy revealed a spatial frequency dependent gain in dose efficiency, which reached more than two orders of magnitude at the decisive spatial frequencies close to the resolution limit. Considering the fact that the crystal reflectivity of over 90 % was confirmed experimentally, and that the measured SNR of the BM system was close to the simulated input SNR, it could be concluded that the BM system operates close to the highest possible dose efficiency.

The high dose efficiency of the BM system expands the horizons of imaging biological and other dose-sensitive samples, creating opportunities for substantially increasing observation times in *in vivo* and *in situ* imaging. As a pilot application, the developed system was applied to an *in vivo* behavioral study of parasitoids wasps with prolonged observation times, revealing their behavior before and during emergence from their host eggs.

As demonstrated by the pilot study, the BM system in its current implementation can readily be employed for dose-efficient investigations of biological samples or soft materials. Yet, an optimized setup may enable an even higher mechanical stability and a larger field of view (FOV) to further increase the reliability and application range of the method. To increase the FOV, both the size of the crystals and the active area of the SPCD would have to be increased. Furthermore, it may be necessary to collimate the incident beam, e.g., using compound refractive lenses [206] or Kirkpatrick-Baez mirrors [207] in order to counteract the curvature of the wavefield at the crystal edges, which results from the finite distance between the source and the BM crystals and causes improper illumination at the crystal edges, especially for accordingly large crystals. Finally, the steps performed during crystal alignment could be automated to simplify the user experience. In this way, high-resolution PB-PCI with highest dose efficiency can become routine in the biological and materials science communities.

6.2. Bragg demagnifier for dose-efficient imaging of large samples at moderate resolution

Although the above approach significantly improves dose efficiency in high-resolution X-ray imaging, high doses are still required due to the high resolution. Imaging at low resolution requires less dose per se, since the dose for a desired SNR scales with the square of the resolution. Keeping the dose to a minimum is especially important for medical diagnostics. Small animal *in vivo* imaging would likewise benefit from a reduced dose at the expense of

lower resolution. However, the generation of propagation-based phase contrast for low spatial frequencies would require unrealistically long propagation distances between the sample and the detector of hundreds to thousands of meters. The second part of this work was therefore devoted to enhancing image contrast in PB-PCI for low spatial frequencies.

For this purpose, a new technique was proposed to generate propagation-based phase contrast within a meter-scale setup. By magnifying the spatial frequency distribution behind the sample, the effective propagation distance is increased by a factor of M^2. In this way, strong image contrast is obtained within a short physical propagation distance. Simultaneously, the source blur is reduced by a factor of M, making imaging at such long effective propagation distances usable in the first place.

The magnification in reciprocal space is tantamount to a demagnification in real space, which was realized here by a Bragg demagnifier. The image formation with the Bragg demagnifier was treated theoretically in analogy to the formalism described previously for the Bragg magnifier. By re-magnifying the propagated wavefield behind the demagnifier with a Bragg magnifier of the same crystal type, the propagated wavefield can be detected in a dose-efficient manner. Moreover, shift-variance effects can be counteracted, as was shown theoretically and by image simulations. A Bragg conditioner in front of the sample allows a large illuminated area at the sample position although synchrotron beams typically have diameters of only a few millimeters. In addition, it was shown that the conditioner reduces the monochromatic divergence, which can, however, only be exploited in combination with a demagnifier, since the latter inverts the energy-dependent shift of the Bragg angle. Image simulations including source blur could show an increase in dose efficiency of two orders of magnitude compared to the currently longest available beamline BM18 at the ESRF with a physical propagation distance of 36 m.

The working principle of the proposed method was demonstrated by a proof-of-concept experiment. The previously developed Bragg magnifier was used as a Bragg conditioner in front of the sample, and the setup was extended by two additional crystals of the same type, but in the opposite direction, serving as demagnifier crystals. After free space propagation of the demagnified wavefield, the image was recorded with a high-resolution indirect detector system. The strong increase in image contrast achieved with the demagnifier was demonstrated on several biological samples. In addition, the expected improvement in source blur was observed.

Since the crystals act as a frequency filter, also two other types of contrast can appear in the images. First, strongly scattering components in the sample are not reflected by the crystals due to their limited angular acceptance, resulting in extinction contrast. Second, if the incident beam is not centered to the crystal reflection curve, diffraction-enhanced contrast forms. Future research should address the suppression or exploitation of these other two types of contrast.

In conclusion, the Bragg demagnifier appears to be a valuable candidate for dose-efficient X-ray imaging of large samples at moderate resolution. The proposed technique paves the way for low-dose studies of large, centimeter-sized radiation-sensitive samples, especially in the context of small animal *in vivo* and biomedical soft tissue imaging.

A future dedicated setup should address several aspects in order to facilitate routine usage. The crystal mechanics require an angular stability and precision $\lesssim 0.1\,\mu\text{rad}$ due to the small angular acceptance of the crystals, which is a factor M smaller than the corresponding magnifier crystals. As for the Bragg magnifier, larger crystals will further increase the FOV. Efforts should also be placed on achieving an even higher quality of the crystal surfaces. Besides, an in-line conditioner in front of the sample will facilitate horizontal sample movement. From a scientific perspective, the imaging performance may be characterized in more detail, especially with respect to the occurrence of extinction contrast and in comparison with other phase contrast techniques for moderate resolution, e.g., grating- and speckle-based imaging [8, 9, 12–14, 208]. The formation of extinction and diffraction-enhanced contrast may be reduced by using even higher energies and by employing a collimator to reduce the curvature of the incident beam, respectively. In parallel with instrumental advances, PB-PCI reconstruction techniques need to be adapted to the rather large phase shifts of large samples [76, 87].

In the future, highest dose efficiency can be achieved by detecting the demagnified wavefield after propagation with a BM system as developed in the first part of the thesis. The high coherence of currently emerging fourth-generation synchrotrons will facilitate even longer effective propagation distances. Ultimately, combining the technique with compact X-ray sources of sufficient coherence may further extend its application area up to low-dose medical diagnostics, e.g., for the early detection of breast cancer or other diseases.

A. Appendix

A.1. Explicit form of the dispersion curve

For a graphical understanding of the dispersion equation (Eq. 2.29), its intersection with the scattering plane is plotted in Fig. 2.2 for coplanar geometry. The procedure is shortly outlined here. The aim is to express the coordinate K_y from Eq. 2.29 as a function of the coordinate K_x. Without loss of generality, the coordinate system is chosen in such a way that the scattering plane lies in the z-plane. Also, the reciprocal lattice vector $\boldsymbol{h}$ is parallel to the x-axis, i.e., $\boldsymbol{h} = (h, 0, 0)^T$, the reciprocal lattice point O is at $-h/2$ and the reciprocal lattice point H is at $+h/2$, see Fig. A.1. With $K_{\boldsymbol{o}x} = K_x - h/2$, $K_{\boldsymbol{o}y} = K_y$ and using $\boldsymbol{K}_H = \boldsymbol{K}_{\boldsymbol{o}} + \boldsymbol{h}$, the dispersion equation

$$\left[\left(K_x - \frac{h}{2}\right)^2 + K_y^2 - K^2\right] \cdot \left[\left(K_x + \frac{h}{2}\right)^2 + K_y^2 - K^2\right] - k_0^4 C^2 \chi_{\boldsymbol{h}} \chi_{\bar{\boldsymbol{h}}} = 0 \tag{A.1}$$

is solved for K_y, resulting in

$$K_y^2 = K^2 - K_x^2 - \frac{h^2}{4} \pm \sqrt{K_x^2 h^2 + k_0^4 C^2 \chi_{\boldsymbol{h}} \chi_{\bar{\boldsymbol{h}}}}. \tag{A.2}$$

Plotting only the real-valued results for K_y over K_x gives the shape of the dispersion curve.

Typical values for $\chi_{\boldsymbol{h}}$ are in the order of 10^{-4} to 10^{-6} [45]. Since the interaction term is so small, the gap in the dispersion surface would hardly be visible when plotting the curve for the physical values. To generate the schematic curves shown in Fig. 2.2, the following parameters have been used: $k_0 = 1$, $h = 1$, $n = 0.8$ so that $K = k_0 n = 0.8$, and the factor $C^2 \chi_{\boldsymbol{h}} \chi_{\bar{\boldsymbol{h}}}$ was set to 0.01 for σ-polarization and 0.005 for π-polarization.

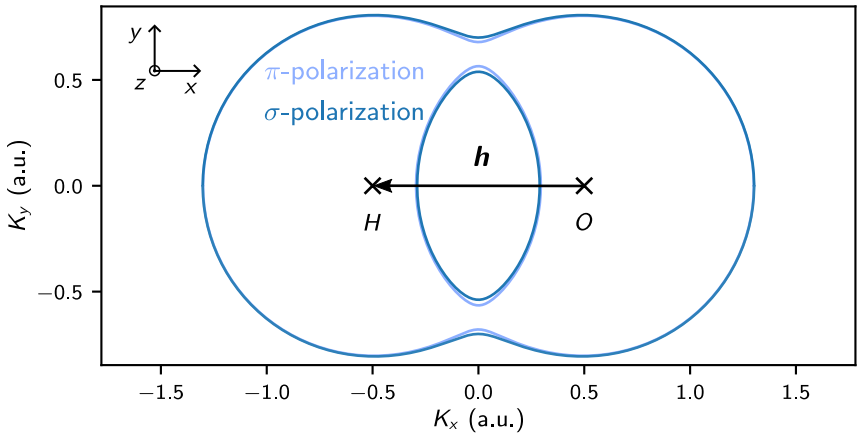

Figure A.1.: Dispersion surface. Definition of the coordinate system used to plot the schematic of the dispersion surface in Fig. 2.2. For details, see text.

A.2. Source blur

As described in Section 2.2.5, an extended X-ray source leads to a blurring of the final image intensity. The aim here is to derive Eq. 2.68, which describes the image intensity obtained when an object is illuminated by an extended X-ray source. For simplicity, only the 1D case is considered here. Furthermore, shift-invariance is assumed. First, the wavefunction in the sample exit plane with oblique plane wave illumination $\hat{k}$ propagated to z is given by

$$\begin{aligned}\psi_{z,\hat{k}}(x) &= \frac{1}{2\pi}\int \tilde{\psi}_{0,\hat{k}}(k)e^{ikx}e^{i\sqrt{k_0^2-k^2}z}\mathrm{d}k \\ &= \frac{1}{2\pi}\int \tilde{f}(k-\hat{k})e^{ikx}e^{i\sqrt{k_0^2-k^2}z}\mathrm{d}k \\ &= \frac{1}{2\pi}\int \tilde{f}(k)e^{i(\hat{k}+k)x}e^{i\sqrt{k_0^2-(k+\hat{k})^2}z}\mathrm{d}k. \end{aligned} \tag{A.3}$$

Here, it was used that $\tilde{\psi}_{0,\hat{k}}(k) = \tilde{f}(k-\hat{k})$, see also Eq. 2.64. The image intensity reads

$$\begin{aligned} I_{z,\hat{k}}(x)/I_0 &= |\psi_{z,\hat{k}}(x)|^2 \\ &= \frac{1}{(2\pi)^2}\iint \tilde{f}(k)[\tilde{f}(k')]^* e^{i(k+\hat{k})x}e^{-i(k'+\hat{k})x}e^{i\sqrt{k_0^2-(k+\hat{k})^2}z}e^{-i\sqrt{k_0^2-(k'+\hat{k})^2}z}\mathrm{d}k\mathrm{d}k' \\ &\overset{\text{Fresnel}}{\approx} \frac{1}{(2\pi)^2}\iint \tilde{f}(k)[\tilde{f}(k')]^* e^{i(k-k')x}e^{-i\frac{k^2-k'^2}{2k_0}z}e^{i\frac{(k'-k)\hat{k}}{k_0}z}\mathrm{d}k\mathrm{d}k'. \end{aligned} \tag{A.4}$$

For plane waves illuminating the sample incoherently from different directions $\hat{k}$, the total image intensity is given by a superposition of the intensities $I_{z,\hat{k}}(x)$, weighted by the source function. For a Gaussian amplitude distribution $S(\hat{k}) = \frac{1}{\sqrt{2\pi\sigma^2}}e^{-\frac{\hat{k}^2}{2\sigma^2}}$, the total intensity

becomes

$$\begin{aligned} I_z(x)/I_0 &= \frac{1}{\sqrt{2\pi\sigma^2}} \int e^{-\frac{\hat{k}^2}{2\sigma^2}} I_{z,\hat{k}}(x)/I_0 \cdot \mathrm{d}\hat{k} \\ &= \frac{1}{(2\pi)^2} \frac{1}{\sqrt{2\pi\sigma^2}} \iiint e^{-\frac{\hat{k}^2}{2\sigma^2}} e^{i\frac{(k'-k)\hat{k}}{k_0}z} \tilde{f}(k)[\tilde{f}(k')]^* e^{i(k-k')x} e^{-i\frac{k^2-k'^2}{2k_0}z} \mathrm{d}k\mathrm{d}k'\mathrm{d}\hat{k} \\ &= \frac{1}{(2\pi)^2} \iint e^{-\frac{\sigma^2}{2}\left(\frac{(k'-k)z}{k_0}\right)^2} \tilde{f}(k)[\tilde{f}(k')]^* e^{i(k-k')x} e^{-i\frac{k^2-k'^2}{2k_0}z} \mathrm{d}k\mathrm{d}k', \end{aligned} \tag{A.5}$$

where the integral over $\hat{k}$ was computed in the last step. In Fourier space, it holds for the intensity

$$\begin{aligned} \tilde{I}_z(k'')/I_0 &= \int I_z(x)/I_0 \cdot e^{-ik''x}\mathrm{d}x \\ &= \frac{1}{(2\pi)^2} \iint e^{-\frac{\sigma^2}{2}\left(\frac{(k'-k)z}{k_0}\right)^2} \tilde{f}(k)[\tilde{f}(k')]^* \underbrace{\int e^{i(k-k'-k'')x}\mathrm{d}x}_{=2\pi\delta(k-k'-k'')} e^{-i\frac{k^2-k'^2}{2k_0}z} \mathrm{d}k\mathrm{d}k' \\ &= \frac{1}{2\pi} e^{-\frac{\sigma^2}{2}\frac{k''^2 z^2}{k_0^2}} \int \underbrace{\tilde{f}(k)e^{-i\frac{k^2}{2k_0}z}}_{=\tilde{\psi}_z(k)} \underbrace{[\tilde{f}(k-k'')]^* e^{i\frac{(k-k'')^2}{2k_0}z}}_{=[\tilde{\psi}_z(k-k'')]^*} \mathrm{d}k \\ &= e^{-\frac{\sigma^2}{2}\frac{k''^2 z^2}{k_0^2}} \cdot \tilde{I}_z^{\mathrm{coh}}(k'')/I_0. \end{aligned} \tag{A.6}$$

In the last step, the intensity $\tilde{I}_z^{\mathrm{coh}}(k'')$ for coherent non-oblique illumination was identified. Thus, incoherent illumination with a Gaussian angular distribution yields a Gaussian envelope function in Fourier space with variance $k_0^2/(\sigma z)^2$, meaning that high spatial frequencies are increasingly suppressed with z. In real space, Eq. A.6 is a convolution between the image intensity $I_z^{\mathrm{coh}}(x)$ for perfect coherence and a Gaussian point spread function, see also Eq. 2.67.

A.3. Derivation of CTF and mean-field CTF by Guigay's approach

The contrast transfer function (CTF) for propagation-based phase contrast imaging gives a linear dependence in Fourier space between the image intensity and the object's phase and absorption, assuming the object is weak and composed of a single material ($\phi/a = -\delta/\beta$). In Section 2.2.6, the phase contrast transfer function (PCTF) was derived by calculating the propagated image intensity $I_z(\boldsymbol{r})$, keeping only first order terms in ϕ [67–70]. J. Guigay et al. [66] proposed another approach, which yields the same expression for the CTF and is outlined here. The mean-field CTF introduced in Section 2.2.10 can also be derived in analogy to Guigay's approach, which is shown here as well. For better readability, only the 1D case is written out, but the considerations are equally valid in 2D.

The normalized Fresnel-propagated image intensity $I_z(x)/I_0 = \psi_z(x) \cdot \psi_z^*(x)$ can be expressed in Fourier space by

$$\begin{aligned}
\tilde{I}_z(k)/I_0 &= \frac{1}{2\pi} \int \tilde{\psi}_z(k') \cdot [\tilde{\psi}_z(k'-k)]^* \mathrm{d}k' \\
&= \frac{1}{2\pi} \iint \psi_0(x) e^{-\mathrm{i}k'x} \mathrm{d}x \cdot e^{-\mathrm{i}\frac{z}{2k_0}k'^2} \int \psi_0^*(x') e^{\mathrm{i}(k'-k)x'} \mathrm{d}x' \cdot e^{\mathrm{i}\frac{z}{2k_0}(k'-k)^2} \mathrm{d}k' \\
&= \frac{1}{2\pi} \iint \psi_0(x) \psi_0^*(x') e^{-\mathrm{i}kx'} e^{\mathrm{i}\frac{z}{2k_0}k^2} \underbrace{\int e^{-\mathrm{i}k'(x-x'+\frac{z}{2k_0}2k)} \mathrm{d}k'}_{=2\pi\delta(x-x'+\frac{z}{2k_0}2k)} \mathrm{d}x\mathrm{d}x' \\
&= \int \psi_0(x) \psi_0^*(x + \frac{z}{2k_0}2k) e^{-\mathrm{i}kx} e^{-\mathrm{i}\frac{z}{2k_0}k^2} \mathrm{d}x \\
&= \int \psi_0(\underbrace{x - \frac{z}{2k_0}k}_{:=x_l}) \psi_0^*(\underbrace{x + \frac{z}{2k_0}k}_{:=x_r}) e^{-\mathrm{i}kx} \mathrm{d}x,
\end{aligned} \tag{A.7}$$

where the x-coordinate was shifted in the last step. The next step is to approximate

$$\psi_0(x_l)\psi_0^*(x_r) = e^{-a(x_l)-a(x_r)+i\frac{\delta}{\beta}[a(x_r)-a(x_l)]} \coloneqq \mathbb{G} \tag{A.8}$$

in such a way that an expression for the image intensity is obtained that can be solved for the absorption a in order to retrieve the object function.

CTF

The standard derivation of J. Guigay makes a first order approximation of $\mathbb{G}$ [66]:

$$\psi_0(x_l)\psi_0^*(x_r) \approx 1 - a(x_l) - a(x_r) + i\frac{\delta}{\beta}[a(x_l) - a(x_r)] \coloneqq \mathbb{L}. \tag{A.9}$$

This condition is satisfied for $\delta/\beta|a(x_l) - a(x_r)| \ll 1$, which is less restrictive than the weak phase assumption $|a(x)| \ll 1$. Inserting $\mathbb{L}$ into Eq. A.7 and using the Fourier shift theorem

as well as the exponential trigonometric identities, one obtains

$$\begin{aligned}\tilde{I}_z(k)/I_0 &\approx \int \left(1 - a(x_l) - a(x_r) + i\frac{\delta}{\beta}[a(x_l) - a(x_r)]\right) e^{-\mathrm{i}kx}\mathrm{d}x \\ &= 2\pi\delta(k) - e^{-\mathrm{i}\frac{z}{2k_0}k^2}\tilde{a}(k) - e^{\mathrm{i}\frac{z}{2k_0}k^2}\tilde{a}(k) + i\frac{\delta}{\beta}[e^{-\mathrm{i}\frac{z}{2k_0}k^2}\tilde{a}(k) - e^{\mathrm{i}\frac{z}{2k_0}k^2}\tilde{a}(k)] \\ &= 2\pi\delta(k) - 2\left[\cos\chi(k) + \frac{\delta}{\beta}\sin\chi(k)\right]\tilde{a}(k) \end{aligned} \tag{A.10}$$

with $\chi = zk^2/(2k_0)$. This expression is equivalent to Eq. 2.75.

Mean-field CTF

To derive the mean-field CTF in analogy to Guigay's approach, $\mathbb{G}$ is approximated as

$$\begin{aligned}\psi(x_l)\psi^*(x_r) &= e^{-a(x_l)-a(x_r)}\left\{\cos\left[\frac{\delta}{\beta}[a(x_r) - a(x_l)]\right] + i\sin\left[\frac{\delta}{\beta}[a(x_r) - a(x_l)]\right]\right\} \\ &\approx e^{-a(x_l)-a(x_r)}\left\{1 + i\frac{\delta}{\beta}[a(x_r) - a(x_l)]\right\} \\ &\approx e^{-a(x_l)-a(x_r)}\left\{\cosh\left[(a(x_l) - a(x_r))\right] + i\frac{\delta}{\beta}\sinh[a(x_l) - a(x_r)]\right\} \coloneqq \mathbb{E}. \end{aligned} \tag{A.11}$$

In the first step, the exponential absorption term is kept. In the second step, a small error is added by writing 1 as $\cosh[a(x_l) - a(x_r)]$ and $[a(x_l) - a(x_r)]$ as $\sinh[a(x_l) - a(x_r)]$. With this modification, the imaginary part remains correct in the second order, while a small error is introduced in the real part, which is however only marginal, since $|a(x_l) - a(x_r)| \ll 1$. The approximation $\mathbb{E}$ leads to an expression for the image intensity that can be solved for a: By rewriting

$$\mathbb{E} = \frac{1}{2}\left[e^{-2a(x_l)} + e^{-2a(x_r)}\right] + i\frac{\delta}{2\beta}\left[e^{-2a(x_l)} - e^{-2a(x_r)}\right], \tag{A.12}$$

using the Fourier shift theorem and the exponential trigonometric identities, one obtains

$$\tilde{I}_z(k)/I_0 = \mathcal{F}\left[e^{-2a(x)}\right]\left(\frac{\delta}{\beta}\sin\chi(k) + \cos\chi(k)\right). \tag{A.13}$$

This leads to the inversion formula

$$a(x) = -\frac{1}{2}\ln\left(\mathcal{F}^{-1}\left[\frac{\mathcal{F}[I_z(x)/I_0]}{\frac{\delta}{\beta}\sin\chi(k) + \cos\chi(k)}\right]\right), \tag{A.14}$$

which corresponds to Eq. 2.90.

A.4. Relation between mapping procedure and RCT method

In Section 3.3, the mapping procedure was introduced, which describes the mapping of plane waves in front of a reflecting crystal surface onto outgoing plane waves. Here, the plane wave mapping procedure is compared with the reciprocal coordinates transformation (RCT) method found in the literature [134, 135]. Without loss of generality, only the 1D image propagation between sample and crystal is considered here. With Eqs. 3.3 and 3.4, one can rewrite

$$k_{\mathrm{in}}^{\mathrm{c}} = k_0 \cos(\beta_{\mathrm{in}} - \arcsin\frac{k_{\mathrm{in}}}{k_0}) \tag{A.15}$$

$$= k_{\mathrm{in}} \sin\beta_{\mathrm{in}} + \sqrt{k_0^2 - k_{\mathrm{in}}^2}\cos\beta_{\mathrm{in}} \tag{A.16}$$

$$\approx k_{\mathrm{in}} \sin\beta_{\mathrm{in}} - \frac{k_{\mathrm{in}}^2}{2k_0}\cos\beta_{\mathrm{in}} + k_0\cos\beta_{\mathrm{in}}, \tag{A.17}$$

where the Fresnel approximation was used in the last step (Eq. 2.57). According to Eq. 3.11, the image wavefront at the crystal surface in Fresnel approximation is given by

$$\begin{aligned} g(x_{\mathrm{c}}) &= \frac{1}{2\pi}\int \tilde{f}(k_{\mathrm{in}})\cdot A(k_{\mathrm{in}})\cdot e^{-iz_{\mathrm{in}}\frac{k_{\mathrm{in}}^2}{2k_0}}\cdot e^{ik_{\mathrm{in}}^{\mathrm{c}}\cdot x_{\mathrm{c}}}\mathrm{d}k_{\mathrm{in}}^{\mathrm{c}} \\ &= \frac{1}{2\pi}\int \tilde{f}(k_{\mathrm{in}})\cdot A(k_{\mathrm{in}})\cdot e^{-iz_{\mathrm{in}}\frac{k_{\mathrm{in}}^2}{2k_0}}\cdot e^{ik_{\mathrm{in}}\sin\beta_{\mathrm{in}}\cdot x_{\mathrm{c}}}\cdot e^{-i\frac{k_{\mathrm{in}}^2}{2k_0}\cos\beta_{\mathrm{in}}\cdot x_{\mathrm{c}}}\cdot e^{ik_0\cos\beta_{\mathrm{in}}\cdot x_{\mathrm{c}}}\frac{\mathrm{d}k_{\mathrm{in}}^{\mathrm{c}}}{\mathrm{d}k_{\mathrm{in}}}\mathrm{d}k_{\mathrm{in}} \\ &= \frac{1}{2\pi}e^{ik_0\cos\beta_{\mathrm{in}}\cdot x_{\mathrm{c}}}\int \tilde{f}(k_{\mathrm{in}})\cdot A(k_{\mathrm{in}})\cdot e^{-iz_{\mathrm{in}}\frac{k_{\mathrm{in}}^2}{2k_0}}\cdot e^{i(k_{\mathrm{in}}\sin\beta_{\mathrm{in}}-\frac{k_{\mathrm{in}}^2}{2k_0}\cos\beta_{\mathrm{in}})x_{\mathrm{c}}}\frac{\mathrm{d}k_{\mathrm{in}}^{\mathrm{c}}}{\mathrm{d}k_{\mathrm{in}}}\mathrm{d}k_{\mathrm{in}}, \end{aligned} \tag{A.18}$$

where x_{c} is the spatial coordinate on the crystal surface. The RCT formula for 1D is given as [135]

$$g(x_{\mathrm{c}}) = \frac{1}{2\pi}\int \tilde{f}(k_{\mathrm{in}})A(k_{\mathrm{in}})\cdot e^{-iz_{\mathrm{in}}\frac{k_{\mathrm{in}}^2}{2k_0}}\cdot e^{ik_{\mathrm{RCT}}^{\mathrm{c}}\cdot x_{\mathrm{c}}}\mathrm{d}k_{\mathrm{in}}. \tag{A.19}$$

In the RCT method, the transformation

$$k_{\mathrm{RCT}}^{\mathrm{c}} = k_{\mathrm{in}}\sin\beta_{\mathrm{in}} - \frac{k_{\mathrm{in}}^2}{2k_0}\cos\beta_{\mathrm{in}} \tag{A.20}$$

of the reciprocal coordinate is mathematically motivated. The equation is similar to the mapping procedure (Eq. A.17) but the last term is missing. Accordingly, the phase modulation $e^{ik_0\cos\beta_{\mathrm{in}}\cdot x_{\mathrm{c}}}$ is missing in the RCT formula, which is physically incorrect. Fig. A.2 illustrates that a plane wave with $k_{\mathrm{in}} = 0$ in the object plane generates a wave with the phase factor $e^{ik_0\cos\beta_{\mathrm{in}}\cdot x_{\mathrm{out}}}$ on the crystal surface.

After propagation to the crystal plane, the crystal adds its crystal momentum h to the plane wave, as considered in the mapping procedure in Eq. 3.5. The crystal momentum $h_{\parallel} = k_0(\cos\beta_{\mathrm{out}} - \cos\beta_{\mathrm{in}})$ counteracts the phase factor $e^{ik_0\cos\beta_{\mathrm{in}}\cdot x_{\mathrm{out}}}$ from propagation to the

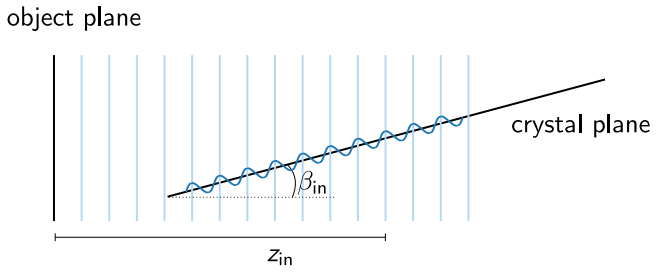

Figure A.2.: Propagation of a plane wave to a tilted plane. A plane wave exiting the object plane with $k_{\text{in}} = 0$ generates a wave with phase $e^{ik_0 \cos\beta_{\text{in}} \cdot x_{\text{out}}}$ on the tilted plane.

inclined plane as well as the phase factor $e^{-ik_0 \cos\beta_{\text{out}} \cdot x_{\text{out}}}$ from propagation from the inclined plane to the detector plane, and causes an incident plane wave with $k_{\text{in}} = 0$ to become a plane wave with $k_{\text{out}} = 0$ in the detector plane. In contrast, the diffraction by the crystal is not described by the RCT method, and it is not clear why the change in propagation direction occurs.

As a further difference, the calculation of the image comes with the challenge to account for the nonlinear dependence of the spatial frequencies. The RCT method solves this problem by interpolating the fast Fourier transform (FFT) of the object such that it can be evaluated at equidistant spatial frequencies in the image plane. This method may introduce numerical instabilities. In contrast, the mapping procedure keeps the original equidistant coefficients of the object FFT by applying a non-uniform discrete Fourier transform (DFT) over the irregular sampling grid in the image plane. This method is exact, but cannot use the FFT for calculating the image intensity. However, there exist fast methods to compute the DFT that are based on the FFT [209].

To summarize, the RCT formula can be obtained from the mapping procedure by using the Fresnel approximation and performing an interpolation of the object Fourier transform. In most cases, the image intensities calculated by the RCT and the mapping procedure will be in good agreement. Still, the plane wave mapping method does not require Fresnel approximation and interpolation of the object FFT, and the propagation and diffraction of plane waves are derived in a rigorous manner.

A.5. Optimization of indirect system

The experimental comparison presented in Section 4.2 was performed for a specific spatial resolution of 1.6 µm, where both the indirect and the Bragg magnifier (BM) system have the same pixel size with respect to the sample. The question arises whether the parameters for the indirect detector, namely the numerical aperture (NA), scintillator thickness, and operating energy could be further optimized and adjusted in dependence of the sample thickness and the desired resolution. The value to be maximized is the normalized SNR^2 as shown in Fig. 4.3c. This optimization is a rather complex problem, for which an idealized upper estimate is presented here.

For each sample thickness, the theoretically achievable SNR^2 over energy at constant dose is calculated, assuming a perfect detector, and its maximum is found for the normalization (see green curves in Fig. 4.3c). Next, the SNR^2 that is maximally detectable by the indirect system at the desired spatial resolution is computed. Varying the NA determines the allowable scintillator thickness. As a rule of thumb, the thickness t can be chosen relative to the depth of field of the objective in the scintillator [42, 210]:

$$t \approx x \frac{\lambda_{\mathrm{vis}} \cdot n}{\mathrm{NA}^2}, \tag{A.21}$$

where the refractive index $n = 1.82$ of the LSO scintillator is taken into account, and x is a factor typically chosen in the range of 1 to 2. Here, the results are shown for $x = 2$. From the thickness, the SNR^2 can be determined for each NA in dependence of the energy, where also the decrease by the optical transfer function (OTF) at the desired spatial resolution is included. For very low energies, care is taken to ensure that at least three optical photons are detected per each absorbed X-ray photon in order not to degrade the X-ray statistics. The highest detectable SNR^2 specifies the optimal NA and energy for each sample thickness and desired resolution. Division by the maximum of the theoretical SNR^2 determines the normalized SNR^2, i.e., the dose efficiency of the indirect system.

Fig. A.3 shows the results of the optimization for different desired resolutions and sample thicknesses. The graphs indicate that for high resolution, the NA should be chosen rather high instead of optimizing the detection efficiency by increasing the scintillator thickness. This could be understood as follows: increasing the OTF contributes linearly to the SNR, while the scintillator absorption contributes with the square root. In the presented experiment, it would probably have been beneficial to use a larger NA of 0.4 rather than increasing the scintillator thickness. This would have increased the OTF by a factor of 1.2 at $q = 0.3\,\mu\mathrm{m}^{-1}$ and by a factor of 1.6 at the desired resolution of $q = 0.6\,\mu\mathrm{m}^{-1}$. For lower resolutions, it is advantageous to decrease the NA in favor of a thicker scintillator and better X-ray statistics. The NA approaches a lower limit due to the collection efficiency of optical photons.

As mentioned in Section 4.1.2, for thin samples (< 5 mm) the ideal operating energy for the

indirect system would be 11 keV. Even in this case and with a larger NA, the dose efficiency of the BM system would be one order of magnitude higher than that of the indirect system at the desired resolution. For higher resolutions, e.g., using Germanium crystals with 0.6 µm achievable resolution, the gain increases further, and liquid immersion would have to be used to achieve such high NAs in the indirect system.

The efficiency calculated here is only an upper estimate. For example, the degradation of the OTF by generation of secondary particles in the scintillator is not included. Ref. [160] describes a method to include these effects using *Geant4* simulations. The authors have kindly provided the simulated modulation transfer function (MTF) curves for several energies and two scintillator thicknesses, see Fig. A.4. The curves show that the MTF for 30 keV deviates from the OTF of an ideal lens. In the case of NA = 0.28, the scintillator thickness could have been increased to 24 µm (Fig. A.4b). This was tested experimentally, but the resulting SNR(q) was very similar to the 12 µm thick LSO, and is therefore not shown here. One explanation for the reduced performance of the 24 µm thick LSO scintillator could be that it becomes increasingly difficult to maintain a high doping concentration during the fabrication process. For an NA of 0.4, Fig. A.4c shows that the 12 µm thick scintillator should be chosen because the microscope optics would cause blurring with the 24 µm thick scintillator.

The curves shown in Fig. A.3 were calculated for an LSO scintillator and a soft tissue sample. The source code is available in Ref. [104] so that the interested reader can adapt the calculations for other sample materials and thicknesses, resolutions or scintillator materials.

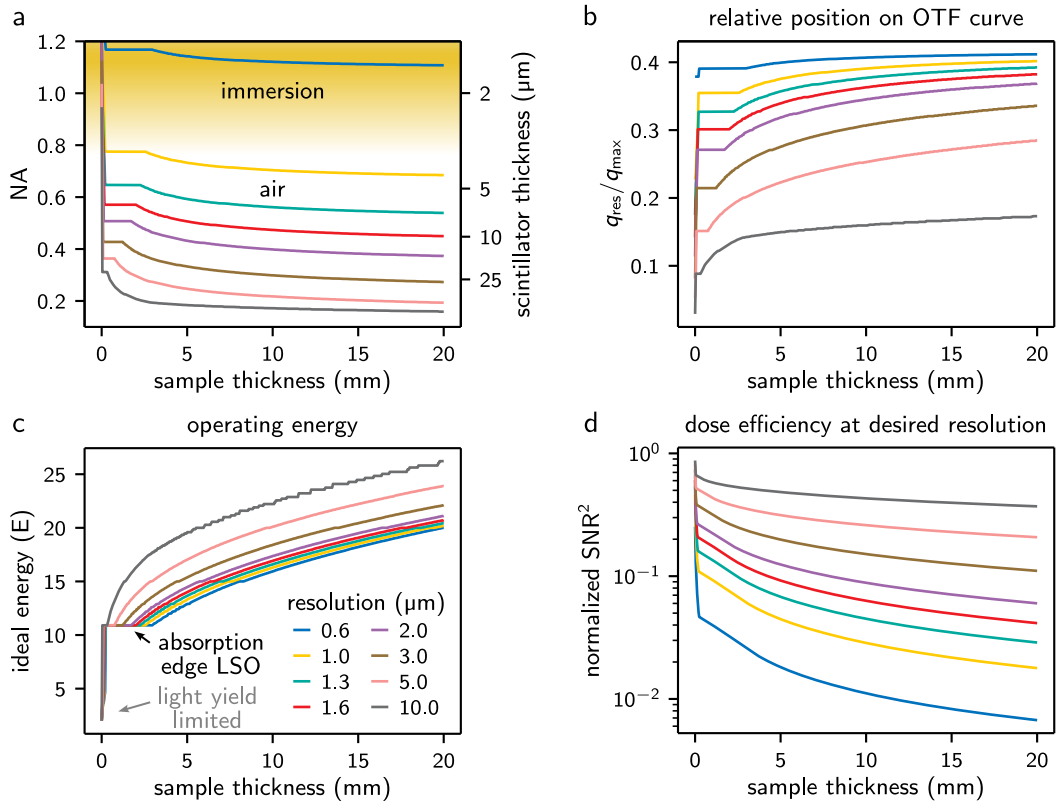

Figure A.3.: Optimized parameters for the indirect system and an LSO scintillator for different sample thicknesses (soft tissue) and resolutions. **a** Optimized numerical aperture versus specimen thickness for different resolutions. The yellow color indicates that objectives with immersion liquids are required for a high NA. **b** Spatial frequency q_{res} corresponding to the desired resolution in relation to the spatial frequency q_{max} at which the OTF of the objective becomes zero. **c** Optimal operating energy. A lower limit is given by the light yield of the scintillator per absorbed X-ray photon (gray arrow). The absorption edge of LSO determines an optimal energy of 11 keV for thin samples (black arrow). **d** Resulting normalized SNR^2 at the desired resolution, which is an upper limit for the dose efficiency compared to an ideal detector. Reproduced from Ref. [104].

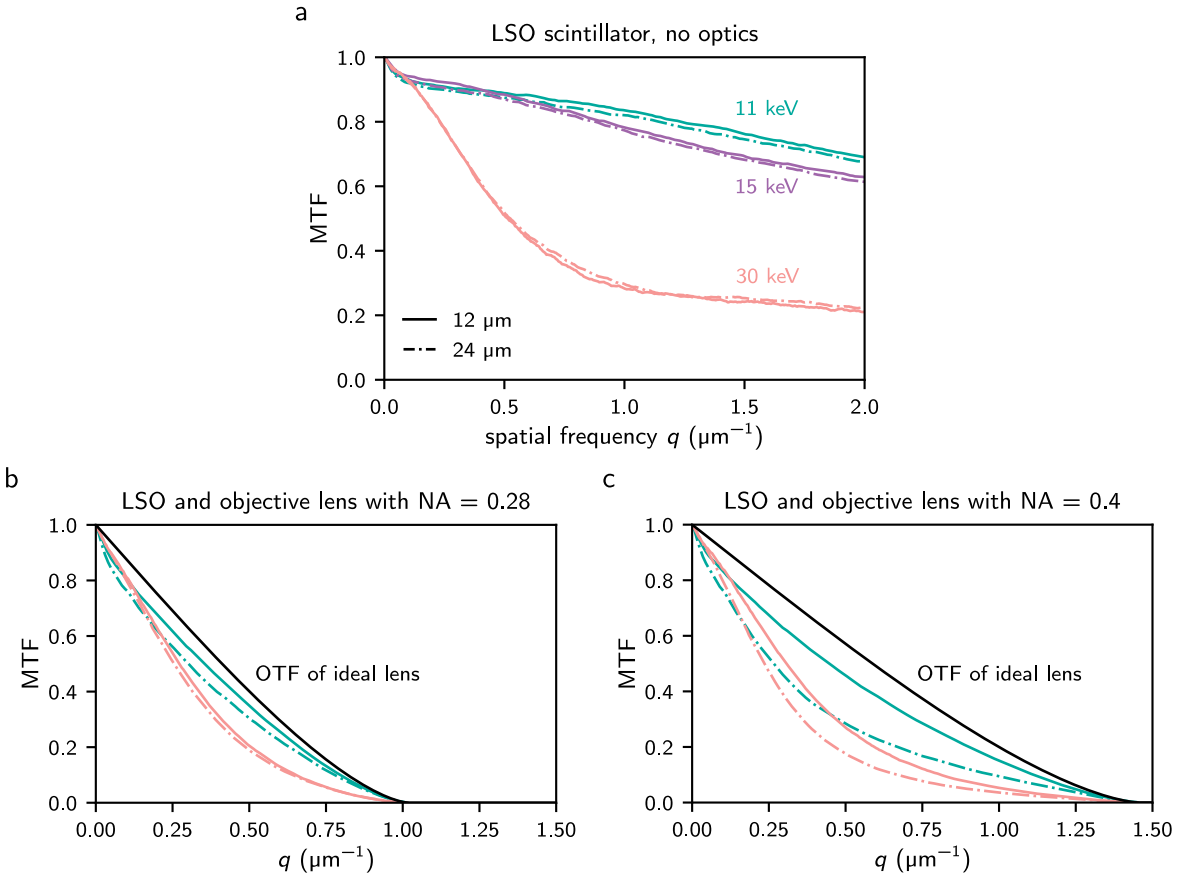

Figure A.4.: Simulated transfer function of a 12 µm and a 24 µm thick LSO:Tb scintillator at different energies. MTF **a** without optics, **b** with an objective lens of NA = 0.28 and **c** with an objective lens of NA = 0.4. The effects of secondary particles generated in the scintillator are simulated by *Geant4* simulations [157, 160], and the effect of blurring introduced by the microscope optics is calculated analytically, as described in Refs. [88, 160, 211]. For low energies, the transfer function of the scintillator (panel a) remains close to unity. For high energies, shown here for 30 keV, it decreases strongly with increasing spatial frequency, which further degrades the overall imaging performance of the indirect detector system, as mentioned in Chapter 4. The combined MTF of the scintillator and the objective lens lies below the OTF of an ideal lens (black curves in panels b and c), and decreases with increasing thickness due to blurring by the optics. The simulation data were kindly provided by Kristof Pauwels and Laura Wollesen (ESRF, Grenoble, France) [160].

A.6. Additional simulations with demagnifier

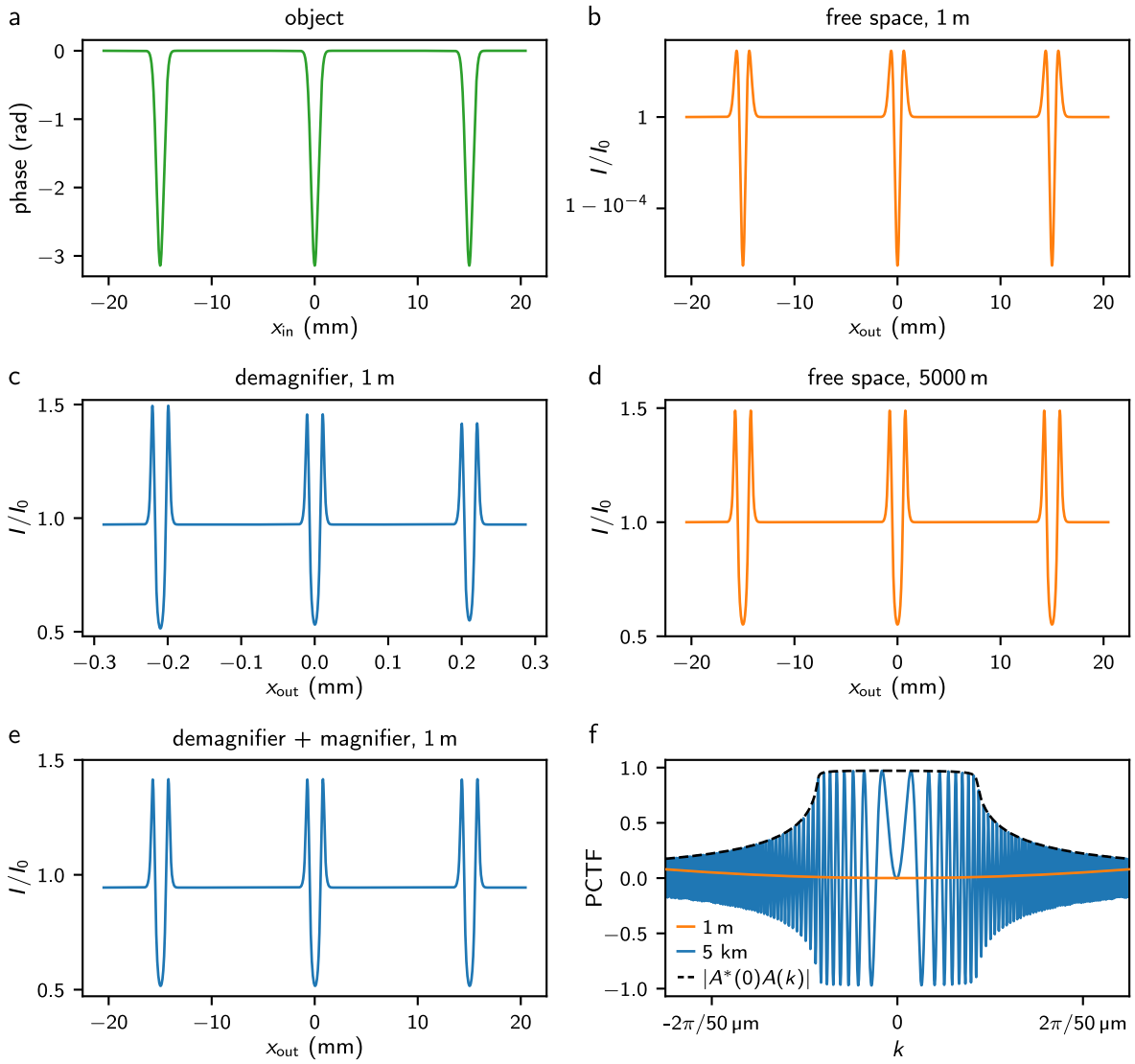

Figure A.5.: Simulated 1D image intensities for conventional propagation-based phase contrast imaging (PB-PCI) and the Bragg demagnifier at 30.5 keV and $M = 71$. PB-PCI of a pure phase object as shown in Fig. 5.8, here for a higher energy and thus even higher magnification. The simulations have been performed for perfect coherence. Note the small intensity scale in panel b.

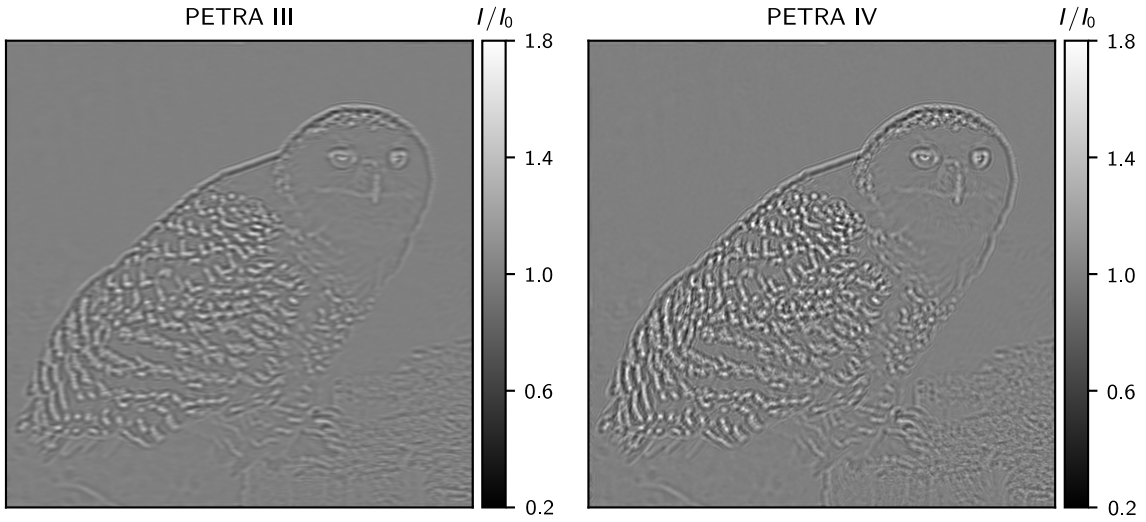

Figure A.6.: Simulated 2D image intensities using the demagnifier for the source size of P23 at PETRA III and the perspective source size at PETRA IV. PB-PCI of a pure phase object as shown in Fig. 5.9, simulated with the Bragg demagnifier at 30.5 keV ($M = 71.3$) and physical propagation distances of $z_x = 1.3\,\mathrm{m}$ and $z_y = 1.5\,\mathrm{m}$, corresponding to effective propagation distances of $z_{\mathrm{eff},x} = 6.6\,\mathrm{km}$ and $z_{\mathrm{eff},y} = 7.6\,\mathrm{km}$. The simulations include source blur from the measured horizontal and vertical source sizes $s_\mathrm{h} = 164\,\mu\mathrm{m}$ and $s_\mathrm{v} = 38\,\mu\mathrm{m}$ of P23 at PETRA III (left), and from the perspective fourth-generation synchrotron radiation facility PETRA IV [201] by assuming a symmetric source size $s = 38\,\mu\mathrm{m}$ (right).

A.7. Divergence formula by J. Härtwig

In Section 5.3, the angular distribution of the illumination from a polychromatic source with a finite source size was discussed in combination with a monochromator, a Bragg conditioner and a Bragg demagnifier, and an example was shown for the P23 source (horizontal direction). Although in general asymmetric Bragg diffraction with a positive asymmetry angle α reduces the monochromatic angular distribution, as is the case in a Bragg conditioner, the overall angular distribution is deteriorated due to the polychromaticity of the incident waves. This effect was simulated in Figs. 5.6 and 5.7. J. Härtwig formulated a dependence of the outgoing beam divergence $\sigma_{\theta,\mathrm{out}}$ from the incident beam divergence $\sigma_{\theta,\mathrm{in}}$, the energy spread $\Delta\lambda_0/\lambda_0$, and the factors $\gamma_o = \sin(\theta_\mathrm{B} - \alpha)$ and $\gamma_h = -\sin(\theta_\mathrm{B} + \alpha)$ introduced in Section 2.1 [199, 212]:

$$|\sigma_{\theta,\mathrm{out}}| \approx \frac{\gamma_o}{\gamma_h}\sigma_{\theta,\mathrm{in}} + \frac{\Delta\lambda_0}{\lambda_0}\frac{\sqrt{1-\gamma_h^2} - \sqrt{1-\gamma_o^2}}{\gamma_h}. \tag{A.22}$$

The Gaussian function obtained from this spread in polychromatic divergence behind the conditioner has been plotted in Fig. 5.7 and agrees well with the results obtained in the simulations.

A.8. Demagnifier setup

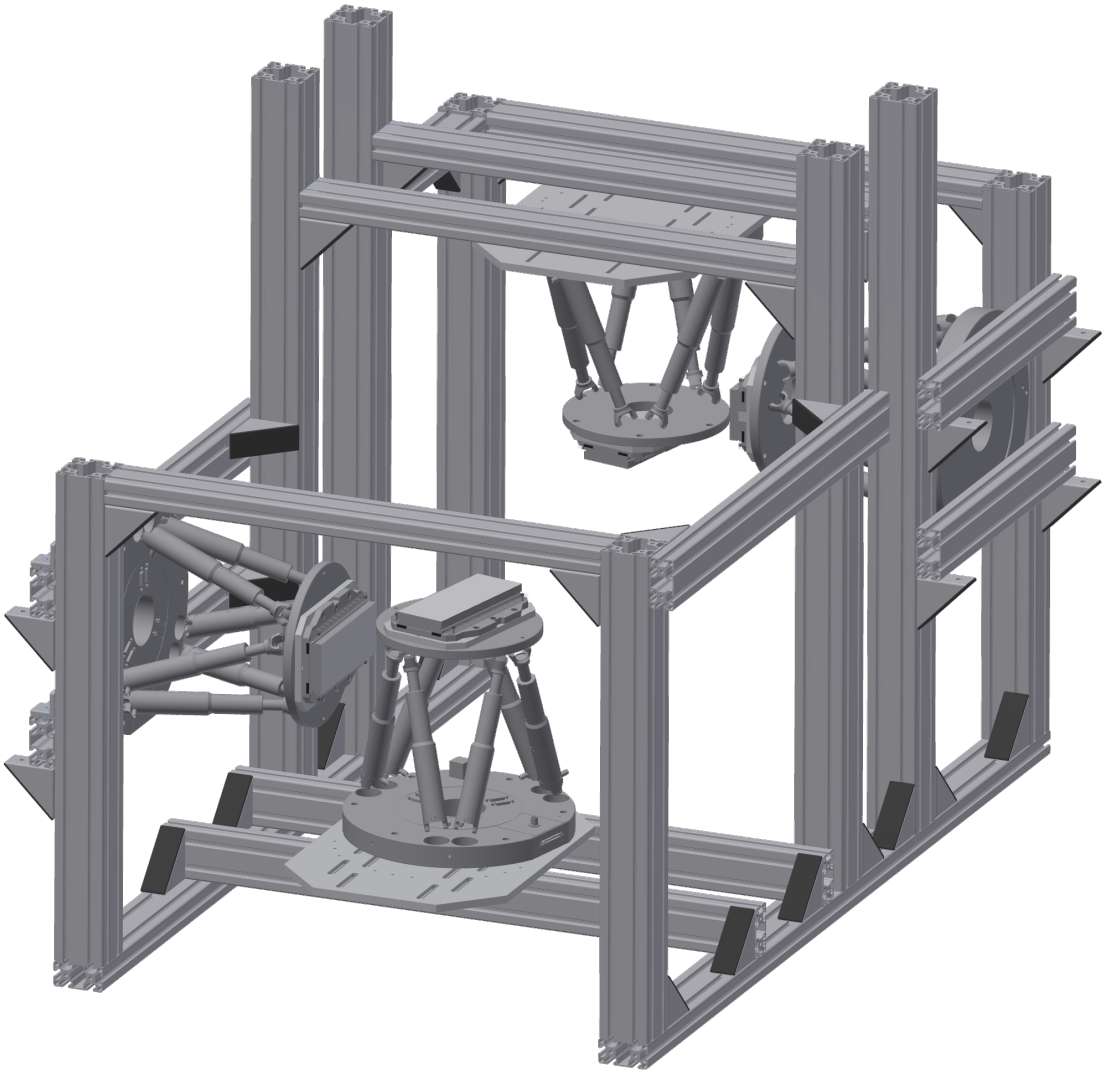

Figure A.7.: Layout of the Bragg demagnifier setup. The four crystals of the Bragg demagnifier are mounted on four separate hexapods. The hexapods are integrated into an item frame such that the crystals are in correct arrangement relative to each other. The frame was designed to provide a high degree of flexibility, allowing adjustments to variable table and beam heights at different synchrotron beamlines. The CAD model of the item frame was constructed with the item online engineering tool (*Item Industrietechnik GmbH, 42653 Solingen, Germany*). The virtual assembly was accomplished with Autodesk Inventor Professional (*Autodesk Inc., 94105 San Francisco, United States of America*) with the help of Kevin Zachmann (IBG, KIT, Karlsruhe, Germany).

List of abbreviations

BM	Bragg magnifier
CCD	charge-coupled device
CdTe	cadmium telluride
CMOS	complementary metal-oxide-semiconductor
CSM	charge-sharing mode
CTF	contrast transfer function
DFT	discrete Fourier transform
DPCI	differential phase contrast imaging
DQE	detective quantum efficiency
FFT	fast Fourier transform
FOV	field of view
FWHM	full width at half maximum
GaAs	gallium arsenide
Ge	germanium
MTF	modulation transfer function
NA	numerical aperture
NLTikh	nonlinear Tikhonov regularization
OTF	optical transfer function
PB-PCI	propagation-based phase contrast imaging
PCTF	phase contrast transfer function
PSF	point spread function
RCT	reciprocal coordinates transformation
sCMOS	scientific CMOS
Si	silicon
SNR	signal-to-noise ratio
SPCD	single photon counting detector
SPM	single-pixel mode
TIE	transport of intensity equation

Bibliography

[1] X. Ou, X. Chen, X. Xu, L. Xie, X. Chen, Z. Hong, H. Bai, X. Liu, Q. Chen, L. Li, and H. Yang, "Recent Development in X-Ray Imaging Technology: Future and Challenges", Research **2021**, 1–18 (2021) (cited on p. 1).

[2] D. H. Bilderback, P. Elleaume, and E. Weckert, "Review of third and next generation synchrotron light sources", J. Phys. B: At. Mol. Opt. Phys. **38**, S773 (2005) (cited on pp. 1, 16).

[3] A. Momose and J. Fukuda, "Phase-contrast radiographs of nonstained rat cerebellar specimen", Med. Phys. **22**, 375–379 (1995) (cited on pp. 1, 16, 18).

[4] S. W. Wilkins, T. E. Gureyev, D. Gao, A. Pogany, and A. W. Stevenson, "Phase-contrast imaging using polychromatic hard X-rays", Nature **384**, 335–338 (1996) (cited on pp. 1, 16).

[5] A. Snigirev, I. Snigireva, V. Kohn, S. Kuznetsov, and I. Schelokov, "On the possibilities of x-ray phase contrast microimaging by coherent high-energy synchrotron radiation", Rev. Sci. Instrum. **66**, 5486–5492 (1995) (cited on pp. 1, 64).

[6] U. Bonse and M. Hart, "An X-ray interferometer", Appl. Phys. Lett. **6**, 155–156 (1965) (cited on p. 1).

[7] A. Momose, T. Takeda, Y. Itai, and K. Hirano, "Phase–contrast X–ray computed tomography for observing biological soft tissues", Nat. Med. **2**, 473–475 (1996) (cited on p. 1).

[8] A. Momose, S. Kawamoto, I. Koyama, Y. Hamaishi, K. Takai, and Y. Suzuki, "Demonstration of X-Ray Talbot Interferometry", Jpn. J. Appl. Phys. **42**, L866 (2003) (cited on pp. 1, 85, 113).

[9] F. Pfeiffer, T. Weitkamp, O. Bunk, and C. David, "Phase retrieval and differential phase-contrast imaging with low-brilliance X-ray sources", Nat. Phys. **2**, 258–261 (2006) (cited on pp. 1, 113).

[10] T. J. Davis, D. Gao, T. Gureyev, A. Stevenson, and S. Wilkins, "Phase-contrast imaging of weakly absorbing materials using hard X-rays", Nature **373**, 595–598 (1995) (cited on pp. 1, 40, 42, 64, 85, 88, 104).

[11] D. Chapman, W. Thomlinson, R. Johnston, D. Washburn, E. Pisano, N. Gmür, Z. Zhong, R. Menk, F. Arfelli, and D. Sayers, "Diffraction enhanced X-ray imaging", Physics in Medicine & Biology **42**, 2015 (1997) (cited on pp. 1, 85, 105).

[12] A. Olivo and R. Speller, "A coded-aperture technique allowing x-ray phase contrast imaging with conventional sources", Appl. Phys. Lett. **91**, 10.1063/1.2772193 (2007) (cited on pp. 1, 113).

[13] K. S. Morgan, D. M. Paganin, and K. K. W. Siu, "X-ray phase imaging with a paper analyzer", Appl. Phys. Lett. **100**, 10.1063/1.3694918 (2012) (cited on pp. 1, 85, 113).

[14] M.-C. Zdora, "State of the Art of X-ray Speckle-Based Phase-Contrast and Dark-Field Imaging", J. Imaging **4**, 60 (2018) (cited on pp. 1, 85, 113).

[15] O. Betz, U. Wegst, D. Weide, M. Heethoff, L. Helfen, W.-K. Lee, and P. Cloetens, "Imaging applications of synchrotron X-ray phase-contrast microtomography in biological morphology and biomaterials science. I. General aspects of the technique and its advantages in the analysis of millimetre-sized arthropod structure", Journal of Microscopy **227**, 51–71 (2007) (cited on pp. 2, 63).

[16] M. Eckermann, B. Schmitzer, F. van der Meer, J. Franz, O. Hansen, C. Stadelmann, and T. Salditt, "Three-dimensional virtual histology of the human hippocampus based on phase-contrast computed tomography", Proc. Natl. Acad. Sci. **118**, e2113835118 (2021) (cited on p. 2).

[17] M. Cotte, K. Dollman, V. Fernandez, V. Gonzalez, F. Vanmeert, L. Monico, C. Dejoie, M. Burghammer, L. Huder, S. Fisher, et al., "New Opportunities Offered by the ESRF to the Cultural and Natural Heritage Communities", Synchrotron Radiation News **35**, 3–9 (2022) (cited on pp. 2, 85, 98).

[18] S. C. Mayo, A. W. Stevenson, and S. W. Wilkins, "In-line phase-contrast X-ray imaging and tomography for materials science", Materials **5**, 937–965 (2012) (cited on p. 2).

[19] P. Pietsch, D. Westhoff, J. Feinauer, J. Eller, F. Marone, M. Stampanoni, V. Schmidt, and V. Wood, "Quantifying microstructural dynamics and electrochemical activity of graphite and silicon-graphite lithium ion battery anodes", Nat. Commun. **7**, 1–11 (2016) (cited on p. 2).

[20] J. J. Socha, M. W. Westneat, J. F. Harrison, J. S. Waters, and W.-K. Lee, "Real-time phase-contrast x-ray imaging: a new technique for the study of animal form and function", BMC Biol. **5**, 1–15 (2007) (cited on pp. 2, 63, 82).

[21] J. Moosmann, A. Ershov, V. Altapova, T. Baumbach, M. S. Prasad, C. LaBonne, X. Xiao, J. Kashef, and R. Hofmann, "X-ray phase-contrast *in vivo* microtomography probes new aspects of *Xenopus* gastrulation", Nature **497**, 374–377 (2013) (cited on pp. 2, 63).

[22] C. Schmitt, A. Rack, and O. Betz, "Analyses of the mouthpart kinematics in Periplaneta americana (Blattodea, Blattidae) using synchrotron-based X-ray cineradiography", J. Exp. Biol. **217**, 3095–3107 (2014) (cited on pp. 2, 63).

[23] T. dos Santos Rolo, A. Ershov, T. van de Kamp, and T. Baumbach, "In vivo X-ray cine-tomography for tracking morphological dynamics", Proc. Natl. Acad. Sci. **111**, 3921–3926 (2014) (cited on pp. 2, 63).

[24] W. J. Boettinger, H. E. Burdette, and M. Kuriyama, "X-ray magnifier", Rev. Sci. Instrum. **50**, 26–30 (1979) (cited on pp. 3, 39, 67, 70).

[25] P. P. Ewald, *Dispersion und Doppelbrechung von Elektronengittern (Kristallen)* (Dieterichsche Universitäts-Buchdruckerei, 1912) (cited on p. 5).

[26] W. Friedrich, P. Knipping, and M. Laue, "Interferenzerscheinungen bei Röntgenstrahlen", Annalen der Physik **346**, 971–988 (1913) (cited on p. 5).

[27] W. L. Bragg, "The structure of some crystals as indicated by their diffraction of X-rays", Proceedings of the Royal Society of London A **89**, 248–277 (1913) (cited on pp. 5, 6).

[28] C. Darwin, "XXXIV. The theory of X-ray reflexion", The London, Edinburgh, and Dublin Philosophical Magazine and Journal of Science **27**, 315–333 (1914) (cited on p. 5).

[29] C. G. Darwin, "LXXVIII. The theory of X-ray reflexion. Part II", The London, Edinburgh, and Dublin Philosophical Magazine and Journal of Science **27**, 675–690 (1914) (cited on p. 5).

[30] P. P. Ewald, "Zur Theorie der Interferenzen der Röntgenstrahlen in Kristallen", Physikalische Zeitschrift **14**, 465 (1913) (cited on p. 5).

[31] P. Ewald, "Zur Begründung der Kristalloptik", Annalen der Physik **49**, 117–143 (1916) (cited on p. 5).

[32] P. Ewald, "Zur Begründung der Kristalloptik (Fortsetzung)", Annalen der Physik **54**, 557–597 (1916) (cited on p. 5).

[33] M. Laue, "Ergebnisse der Exakten Naturwissenschaften", **10**, 133–158 (1931) (cited on p. 6).

[34] A. Authier, *Dynamical theory of X-ray diffraction*, Vol. 11 (Oxford University Press, 2004) (cited on pp. 6, 8–11, 13–16, 41, 69).

[35] P. P. Ewald, "Chapter 4: Laue's Discovery of X-ray Diffraction by Crystals", in *Fifty Years of X-Ray Diffraction: Dedicated to the International Union of Crystallography on the Occasion of the Commemoration Meeting in Munich July 1962* (Springer Science & Business Media, 2012) (cited on p. 6).

[36] W. H. Zachariasen and E. Hill, "Theory of X-ray Diffraction in Crystals", The Journal of Physical Chemistry **50**, 289–290 (1946) (cited on p. 6).

[37] B. W. Batterman and H. Cole, "Dynamical Diffraction of X Rays by Perfect Crystals", Rev. Mod. Phys. **36**, 681–717 (1964) (cited on pp. 6, 13).

[38] A. Authier and C. Malgrange, "Diffraction Physics", Acta Crystallogr., Sect. A: Found. Crystallogr. **54**, 806–819 (1998) (cited on pp. 6, 7).

[39] J. Stöhr, *The Nature of X-Rays and Their Interactions with Matter*, Vol. 288 (Springer Nature, 2023) (cited on p. 6).

[40] D. J. Griffiths and C. Inglefield, *Introduction to Electrodynamics*, Vol. 73, 6 (AIP Publishing, 2005) (cited on p. 8).

[41] D. Paganin, *Coherent X-ray Optics* (Oxford University Press, 2013) (cited on pp. 8, 17, 20, 21, 24).

[42] M. Born and E. Wolf, *Principles of Optics: Electromagnetic Theory of Propagation, Interference and Diffraction of Light* (Elsevier, 2013) (cited on pp. 9, 20, 122).

[43] T. Salditt, T. Aspelmeier, and S. Aeffner, *Biomedical Imaging* (De Gruyter, Berlin, Germany, 2017) (cited on pp. 9, 17–20, 22, 31, 77).

[44] F. Bloch, "Über die Quantenmechanik der Elektronen in Kristallgittern", Z. Phys. **52**, 555–600 (1929) (cited on p. 10).

[45] J. Härtwig, "Review of the X-ray diffraction in extreme asymmetric cases", Krist. Tech. **13**, 1117–1126 (1978) (cited on pp. 13, 115).

[46] X. Huang and M. Dudley, "A universal computation method for two-beam dynamical X-ray diffraction", Acta Crystallogr., Sect. A: Found. Crystallogr. **59**, 163–167 (2003) (cited on pp. 15, 48).

[47] R. S. Ledley, G. Di Chiro, A. J. Luessenhop, and H. L. Twigg, "Computerized Transaxial X-ray Tomography of the Human Body", Science **186**, 207–212 (1974) (cited on p. 16).

[48] A. C. Kak and M. Slaney, *Principles of Computerized Tomographic Imaging* (SIAM, 2001) (cited on p. 16).

[49] P. Cloetens, W. Ludwig, J. Baruchel, D. Van Dyck, J. Van Landuyt, J. P. Guigay, and M. Schlenker, "Holotomography: Quantitative phase tomography with micrometer resolution using hard synchrotron radiation x rays", Appl. Phys. Lett. **75**, 2912–2914 (1999) (cited on pp. 16, 17, 26, 30, 31, 74).

[50] D. Paganin, S. C. Mayo, T. E. Gureyev, P. R. Miller, and S. W. Wilkins, "Simultaneous phase and amplitude extraction from a single defocused image of a homogeneous object", J. Microsc. **206**, 33–40 (2002) (cited on pp. 16, 17, 30, 31, 80).

[51] T. Weitkamp, A. Diaz, C. David, F. Pfeiffer, M. Stampanoni, P. Cloetens, and E. Ziegler, "X-ray phase imaging with a grating interferometer", Opt. Express **13**, 6296–6304 (2005) (cited on p. 16).

[52] A. Momose, W. Yashiro, Y. Takeda, Y. Suzuki, and T. Hattori, "Phase Tomography by X-ray Talbot Interferometry for Biological Imaging", Jpn. J. Appl. Phys. **45**, 5254 (2006) (cited on p. 16).

[53] P. C. Diemoz, P. Coan, C. Glaser, and A. Bravin, "Absorption, refraction and scattering in analyzer-based imaging: comparison of different algorithms", Optics Express **18**, 3494–3509 (2010) (cited on p. 16).

[54] J. Als-Nielsen and D. McMorrow, *Elements of Modern X-ray Physics* (John Wiley & Sons, 2011) (cited on p. 18).

[55] E. Hecht, *Optics* (Pearson Education, 2017), p. 139 (cited on p. 18).

[56] J. H. Hubbell and S. M. Seltzer, "Tables of X-ray mass attenuation coefficients and mass energy-absorption coefficients 1 keV to 20 MeV for elements Z=1 to 92 and 48 additional

substances of dosimetric interest", National Inst. of Standards and Technology-PL, Ionizing Radiation Div. (1995) (cited on pp. 18, 65, 68, 71).

[57] P. Cloetens, W. Ludwig, J. Baruchel, J.-P. Guigay, P. Pernot-Rejmánková, M. Salomé-Pateyron, M. Schlenker, J.-Y. Buffière, E. Maire, and G. Peix, "Hard x-ray phase imaging using simple propagation of a coherent synchrotron radiation beam", J. Phys. D: Appl. Phys. **32**, A145 (1999) (cited on pp. 22, 32, 33).

[58] N. Wiener, "Generalized harmonic analysis", Acta Mathematica **55**, 117–258 (1930) (cited on p. 24).

[59] A. Khintchine, "Korrelationstheorie der stationären stochastischen Prozesse", Mathematische Annalen **109**, 604–615 (1934) (cited on p. 24).

[60] H. Tajiri, H. Yamazaki, H. Ohashi, S. Goto, O. Sakata, and T. Ishikawa, "A middle energy-bandwidth X-ray monochromator for high-flux synchrotron diffraction: revisiting asymmetrically cut silicon crystals", J. Synchrotron Radiat. **26**, 750–755 (2019) (cited on p. 24).

[61] A. Pogany, D. Gao, and S. W. Wilkins, "Contrast and resolution in imaging with a microfocus x-ray source", Rev. Sci. Instrum. **68**, 2774–2782 (1997) (cited on p. 24).

[62] B. Kozioziemski, B. Bachmann, A. Do, and R. Tommasini, "X-ray imaging methods for high-energy density physics applications", Rev. Sci. Instrum. **94**, 10.1063/5.0130689 (2023) (cited on p. 25).

[63] J. Moosmann, A. Ershov, V. Weinhardt, T. Baumbach, M. S. Prasad, C. LaBonne, X. Xiao, J. Kashef, and R. Hofmann, "Time-lapse X-ray phase-contrast microtomography for *in vivo* imaging and analysis of morphogenesis", Nat. Protoc. **9**, 294–304 (2014) (cited on p. 25).

[64] D. Gabor, "A New Microscopic Principle", Nature **161**, 777–778 (1948) (cited on p. 26).

[65] O. Scherzer, "The Theoretical Resolution Limit of the Electron Microscope", J. Appl. Phys. **20**, 20–29 (1949) (cited on p. 26).

[66] P. Guigay, "Fourier-transform analysis of Fresnel diffraction patterns and in-line holograms", Optik **49**, 121–125 (1977) (cited on pp. 26, 118).

[67] F. Lenz and W. Scheffels, "Das Zusammenwirken von Phasen- und Amplitudenkontrast in der elektronenmikroskopischen Abbildung", Zeitschrift für Naturforschung A **13**, 226–230b (1958) (cited on pp. 26, 118).

[68] V. E. Cosslett and R. Barer, *Advances in Optical and Electron Microscopy: Volume 4* (Academic Press, Jan. 1971), pp. 1–82 (cited on pp. 26, 118).

[69] V. E. Cosslett and R. Barer, *Advances in Optical and Electron Microscopy: Volume 5* (Academic Press, 1973), pp. 163–181 (cited on pp. 26, 118).

[70] E. J. Kirkland, "Some Image Approximations", in *Advanced Computing in Electron Microscopy* (Springer, 2020), pp. 37–80 (cited on pp. 26, 27, 118).

[71] J. M. Blackledge, *Digital Image Processing: Mathematical and Computational Methods* (Elsevier, 2005) (cited on pp. 26, 69).

[72] F. Thon, “Notizen: Zur Defokussierungsabhängigkeit des Phasenkontrastes bei der elektronenmikroskopischen Abbildung”, Zeitschrift für Naturforschung A **21**, 476–478 (1966) (cited on p. 29).

[73] M. Vulović, E. Franken, R. B. G. Ravelli, L. J. van Vliet, and B. Rieger, “Precise and unbiased estimation of astigmatism and defocus in transmission electron microscopy”, Ultramicroscopy **116**, 115–134 (2012) (cited on p. 29).

[74] R. Pretzsch, M. Dries, S. Hettler, M. Spiecker, M. Obermair, and D. Gerthsen, “Investigation of hole-free phase plate performance in transmission electron microscopy under different operation conditions by experiments and simulations”, Adv. Struct. Chem. Imag. **5**, 1–11 (2019) (cited on pp. 29, 105).

[75] A. Burvall, U. Lundström, P. A. C. Takman, D. H. Larsson, and H. M. Hertz, “Phase retrieval in X-ray phase-contrast imaging suitable for tomography”, Optics Express **19**, 10359–10376 (2011) (cited on p. 30).

[76] J. Hagemann, M. Töpperwien, and T. Salditt, “Phase retrieval for near-field X-ray imaging beyond linearisation or compact support”, Appl. Phys. Lett. **113**, 041109 (2018) (cited on pp. 30, 34, 113).

[77] L. M. Lohse, A.-L. Robisch, M. Töpperwien, S. Maretzke, M. Krenkel, J. Hagemann, and T. Salditt, “A phase-retrieval toolbox for X-ray holography and tomography”, Journal of Synchrotron Radiation **27**, 852–859 (2020) (cited on pp. 30, 51, 58, 60, 75, 82).

[78] T. E. Gureyev, A. Roberts, and K. A. Nugent, “Phase retrieval with the transport-of-intensity equation: matrix solution with use of Zernike polynomials”, J. Opt. Soc. Am. A, JOSAA **12**, 1932–1941 (1995) (cited on p. 30).

[79] S. Huhn, L. M. Lohse, L. M. Lohse, J. Lucht, T. Salditt, and T. Salditt, “Fast algorithms for nonlinear and constrained phase retrieval in near-field X-ray holography based on Tikhonov regularization”, Optics Express **30**, 32871–32886 (2022) (cited on pp. 31, 34, 58, 75, 82).

[80] J. Moosmann, R. Hofmann, and T. Baumbach, “Single-distance phase retrieval at large phase shifts”, Opt. Express **19**, 12066–12073 (2011) (cited on p. 31).

[81] W. Coene, G. Janssen, M. Op de Beeck, and D. Van Dyck, “Phase retrieval through focus variation for ultra-resolution in field-emission transmission electron microscopy”, Phys. Rev. Lett. **69**, 3743–3746 (1992) (cited on p. 32).

[82] T. Faragó, R. Spiecker, M. Hurst, M. Zuber, A. Cecilia, and T. Baumbach, “Phase retrieval in propagation-based X-ray imaging beyond the limits of transport of intensity and contrast transfer function approaches”, Optics Letters **49**, 5159–5162 (2024) (cited on p. 32).

[83] T. E. Gureyev, A. Pogany, D. M. Paganin, and S. W. Wilkins, “Linear algorithms for phase retrieval in the Fresnel region”, Opt. Commun. **231**, 53–70 (2004) (cited on p. 32).

[84] V. Davidoiu, B. Sixou, M. Langer, and F. Peyrin, "Non-linear iterative phase retrieval based on Frechet derivative", Optics Express **19**, 22809–22819 (2011) (cited on p. 34).

[85] S. Maretzke, M. Bartels, M. Krenkel, T. Salditt, and T. Hohage, "Regularized Newton methods for x-ray phase contrast and general imaging problems", Optics Express **24**, 6490–6506 (2016) (cited on p. 34).

[86] M. Langer, Y. Zhang, D. Figueirinhas, J.-B. Forien, K. Mom, C. Mouton, R. Mokso, and P. Villanueva-Perez, "PyPhase – a Python package for X-ray phase imaging", J. Synchrotron Radiat. **28**, 1261–1266 (2021) (cited on p. 34).

[87] F. Wittwer, J. Hagemann, D. Brückner, S. Flenner, and C. G. Schroer, "Phase retrieval framework for direct reconstruction of the projected refractive index applied to ptychography and holography", Optica **9**, 295–302 (2022) (cited on pp. 34, 113).

[88] F. Riva, "Development of new thin film scintillators for high-resolution X-ray imaging", PhD thesis (Université de Lyon, Oct. 2016) (cited on pp. 34, 35, 125).

[89] T. Martin, P.-A. Douissard, M. Couchaud, A. Cecilia, T. Baumbach, K. Dupre, and A. Rack, "LSO-Based Single Crystal Film Scintillator for Synchrotron-Based Hard X-Ray Micro-Imaging", IEEE Trans. Nucl. Sci. **56**, 1412–1418 (2009) (cited on p. 34).

[90] P.-A. Douissard, A. Cecilia, X. Rochet, X. Chapel, T. Martin, T. van de Kamp, L. Helfen, T. Baumbach, L. Luquot, X. Xiao, J. Meinhardt, and A. Rack, "A versatile indirect detector design for hard X-ray microimaging", Journal of Instrumentation **7**, P09016 (2012) (cited on pp. 35, 36, 72).

[91] M. Muller, "Appendix B: Formulae, Relations and Definitions", in *Introduction to Confocal Fluorescence Microscopy*, Vol. 69 (SPIE Press, 2005) (cited on p. 35).

[92] J. W. Goodman, *Introduction to Fourier Optics* (Roberts and Company Publishers, 2005), pp. 143, 372 (cited on pp. 35, 36, 66, 67).

[93] L. Rayleigh, "XII. On the manufacture and theory of diffraction-gratings", The London, Edinburgh, and Dublin Philosophical Magazine and Journal of Science **47**, 81–93 (1874) (cited on p. 36).

[94] E. Hamann, T. Koenig, M. Zuber, A. Cecilia, A. Tyazhev, O. Tolbanov, S. Procz, A. Fauler, T. Baumbach, and M. Fiederle, "Performance of a Medipix3RX Spectroscopic Pixel Detector With a High Resistivity Gallium Arsenide Sensor", IEEE Trans. Med. Imaging **34**, 707–715 (2014) (cited on pp. 36, 37, 68–70, 77).

[95] M. Fiederle, S. Procz, E. Hamann, A. Fauler, and C. Fröjdh, "Overview of GaAs und CdTe Pixel Detectors Using Medipix Electronics", Cryst. Res. Technol. **55**, 2000021 (2020) (cited on p. 36).

[96] S. Procz, G. Roque, C. Avila, J. Racedo, R. Rueda, I. Santos, and M. Fiederle, "Investigation of CdTe, GaAs, Se and Si as Sensor Materials for Mammography", IEEE Trans. Med. Imaging **39**, 3766–3778 (2020) (cited on p. 36).

[97] J. Scholz, L. Birnbacher, C. Petrich, M. Riedel, L. Heck, S. Gkoumas, T. Sellerer, K. Achterhold, and J. Herzen, "Biomedical x-ray imaging with a GaAs photon-counting

detector: A comparative study", APL Photonics **5**, 106108 (2020) (cited on pp. 36, 37, 68–70).

[98] D. Pennicard, S. Smoljanin, B. Struth, H. Hirsemann, A. Fauler, M. Fiederle, O. Tolbanov, A. Zarubin, A. Tyazhev, G. Shelkov, and H. Graafsma, "The LAMBDA photon-counting pixel detector and high-Z sensor development", J. Instrum. **9**, C12026 (2014) (cited on pp. 36, 41, 53, 71, 77).

[99] R. Ballabriga, M. Campbell, and X. Llopart, "Asic developments for radiation imaging applications: The medipix and timepix family", Nucl. Instrum. Methods Phys. Res., Sect. A **878**, 10–23 (2018) (cited on p. 36).

[100] R. Ballabriga, J. Alozy, F. N. Bandi, M. Campbell, N. Egidos, J. M. Fernandez-Tenllado, E. H. M. Heijne, I. Kremastiotis, X. Llopart, B. J. Madsen, D. Pennicard, V. Sriskaran, and L. Tlustos, "Photon Counting Detectors for X-Ray Imaging With Emphasis on CT", IEEE Trans. Radiat. Plasma Med. Sci. **5**, 422–440 (2020) (cited on p. 36).

[101] R. Ballabriga, J. Alozy, G. Blaj, M. Campbell, M. Fiederle, E. Frojdh, E. H. M. Heijne, X. Llopart, M. Pichotka, S. Procz, L. Tlustos, and W. Wong, "The Medipix3RX: a high resolution, zero dead-time pixel detector", Journal of Instrumentation **8**, C02016 (2013) (cited on pp. 36, 37, 67).

[102] P. Zambon, "Enhanced DQE and sub-pixel resolution by single-event processing in counting hybrid pixel electron detectors: A simulation study", Front. Phys. **11**, 1123787 (2023) (cited on p. 37).

[103] E. Frojdh, R. Ballabriga, M. Campbell, M. Fiederle, E. Hamann, T. Koenig, X. Llopart, D. de Paiva Magalhaes, and M. Zuber, "Count rate linearity and spectral response of the Medipix3RX chip coupled to a 300 µm silicon sensor under high flux conditions", Journal of Instrumentation **9**, C04028 (2014) (cited on pp. 37, 71).

[104] R. Spiecker, P. Pfeiffer, A. Biswal, M. Shcherbinin, M. Spiecker, H. Hessdorfer, M. Hurst, Y. Zharov, V. Bellucci, T. Faragó, M. Zuber, A. Herz, A. Cecilia, M. Czyzycki, C. S. B. Dias, D. Novikov, L. Krogmann, E. Hamann, T. van de Kamp, and T. Baumbach, "Dose-efficient *in vivo* X-ray phase contrast imaging at micrometer resolution by Bragg magnifiers", Optica **10**, 1633–1640 (2023) (cited on pp. 39, 41, 53, 57, 59, 63, 65, 68–70, 74, 79, 81, 82, 123, 124).

[105] K. Sakamoto, Y. Suzuki, T. Hirano, and K. Usami, "Improvement of Spatial Resolution of Monochromatic X-ray CT Using Synchrotron Radiation", Jpn. J. Appl. Phys. **27**, 127 (1988) (cited on p. 39).

[106] M. Kuriyama, B. W. Steiner, and R. C. Dobbyn, "Dynamical Diffraction Imaging (Topography) with X-Ray Synchrotron Radiation", Annu. Rev. Mater. Sci. **19**, 183–207 (1989) (cited on p. 39).

[107] D. Korytár, "Basic equations for multiple successive diffraction and angle distortion minimization in X-ray magnifiers", Czech. J. Phys. **40**, 495–512 (1990) (cited on pp. 39, 40).

[108] M. Kuriyama, R. C. Dobbyn, R. D. Spal, H. E. Burdette, and D. R. Black, "Hard X-Ray Microscope With Submicrometer Spatial Resolution", J. Res. Nat. Inst. Stand. Technol. **95**, 559 (1990) (cited on p. 39).

[109] U. Bonse, R. Nusshardt, F. Busch, R. Pahl, J. H. Kinney, Q. C. Johnson, R. A. Saroyan, and M. C. Nichols, "X-ray tomographic microscopy of fibre-reinforced materials", J. Mater. Sci. **26**, 4076–4085 (1991) (cited on pp. 39, 40).

[110] Y. Kagoshima, Y. Tsusaka, K. Yokoyama, K. Takai, S. Takeda, and J. Matsui, "Phase-Contrast X-Ray Imaging Using Both Vertically and Horizontally Expanded Synchrotron Radiation X-Rays with Asymmetric Bragg Reflection", Jpn. J. Appl. Phys. **38**, L470 (1999) (cited on p. 40).

[111] R. D. Spal, "Submicrometer Resolution Hard X-Ray Holography with the Asymmetric Bragg Diffraction Microscope", Phys. Rev. Lett. **86**, 3044–3047 (2001) (cited on pp. 40, 44, 67).

[112] P. Modregger, D. Lübbert, P. Schäfer, and R. Köhler, "Magnified x-ray phase imaging using asymmetric Bragg reflection: Experiment and theory", Phys. Rev. B **74**, 054107 (2006) (cited on pp. 40, 46, 49, 50, 62, 67).

[113] M. Stampanoni, G. Borchert, R. Abela, and P. Rüegsegger, "Bragg magnifier: A detector for submicrometer x-ray computer tomography", J. Appl. Phys. **92**, 7630–7635 (2002) (cited on pp. 40, 41, 67).

[114] R. Köhler and P. Schäfer, "Asymmetric Bragg Reflection as Magnifying Optics", Cryst. Res. Technol. **37**, 734–746 (2002) (cited on p. 40).

[115] M. Stampanoni, G. Borchert, R. Abela, and P. Rüegsegger, "Nanotomography based on double asymmetrical Bragg diffraction", Appl. Phys. Lett. **82**, 2922–2924 (2003) (cited on p. 40).

[116] M. Stampanoni, G. Borchert, and R. Abela, "Progress in microtomography with the Bragg Magnifier at SLS", Radiat. Phys. Chem. **75**, 1956–1961 (2006) (cited on p. 40).

[117] E. F. Eikenberry, C. Brönnimann, G. Hülsen, H. Toyokawa, R. Horisberger, B. Schmitt, C. Schulze-Briese, and T. Tomizaki, "PILATUS: a two-dimensional X-ray detector for macromolecular crystallography", Nucl. Instrum. Methods Phys. Res., Sect. A **501**, 260–266 (2003) (cited on p. 40).

[118] P. Vagovič, D. Korytár, P. Mikulík, A. Cecilia, C. Ferrari, Y. Yang, D. Hänschke, E. Hamann, D. Pelliccia, T. A. Lafford, M. Fiederle, and T. Baumbach, "In-line Bragg magnifier based on V-shaped germanium crystals", Journal of Synchrotron Radiation **18**, 753–760 (2011) (cited on pp. 40, 42).

[119] P. Vagovič, D. Korytár, A. Cecilia, E. Hamann, L. Švéda, D. Pelliccia, J. Härtwig, Z. Zápražný, P. Oberta, I. Dolbnya, K. Shawney, U. Fleschig, M. Fiederle, and T. Baumbach, "High-resolution high-efficiency X-ray imaging system based on the in-line Bragg magnifier and the Medipix detector", Journal of Synchrotron Radiation **20**, 153–159 (2013) (cited on pp. 40, 67).

[120] K. Hirano, Y. Yamashita, Y. Takahashi, and H. Sugiyama, "Development of variable-magnification X-ray Bragg optics", J. Synchrotron Radiat. **22**, 956–960 (2015) (cited on p. 40).

[121] N. Watanabe, M. Suzuki, Y. Higashi, and N. Sakabe, "Rotated-inclined focusing monochromator with simultaneous tuning of asymmetry factor and radius of curvature over a wide wavelength range", J. Synchrotron Radiat. **6**, 64–68 (1999) (cited on pp. 40, 88).

[122] Y. Tsusaka, K. Yokoyama, S. Takeda, M. Urakawa, Y. Kagoshima, J. Matsui, S. Kimura, H. Kimura, K. Kobayashi, and K. Izumi, "Formation of Parallel X-Ray Microbeam and Its Application", Jpn. J. Appl. Phys. **39**, L635 (2000) (cited on pp. 40, 88).

[123] K. Hirano and Y. Takahashi, "Applications of x-ray magnifier and demagnifier to angle-resolved x-ray computed tomography", J. Phys. Conf. Ser. **425**, 192004 (2013) (cited on pp. 40, 88).

[124] J. Kirz, "Phase zone plates for x rays and the extreme uv", JOSA **64**, 301–309 (1974) (cited on p. 40).

[125] A. Snigirev, V. Kohn, I. Snigireva, A. Souvorov, and B. Lengeler, "Focusing high-energy x rays by compound refractive lenses", Appl. Opt. **37**, 653–662 (1998) (cited on p. 40).

[126] P. Kirkpatrick and A. V. Baez, "Formation of Optical Images by X-Rays", JOSA **38**, 766–774 (1948) (cited on p. 40).

[127] R. Mokso, P. Cloetens, E. Maire, W. Ludwig, and J.-Y. Buffière, "Nanoscale zoom tomography with hard x rays using Kirkpatrick-Baez optics", Appl. Phys. Lett. **90**, 144104 (2007) (cited on p. 40).

[128] S. Flenner, A. Kubec, C. David, M. Storm, C. F. Schaber, F. Vollrath, M. Müller, I. Greving, and J. Hagemann, "Hard X-ray nano-holotomography with a Fresnel zone plate", Optics Express **28**, 37514–37525 (2020) (cited on p. 40).

[129] H. Hessdorfer, "A novel 2D in-line Bragg magnifier imaging system for dose-efficient X-ray imaging at synchrotrons", PhD thesis (Universität Freiburg, 2020), 29, 54ff (cited on pp. 42–44, 53, 57).

[130] A. Limaye, "Drishti: a volume exploration and presentation tool", in *Proceedings Volume 8506, Developments in X-Ray Tomography VIII*, Vol. 8506 (SPIE, Oct. 2012), pp. 191–199 (cited on pp. 42, 82).

[131] T. Matsushita and H. Hashizume, *Handbook on Synchrotron Radiation*, edited by E. Koch, Vol. 1 (North Holland Publishing Company, 1983) Chap. 4 (cited on p. 42).

[132] F. E. Christensen, A. Hornstrup, P. K. Frederiksen, S. Abdali, P. Grundsoe, H. W. Schnopper, R. A. Lewis, C. J. Hall, and K. N. Borozdin, "Expanded beam X-ray optics calibration facility at the Daresbury Synchrotron", in Multilayer and Grazing Incidence X-ray/EUV Optics II, Vol. 2011 (SPIE, 1994), pp. 540–548 (cited on p. 42).

[133] C. Kamezawa, K. Hyodo, C. Tokunaga, T. Tsukada, and S. Matushita, "Large-view X-ray imaging for medical applications using the world's only vertically polarized syn-

chrotron radiation beam and a single asymmetric Si crystal", Phys. Med. Biol. **68**, 195010 (2023) (cited on p. 42).

[134] P. Modregger, D. Lübbert, P. Schäfer, R. Köhler, T. Weitkamp, M. Hanke, and T. Baumbach, "Fresnel diffraction in the case of an inclined image plane", Optics Express **16**, 5141–5149 (2008) (cited on pp. 43, 51, 62, 120).

[135] S. Hrivňak, J. Uličný, and P. Vagovič, "Fast Fresnel propagation through a set of inclined reflecting planes applicable for X-ray imaging", Optics Express **26**, 34569–34579 (2018) (cited on pp. 43, 50, 51, 62, 75, 120).

[136] K. Kobayashi, K. Izumi, H. Kimura, S. Kimura, T. Ibuki, Y. Yokoyama, Y. Tsusaka, Y. Kagoshima, and J. Matsui, "X-ray phase-contrast imaging with submicron resolution by using extremely asymmetric Bragg diffractions", Appl. Phys. Lett. **78**, 132–134 (2001) (cited on pp. 43, 67).

[137] E. Abbe, "Ueber einen neuen Beleuchtungsapparat am Mikroskop", Archiv für mikroskopische Anatomie **9**, 469–480 (1873) (cited on p. 44).

[138] P. Modregger, "The Bragg magnifier: a phase sensitive X-ray imaging technique for sub-micrometer resolution", PhD thesis (Humbold-Universität zu Berlin, 2009) (cited on p. 44).

[139] P. Vagovič, L. Švéda, A. Cecilia, E. Hamann, D. Pelliccia, E. N. Gimenez, D. Korytár, K. M. Pavlov, Z. Zápražný, M. Zuber, T. Koenig, M. Olbinado, W. Yashiro, A. Momose, M. Fiederle, and T. Baumbach, "X-ray Bragg magnifier microscope as a linear shift invariant imaging system: image formation and phase retrieval", Optics Express **22**, 21508–21520 (2014) (cited on pp. 49, 51).

[140] S. Hrivňak, A. Hovan, J. Uličný, and P. Vagovič, "Phase retrieval for arbitrary Fresnel-like linear shift-invariant imaging systems suitable for tomography", Biomed. Opt. Express **9**, 4390–4400 (2018) (cited on p. 51).

[141] T. Faragó, S. Gasilov, I. Emslie, M. Zuber, L. Helfen, M. Vogelgesang, and T. Baumbach, "Tofu: a fast, versatile and user-friendly image processing toolkit for computed tomography", Journal of Synchrotron Radiation **29**, 916–927 (2022) (cited on pp. 51, 60, 80, 81).

[142] M. Vogelgesang, T. Faragó, T. F. Morgeneyer, L. Helfen, T. dos Santos Rolo, A. Myagotin, and T. Baumbach, "Real-time image-content-based beamline control for smart 4D X-ray imaging", Journal of Synchrotron Radiat. **23**, 1254–1263 (2016) (cited on p. 53).

[143] K. Hirano, Y. Takahashi, and H. Sugiyama, "Development and application of variable-magnification x-ray Bragg magnifiers", Nucl. Instrum. Methods Phys. Res., Sect. A **741**, 78–83 (2014) (cited on p. 57).

[144] D. H. Bilderback, P. Elleaume, and E. Weckert, "Review of third and next generation synchrotron light sources", J. Phys. B: At. Mol. Opt. Phys. **38**, S773 (2005) (cited on p. 59).

[145] M. Bartels, M. Krenkel, P. Cloetens, W. Möbius, and T. Salditt, "Myelinated mouse nerves studied by X-ray phase contrast zoom tomography", J. Struct. Biol. **192**, 561–568 (2015) (cited on pp. 59, 60).

[146] T. van de Kamp, P. Vagovič, T. Baumbach, and A. Riedel, "A Biological Screw in a Beetle's Leg", Science **333**, 52 (2011) (cited on p. 63).

[147] M. E. Dickinson, A. M. Flenniken, X. Ji, L. Teboul, M. D. Wong, J. K. White, T. F. Meehan, W. J. Weninger, H. Westerberg, H. Adissu, et al., "High-throughput discovery of novel developmental phenotypes", Nature **537**, 508–514 (2016) (cited on p. 63).

[148] A. Cau, V. Beyrand, D. F. A. E. Voeten, V. Fernandez, P. Tafforeau, K. Stein, R. Barsbold, K. Tsogtbaatar, P. J. Currie, and P. Godefroit, "Synchrotron scanning reveals amphibious ecomorphology in a new clade of bird-like dinosaurs", Nature **552**, 395–399 (2017) (cited on p. 63).

[149] M. Töpperwien, F. van der Meer, C. Stadelmann, and T. Salditt, "Three-dimensional virtual histology of human cerebellum by X-ray phase-contrast tomography", Proc. Natl. Acad. Sci. **115**, 6940–6945 (2018) (cited on p. 63).

[150] Y. Ding, D. J. Vanselow, M. A. Yakovlev, S. R. Katz, A. Y. Lin, D. P. Clark, P. Vargas, X. Xin, J. E. Copper, V. A. Canfield, K. C. Ang, Y. Wang, X. Xiao, F. De Carlo, D. B. van Rossum, P. La Riviere, and K. C. Cheng, "Computational 3D histological phenotyping of whole zebrafish by X-ray histotomography", eLife **8**, e44898 (2019) (cited on p. 63).

[151] K. Trinajstic, J. A. Long, S. Sanchez, C. A. Boisvert, D. Snitting, P. Tafforeau, V. Dupret, A. M. Clement, P. D. Currie, B. Roelofs, J. J. Bevitt, M. S. Y. Lee, and P. E. Ahlberg, "Exceptional preservation of organs in Devonian placoderms from the Gogo lagerstätte", Science **377**, 1311–1314 (2022) (cited on p. 63).

[152] M. W. Westneat, O. Betz, R. W. Blob, K. Fezzaa, W. J. Cooper, and W.-K. Lee, "Tracheal Respiration in Insects Visualized with Synchrotron X-ray Imaging", Science **299**, 558–560 (2003) (cited on p. 63).

[153] S. M. Walker, D. A. Schwyn, R. Mokso, M. Wicklein, T. Müller, M. Doube, M. Stampanoni, H. G. Krapp, and G. K. Taylor, "In Vivo Time-Resolved Microtomography Reveals the Mechanics of the Blowfly Flight Motor", PLoS Biol. **12**, e1001823 (2014) (cited on p. 63).

[154] R. Mokso, D. A. Schwyn, S. M. Walker, M. Doube, M. Wicklein, T. Müller, M. Stampanoni, G. K. Taylor, and H. G. Krapp, "Four-dimensional in vivo X-ray microscopy with projection-guided gating", Sci. Rep. **5**, 1–6 (2015) (cited on p. 63).

[155] O. Bolmin, J. J. Socha, M. Alleyne, A. C. Dunn, K. Fezzaa, and A. A. Wissa, "Nonlinear elasticity and damping govern ultrafast dynamics in click beetles", Proc. Natl. Acad. Sci. **118**, e2014569118 (2021) (cited on p. 63).

[156] J. B. Wolfgang Schlegel, *Medizinische Physik 2* (Springer, Berlin, Germany, 2002), p. 49 (cited on pp. 64, 65).

[157] J. Allison, K. Amako, J. Apostolakis, P. Arce, M. Asai, T. Aso, E. Bagli, A. Bagulya, S. Banerjee, G. Barrand, et al., "Recent developments in Geant4", Nucl. Instrum. Methods Phys. Res., Sect. A **835**, 186–225 (2016) (cited on pp. 65, 125).

[158] N. Hünemohr, H. Paganetti, S. Greilich, O. Jäkel, and J. Seco, "Tissue decomposition from dual energy CT data for MC based dose calculation in particle therapy", Med. Phys. **41**, 061714 (2014) (cited on p. 65).

[159] T. Martin and A. Koch, "Recent developments in X-ray imaging with micrometer spatial resolution", Journal of Synchrotron Radiation **13**, 180–194 (2006) (cited on p. 67).

[160] L. Wollesen, F. Riva, P.-A. Douissard, K. Pauwels, T. Martin, and C. Dujardin, "Scintillating thin film design for ultimate high resolution X-ray imaging", J. Mater. Chem. C **10**, 9257–9265 (2022) (cited on pp. 67, 69, 74, 79, 123, 125).

[161] I. Johnson, A. Bergamaschi, H. Billich, S. Cartier, R. Dinapoli, D. Greiffenberg, M. Guizar-Sicairos, B. Henrich, J. Jungmann, D. Mezza, A. Mozzanica, B. Schmitt, X. Shi, and G. Tinti, "Eiger: a single-photon counting x-ray detector", J. Instrum. **9**, C05032 (2014) (cited on p. 67).

[162] K. Hirano, Y. Yamashita, Y. Takahashi, and H. Sugiyama, "Development of variable-magnification X-ray Bragg optics", Journal of Synchrotron Radiation **22**, 956–960 (2015) (cited on p. 67).

[163] A. Mittone, I. Manakov, L. Broche, C. Jarnias, P. Coan, and A. Bravin, "Characterization of a sCMOS-based high-resolution imaging system", Journal of Synchrotron Radiation **24**, 1226–1236 (2017) (cited on pp. 68, 69).

[164] T. J. Davis, "X-Ray Diffraction Imaging Using Perfect Crystals", J. X-Ray Sci. Technol. **6**, 317–342 (1996) (cited on p. 69).

[165] I. A. Cunningham and R. Shaw, "Signal-to-noise optimization of medical imaging systems", J. Opt. Soc. Am. A, JOSAA **16**, 621–632 (1999) (cited on p. 70).

[166] P.-A. Douissard, A. Cecilia, T. Martin, V. Chevalier, M. Couchaud, T. Baumbach, K. Dupré, M. Kühbacher, and A. Rack, "A novel epitaxially grown LSO-based thin-film scintillator for micro-imaging using hard synchrotron radiation", J. Synchrotron Radiat. **17**, 571–583 (2010) (cited on p. 72).

[167] C. Homann, T. Hohage, J. Hagemann, A.-L. Robisch, and T. Salditt, "Validity of the empty-beam correction in near-field imaging", Phys. Rev. A **91**, 013821 (2015) (cited on p. 76).

[168] *Modelling of the MTF performance of high spatial resolution X-ray detectors*, `https://www.esrf.fr/home/UsersAndScience/Publications/Highlights/highlights-2014/ET/ET04.html`, [online; accessed 18/07/2023] (cited on p. 79).

[169] L.-Y. Li, "Worldwide use of *Trichogramma* for biological control on different crops: a survey", Biological control with egg parasitoids, 37–53 (1994) (cited on p. 80).

[170] Z.-Y. Wang, K.-L. He, F. Zhang, X. Lu, and D. Babendreier, "Mass rearing and release of *Trichogramma* for biological control of insect pests of corn in China", Biol. Control **68**, 136–144 (2014) (cited on p. 81).

[171] L.-S. Zang, S. Wang, F. Zhang, and N. Desneux, "Biological Control with *Trichogramma* in China: History, Present Status, and Perspectives", Annu. Rev. Entomol. **66**, 463–484 (2021) (cited on p. 81).

[172] A. Cherif, R. Mansour, and K. Grissa-Lebdi, "The egg parasitoids *Trichogramma*: from laboratory mass rearing to biological control of lepidopteran pests", Biocontrol Science and Technology **31**, 661–693 (2021) (cited on p. 81).

[173] A. Ivezić, B. Trudić, and G. Draškić, "The usage of beneficial insects as a biological control measure in large-scale farming - a case study review on *Trichogramma* spp.", Acta agriculturae Slovenica **118**, 1–13 (2022) (cited on p. 81).

[174] X. Yang, R. Hofmann, R. Dapp, T. van de Kamp, T. dos Santos Rolo, X. Xiao, J. Moosmann, J. Kashef, and R. Stotzka, "TV-based conjugate gradient method and discrete L-curve for few-view CT reconstruction of X-ray *in vivo* data", Optics Express **23**, 5368–5387 (2015) (cited on p. 81).

[175] J. Dong, J. Fu, and Z. He, "A deep learning reconstruction framework for X-ray computed tomography with incomplete data", PLoS One **14**, e0224426 (2019) (cited on p. 81).

[176] X. Duan, X. F. Ding, N. Li, F.-X. Wu, X. Chen, and N. Zhu, "Sparse2Noise: Low-dose synchrotron X-ray tomography without high-quality reference data", Comput. Biol. Med. **165**, 107473 (2023) (cited on p. 81).

[177] J. Lehtinen, J. Munkberg, J. Hasselgren, S. Laine, T. Karras, M. Aittala, and T. Aila, "Noise2Noise: Learning Image Restoration without Clean Data", arXiv, `10.48550/arXiv.1803.04189` (2018) (cited on p. 82).

[178] Y. Zharov, E. Ametova, R. Spiecker, T. Baumbach, G. Burca, and V. Heuveline, "Shot noise reduction in radiographic and tomographic multi-channel imaging with self-supervised deep learning", Optics Express **31**, 26226–26244 (2023) (cited on p. 82).

[179] T. van de Kamp, I. Mikó, A. H. Staniczek, B. Eggs, D. Bajerlein, T. Faragó, L. Hagelstein, E. Hamann, R. Spiecker, T. Baumbach, P. Janšta, and L. Krogmann, "Evolution of flexible biting in hyperdiverse parasitoid wasps", Proc. R. Soc. B. **289**, 20212086 (2022) (cited on p. 83).

[180] Z. Zhang, H. Dierks, N. Lamers, C. Sun, K. Nováková, C. Hetherington, I. G. Scheblykin, and J. Wallentin, "Single-Crystalline Perovskite Nanowire Arrays for Stable X-ray Scintillators with Micrometer Spatial Resolution", ACS Appl. Nano Mater. **5**, 881–889 (2022) (cited on p. 83).

[181] M. Bührer, M. Stampanoni, X. Rochet, F. Büchi, J. Eller, and F. Marone, "High-numerical-aperture macroscope optics for time-resolved experiments", Journal of Synchrotron Radiation **26**, 1161–1172 (2019) (cited on p. 83).

[182] Z. Wang, K. Anagnost, C. W. Barnes, D. M. Dattelbaum, E. R. Fossum, E. Lee, J. Liu, J. J. Ma, W. Z. Meijer, W. Nie, C. M. Sweeney, A. C. Therrien, H. Tsai, and X. Yue, "Billion-pixel X-ray camera (BiPC-X)", Rev. Sci. Instrum. **92**, 043708 (2021) (cited on p. 83).

[183] A. Zamir, O. J. Arthurs, C. K. Hagen, P. C. Diemoz, T. Brochard, A. Bravin, N. J. Sebire, and A. Olivo, "X-ray phase contrast tomography; proof of principle for post-mortem imaging", The British Journal of Radiology **89**, 20150565 (2016) (cited on p. 85).

[184] M. Donnelley, K. S. Morgan, R. Gradl, M. Klein, D. Hausermann, C. Hall, A. Maksimenko, and D. W. Parsons, "Live-pig-airway surface imaging and whole-pig CT at the Australian Synchrotron Imaging and Medical Beamline", Journal of Synchrotron Radiation **26**, 175–183 (2019) (cited on p. 85).

[185] W. L. Wagner, F. Wuennemann, S. Pacilé, J. Albers, F. Arfelli, D. Dreossi, J. Biederer, P. Konietzke, W. Stiller, M. O. Wielpütz, et al., "Towards synchrotron phase-contrast lung imaging in patients - a proof-of-concept study on porcine lungs in a human-scale chest phantom", Journal of Synchrotron Radiation **25**, 1827–1832 (2018) (cited on p. 85).

[186] K. S. Morgan, D. Parsons, P. Cmielewski, A. McCarron, R. Gradl, N. Farrow, K. Siu, A. Takeuchi, Y. Suzuki, K. Uesugi, M. Uesugi, N. Yagi, C. Hall, M. Klein, A. Maksimenko, A. Stevenson, D. Hausermann, M. Dierolf, F. Pfeiffer, and M. Donnelley, "Methods for dynamic synchrotron X-ray respiratory imaging in live animals", J. Synchrotron Radiat. **27**, 164–175 (2020) (cited on p. 85).

[187] C. David, B. Nöhammer, H. H. Solak, and E. Ziegler, "Differential X-ray phase contrast imaging using a shearing interferometer", Appl. Phys. Lett. **81**, 3287–3289 (2002) (cited on p. 85).

[188] F. Pfeiffer, J. Herzen, M. Willner, M. Chabior, S. Auweter, M. Reiser, and F. Bamberg, "Grating-based X-ray phase contrast for biomedical imaging applications", Z. Med. Phys. **23**, 176–185 (2013) (cited on p. 85).

[189] C. Tavakoli, E. Cuccione, C. Dumot, D. Cormode, M. Wiart, H. Elleaume, and E. Brun, "Tracking cells in the brain of small animals using synchrotron multi-spectral phase contrast imaging", in Medical Imaging 2021: Physics of Medical Imaging, Vol. 11595 (SPIE, 2021), pp. 1218–1224 (cited on pp. 85, 98).

[190] C. Walsh, P. Tafforeau, W. Wagner, D. Jafree, A. Bellier, C. Werlein, M. Kühnel, E. Boller, S. Walker-Samuel, J. Robertus, et al., "Imaging intact human organs with local resolution of cellular structures using hierarchical phase-contrast tomography", Nature Methods **18**, 1532–1541 (2021) (cited on p. 85).

[191] B. D. Arhatari, A. W. Stevenson, B. Abbey, Y. I. Nesterets, A. Maksimenko, C. J. Hall, D. Thompson, S. C. Mayo, T. Fiala, H. M. Quiney, et al., "X-ray Phase-Contrast Computed Tomography for Soft Tissue Imaging at the Imaging and Medical Beamline

(IMBL) of the Australian Synchrotron", Applied Sciences **11**, 4120 (2021) (cited on pp. 85, 98).

[192] I. Häggmark, K. Shaker, S. Nyrén, B. Al-Amiry, E. Abadi, W. P. Segars, E. Samei, and H. M. Hertz, "Phase-contrast virtual chest radiography", Proc. Natl. Acad. Sci. **120**, e2210214120 (2023) (cited on p. 85).

[193] F. Cianciosi, A.-L. Buisson, P. Tafforeau, and P. Van Vaerenbergh, "BM18, the New ESRF-EBS Beamline for Hierarchical Phase-Contrast Tomography", JACOW Publishing, 1–5 (2021) (cited on pp. 85, 98).

[194] T. Lang, N. Saeidnezhad, K. Dremel, D. Weller, M. Diez, A. M. Stock, T. Sauer, F. Cianciosi, C. Jarnias, P. Tafforeau, and S. Zabler, "Multiscale Phase-Contrast Tomography at BM18", e-Journal of Nondestructive Testing **28**, 3 (2023) (cited on pp. 85, 98).

[195] R. Spiecker, M. Spiecker, A. Biswal, M. Shcherbinin, and T. Baumbach, "The Bragg demagnifier: X-ray imaging with kilometer propagation distance within a meter", arXiv, `10.48550/arXiv.2310.16771` (2023) (cited on pp. 85, 92, 93, 104, 106).

[196] Z. Huang and R. D. Ruth, "Laser-electron storage ring", Phys. Rev. Lett. **80**, 976 (1998) (cited on pp. 91, 107).

[197] B. Günther, R. Gradl, C. Jud, E. Eggl, J. Huang, S. Kulpe, K. Achterhold, B. Gleich, M. Dierolf, and F. Pfeiffer, "The versatile X-ray beamline of the Munich Compact Light Source: design, instrumentation and applications", Journal of Synchrotron Radiation **27**, 1395–1414 (2020) (cited on pp. 91, 107).

[198] B. Hornberger, J. Kasahara, R. Ruth, R. Loewen, and J. Khaydarov, "Inverse Compton scattering X-ray source for research, industry and medical applications", in *Proceedings Volume 11886, International Conference on X-Ray Lasers 2020*, Vol. 11886 (SPIE, July 2021), pp. 51–60 (cited on pp. 91, 107).

[199] J. Härtwig, *Introduction into the dynamical theory of X-ray diffraction for perfect crystals*, `https://www.esrf.fr/files/live/sites/www/files/Instrumentation/friday-lectures-slides/Talk_Hartwig.pdf`, [online; accessed 10/10/2023] (cited on pp. 93, 97, 127).

[200] X. Huang, A. Macrander, M. Honnicke, Y. Cai, and P. Fernandez, "Dispersive spread of virtual sources by asymmetric X-ray monochromators", Journal of Applied Crystallography **45**, 255–262 (2012) (cited on p. 93).

[201] C. G. Schroer, H.-C. Wille, O. H. Seeck, K. Bagschik, H. Schulte-Schrepping, M. Tischer, H. Graafsma, W. Laasch, K. Baev, S. Klumpp, R. Bartolini, H. Reichert, W. Leemans, and E. Weckert, "The synchrotron radiation source PETRA III and its future ultra-low-emittance upgrade PETRA IV", Eur. Phys. J. Plus **137**, 1312 (2022) (cited on pp. 98, 127).

[202] G. E. Barbone, A. Bravin, A. Mittone, S. Grosu, J. Ricke, G. Cavaletti, V. Djonov, and P. Coan, "High-Spatial-Resolution Three-dimensional Imaging of Human Spinal Cord

and Column Anatomy with Postmortem X-ray Phase-Contrast Micro-CT", Radiology (2020) (cited on p. 98).

[203] A. Bravin, "Exploiting the X-ray refraction contrast with an analyser: the state of the art", Journal of Physics D: Applied Physics **36**, A24 (2003) (cited on p. 105).

[204] A. J. Morgan, K. T. Murray, M. Prasciolu, H. Fleckenstein, O. Yefanov, P. Villanueva-Perez, V. Mariani, M. Domaracky, M. Kuhn, S. Aplin, I. Mohacsi, M. Messerschmidt, K. Stachnik, Y. Du, A. Burkhart, A. Meents, E. Nazaretski, H. Yan, X. Huang, Y. S. Chu, H. N. Chapman, and S. Bajt, "Ptychographic X-ray speckle tracking with multilayer Laue lens systems", J. Appl. Crystallogr. **53**, 927–936 (2020) (cited on p. 105).

[205] A. Rohou and N. Grigorieff, "CTFFIND4: Fast and accurate defocus estimation from electron micrographs", J. Struct. Biol. **192**, 216–221 (2015) (cited on p. 105).

[206] S. D. Shastri, "Combining flat crystals, bent crystals and compound refractive lenses for high-energy X-ray optics", Journal of Synchrotron Radiatiation **11**, 150–156 (2004) (cited on pp. 107, 111).

[207] P. Kirkpatrick and A. V. Baez, "Formation of Optical Images by X-Rays", JOSA **38**, 766–774 (1948) (cited on pp. 107, 111).

[208] D. Berthe, L. Heck, S. Resch, M. Dierolf, J. Brantl, G. Benedikt, C. Petrich, K. Achterhold, F. Pfeiffer, S. Grandl, K. Hellerhoff, and J. Herzen, "Grating-Based Phase-Contrast Breast ComputedTomography at an Inverse Compton Source", Research Square, `10.21203/rs.3.rs-3891369/v1` (2024) (cited on p. 113).

[209] A. H. Barnett, J. F. Magland, and L. af Klinteberg, "A parallel non-uniform fast Fourier transform library based on an "exponential of semicircle" kernel", arXiv, `10.48550/arXiv.1808.06736` (2019) (cited on p. 121).

[210] X. Chen, L. Ren, Y. Qiu, and H. Liu, "New method for determining the depth of field of microscope systems", Appl. Opt. **50**, 5524–5533 (2011) (cited on p. 122).

[211] H. Hopkins H., "The frequency response of a defocused optical system", Proc. R. Soc. London A - Math. Phys. Sci. **231**, 91–103 (1955) (cited on p. 125).

[212] F. Masiello, "X-ray diffraction and imaging with a coherent beam: application to X-Ray optical elements and crystal exhibiting phase inhomogeneities", PhD thesis (Université de Grenoble; Università di Torino, 2011), p. 24 (cited on p. 127).

List of publications

T. Faragó, **R. Spiecker**, M. Hurst, M. Zuber, A. Cecilia, and T. Baumbach, "Phase retrieval in propagation-based X-ray imaging beyond the limits of transport of intensity and contrast transfer function approaches", Optics Letters **49**, 5159–5162 (2024).

R. Spiecker, P. Pfeiffer, A. Biswal, M. Shcherbinin, M. Spiecker, H. Hessdorfer, M. Hurst, Y. Zharov, V. Bellucci, T. Faragó, M. Zuber, A. Herz, A. Cecilia, M. Czyzycki, C. S. B. Dias, D. Novikov, L. Krogmann, E. Hamann, T. van de Kamp, and T. Baumbach, "Dose-efficient *in vivo* X-ray phase contrast imaging at micrometer resolution by Bragg magnifiers", Optica **10**, 1633–1640 (2023).

R. Spiecker, M. Spiecker, A. Biswal, M. Shcherbinin, and T. Baumbach, "The Bragg demagnifier: X-ray imaging with kilometer propagation distance within a meter", arXiv, `10.48550/arXiv.2310.16771` (2023).

Y. Zharov, E. Ametova, **R. Spiecker**, T. Baumbach, G. Burca, and V. Heuveline, "Shot noise reduction in radiographic and tomographic multi-channel imaging with self-supervised deep learning", Optics Express **31**, 26226–26244 (2023).

T. van de Kamp, I. Mikó, A. H. Staniczek, B. Eggs, D. Bajerlein, T. Faragó, L. Hagelstein, E. Hamann, **R. Spiecker**, T. Baumbach, P. Janšta, and L. Krogmann, "Evolution of flexible biting in hyperdiverse parasitoid wasps", Proc. R. Soc. B. **289**, 20212086 (2022).

M. Obermair, S. Hettler, M. Dries, M. Hugenschmidt, **R. Spiecker**, and D. Gerthsen, "Carbon-film-based Zernike phase plates with smooth thickness gradient for phase-contrast transmission electron microscopy with reduced fringing artefacts", J. Microsc. **287**, 45–58 (2022).

R. Pretzsch, M. Dries, S. Hettler, M. Spiecker, M. Obermair, and D. Gerthsen, "Investigation of hole-free phase plate performance in transmission electron microscopy under different operation conditions by experiments and simulations", Adv. Struct. Chem. Imag. **5**, 1–11 (2019).

Acknowledgments

Many people supported me in accomplishing the project presented in this thesis. I would like to thank everyone involved during these years.

First of all, I would like to thank Prof. Tilo Baumbach for giving me the opportunity to join the institute and for supervising my thesis. You woke my fascination about the topic of X-ray imaging and Bragg magnifiers, and gave me the perfect balance between guidance, support and new perspectives on the one hand, and freedom and encouragement to follow my own ideas on the other hand. I am grateful for your supervision and mentorship throughout these years, as well as the possibility to travel to conferences for presenting and discussing my research. I always felt encouraged and appreciated by you, and I value the discussions we had together, your never-ending energy that gave me courage when needed, and the joy we had experimenting not only with electromagnetic but also with acoustic waves.

I also express my gratitude to Prof. Michael Fiederle for his willingness to serve as second referee for my thesis and for sharing his expertise on X-ray detectors.

I would like to thank all my colleagues at IPS and LAS with whom I have shared unforgettable moments at the institute, at beamlines and conferences, during lunches and coffee breaks, as well as activities outside of work. Special thanks go to Holger for introducing me to the topic and working closely with me during the first years. Ady and Mykola, since you joined the institute, we have shared both stressful and enjoyable moments during experiments, discussions, and breaks. I appreciate your friendly and cooperative nature. Elias, Mathias and Valerio, thank you for sharing your experience and joining beamtimes. Pauline and Thomas, the *in vivo* study would not have been possible without you, thanks a lot for your commitment. I am also grateful to Thomas for always having an open ear for me and supporting me whenever possible. Angelica, I could always come to you and count on your support. Your Italian spirit enriches our institute. I extend my thanks to Angelica, Dmitri, Sato, and Mateusz for their support during beamtimes. Marcus and Tomáš, thank you for teaching me how to operate concert and helping me with motor and camera control issues, not to mention the smooth management of endless storage space and computing power on the servers. I would also like to thank Daniel for his support, Ralf for passionate discussions during my early time at IPS, all the colleagues from the computing group for bringing in fresh wind during the last year, Janes for his never-ending thoughtfulness, and Jenny for being an excellent office mate.

Finally, I thank Michał for insightful and instructive discussions on dynamical diffraction theory.

The realization of this work would not have been possible without the unwavering support of our administration, IT and technical staff, and the mechanical workshop. A big thank you to all of you, especially Bianca, Margit, Jan, Stefan, David, Julian and Tobias.

My special thanks go to my parents, who made this education possible for me and have always believed in me, to my sisters, who were always by my side, and to my father-in-law for his interest in my work and support. Lastly, I cannot express enough gratitude to my husband, Martin. Your unwavering support, both scientifically and emotionally, has been truly incredible.